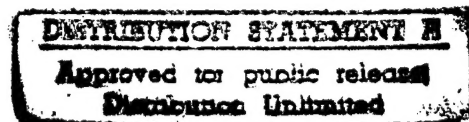


Semiannual Technical Report

Interface Properties of Wide Bandgap Semiconductor Structures

Supported under Grant #N00014-92-J-1477
Office of the Chief of Naval Research
Report for the period 1/1/97-6/30/97

R. F. Davis, S. Bedair*, J. Bernholc†, R. J. Nemanich†, and Z. Sitar
c/o Materials Science and Engineering Department,
*Electrical and Computer Engineering Department
and †Department of Physics
North Carolina State University
Campus Box 7907
Raleigh, NC 27695-7907



June, 1997

DTIC QUALITY INSPECTED 3

19970909 079

REPORT DOCUMENTATION PAGE

Form Approved
OMB No. 0704-0188

Public reporting burden for this collection of information is estimated to average 1 hour per response, including the time for reviewing instructions, searching existing data sources, gathering and maintaining the data needed, and completing and reviewing the collection of information. Send comments regarding this burden estimate or any other aspect of this collection of information, including suggestions for reducing this burden to Washington Headquarters Services, Directorate for Information Operations and Reports, 1215 Jefferson Davis Highway, Suite 1204, Arlington, VA 22202-4302, and to the Office of Management and Budget Paperwork Reduction Project (0704-0188), Washington, DC 20503.

| | | | | | |
|---|--|---|-----------------------------------|---|--|
| 1. AGENCY USE ONLY (Leave blank) | | 2. REPORT DATE June, 1997 | | 3. REPORT TYPE AND DATES COVERED Semiannual Technical 1/1/97-6/30/97 | |
| 4. TITLE AND SUBTITLE Interface Properties of Wide Bandgap Semiconductor Structures | | | | 5. FUNDING NUMBERS uri41114a-01 1114SS N00179 N66005 4B855 | |
| 6. AUTHOR(S) R. F. Davis, S. Bedair, J. Bernholc, R. J. Nemanich, and Z. Sitar | | | | | |
| 7. PERFORMING ORGANIZATION NAME(S) AND ADDRESS(ES) North Carolina State University Hillsborough Street Raleigh, NC 27695 | | | | 8. PERFORMING ORGANIZATION REPORT NUMBER N00014-92-J-1477 | |
| 9. SPONSORING/MONITORING AGENCY NAMES(S) AND ADDRESS(ES) Sponsoring: ONR, 800 N. Quincy, Arlington, VA 22217-5660 Monitoring: Administrative Contracting Officer, Office of Naval Research Regional Office Atlanta, 101 Marietta Tower, Suite 2805 101 Marietta Street Atlanta, GA 30323-6145 | | | | 10. SPONSORING/MONITORING AGENCY REPORT NUMBER | |
| 11. SUPPLEMENTARY NOTES | | | | | |
| 12a. DISTRIBUTION/AVAILABILITY STATEMENT Approved for Public Release; Distribution Unlimited | | | | 12b. DISTRIBUTION CODE | |
| 13. ABSTRACT (Maximum 200 words) Page 2 of 2 on GaN films ICP etched at low power did not differ from unetched GaN. Leakage currents for the low power and unetched GaN were similar to -10V (less than -1nA). The forward and reverse characteristics for 100 μ m diameter Pt contacts on GaN etched at high power were similar to those of large (150-200 μ m diameter) unetched GaN contacts. The barrier heights for these contacts were low and the ideality factors high. Molecular dynamics calculations showed that Si and Ge are effective-mass donors, and C is an effective-mass acceptor in wurtzite GaN. The doping efficiency may be severely limited by self-compensation and formation of nearest-neighbor pairs under certain growth conditions. Samples of GaN were implanted at energies (doses) of 160 KeV or 200 KeV ($1e14$ cm^{-2} to $1e15$ cm^{-2}) with Si; 120 KeV ($1e14$ cm^{-2} to $1e15$ cm^{-2}) with Mg; and 180 KeV/130 KeV ($5e14$ cm^{-2} to $5e15$ cm^{-2}) with Ca/P at 25°C, 550°C, and 650°C. Electrical activation has been observed; however, it was very small in all samples even after repeated annealing steps. The insulators of SiO ₂ , GaO and AlN were grown or deposited on GaN films. MIS capacitors were fabricated using plasma deposited SiO ₂ . The flatband voltage for the SiO ₂ was 1.1 V; the calculated fixed oxide charge was 4.1×10^{11} cm^{-2} . The lineshapes of the Raman E2 mode of Al _x Ga _{1-x} N in the composition range $0 < x < 1$ exhibited significant asymmetry and broadening toward the high energy range. The spatial correlation model accounted for these results. Calculations indicated and X-ray scattering confirmed the absence of long-range order. The relative intensity of the superlattice line was negligible. The line broadening of the E2 mode exhibited a maximum at $x = 0.5$ indicative of a random disordered alloy system. The effects of strain on the band offsets range from 20 to 40%. The AlN/GaN/InN interfaces are all of type I; the Al _{0.5} Ga _{0.5} N interface with cubic AlN(001) is of type II. The valence band- and conduction band-offset in the (0001) GaN on AlN interface is -0.57 eV and 1.87 eV, respectively. | | | | | |
| 14. SUBJECT TERMS diamond, silicon carbide, gallium nitride, aluminum nitride, C, SiC, GaN, AlN, field emission, heterostructures, MBE, flow dynamics, N ₂ diluent, dry etching, ion implantation, Schottky diode, doping, band offset | | | | 15. NUMBER OF PAGES 188 | |
| | | | | 16. PRICE CODE | |
| 17. SECURITY CLASSIFICATION OF REPORT UNCLAS | 18. SECURITY CLASSIFICATION OF THIS PAGE UNCLAS | 19. SECURITY CLASSIFICATION OF ABSTRACT UNCLAS | 20. LIMITATION OF ABSTRACT SAR | | |

Table of Contents

| | |
|---|-----|
| I. Introduction | 1 |
| Carbon-based Materials | |
| II. Field Emission Energy Distribution Analysis of Wide Band Gap Field Emitters <i>R. Schlessner, B. L. McCarson, M. T. McClure and Z. Sitar</i> | 3 |
| III. Surface Cleaning, Electronic States and Electron Affinity of Diamond (100), (111) and (110) Surfaces <i>P. K. Baumann and R. J. Nemanich</i> | 10 |
| IV. Electron Affinity and Schottky Barrier Height of Metal Diamond (100), (111) and (110) Interfaces <i>P. K. Baumann and R. J. Nemanich</i> | 30 |
| V. Electrical Characterization of Metal/AlN/6H-SiC(0001) Heterostructures <i>M. O. Aboelfotoh, R. S. Kern, and R. F. Davis</i> | 56 |
| Nitrogen-based Materials | |
| VI. Analysis of Reactor Geometry and Diluent Gas Flow Effects on the Metalorganic Vapor Phase Epitaxy of AlN and GaN Thin Films on α (6H)-SiC Substrates <i>D. Hanser and R. F. Davis</i> | 64 |
| VII. Effect of Hydrogen on the Indium Incorporation in InGaN Epitaxial Films <i>E. L. Piner, M. K. Behbehani, N. A. El-Masry, F. G. McIntosh, J. C. Roberts, K. S. Boutros, and S. M. Bedair</i> | 80 |
| VIII. Impurity Dependence on Hydrogen and Ammonia Flow Rates in InGaN Bulk Films <i>E. L. Piner, M. K. Behbehani, N. A. El-Masry, J. C. Roberts, F. G. McIntosh, and S. M. Bedair</i> | 86 |
| IX. Optical Memory Effect in GaN Epitaxial Films <i>V. A. Joshkin, J. C. Roberts, F. G. McIntosh, S. M. Bedair, E. L. Piner, M. K. Behbehani and N. A. El-Masry</i> | 93 |
| X. Dry Etching of Gallium Nitride <i>S. Smith and R. F. Davis</i> | 100 |
| XI. Platinum Schottky Contacts on Etched and Unetched n-type GaN <i>K. Tracy, S. Smith and R. Davis</i> | 106 |
| XII. Theory of Group-IV Impurities in Wide Gap Nitrides <i>E. Carlson and R. F. Davis</i> | 113 |
| XIII. Ion Implantation of N- and P-type Dopants Into GaN <i>E. L. Piner, M. K. Behbehani, N. A. El-Masry, F. G. McIntosh, J. C. Roberts, K. S. Boutros, and S. M. Bedair</i> | 117 |

| | | |
|--------|--|-----|
| XIV. | Multicolor Emission from Stacked AlGa _N /InGa _N Double Heterostructures <i>J. C. Roberts, C. A. Parker, M. E. Aumer, F. G. McIntosh, S. M. Bedair, E. L. Piner, and M. K. Behbehani</i> | 128 |
| XV. | III-V Nitrides for Use in Semiconductor Microelectronic Device Applications <i>R. Therrien and R. F. Davis</i> | 134 |
| XVI. | Raman Analysis of the Configurational Disorder in Al _x Ga _{1-x} N Films <i>L. Bergman, M. D. Bremser, W. G. Perry, R. F. Davis, M. Dutta and R. J. Nemanich</i> | 142 |
| XVII. | Theory of C, Si, and Ge Impurities in GaN and AlN <i>P. Boguslawski and J. Bernholc</i> | 149 |
| XVIII. | Strain Effects on the Interface Properties of Nitride Semiconductors <i>M. Buongiorno Nardelli, K. Rapcewicz and J. Bernholc</i> | 156 |
| XIX. | UV Photoemission Study of Heteroepitaxial AlGa _N Films Grown on 6H-SiC Surfaces <i>M. C. Benjamin, S. W. King, R. F. Davis and R. J. Nemanich</i> | 169 |
| XX. | Thin Films of Aluminum Nitride and Aluminum Gallium Nitride for Cold Cathode Applications <i>A. T. Sowers, J. A. Christman, M. D. Bremser, B. L. Ward, R. F. Davis, and R. J. Nemanich</i> | 175 |
| XXI. | Theory of Interfaces in Wide Gap Nitrides <i>M. Buongiorno Nardelli, K. Rapcewicz, E. L. Briggs, C. Bungaro and J. Bernholc</i> | 182 |
| XXII. | Distribution List | 188 |

I. Introduction

Heteroepitaxy is the growth of a crystal (or a film) on a foreign crystalline substrate that determines its orientation. Such oriented growth requires that lattice planes in both materials have similar structure. In general, an epitaxial relationship is probable whenever the orientation of the substrate and overgrowth produces an interface with a highly coincident atomic structure having low interfacial energy relative to a random arrangement.

During the past decade, nonequilibrium techniques have been developed for the growth of epitaxial semiconductors, superconductors, insulators and metals which have led to new classes of artificially structured materials. In many cases, the films were deposited on substrates having a different chemistry from that of the film, and heteroepitaxy was achieved. Moreover, layered structures with a periodicity of a few atomic layers have also been produced by the sequential heteroepitaxial deposition of a film of one type on another. Metastable structures can be generated which possess important properties not present in equilibrium systems. A consideration of the materials under consideration for next generation electronic and optoelectronic devices, e.g., the III-V nitrides show that only a few of them can currently be grown in bulk, single crystal form having a cross-sectional area of $>3 \text{ cm}^2$. Thus other, commercially available substrates must be used. This introduces a new set of challenges for the successful growth of device quality films which are not present in homoepitaxial growth and which must be surmounted if these materials are to be utilized in device structures.

In addition to providing structures which do not exist in nature, applications of advanced heteroepitaxial techniques permit the growth of extremely high quality heterostructures involving semiconductors, metals, and insulators. These heterostructures offer the opportunity to study relationships between the atomic structure and the electrical properties of both the film itself and the interface between the two dissimilar materials. They also allow the study of epitaxial growth between materials exhibiting very different types (ionic, covalent, or metallic) of bonding.

While the potential of heteroepitaxial deposition has been demonstrated, significant advances in theoretical understanding, experimental growth and control of this growth, and characterization are required to exploit the capabilities of this process route. It is particularly important to understand and control the principal processes which control heteroepitaxy at the atomic level. It is this type of research, as well as the chemistry of dry etching via laser and plasma processing, which forms the basis of the research in this grant.

The materials of concern in this report are classified as wide bandgap semiconductors and include diamond, SiC and the III-V nitrides of Al, Ga, and In and their alloys. The extremes in electronic and thermal properties of diamond and SiC allow the types and numbers of current and conceivable applications of these materials to be substantial. However, a principal driving force for the interest in the III-V nitrides is their potential for solid-state optoelectronic devices

for light emission and detection from the visible through the far ultraviolet range of the spectrum.

The principal objectives of the research program are the determination of (1) the fundamental physical and chemical processes ongoing at the substrate surface and substrate/film interface during the heteroepitaxial deposition of both monocrystalline films of the materials noted above, as well as metal contacts on these materials, (2) the mode of nucleation and growth of the materials noted in (1) on selected substrates and on each other in the fabrication of multilayer heterostructures, (3) the resulting properties of the individual films and the layered structures and the effect of interfacial defects on these properties, (4) the development and use of theoretical concepts relevant to the research in objectives (1-3) to assist in the fabrication of improved films and structures and (5) the determination of process chemistry which leads to the laser assisted and plasma etching of these wide bandgap compound semiconductors.

This is the tenth bi-annual report since the initiation of the project. The following sections introduce each topic, detail the experimental approaches, report the latest results and provide a discussion and conclusion for each subject. Each major section is self-contained with its own figures, tables and references.

Carbon-based Materials

II. Field Emission Energy Distribution Analysis of Wide Band Gap Field Emitters

A. Introduction

Wide band gap materials have been identified as particularly suitable for field emission purposes due to their low or even negative [1-3] electron affinities, as well as their thermal, chemical, and mechanical stability. Although progress has been made in technologically relevant areas of the field, the underlying physical mechanisms of field emission are not yet completely understood. In many studies, the characterization of field emitters was limited to application-oriented I - V measurements. However, additional and qualitatively different analytical information is required to extensively characterize field emission from wide bandgap materials and to promote our understanding of the underlying phenomena. Field emission energy distribution (FEED) measurements were performed on tip-shaped Mo field emitters coated with intrinsic diamond and cubic boron nitride (c-BN) powders, in order to determine the origin of field emitted electrons.

Voltage dependent FEED analysis, termed V-FEED in the following, was applied to directly evidence field induced band bending, which is generally believed to play an essential role in the electron emission process from semiconductors.

B. Experimental Technique

Field emission energy distribution analysis consists of measuring energy spectra of field emitted electrons by means of an electron spectrometer. As had already been predicted for the case of metallic field emitters by Fowler and Nordheim [4], electrons originate from energy levels close to the Fermi level, E_F . Figure 1 illustrates the relationship between the measured kinetic energy, E_{kin} , of an electron emitted from an energy level E , the potential, V , applied between the cathode and the analyzer, and the analyzer work function, Φ_A .

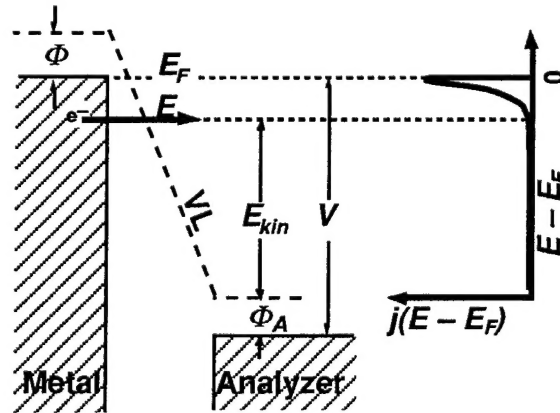


Figure 1. Definition of energy scale $(E - E_F)$ used in FEED measurements. $j(E - E_F)$: electron energy distribution, V : applied voltage, Φ : metal work function, Φ_A : detector work function, VL : vacuum level, E_{kin} : measured kinetic energy.

The Fermi level of the metal, E_F , serves as a reference energy level, as its energy relative to the Fermi level of the analyzer depends only on the applied voltage. Hence, it is convenient to plot all FEED spectra in terms of $(E - E_F)$:

$$(E - E_F) = E_{kin} - eV + \Phi_A . \quad (1)$$

This energy scale implicitly takes into account any changes in electron energy E_{kin} due to changes in the extraction voltage V . The emitter work function, Φ , does not influence the energy $(E - E_F)$ of emitted electrons, but determines the tunneling probability and thus the field emission current.

In the case of coated Mo emitters, the potential between the Fermi level of Mo and the Fermi level of the analyzer is defined by the applied voltage V . Depending on thickness, permittivity, and conductivity of the semiconductor coating, band bending induced by space charge or by the penetration of applied electric field may shift the Fermi level at the semiconductor-vacuum interface relative to its position at the Mo-semiconductor interface. If field emission occurs from the semiconductor/vacuum interface, any band bending in the coating will be reflected in FEED spectra.

C. Experimental Set-up

Field emission energy distribution experiments were carried out using a test device that consisted of a tip holder facing a metallic gate with a circular opening of 500 μm diameter. A tip was positioned 500 μm from the gate, and was centered with the gate opening. All FEED measurements were performed in a UHV analysis chamber with a base pressure of 10^{-9} Torr. The test device could be transferred *in vacuo* to a heating stage, in order to clean the surface of the field emitter by thermal desorption, and to anneal emitter coatings.

The test device was aligned with the collection lens system of a hemispherical electron analyzer (VG Instruments CLAM II); the gate and spectrometer were both kept at ground potential, while a negative bias voltage was applied to the tip-shaped emitter. Individual FEED spectra were recorded at a constant applied voltage. Typically, several scans were recorded and added to improve the signal-to-noise ratio. The spectrometer pass energy was set between 2 and 20 eV, dwell time was 0.2 s, and the energy step was 0.05 eV. Voltage dependent-FEED measurements were performed as a series of individual FEED spectra taken sequentially at different, systematically varied, applied voltages.

D. Sample Preparation

Diamond and cubic boron nitride (c-BN) powders were used to coat tip-shaped Mo emitters. Diamond is an interesting coating material due to its large thermal conductivity, its chemical stability, and a negative electron affinity (NEA) of its H terminated (111) [1] and

(100) [2] surfaces. I - V characterization data of diamond coated Mo field emitters have been published recently [5] and featured an enhancement of the field emission current, as compared to uncoated Mo tips. The diamond powder used was nominally undoped and Raman spectroscopy evidenced no Raman active defects. Cubic boron nitride also features NEA behavior, as has been demonstrated recently by UV-photoemission measurements [3].

Single Mo emitter tips were made from 125 μm thick Mo wire and were sharpened by electrochemical etching in a concentrated KOH solution. The wire was biased by 10 V DC against a Pt counterelectrode. Typical radii of curvature of the sharpened Mo tips were less than 100 nm as measured by Scanning electron microscopy (SEM). Diamond and c-BN coatings were deposited subsequently by electrophoresis [6]. The field emitters were thermally annealed to 500°C for several hours after the electrophoretic coating was applied and prior to FEED characterization. The shape of the bare Mo tips, as well as the thickness and uniformity of electrophoretic coatings was monitored by SEM, before and after the FEED experiments.

E. Results

Voltage dependent-FEED measurements were performed on both diamond and c-BN coated Mo tips, and extraction voltage dependent potential drops across both types of coatings were observed. As was reported previously [7], FEED analysis of annealed, diamond coated Mo emitters revealed a linear decrease in the energy loss ($E - E_F$) of emitted electrons with the applied voltage, as seen in Fig. 2. In contrast, the bare Mo tip showed no FEED peak shift. The observed peak shift for coated emitters was attributed to field-induced band bending.

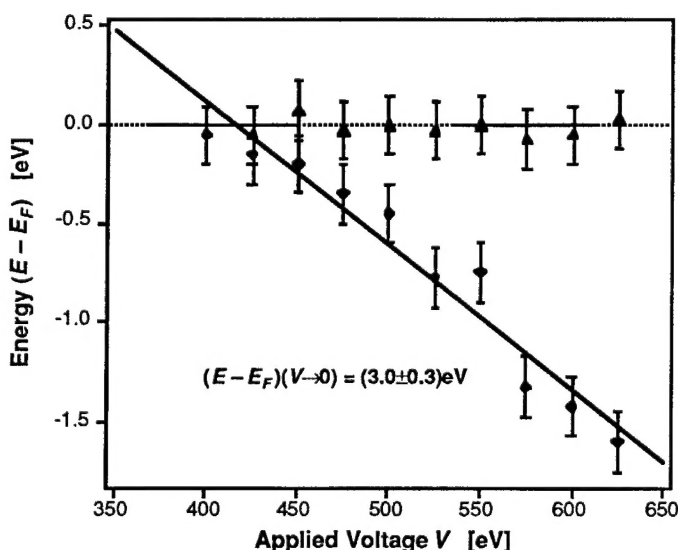


Figure 2. Measured FEED peak shifts from an annealed, diamond coated Mo emitter (solid line). Coating thickness: 100 nm. Peak positions vary linearly with bias voltage. Data from the same emitter prior to coating are shown for comparison (dashed line).

Peak shifts on the order of several eV were also measured in the case of c-BN coated emitters. Figure 3 shows the voltage dependent FEED peak shift observed on a Mo tip coated with a 1 μm thick c-BN coating. Similar to the annealed, diamond coated Mo tip an energy loss, depending linearly on the applied voltage, was observed.

In both cases, peak shifts of several eV occurred at applied voltages on the order of $V = 1$ kV, the distance between the tip and extraction grid was constant at 500 μm for all measurements. The magnitude of the observed shifts is in agreement with earlier data [8]. The coatings investigated in this work were nominally undoped. It can be expected that considerably smaller potential drops occur across more conductive, doped emitter structures. No noticeable potential drops across boron-doped diamond samples have been reported to date.

In comparison with annealed samples, the non-annealed emitters showed larger FEED peak shifts depending nonlinearly on the bias voltage. The annealing step was found essential to enhance the field emission current by up to one order of magnitude for a given bias voltage, and to improve its stability.

F. Interpretation

A two-barrier mechanism has been proposed [9, 10] to explain field emission from diamond samples, see Fig. 4. It consists of electron injection from the Fermi level of Mo into the conduction band of diamond, thermalization to the conduction band minimum (CBM), and subsequent field emission from the CBM at the diamond/vacuum interface.

The proposed model explains the measured FEED spectra and, in particular, the observed linear dependence of FEED peak position vs. the applied voltage.

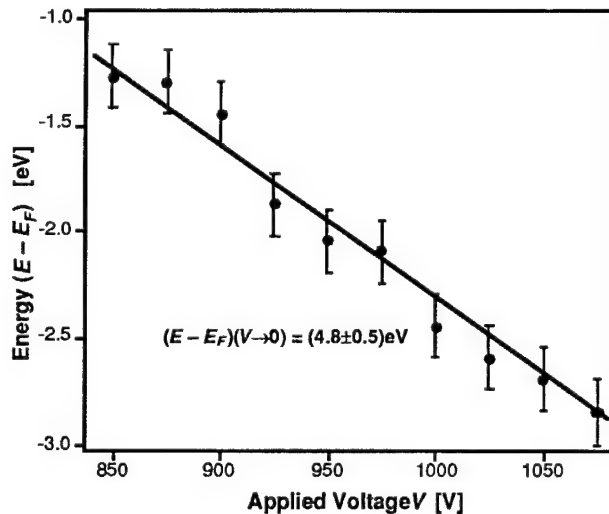


Figure 3. Measured FEED peak shifts from an annealed, c-BN coated Mo emitter. Coating thickness: 1 μm . Similar to the case of diamond coatings, peak positions were found to vary linearly with bias voltage.

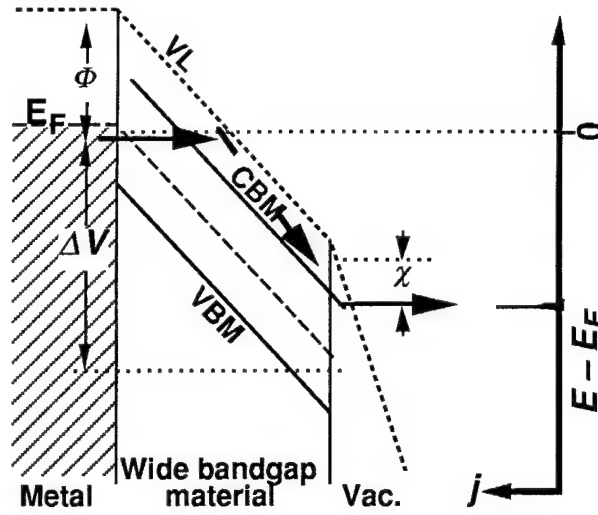


Figure 4. Two-barrier model describing field emission from a wide band gap material with electron affinity χ , coated on a metal electrode with work function Φ . Electrons are injected from the Fermi level E_F of the metal into the conduction band of the wide band gap material. After thermalization to the conduction band minimum (CBM), emission takes place at the semiconductor/vacuum interface. Due to field induced band bending a potential drop ΔV occurs across the wide band gap material, and induces a FEED peak shift as illustrated. VL: vacuum level, VBM: valence band maximum.

An extrapolation of measured FEED peak positions toward $V = 0$ has been used to determine the origin of field emitted electrons [7]. This extrapolation to flat band condition yields the approximate energy of the band in the semiconductor from which field emitted electrons originated. As the diamond powder used in this experiment was nominally intrinsic, its Fermi level would be close to midgap. The band gap of diamond is 5.5 eV, so that under ideally intrinsic conditions, its CBM is located 2.8 eV above the Fermi level. Linear extrapolation of FEED peak positions to $V = 0$ led to $(E - E_F) = (3 \pm 0.3)$ eV, as shown in Fig. 2. This is in good agreement with the expected position of the CBM. Emission from the valence band maximum (VBM), as was observed in the case of boron doped diamond [11], could be ruled out for the samples investigated here; as the VBM of diamond is located below its Fermi level, extrapolation towards flat band condition would yield $(E - E_F) < 0$. Hence, in agreement with the proposed model, field emission originated from the CBM of diamond.

A similar behavior was observed in the case of a c-BN coating, see Fig. 3. Linear extrapolation of FEED positions to flat band condition yielded in this case $(E - E_F) = (4.8 \pm 0.5)$ eV at $V = 0$. The band gap of c-BN is 6.2 eV, so that the CBM of an intrinsic sample would be 3.1 eV above the Fermi level. The fact that the extrapolation led to a larger energy than that of the CBM under ideally intrinsic conditions, indicated that the c-BN powder used was slightly *p*-type doped and that the Fermi level was shifted below midgap. Again, field emission from the VBM could be excluded as an explanation of the experimental data. The investigated c-BN

coatings featured a behavior very similar to that of the diamond coatings, and the essential field emission properties could be understood using the same two-barrier model.

The extrapolated FEED peak positions towards flat band condition also allow estimation of the relative importance of the two barriers. According to Fig. 4, the injection barrier height at the metal/semiconductor interface can be estimated from the extrapolated FEED peak positions. It is considerably higher than the field emission barrier at the semiconductor/vacuum interface, which is given by the electron affinity of the semiconductor. As both diamond and c-BN may feature a NEA surface, the field emission barrier into vacuum may vanish completely. Additionally, the electric field inside the semiconductor is reduced by a factor ϵ , which furthermore reduces the tunneling probability at the Mo/semiconductor interface. Hence, the results indicate that the field emission current was limited by electron injection into the semiconductor's conduction band rather than by field emission from the conduction band into vacuum.

The proposed model accurately describes the field emission properties of annealed emitters; non-annealed samples, however, featured a nonlinear dependence of peak shift on the applied voltage. A possible explanation may be found in the initial presence of an insulating oxide layer on the Mo tip which limited current injection into the semiconductor layer. Under steady state conditions, a positive space charge may have built up in the semiconductor layer due to electron depletion by field emission, and only partial compensation by limited electron injection. This conjecture has been supported by a TEM study that identified 100 Å thick oxide layers on similarly prepared Mo tips [12]. Also, in the case of annealed diamond coatings, a conductive Mo₂C interlayer was observed by TEM [13], which explains the observed improvement in field emission current after annealing.

G. Conclusions

The field emission behavior of tip-shaped Mo emitters coated with nominally undoped diamond and cubic boron nitride has been studied in detail. The use of voltage dependent field emission energy distribution measurements led to an improved understanding of the field emission process. Direct evidence of relevant, field-induced band bending has been found in both, diamond and c-BN coatings. Voltage drops on the order of several V were measured across layer thicknesses of several 100 nm, at a cathode-gate distance of 500 μm, and applied voltages on the order of 1 kV. Extrapolation of FEED data to flat band condition allowed identification of the origin of field emitted electrons. Nominally undoped diamond and c-BN coatings were found to emit from their CBM. FEED measurements confirmed a two-barrier model, which consists of (1) electron injection at the metal/semiconductor interface into the semiconductor's conduction band, (2) relaxation to the CBM, and (3) subsequent field emission from the CBM at the semiconductor/vacuum interface.

H. References

1. F.J. Himpsel, J.A. Knapp, J.A. Van Vechten, and D.E. Eastman, *Phys. Rev. B* **20**, 624-7 (1979).
2. J. van der Weide, Z. Zhang, P.K. Baumann, M.G. Wensell, J. Bernholc, and R.J. Nemanich, *Phys. Rev. B* **50**, 5803-6 (1994).
3. M.J. Powers, M.C. Benjamin, L.M. Porter, R.J. Nemanich, R.F. Davis, J.J. Cuomo, G.L. Doll, and S.J. Harris, *Appl. Phys. Lett.* **67**, 3912-14 (1995).
4. R.H. Fowler and L.W. Nordheim, *Proc. R. Soc. London Ser. A* **119**, 173 (1928).
5. W.B. Choi, J. Liu, M.T. McClure, A.F. Myers, V.V. Zhirnov, J.J. Cuomo, and J.J. Hren, *J. Vac. Sci. Technol. B* **14**, 2050-5 (1996).
6. W.B. Choi, J.J. Cuomo, V.V. Zhirnov, A.F. Myers, and J.J. Hren, *Appl. Phys. Lett.* **68**, 720 (1996).
7. R. Schlessler, M.T. McClure, W.B. Choi, J.J. Hren, and Z. Sitar, *Appl. Phys. Lett.* **70**, 1596-8 (1997).
8. N.S. Xu, Y. Tzeng, and R.V. Latham, *J. Phys. D* **27**, 1988-91 (1994).
9. E.I. Givargizov, V.V. Zhirnov, A.N. Stepanova, E.V. Rakova, A.N. Kiselev, and P.S. Plekhanov, *Appl. Surf. Sci.* **87/88**, 24 (1995).
10. M.W. Geis, J.C. Twichell, N.N. Efremov, K. Krohn, and T.M. Lyszczarz, *Appl. Phys. Lett.* **68**, 2294-6 (1996).
11. C. Bandis and B.B. Pate, *Appl. Phys. Lett.* **69**, 366-8 (1996).
12. A. Myers, *Ph.D. thesis*, North Carolina State University (1996).
13. W.B. Choi, A.F. Myers, G.J. Wojak, M.T. McClure, J.J. Cuomo, and J.J. Hren, *9th International Vacuum Microelectronics Conference* (Saint-Petersburg, Russia, 1996), pp. 288.

III. Surface Cleaning, Electronic States and Electron Affinity of Diamond (100), (111) and (110) Surfaces

Abstract

The effects of cleaning natural type IIb diamond (100), (111) and (110) samples by annealing and hydrogen - or deuterium plasma exposure were investigated by means of ultraviolet photoemission spectroscopy (UPS). Two wet chemical cleaning processes (a conventional chromic acid clean and an electrochemical etch) and a H plasma exposure have been employed to clean natural type IIb semiconducting diamond C(100) wafers. The effects of these processes on the diamond surface have been assessed and compared. As evidenced by Auger electron spectroscopy (AES), an oxygen free surface could be obtained following vacuum annealing to 900°C for the electrochemical process compared to 1050°C for the chromic acid etch. In addition, the technique of atomic force microscopy (AFM) demonstrated the presence of oriented pits on the surface of samples that were electrochemically etched for long times at high currents. After a H plasma exposure the NEA peak in the UPS spectra doubled in intensity. An anneal to 1100°C resulted in the removal of the sharp NEA feature. A second H plasma treatment resulted in the reappearance of the NEA peak similar to that after the first H plasma exposure. A 2×1 reconstructed low energy electron diffraction (LEED) pattern was observed subsequent to the anneals as well as the H plasma treatments. The fact that a NEA can be induced or removed repeatedly by means of a H plasma exposure or a 1100°C anneal, respectively provides evidence to correlate the appearance of a NEA with the presence of a monohydride terminated surface. Corresponding effects were found for (111) and (110) surfaces. A NEA could be induced by a H plasma and removed by a 900°C or 800°C anneal for diamond (111) or (110) surfaces, respectively. Following a deuterium plasma clean the diamond surfaces exhibited a NEA like the ones treated by a hydrogen plasma, but higher annealing temperatures were necessary to remove the NEA due to deuterium than for hydrogen.

A. Introduction

The electron affinity of a semiconductor is defined as the energy difference between the vacuum level and the conduction band minimum. For most materials the vacuum level lies above the conduction band minimum, corresponding to a positive electron affinity. Surfaces of wide band gap semiconductors like diamond have the potential of exhibiting a negative electron affinity (NEA) since the conduction band minimum lies near the vacuum level to begin with. Electrons present in the conduction band have sufficient energy to overcome the workfunction of a NEA surface and can be emitted into vacuum. Indeed, different surface terminations can shift the position of the bands with respect to the vacuum level and, therefore, induce a NEA or remove it [1-5]. These changes have been found to be due to surface adsorbates. Different

surface adsorbates result in changes of the surface dipole. The surface dipole can lead to a positive or negative electron affinity. For example hydrogen has been reported to induce a NEA on the diamond (111) and (100) surfaces. Whereas oxygen leads to a dipole such that a positive electron affinity is observed on these surfaces.

The surface cleaning and following processing steps will directly affect the surface termination of the diamond and, therefore, affect the electron affinity. In this study, several common surface preparation techniques are employed to clean different surfaces of natural diamond samples, and electronic structure and electron affinity are measured. In particular, the study focuses on the role of oxygen or hydrogen termination in comparison to the adsorbate free surface.

Different wet chemical cleaning methods have been employed to remove non diamond carbon and metal impurities from the diamond surface. One approach includes immersion in boiling chromic acid and aqua regia. Another is an electrochemical etch to remove conductive surface layers [6]. It has been shown that either procedure is capable of removing non diamond carbon [6, 7]. Following both approaches the diamond surfaces were found to be covered with oxygen. To remove these contaminants vacuum cleaning steps such as annealing or plasma exposure can be used.

Oxygen termination on the C(100) surface has been reported to lead to a 1×1 structure [8]. Two possible bonding configurations have been proposed for the oxygen terminated surface [9]. In one an oxygen atom is double-bonded to a carbon atom. Or an oxygen atom could form a bridge between two adjacent carbon atoms. Both structures are consistent with a 1×1 LEED pattern. In contrast a 2×1 reconstruction has been observed following a 900°C to 1000°C anneal or a H plasma exposure. Also, these surfaces were found to exhibit a NEA [8]. The 2×1 structure and the NEA are indicative of a monohydride termination. In the presence of atomic hydrogen, a 2×1 monohydride structure has been found to be the most stable according to theoretical studies [8]. Furthermore, for the 2×1 reconstructed surface *ab initio* calculations determined a NEA for a monohydride terminated surface and a positive electron affinity for a surface free of adsorbates.

As-loaded diamond C(111) samples have been reported to be at least partially covered with a monohydride. The monohydride terminated surfaces show a 1×1 unreconstructed LEED pattern. Also a NEA was detected for these samples experimentally by UPS [1-5]. Zhang *et al.* deduced a value of -1.56 eV for the electron affinity from pseudo potential calculations. Annealing these surfaces to above 950°C leads to a 2×1 reconstruction, and a positive electron affinity is observed. These changes are attributed to the removal of hydrogen. An Ar plasma clean was found to have the same effects on the electron affinity [5].

The clean diamond C(110) surface has been reported to exhibit a 1×1 LEED pattern [4, 10-12]. However, there has been considerable difficulty in obtaining a high quality (110)

surface [13]. Pate *et al.* observed only washed out photoemission spectra from the (110) surface and attributed this to a poor quality (110) surface [11]. Desorption of hydrogen from the C(110) surface has been addressed in several studies. Using photon stimulated ion desorption Pate found a significant reduction in hydrogen on the (110) surface at 800°C [4]. By means of ionization loss spectroscopy Pepper reported changes in the electronic structure at 850–900°C that were attributed to hydrogen desorption from the surface [14]. Employing multiple internal reflection infrared spectroscopy McGonigal *et al.* determined that the C-H stretching mode on a (110) surface vanished for annealing temperatures between 800 and 900°C [15]. This effect has been associated with the desorption of hydrogen. But hydrogen desorption has been reported up to 1050°C [4] from a C(110) surface.

Deuterium terminated C(100) surfaces have been examined by Francz and Oelhafen [16] by means of UV photoemission spectroscopy. A weak low energy feature indicative of a NEA was detected for a deuterium exposed (100) surface. UPS spectra of the clean surface were found to exhibit a peak at 1.5 eV to 2.0 eV below the Fermi level. This peak was reduced following deuterium exposure. As determined by means of X-ray photoemission spectroscopy (XPS), deuterium could be desorbed from C(100) surfaces at 1177°C [17]. Using time-of-flight scattering and recoil spectroscopy, Koleske *et al.* have studied the abstraction of hydrogen and deuterium from polycrystalline diamond surfaces [18]. The rate of H abstraction of D was determined to be about 1/3 the rate found for D abstraction of H. This result was interpreted by means of differences in momentum transfer for the two isotopes.

Photoemission spectroscopy is a very sensitive method to determine whether a surface exhibits a NEA or to measure the positive electron affinity. The incident light excites electrons from the valence band into states in the conduction band. Some of these electrons quasithermalize to the conduction band minimum. For NEA surfaces these secondary electrons may be emitted into vacuum and are detected as a sharp feature at the low energy end of photoemission spectra [4, 19]. A careful measurement of the width of the photoemission spectrum can be used to determine if the low energy emission occurs from the conduction band minimum. However, for a positive electron affinity emission from the conduction band minimum will not occur and the value of the electron affinity can be deduced.

In this study, the effects of different wet chemical and *in vacuo* cleaning processes on diamond (100), (111), and (110) samples are analyzed in terms of surface structure, chemistry, morphology and electron emission.

B. Experimental Details

The ultra high vacuum (UHV) system employed in this study consists of several interconnected chambers including systems used for annealing, H plasma cleaning, ultraviolet photoemission spectroscopy (UPS), low energy electron diffraction (LEED) and Auger

electron spectroscopy (AES). Samples can be moved between the chambers by a rail mounted UHV transfer system.

Natural type IIb single crystal semiconducting diamond (100), (111) and (110) samples (3.0×3.0×0.25 mm) were used in this study. The semiconducting wafers were necessary since undoped samples were charging up and did not yield any signal. The resistivity of the samples was typically about $10^4 \Omega\text{cm}$. The samples were commercially polished by 0.1 μm diamond grit. Prior to loading in the UHV system the samples were cleaned by an electrochemical etch [6]. This included applying a DC bias of 350V between two Pt electrodes that were placed in deionized (DI) water as an electrolyte. The samples were suspended in water between the two electrodes. The surface of the sample that was to be cleaned of non-diamond carbon and metal contaminants was positioned to face the cathode. A constant current of about 0.5 mA was measured, and a typical etch lasted two hours. Following the electrochemical etch SiO_2 residue was detected and a HF dip was employed to remove the residue from the surface [7].

To examine the effect of different wet chemical etches on the surface properties, some diamond (100) samples were cleaned by a chromic acid etch. This cleaning step involved immersing the samples for 15 min in boiling chromic acid ($\text{CrO}_3:\text{H}_2\text{SO}_4$) to remove non-diamond carbon. This was followed by boiling for 15 min. in aqua regia ($3\text{HCl}:\text{HNO}_3$) to remove metal contaminants. Finally the samples were rinsed in deionized (DI) water. After each of the two cleaning processes the samples were blown dry with N_2 , mounted on a molybdenum holder and transferred into the UHV system. This system consists of several chambers that are interconnected with a transfer line. The transfer line has a base pressure of 1×10^{-9} Torr. The base pressure in the chamber used for annealing and UPS measurements was 2×10^{-10} Torr.

As *in vacuo* cleaning steps the diamond (100) samples were annealed between 500 and 1150°C . This caused the pressure to rise to between 8×10^{-10} - 7×10^{-9} Torr during the various anneals. These same wafers were also cleaned with a H plasma. For this purpose the diamond crystals were heated to 500°C and exposed to a remotely excited rf H plasma. The details of the plasma chamber have been described previously [20]. During the plasma clean the H pressure was held at 50 mTorr.

In a similar manner annealing and H plasma exposure were used to clean diamond (111) and (110) samples. An optical pyrometer focused on the Mo plate holding the sample was employed to measure the temperature during the anneals.

For comparison, diamond (100) and (110) samples have also been exposed to a deuterium instead of a hydrogen plasma. Except for using a different gas the process parameters for either plasma were the same. These experiments were done to determine whether deuterium with its higher mass than hydrogen would change the surface characteristics in terms of emission and stability.

Following the different cleaning steps, UPS, LEED and AES were employed to analyze the surface properties. The photoemission was excited by HeI (21.21 eV) radiation from a gas discharge lamp. A 50 mm hemispherical analyzer was employed to detect the emitted electrons. The system had an energy resolution of 0.15 eV and an acceptor angle of 2° . To determine the Fermi level UPS measurements were performed on reference samples of freshly deposited gold layers. A bias of 1 or 2V was applied to the sample to overcome the workfunction of the analyzer and thus to detect the low energy electrons emitted from the NEA surface. The position of the sharp NEA peak at the low energy end of photoemission spectra corresponds to the energy position of the conduction band minimum, E_C (Fig. 1). Emission from E_C appears at $E_V + E_G$ in the spectrum, where E_V is the energy of the valence band maximum and E_G that of the band gap. Emission from the valence band maximum is positioned at $E_V + h\nu$ in the spectrum. This is the high energy end of the spectrum. The spectral width or the distance between emission from the valence band maximum and the conduction band minimum is therefore $h\nu - E_G$. With the values for He I radiation $h\nu = 21.21$ eV and the band gap of diamond $E_G = 5.45$ eV, a spectral width of ~ 15.7 eV is determined for a NEA surface. It can only be determined that the surface exhibits a NEA. However, the magnitude of the NEA can not be measured by UPS since there is no emission from states below the conduction band minimum. In comparison, for the case of a positive electron affinity surface, the low energy cutoff will be determined by the position of the vacuum level, and the spectral width will be

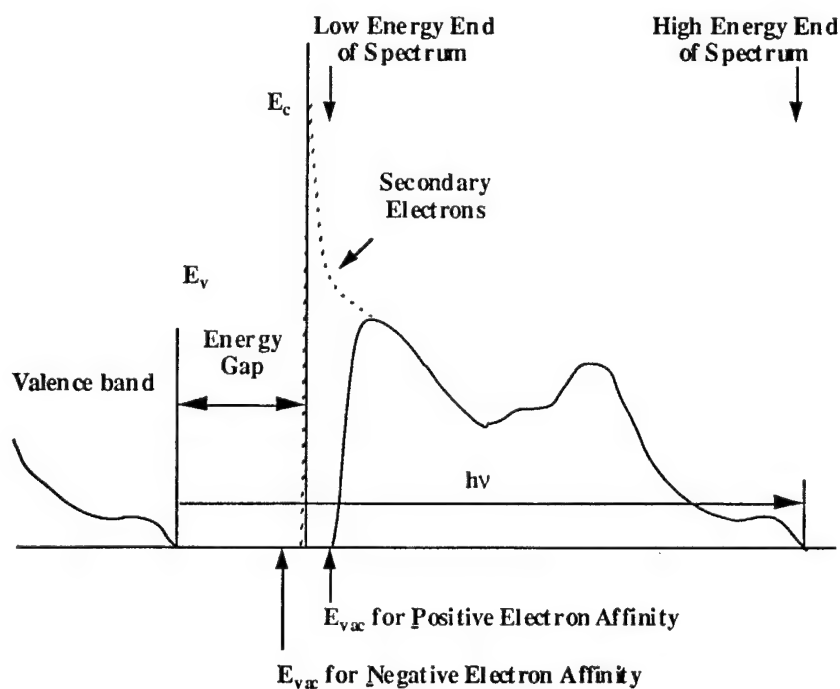


Figure 1. Schematic diagram of photoemission spectra for a negative electron affinity surface (dotted line) and a positive electron affinity surface (solid line).

smaller. Thus, the actual value of the electron affinity can be deduced from the position of the low energy end. This means the low energy cutoff will change in proportion to the magnitude of the electron affinity.

C. Results

Comparison of Chromic Acid and Electrochemical Etch for Diamond (100). Subsequent to either of the two wet chemical cleaning procedures the as-loaded diamond (100) crystals exhibited a comparable unreconstructed (1×1) LEED pattern. Furthermore, AES spectra showed peaks indicative of the presence of oxygen on all samples. A 500°C anneal did not remove a significant portion of the oxygen from the surface as detected by means of AES indicating that most of the oxygen was chemisorbed. Upon heating to 900°C a reduction of the surface oxygen (Fig. 2 a) was observed for diamond substrates cleaned by employing chromic acid, but the surfaces remained in the 1×1 structure. The UPS spectra of the as-loaded samples as well as those heated to 500 or 900°C showed a positive electron affinity. The position of the low energy cutoff moved to lower energies with increasing annealing temperature. This is indicative of a lowering in electron affinity. Values for the electron affinity of 1.0 eV and 0.7 eV were detected following 500 and 900°C anneals, respectively. These values are consistent with previous results [8]. Following an anneal to 1050°C the amount of oxygen on the surface dropped below the detection limit of the AES instrument. A reconstructed (2×1) LEED pattern appeared. In addition, the width of the UPS spectra increased to ~ 15.7 eV, and a sharp low energy feature appeared indicating a NEA following the last annealing step.

Following a hydrogen plasma clean the 2×1 LEED pattern was still observed. Interestingly, the intensity of the NEA peak in the UPS spectra had increased. A 1150°C anneal resulted in a positive electron affinity, but a second H plasma exposure could re-induce the NEA peak. Following the second H plasma exposure the secondary peaks of the 2×1 LEED diffraction was weaker. This may be attributed to a reduction in size of the 2×1 reconstructed domains.

In comparison, AES spectra of the as-loaded electrochemically etched diamond (100) samples displayed features indicative of the presence of SiO_2 surface residue. A UV ozone exposure and an HF dip removed these contaminations as evidenced by AES (Fig. 2b). Also the amount of fluorine was below the detection limit of the AES equipment. The amount of oxygen remaining after the clean appeared to be somewhat less than for the surface cleaned by the chromic acid etch. A 500°C anneal basically did not change the oxygen feature in the AES spectra, and a positive electron affinity of 1.45 eV was detected by using UPS.

After annealing to 900°C oxygen was no longer detected by AES. Again, the surface exhibited a 2×1 reconstructed structure. Furthermore, a sharp low energy peak positioned at the conduction band minimum was detected in the UPS spectra (Fig. 3). Thus a NEA was

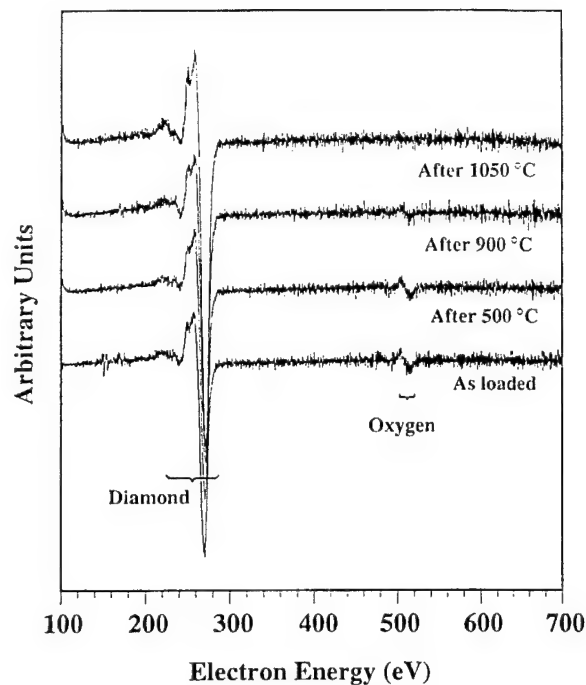


Figure 2a. Auger spectra of diamond C(100) following chromic acid clean as a function of annealing temperature. The as-loaded surface exhibits features indicative of oxygen which can be reduced at 900°C and removed at 1050°C. A reconstructed 2×1 LEED pattern and a NEA were observed following the 1050°C anneal.

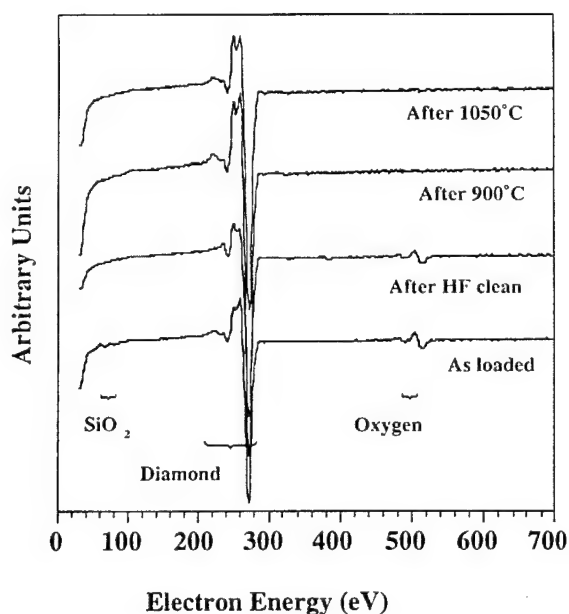


Figure 2b. Auger spectra of diamond C(100) following chromic acid clean as a function of annealing temperature. The as-loaded surface exhibits features indicative of oxygen which can be removed at 900°C. A reconstructed 2×1 LEED pattern and a NEA were observed following the 900°C and 1050°C anneal.

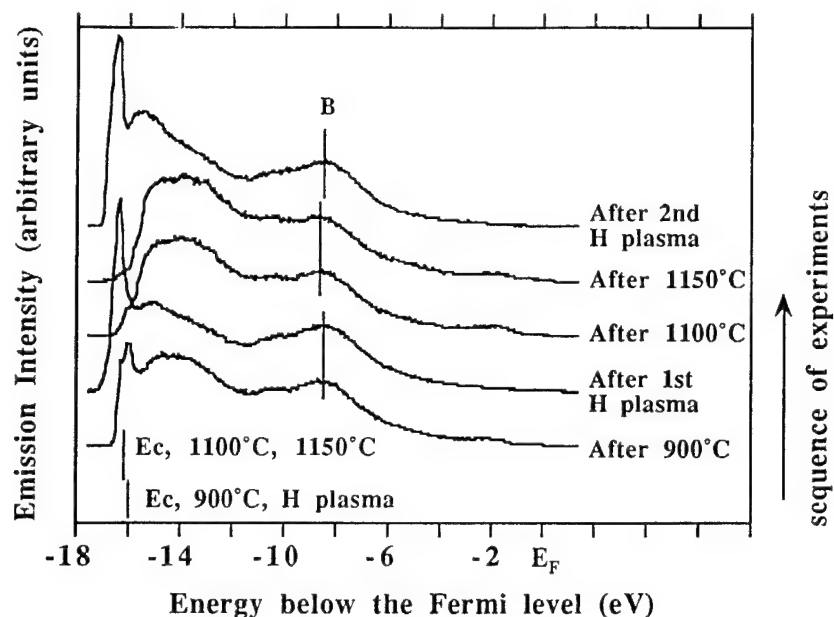


Figure 3. UV photoemission spectra of a diamond (100) surface cleaned by means of an electrochemical etch. The sequence of spectra follows from bottom to top: 900°C anneal, first hydrogen plasma, 1100°C anneal, 1150°C anneal, second hydrogen plasma.

induced at lower temperatures than for the chromic acid etch. Upon heating to 1050°C neither the AES spectrum nor the LEED pattern changed. Also, the NEA surface was retained. Exposing the sample to a H plasma resulted in about double the intensity for the NEA peak. In addition, emission extending to 0.3 eV below the conduction band minimum was observed. A 1100°C anneal resulted in the removal of the sharp NEA peak and a shift of the low energy end by 0.5 eV to higher energies. As evidenced from the position of the strong feature labeled "B", the entire spectrum shifted by 0.3 eV to lower energies. The low energy end still exhibited a small shoulder that was removed after a 1150°C anneal. This small shoulder may be due to some hydrogen remnants on the surface following the 1100°C anneal. A feature positioned at 1.2 eV below the valence band maximum was detected subsequent to the 900, 1000 and 1150°C anneals. (Due to shifts in the spectra, this peak appeared at 1.8 eV below the Fermi level following a 900°C anneal and at 2.1 eV below the Fermi level after a 1100 and 1150°C anneal.)

A second H plasma clean resulted in a UPS spectrum similar to that obtained after the initial H plasma. The LEED pattern remained reconstructed 2×1. But the secondary spots were again lower in intensity after the second H plasma clean. Following an extended hydrogen plasma exposure the diamond (100) surface exhibits emission at the low energy end of UPS spectra to 0.2 eV below the expected position of the conduction band minimum. (For further discussion of this feature see paragraph "E." in the Results section.) See Table I for a summary of results.

Table 1. Summary of the UPS measurements on diamond (100), (111) and (110) surfaces. RT: room temperature, PEA: positive electron affinity, NEA: negative electron affinity. Unless noted otherwise the surfaces have been cleaned by an electrochemical etch. The experimental uncertainties are 0.1 eV.

| Surface | | | | |
|--|---|---|---|-------------------------------|
| C(100) after chromic acid clean C(100) after electrochemical etch | 500°C PEA, $\chi = 1.00$ eV PEA, $\chi = 1.45$ eV | 900°C PEA, $\chi = 0.70$ eV NEA, $\chi < 0$ | 1100°C NEA, $\chi < 0$ PEA, = 0.75 eV | |
| | 900°C NEA, $\chi < 0$ | H-plasma NEA, $\chi < 0$ | 1100°C PEA, = 0.75 eV | H-plasma NEA, $\chi < 0$ |
| C(100) after H plasma treatment C(100) after D plasma treatment | 1100°C PEA, = 0.75 eV NEA, $\chi < 0$ | 1250°C PEA, = 0.75 eV PEA, = 0.75 eV | | |
| | RT to 600°C NEA, $\chi < 0$ | H-plasma NEA, $\chi < 0$ | 900°C PEA, $\chi = 0.5$ eV | |
| C(110) after H plasma treatment C(110) after D plasma treatment | 700°C NEA, $\chi < 0$ | 800°C PEA, $\chi = 0.6$ eV | H plasma NEA, $\chi < 0$ | 800°C PEA, $\chi = 0.6$ eV |
| | 800°C PEA, $\chi = 0.6$ eV NEA, $\chi < 0$ | 900°C PEA, $\chi = 0.6$ eV PEA, $\chi = 0.6$ eV | | |

As determined by AFM measurements all the samples used in this study exhibited parallel linear grooves to each other with a depth of ~ 20 Å (Fig. 4a). These features are attributed to polishing procedure of the supplier. Subsequent to a chromic acid etch no changes in surface morphology of the samples was observed. Even after the substrates had been boiled in chromic acid and aqua regia for 2 hours each, no changes were detected in the AFM scans. Also, AFM images of crystals electrochemically etched for 2 hours at 0.5 mA did not reveal any changes either. For one diamond (100) sample the duration of the electrochemical etch was extended to study possible effects on the morphology. Also, the current was increased. Following an extended electrochemical etch of 12 hours at 50 mA, scattered pits could be detected on the diamond surface. In fact it was determined that these etch pits were oriented along the $\langle 110 \rangle$ crystallographic directions (Fig. 4b). AES scans of these surfaces displayed larger peaks attributed to SiO_2 . In a comparative experiment graphite and damaged amorphized diamond surface layers were removed by this electrochemical etch [7]. Based on these observations we

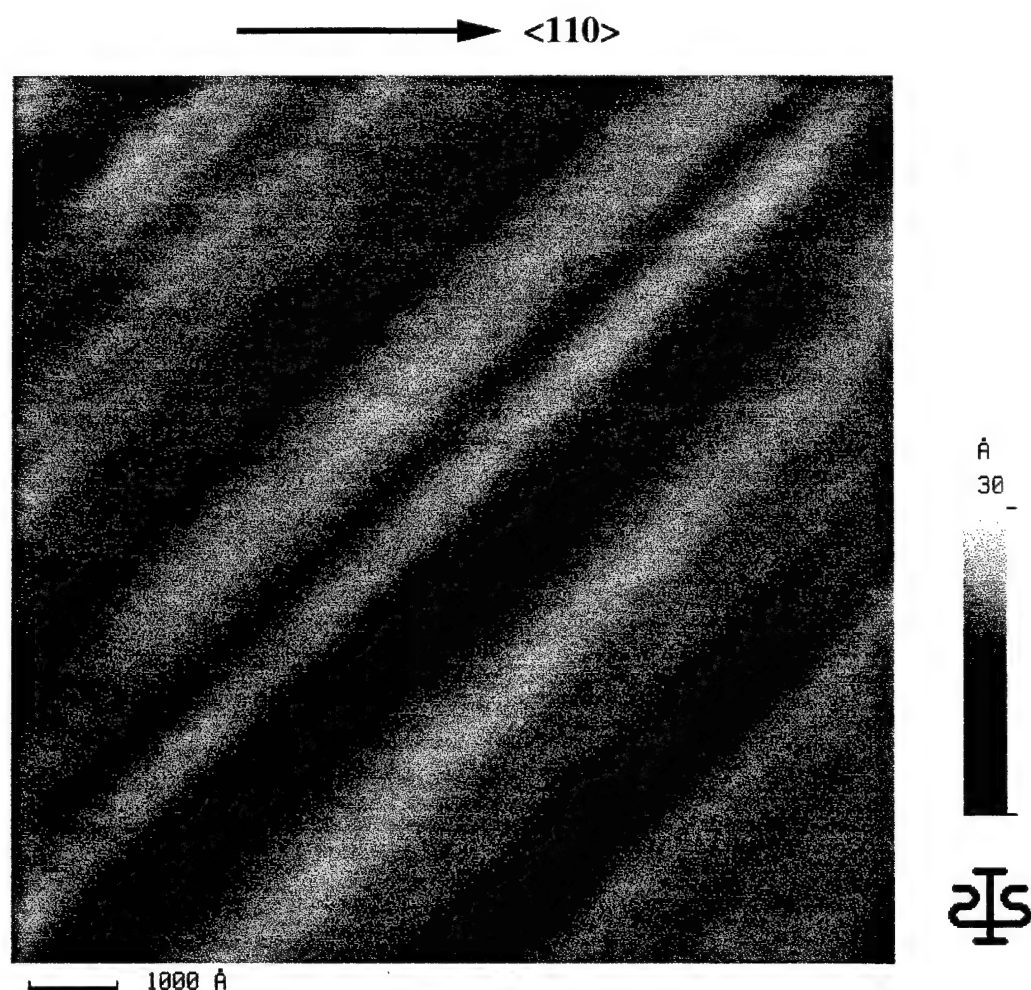


Figure 4a. AFM image of diamond (100) following polish.

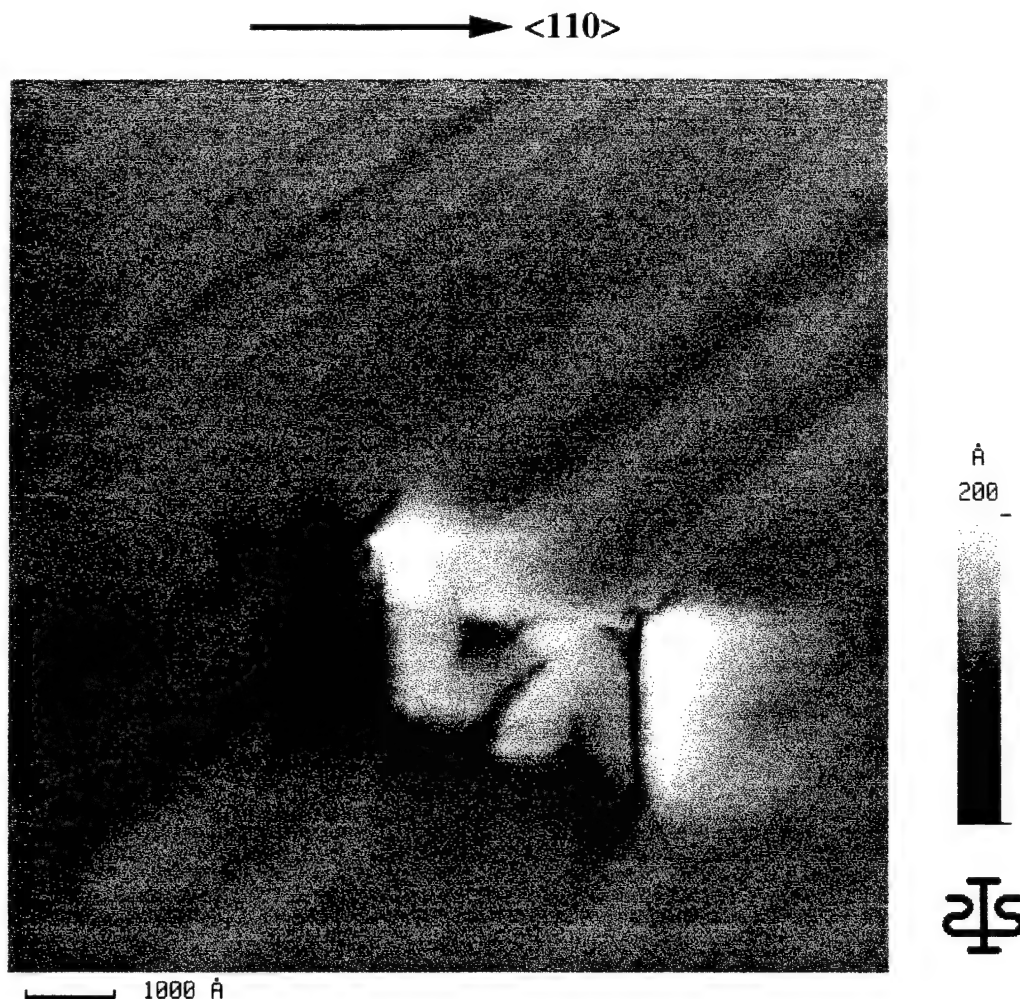


Figure 4b. AFM image of diamond (100) after electrochemical etching for 12 h at 50 mA. Etch pits oriented along the $\langle 110 \rangle$ crystallographic direction are detected.

propose that the etch pits actually mark the location of defects in the surface region of the diamond. Such defects may be a result of the polishing procedure or could also be intrinsic to the natural diamond crystals.

Diamond (111) Surfaces. It has been reported previously that as-loaded diamond (111) samples may be at least partially terminated with a monohydride [4, 5]. The C(111) samples studied here have been cleaned by an electrochemical etch. Most of the as-loaded diamond (111) samples exhibited a positive electron affinity. A few displayed a sharp low energy peak in the UPS spectra indicative of a NEA. Annealing to 600°C resulted in a NEA for all of the samples studied. A H plasma exposure resulted in a NEA which could be removed by a subsequent 950°C anneal. Diamond (111) surfaces cleaned by a chromic acid etch have been examined previously [5]. This reference also reports that a peak positioned 1.2 eV below the valence band maximum was detected following the 950°C anneal. As far as can be told from

our and previous [5] experiments the properties of the diamond surfaces following either one of the two wet chemical cleaning processes did not differ significantly. Various portions of the surface may be hydrogen terminated subsequent to either one of the two wet chemical cleaning processes. In addition, we've observed that subsequent to a hydrogen or deuterium plasma treatment several diamond (111) surfaces exhibited not only a NEA peak but also an additional low energy feature positioned about 0.4 eV below the expected position of the conduction band minimum. (This effect is discussed further in paragraph "E." of the Results section.) The results are summarized in Table I.

Diamond (110) Surfaces. An electrochemical etch has been used to clean the C(110) samples. The as-loaded (110) samples exhibited features indicative of oxygen in the AES spectrum. Also a positive electron affinity was observed by means of UPS. Subsequent to annealing the samples to 700°C, a 1×1 LEED pattern was observed, and the oxygen concentration on the surface dropped to below the detection limit of the AES instrument. The low energy cut off of the UPS spectrum shifted to lower energies (Fig. 5), indicating a reduction of the electron affinity. In addition, a sharp low energy peak attributed to a NEA appeared. A 800°C anneal removed the sharp NEA feature, and the width of the spectrum was reduced by 0.7 eV. Only for one (110) surface studied a 2×1 LEED pattern was observed. The other (110) surfaces showed a 1×1 LEED pattern. All these surfaces exhibited equivalent UPS spectra. In particular, at the high energy end of the spectra a feature positioned at 1.8 eV below

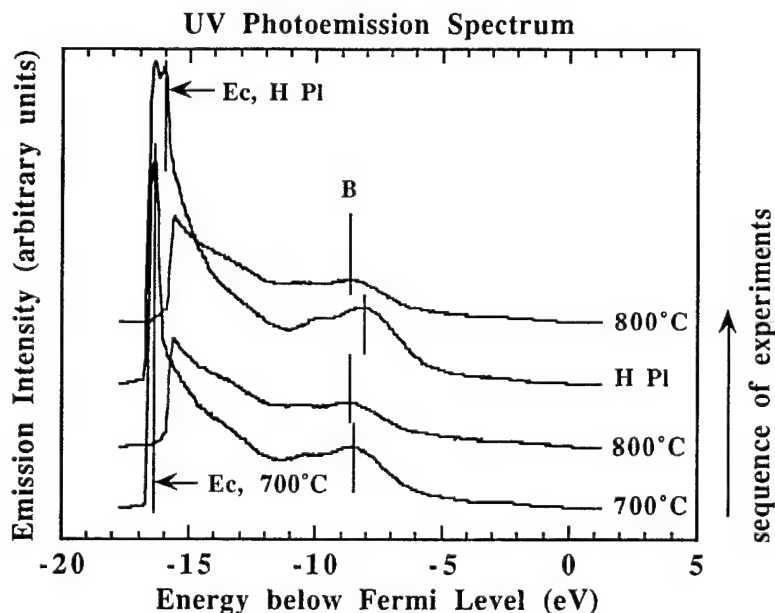


Figure 5. UV photoemission spectra of a diamond (110) surface. A NEA was observed following a 700°C anneal. A 800°C anneal removes the NEA. The NEA can be induced and removed again by a hydrogen plasma etch and a 800°C anneal, respectively.

the valence band edge appeared following a 700 or 800°C anneal (Fig. 5). Exposing the surfaces to a H plasma resulted in the re-appearance of the NEA characteristics. It was also determined that the emission extended about 0.4 eV below the conduction band minimum (E_c). (See paragraph "E." of the Results section.) In addition, the peak located at 1.8 eV below the valence band edge was reduced significantly (Fig. 5). Following a H plasma exposure a 1×1 LEED pattern was found for all the (110) surfaces studied. Employing a 800°C anneal the NEA could be removed again. And the peak at 1.8 eV below the valence band edge reappeared. The characteristics of the high energy end of the spectrum observed subsequent to a 700°C anneal appeared to be in between those detected following a 800°C anneal and those observed after a H plasma exposure. Refer to Table 1 for a summary of the results.

Effects of Deuterium Plasma Cleaning. Deuterium plasma exposure at a temperature of 500°C resulted in the removal of oxygen from the diamond (100) and (110) samples, as evidenced by AES. Also, a 2×1 LEED pattern was detected for C(100) and a 1×1 structure for C(110). These effects are equivalent to the case of a hydrogen plasma. Following a deuterium plasma clean the diamond surfaces exhibited a NEA like the surfaces treated by a hydrogen plasma. However, differences in the thermal stability were found between deuterium versus hydrogen on diamond surfaces.

While the NEA attributed to hydrogen termination of diamond (100) surfaces could be removed by a 1100°C anneal, the NEA was still observed after annealing deuterium terminated diamond (100) surfaces to 1200°C. Heating to 1250°C was necessary to remove the NEA from these surfaces.

Similarly, annealing hydrogen terminated diamond (110) surfaces to 800°C resulted in a positive electron affinity. But following a 850°C anneal a NEA due to deuterium was still detected. Only after a 900°C anneal could the NEA be removed from diamond (110) surfaces. Figure 6 shows the thermal characteristics of the deuterium terminated diamond (110) surface. The results show that annealing a deuterium terminated (110) surface to 800°C causes an apparent increase in the intensity of the NEA peak while the low energy shoulder is no longer detected.

In our study, high temperature anneals were employed (up to 1250°C) to clean the diamond surfaces. It is important to ensure that none of these processes caused graphitization of the diamond surfaces. UV photoemission is very surface sensitive and could detect graphite contamination on these surfaces. Graphite shows a strong secondary peak positioned 13.5 eV below the Fermi level in UPS spectra, and a workfunction of 4.0 eV has been measured for diamond samples that had been graphitized [21]. In our experiments, no indication of graphitization was found in UPS spectra following any of the high temperature anneals.

Low Energy Emission in UPS Spectra. Subsequent to a hydrogen or deuterium plasma treatment, several diamond (100), (111) and (110) surfaces exhibited not only a NEA peak but

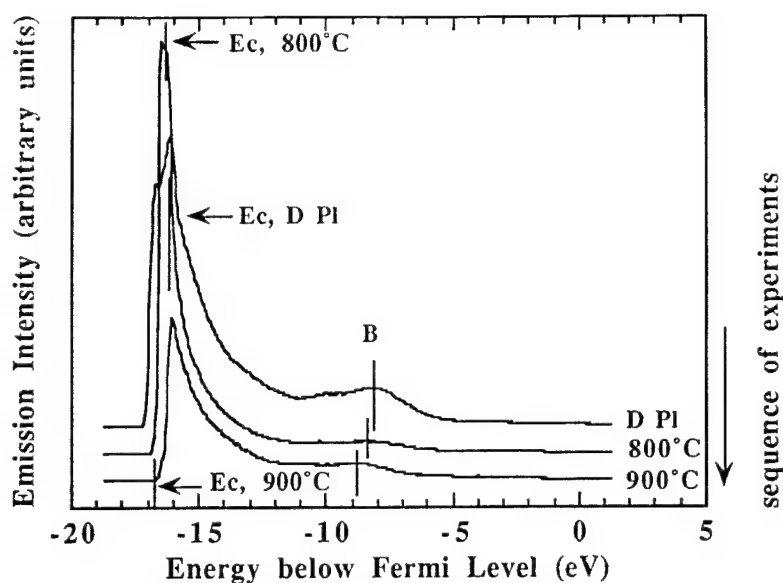


Figure 6. UV photoemission spectra of a diamond (110) surface exposed to a deuterium plasma. The surface still exhibits a NEA following a 800°C anneal. A 900°C anneal is necessary to remove the NEA characteristics.

also an additional feature at the low energy end of UPS spectra. This feature extended to 0.2–0.4 eV below the expected position of the conduction band minimum. To examine this effect further diamond surfaces have been cleaned by H plasma exposures of different duration. For a brief (10 s) H plasma clean of diamond (100) surfaces, only a NEA peak has been observed at the low energy end (Fig. 7). The surfaces did exhibit a 2×1 LEED pattern, and the oxygen had been removed as determined by means of AES. For a subsequent (30 s) H plasma exposure, an additional low energy emission feature emerged. The intensity of the original NEA peak increased by about 10%. We have also observed that with increased time of H plasma exposure, the secondary spots in the 2×1 LEED pattern became weaker. It may be that the H plasma leads to a breakup of the surface into domains, each exhibiting a 2×1 reconstruction. We'd like to note that for all the experiments reported in this study a gas purifier was used on the hydrogen and deuterium gas lines of the rf plasma system. Prior to the installation of this purifier it was possible to induce a NEA on diamond surfaces by means of a H plasma. But no features below the conduction band edge were observed in the UPS spectra even for extended hydrogen plasma exposures.

D. Discussion

It is suggested that the appearance of a NEA on the diamond (100) surface and a 2×1 reconstruction is due to the removal of oxygen as discussed previously [8, 22]. It is interesting to note that the intensity of the NEA peak in the UPS spectra could be increased by employing

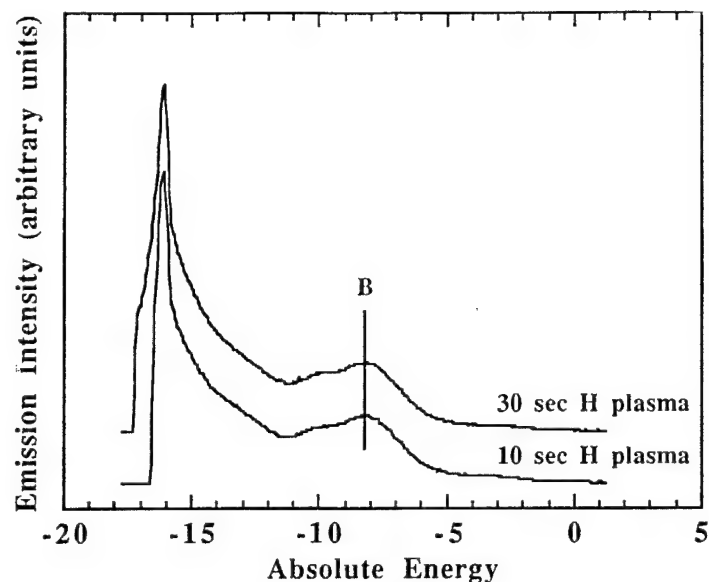


Figure 7. UV photoemission spectra of a diamond (100) surface following two consecutive hydrogen plasma exposures. A 10 second hydrogen plasma clean results in a NEA but no emission below the conduction band minimum. After a 30 second hydrogen plasma etch, a low energy emission feature below the conduction band minimum emerges.

a H plasma clean. Indeed, a H plasma could also induce a NEA on a positive electron affinity surface. However, a reconstructed (2×1) LEED pattern could be detected after every anneal (900°C , 1100°C and 1150°C) and H plasma exposure. Therefore, the surface is thought to be terminated with a monohydride after a 1050°C or a 900°C anneal for the (100) surfaces cleaned by a chromic acid or an electrochemical etch, respectively. The hydrogen that terminates the surface after annealing may come from hydrogen that has diffused into the diamond. Subsequent to the removal of oxygen from the surfaces, hydrogen could bond to the vacant sites on the surface. A NEA for the monohydride terminated 2×1 reconstructed (100) surface has been reported before experimentally as well as based on *ab initio* calculations [8, 23]. From these same studies a positive electron affinity was reported for the clean 2×1 surface. Our data suggest that an adsorbate free surface could be obtained following a $1100^{\circ}\text{C}/1150^{\circ}\text{C}$ anneal. This means a sufficient amount of hydrogen was desorbed to remove the NEA. The feature detected at 1.2 eV below the valence band maximum following the anneals is suggested to be due to surface states. Such a feature has been observed previously at 0.95 eV below the valence band maximum [24].

A NEA peak of lower intensity was measured following the 1050°C (for samples cleaned by a chromic acid etch) or 900°C (for samples cleaned by an electrochemical etch) anneal than for a H plasma clean. After the anneals the surface is proposed to be partially terminated with a monohydride. From the intensity difference of the NEA peaks, we estimate that about half the surface was terminated by a monohydride following the 900°C anneal. Furthermore, the

remaining small low energy feature in the photoemission spectra following the 1100°C and 1150°C anneals may be an indication that the hydrogen has not been removed completely from the surface. In comparison it is suggested that the H plasma resulted in a more complete hydrogen surface termination.

It is noted that after an electrochemical etch and a HF dip an oxygen free diamond C(100) surface can be obtained at lower annealing temperatures than for a chromic acid clean. The electrochemical etch may oxidize the diamond surfaces differently than is the case for the chromic acid process. This could result in a higher temperature required to clean the surface from oxygen. But it also needs to be considered whether the HF dip contributes to the lowering of this annealing threshold for the (100) surface. Different configurations for oxygen bonding on diamond (100) surfaces have been proposed [9]. In one an oxygen atom is double-bonded to a carbon atom. Or an oxygen atom could form a bridge between two adjacent carbon atoms. Both structures are consistent with a 1×1 LEED pattern. The surface characterization techniques available for this study were not capable of distinguishing between these two structures. Thus we are not able to determine how the oxygen was bonded to the diamond surfaces subsequent to a chromic acid clean or electrochemical etch. Based on a surface dipole model Rutter and Robertson have calculated that the bridge bonding is expected to be more stable by 0.5 eV than the double bonding [25]. We have also observed that a 500°C anneal of chromic acid treated C(100) surfaces results in a value of +1.0 eV for the electron affinity. A value of +1.45 eV was found for annealing electrochemically etched C(100) surfaces to 500°C. Rutter and Robertson have calculated a lower positive electron affinity for oxygen on C(100) in a bridge bonded configuration than in a double bonded one. The results may suggest that a chromic acid clean results in a preferentially bridge bonded oxygen termination while an electrochemical etch may, on the other hand, lead to preferential double bonding of the oxygen. This may be a factor in the differences in the annealing temperature that is necessary to remove the oxygen from the (100) surface as well as the differences in electron affinity following a chromic acid etch or an electrochemical clean. Independent whether a chromic acid clean or an electrochemical etch had been used the clean (100) surfaces exhibited equivalent (within the experimental uncertainties of 0.1 eV) values for the positive electron affinity of 0.70 eV to 0.75 eV (Table I). Further studies may be necessary to clearly understand the mechanism of the different wet chemical etching procedures, but it can be said that the electrochemical clean in combination with a HF dip apparently oxidizes the surface differently than a chromic acid etch.

Oxygen is expected to increase the workfunction due to a stronger surface dipole in comparison to the clean surface. An adsorbate free surface would exhibit dangling bonds resulting in a dipole of the same polarity as for an oxygen terminated surface. A hydrogen layer on the surface results in a dipole such that the workfunction is reduced. However, the surface dipole may not only result from the differences in electronegativity between C and H or C and

O, but also the symmetry of the charge distribution at the site. Robertson [26] pointed out that both hydrogen and oxygen sites on the diamond surface are asymmetric, and this should lead to additional dipole effects and thus affect the electron affinity.

Our data of the C(110) surface suggest that a reduction of electron affinity is correlated with the desorption of oxygen following a 700°C anneal, and the NEA characteristics are suggested to be due to hydrogen present at the surface. A 800°C appears to desorb a sufficient amount of hydrogen from the surface to result in a positive electron affinity. The reports by Pate [4], Pepper [14] and McGonigal *et al.* [15] indicate that a large portion of the hydrogen present on the surface was desorbed between 800 and 900°C while hydrogen desorption was observed up to 1050°C [4]. If any significant portions of the surface were still terminated by hydrogen, a peak characteristic of a NEA would be expected in the photoemission spectra. Hydrogen could also be present in the bulk of the diamond. This may contribute to some H desorption up to higher temperatures. It should be noted that it is difficult to measure the temperature of diamond due to its transparent nature. The temperature values mentioned in this and other studies may be off somewhat with respect to each other. This may reconcile some of the apparent differences in the results. In addition, differences in heating rate may play a role. Also, different surface cleaning processes may effect the surface characteristics.

In previous studies, the diamond (110) surface has always been reported to exhibit a 1×1 LEED pattern [4, 10-12]. There has been considerable difficulty in producing high quality (110) diamond surfaces [13]. We have observed a 2×1 LEED pattern for one (110) surface following a 800°C anneal. However all the other surfaces studied exhibited a 1×1 LEED pattern. In the photoemission spectra, we have consistently observed a feature about 1.8 eV below the valence band edge subsequent to annealing. A H plasma reduced this feature significantly. This peak may be associated with surface states. Sometimes LEED is not representative of the actual surface structure. LEED may not detect local reconstructions that can result in electronic structures observable by photoemission spectroscopy. Previous studies reported that certain C(111) surfaces did not show reconstructed LEED patterns upon annealing [10, 19]. However, Himpsel *et al.* observed photoemission spectra indicative of a 2×1 reconstruction for such a sample [19]. The long range order of a reconstructed surface could be disrupted as a result of roughening or etching following process cycles such as hydrogen adsorption and desorption. For the hydrogen terminated C(100) we have observed a weakening of the 1/2 order LEED spots following several cycles of annealing and H plasma exposure.

In our experiments, it was observed that oxygen could be removed at lower annealing temperatures from diamond (110) than from (100) surfaces. Correspondingly a NEA could be induced at lower temperatures also. And a clean surface could be obtained at lower temperatures for the case of (110) surfaces than for (100). For diamond (111) surfaces a NEA

could be obtained at even lower temperatures. From the experimental evidence it can be concluded that oxygen is bonded the most strongly on diamond (100) surfaces. The top layer of atoms on the unreconstructed surface are bonded with two bonds to the atoms beneath while the other two bonds are free. It has been reported before that oxygen can be attached easily to the diamond (100) surface forming either a bridge bond between two carbon atoms or a double bond to one carbon atom [9]. On the C(111) surface the carbon atoms in the top layer are connected with three bonds to the next layer underneath. The fourth bond is oriented perpendicular to the surface. Assuming a truncated-bulk C(110) 1×1 surface the carbon atoms in the top layer have one bond available. Thus the 1×1 C(111) and (110) surfaces each have one bond available. It makes sense that for a C(110) surface the temperature necessary to induce a NEA (700°C) is close to the one for the C(111) surface (600°C). (A few C(111) surfaces exhibited a NEA already after a wet chemical clean.) The temperature necessary to remove oxygen from C(100) (900°C) is somewhat higher.

Our results of deuterium on C(100) are in agreement with the study on C(100) by Francz *et al.* in that (a) deuterium exposure of the C(100) surface reduced the emission feature at 1.2 eV below E_v and (b) a NEA was observed for the deuterated C(100) surface. But we have found strong NEA peaks of similar high intensity for both hydrogen and deuterium termination. Our value of 1250°C for the deuterium desorption temperature from a C(100) surface is somewhat higher than the value of 1177°C found by Smentkowski *et al.* [17]. But the different temperature values may be off somewhat with respect to each other due to the difficulty of determining the temperature of diamond. For C(100) and C(110) surfaces the annealing temperature necessary to remove a NEA due to deuterium was higher than for the case of hydrogen. This is attributed to the higher mass of deuterium which leads to a higher desorption temperature. Otherwise the NEA characteristics of hydrogen—or deuterium terminated diamond surfaces were found to be equivalent. Similar effects may be expected for the C(111) surface. The dipole induced by hydrogen or deuterium on diamond is expected to be the same.

The emission observed below the conduction band minimum after an extended hydrogen or deuterium plasma may be a result of band bending. The band bending may be due to states in the band gap that cause Fermi level pinning. Another possibility is H passivation of the boron acceptors near the surface which will lead to different band bending for the different regions on the surface. In either one of these two cases the surface could consist of different domains exhibiting differences in band bending. If the spectrum is a superposition from regions with different Fermi levels, the spectrum will appear broader with additional features at both the valence band and the low energy cutoff. Since the spectral intensity is strongest at the low energy end, it is likely to be most evident here. Another explanation may be that emission due to excitons occurs. Bandis and Pate have described this effect for C(111) surfaces exhibiting a

NEA [27]. Such an effect could lead to emission below the conduction band edge even while the band bending is constant for the entire surface.

E. Conclusions

The replacement of oxygen with hydrogen has been found to induce a NEA on C(100), (111) and (110) surfaces. This could be achieved by an anneal or a H plasma exposure. A high temperature anneal capable of removing the adsorbed hydrogen resulted in clean surfaces exhibiting a positive electron affinity. Our studies indicate that oxygen was bonded the most strongly to the diamond (100) - and the most weakly to the diamond (111) surface. According to the annealing temperatures necessary to remove a NEA from hydrogenated diamond surfaces, the hydrogen termination on the diamond (100) surface appears to be the most stable while that of the (110) the least thermally stable. Deuterium termination of diamond surfaces was found to be stable up to higher temperatures than a corresponding hydrogen termination. This was attributed to a higher thermal desorption temperature due to the increased mass relative to H.

F. Acknowledgments

We wish to thank J. J. Cuomo for helpful discussions regarding deuterium vs. hydrogen termination on diamond. This work has been supported in part by the Office of Naval Research (Contract No. N00014-92-J-1477).

G. References

1. F.J. Himpsel, J.A. Knapp, J.A. van Vechten, D.E. Eastman, Phys. Rev. B **20**, 624 (1979).
2. F.J. Himpsel, D.E. Eastman, P. Heimann and J.F. van der Veen, Phys. Rev. B **24**, 7270 (1981).
3. B.B. Pate, M.H. Hecht, C. Binns, I. Lindau and W.E. Spicer, J. Vac. Sci. Technol. **21**, 364 (1982).
4. B.B. Pate, Surf. Sci. **165**, 83 (1986).
5. J. van der Weide and R.J. Nemanich, Appl. Phys. Lett. **62** (1993) 1878.
6. M. Marchywka, P.E. Pehrsson, S.C. Binari and D. Moses, J. Electrochem. Soc., **140**, No. 2 (1993) L19.
7. P.K. Baumann, T.P. Humphreys and R.J. Nemanich, in *Diamond, SiC and Nitride Wide Band Gap Semiconductors*, edited by C.H. Carter, G. Gildenblat, S. Nakamura, R.J. Nemanich, Mater. Res. Soc. Proc. **339**, Pittsburgh, PA, 69 (1994).
8. J. van der Weide, Z. Zhang, P.K. Baumann, M.G. Wensell, J. Bernholc and R.J. Nemanich, Phys. Rev. B **50** (1994) 5803.
9. R.E. Thomas, R.A. Rudder and R.J. Markunas, J. Vac. Sci. Technol. A **10**, 2451 (1992).
10. P.G. Lurie and J.M. Wilson, Surf. Sci. **65**, 453 (1977).
11. B.B. Pate, J. Woicik, J. Hwang and J. Wu, in *Science and Technology of New Diamond*, edited by S. Saito, O. Fukunaga and M. Yoshikawa, 345 (1990).
12. B.B. Pate, in *Diamond: Electronic Properties and Applications*, edited by L.S. Pan, D.R. Kania, 35 (1995).

13. J. Wilks and E. Wilks, *Properties and Applications of Diamond*, Oxford, UK, 192 (1992).
14. S.V. Pepper, J. Vac. Sci. Technol. **20**, 643 (1982).
15. M. McGonigal, J.N. Russel, Jr., R.E. Pehrsson, H.G. Maguire and J.E. Butler, J. Appl. Phys. **77**, 4049 (1995).
16. G. Francz and P. Oelhafen, Surf. Sci. **329**, 193 (1995).
17. V.S. Smentkowski, H. Jänsch, M.A. Henderson, J.T. Yates, Jr., Surf. Sci. **330**, 207 (1995).
18. D.D. Koleske, S.M. Gates, B.D. Thom, J.N. Russel, Jr. and J.E. Butler, J. Chem. Phys. **102**, 992 (1995).
19. F.J. Himpsel, P. Heimann and D.E. Eastman, Sol. State Commun. **36**, 631 (1980).
20. T.P. Schneider, J. Cho, Y.L. Chen, D.H. Mahler and R.J. Nemanich, in *Surface Chemical Cleaning and Passivation for Semiconductor Processing*, edited by G.S. Higashi, E.A. Irene, T. Ohmi, Mater. Res. Soc. Proc. **315**, Pittsburgh, PA, 197 (1993).
21. F.J. Himpsel, D.E. Eastman and J.F. van der Veen, J. Vac. Sci. Technol. **17**, 1085 (1980).
22. P.K. Baumann and R.J. Nemanich, Proc. of the 5th European Conference on Diamond, Diamond-like and Related Materials, edited by P.K. Bachmann, I.M. Buckley-Golder, J.T. Glass, M. Kamo: J. Diamond Rel. Mat., **4**, 802 (1995).
23. Z. Zhang, M. Wensell and J. Bernholc, Phys. Rev. B **51**, 5291 (1995).
24. L. Diederich, O.M. Küttel, E. Schaller and L. Schlapbach, Surf. Sci. **349**, 176 (1996).
25. M.J. Rutter and J. Robertson, submitted to Phys. Rev. B
26. J. Robertson, Proc. of the 6th European Conference on Diamond, Diamond-like and Related Materials, edited by P.K. Bachmann, I.M. Buckley-Golder, J.T. Glass, M. Kamo: J. Diamond Rel. Mat., **5**, 797 (1996).
27. C. Bandis, B.B. Pate, Phys. Rev. B **52**, 12056 (1995).

IV. Electron Affinity and Schottky Barrier Height of Metal Diamond (100), (111) and (110) Interfaces

Abstract

The electron emission properties of metal diamond (100), (111) and (110) interfaces were characterized by means of UV photoemission spectroscopy (UPS) and field emission measurements. Different surface cleaning procedures including annealing plasma cleaning in ultra-high vacuum (UHV) and rf plasma treatments were used before metal deposition. This resulted in diamond surfaces terminated by oxygen, hydrogen or free of adsorbates. The electron affinity and Schottky barrier height of Zr or Co thin films were correlated by means of UPS. A NEA was observed for Zr on any diamond surface. Co on diamond resulted in NEA characteristics except for oxygen terminated surfaces. The lowest Schottky barrier heights were obtained for the clean diamond surfaces. Higher values were measured for H termination, and the highest values were obtained for O on diamond. For Zr the Schottky barrier height ranged from 0.70 eV for the clean - to 0.90 eV for the O terminated diamond (100) surface. Values for Co ranged from 0.35 eV to 1.40 eV for clean and O covered (100) surfaces, respectively. The metal induced NEA proved to be stable after exposure to air. For the oxygen terminated diamond (100) surface a field emission threshold of 79 V/ μm was measured. Zr or Co deposition resulted in lower thresholds. Values as low as 20 V/ μm were observed for Zr on the clean diamond (100) surface. Results for Zr or Co on H - or O terminated surfaces were higher. H or O layers on diamond tend to cause an increase in the Schottky barrier height and the field emission threshold field of Zr- and Co-diamond interfaces. The value of the electron affinity and Schottky barrier were correlated with work function and different initial surface preparation. The results were largely consistent with a model in which the vacuum level was related to the metal workfunction and the measured Schottky barrier.

A. Introduction

Metal-diamond interfaces may be useful for potential applications in electronic devices based on diamond. These may include metallic surface coatings exhibiting a negative electron affinity (NEA) for use in cold cathode devices, or for more traditional electronic devices, carrier injecting or rectifying electrical contacts will be necessary. For these applications, a fundamental understanding of the Schottky barrier and the relationship to the vacuum level is necessary.

Ultraviolet photoemission spectroscopy (UPS) can be used to measure Schottky barrier heights of rectifying contacts. The technique can even be employed for accurate measurements of contacts with high ideality factors, for which I-V measurements would be unsuitable. UPS is also very sensitive to determine whether a surface exhibits a NEA. Electrons from the valence band are photoexcited into states in the conduction band and some will quasi thermalize

to the conduction band minimum. Indeed, these secondary electrons can escape freely from a NEA surface. The spectra then exhibit a sharp feature at the low kinetic energy end of the photo-emitted electrons [1, 2]. By means of UPS the surface emission properties can be characterized independent of carrier injection and conduction mechanisms.

Field emission measurements integrate the effects of injecting electrons into the semiconductor, transporting the carriers through the bulk and emission from the surface into vacuum. To facilitate these measurements a bias is applied between a metal anode and the sample. Then the emission current is detected.

It has been reported that depositing a few Å of metals like Ti, Ni, Cu, Co or Zr on diamond can induce a NEA [3-8]. The presence of a NEA or positive electron affinity has been correlated with different structures of the metal - diamond interface. Indeed, metal-diamond interfaces exhibiting a NEA have been found to exhibit lower Schottky barrier heights than those exhibiting a positive electron affinity.

The primary focus of this paper is on the relationship of the vacuum level to the diamond conduction band when thin metal layers are deposited on the surface of the diamond. The configuration may be modeled as two separate interfaces, namely the vacuum-metal and metal-diamond interface. For very thin metal layers, electrons could travel through the metal layer without scattering. Thus the Schottky barrier height of the metal-diamond interface plays a critical role in determining the relationship of the diamond conduction band and the vacuum level and whether the structure exhibits a NEA.

A number of studies have dealt with Schottky barrier height measurements of metals deposited on (100) and (111) oriented diamond surfaces as well as polycrystalline diamond films [1, 5-16]. It has been found that the Schottky barrier height of metals on diamond is virtually independent of the workfunction of the metal. But it has been reported that the Schottky barrier height clearly depends on the surface treatment of the diamond before metal deposition. In general, cleaning the diamond surfaces chemically in air results in a higher value for the Schottky barrier height than cleaning in vacuum. For Cu it has also been observed that a reduction in the field emission threshold is correlated with a lowering in electron affinity [5].

Zirconium has been chosen since the material exhibits a low workfunction which may be useful for inducing a NEA. It is also in the same column of the periodic table as Ti, and the Ti diamond interface has been studied previously. Ti has been found to be reactive with C and O. Cobalt is next to nickel and copper in the periodic table. The workfunction of Co (5.0 eV) is higher than for Zr (4.05 eV) or Ti (4.33 eV) and comparable to Ni (5.04-5.35 eV) and Cu (4.48-4.65 eV). Another aspect that is important is that Co may be less reactive than Zr or Ti.

Various approaches may be used to model metal - semiconductor interfaces. The Schottky-Mott model describes an ideal interface, assuming that the difference between the metal

workfunction and the electron affinity of the semiconductor does not change during interface formation. For a p-type semiconductor one can write:

$$\Phi_B = E_G - (\Phi_M - \chi) \quad (1)$$

where Φ_B is the Schottky barrier height, E_G is the band gap, Φ_M is the metal workfunction and χ the electron affinity of the semiconductor.

In many instances the Schottky-Mott model is not realized in practice. For instance, an insulating layer or an interface reaction may cause a high density of interface states in the semiconductor band gap. This may result in pinning of the Fermi level, and the Schottky barrier height is then independent of the metal workfunction.

Thin metal films (less than the electron mean free path) can be thought of as a dipole layer on the semiconductor surface. For such a structure to exhibit a NEA the conduction band minimum has to lie above the vacuum level. Adsorbates or states on the semiconductor surface prior to metal deposition as well as the metal itself may have an impact on whether the metal-semiconductor interface exhibits a NEA or a positive electron affinity.

In this study, results are described for thin Zr or Co films deposited on diamond (100), (111) and (110) surfaces. Prior to metal deposition different in vacuo cleaning procedures were employed to obtain clean, hydrogen terminated or oxygen terminated diamond surfaces. Subsequent to Zr or Co deposition the effects of the different surface treatments on the Zr - or Co-diamond interface were examined. In particular the results of UV photoemission and field electron emission were correlated. The results were compared to previous reports on the properties of thin metal layers on diamond.

B. Experimental Details

Several natural type IIb p-type (boron doped) semiconducting single crystal diamond (100), (111) and (110) crystals (3.0 x 3.0 x 0.25 mm) were employed in this study. Typical resistivities were $10^4 \Omega\text{-cm}$. To remove non diamond carbon and metal contaminants an electrochemical etch has been employed [19]. This cleaning step involved placing the diamond samples between two Pt electrodes in deionized (DI) water as an electrolyte. A DC voltage of 350 V was applied between the electrodes. A typical value for the current was 0.5 mA. The crystals were then exposed to UV/ozone and rinsed in a HF solution to clean the surface from SiO_2 contaminants. It has previously been reported that SiO_2 was present on the surface after an electrochemical etch [20]. Small amounts of these contaminants may be released into the water from the ion exchanger matrix. Subsequent to the wet chemical cleaning step the samples were blown dry with N_2 , mounted on a Mo holder and then transferred into the loadlock of the UHV system. This UHV system consists of several interconnected chambers including capabilities for annealing, H plasma cleaning, metal deposition, angle-resolved ultraviolet

photoemission spectroscopy (ARUPS), Auger electron spectroscopy (AES) and low energy electron diffraction (LEED).

Three different *in vacuo* cleaning procedures were employed to assess the influence of surface preparation on the properties of the metal - diamond interfaces. One procedure involved annealing the samples to 500°C for 10 minutes while another included a 1150°C anneal for 10 minutes. An optical pyrometer was used to measure the temperature of the Mo holder on which the samples were mounted. During the anneals the pressure increased to 8×10^{-10} Torr and 7×10^{-9} Torr, respectively. The third surface cleaning procedure consisted of an exposure to a remotely excited rf H-plasma. The plasma cleaning chamber has been described in an earlier report [21]. Using a remote plasma results in significantly lower electron and ion densities at the surface of the sample. This reduces the possibility of damaging the surface. Atomic force microscopy (AFM) was employed to characterize the morphology of the diamond samples. Linear grooves of ~ 20 Å in depth were detected on the diamond substrates. These are attributed to the polishing process with 0.1 μm diamond grit.

The photoemission spectra were excited by HeI (21.21 eV) radiation. A 50 mm VSW HAC50 hemispherical analyzer was employed to measure the emitted electrons. In this study the energy resolution was 0.15 eV and the acceptance angle was 2° . To overcome the workfunction of the analyzer a bias of 2 V was applied to the sample. It was therefore possible to detect the low energy electrons emitted from the NEA surface. These electrons appear as a sharp peak at the low energy end of UPS spectra. The position of this feature corresponds to the energy position of the conduction band minimum, E_C (Fig. 1). Electrons emitted from E_C appear at $E_V + E_G$ in the spectra, where E_V is the energy of the valence band maximum and E_G the band gap energy. Electrons from E_V get photoexcited to an energy level at $E_V + h\nu$ in the conduction band and are then detected at $E_V + h\nu$ in the UPS spectra. This corresponds to the high kinetic energy end of the spectra. Therefore the spectral width for a NEA surface is $h\nu - E_G$. Using the value of $h\nu = 21.21$ eV for HeI radiation and $E_G = 5.47$ eV for the band gap of diamond, a spectral width of ~ 15.7 eV is obtained. For a surface with a positive electron affinity the low energy cutoff is determined by the vacuum level and will therefore be shifted to higher energies in the spectra compared to the case of a NEA surface. This results in a smaller value for the spectral width.

Photoemission spectra can also be used to determine the Schottky barrier height Φ_B . For p-type semiconductors like diamond, Φ_B corresponds to the difference between the position of the valence band edge, E_V , of the semiconductor and the Fermi level of the metal, E_F (Fig. 2). Since features from both the semiconductor and the metal need to be visible this method is only suitable for metal films with thicknesses equal to or less than the electron mean free path (≤ 5 Å). The relatively weak onset of emission at E_V may, however, be obscured by

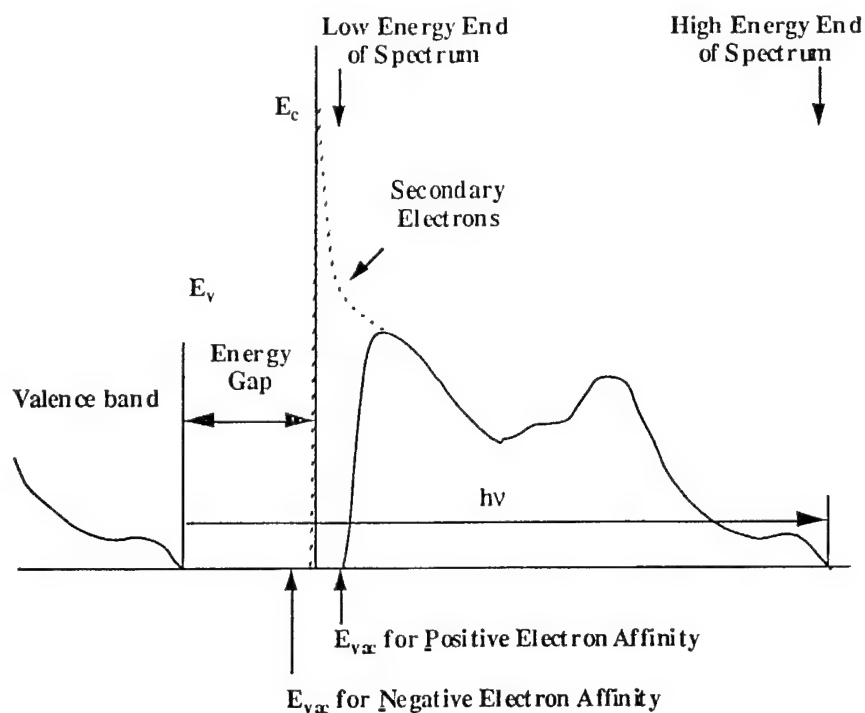


Figure 1. Schematic diagram of photoemission spectra for a negative electron affinity surface (dotted line) and a positive electron affinity surface (solid line).

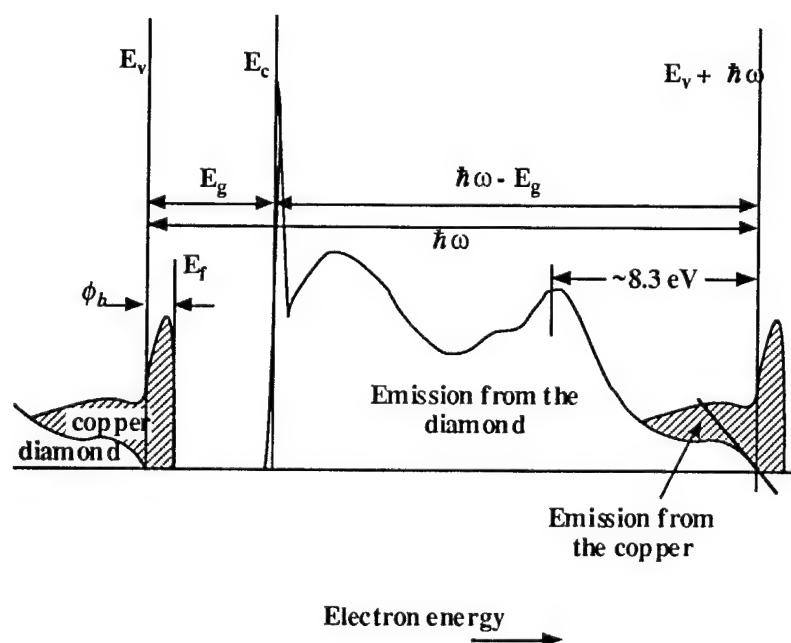


Figure 2. Schematic diagram of photoemission spectra for copper deposited on diamond. The Schottky barrier height Φ_B is determined from the difference between the position of the valence band edge of diamond E_v and the metal Fermi level E_F .

the metal Fermi level even for metal layers thinner than the mean free path. As an independent method E_V can be referenced to some strong features in the diamond spectrum before metal deposition. These features can still be detected following the overgrowth of a thin metal layer. Here we have chosen a peak positioned 8.3 eV below E_V . In case of a NEA the position of the low energy turnon (which corresponds to E_C) can also be used as a reference point to find E_V (which is the high energy turnon of the spectrum). The distance between E_C and E_V has to be $h\nu - E_G$ (Fig. 2). A change in band bending (e.g. due to metal deposition) can be detected as a shift of the spectrum with respect to the Fermi level. Again since the position of E_V may be difficult to discern such a shift can be detected from the position of bulk features in the spectra.

The UPS spectra of wide band gap semiconductors may be shifted due to photovoltaic effects [22]. A recent study showed such shifts for diamond (111) surfaces [23]. However, these shifts are uniform for the entire spectrum. This means that the relative distance between the Fermi level and the valence band maximum will not change. A separate vacuum chamber with a base pressure of $\sim 2 \times 10^{-8}$ Torr was used to carry out the field emission measurements. To determine the I-V characteristics a bias of 0–1100V was applied between the sample and a 2 mm diameter stainless steel anode with a rounded tip. The I-V measurements were conducted with a Keithley 237 source measure unit. The distance between the sample and the anode could be varied in vacuum by means of a stepper motor. The distances ranged from 2 to 30 μm . The mechanism of electron emission by field emission is more complex than by photoemission spectroscopy. With photoemission only the emission properties of the surface are characterized. The samples only need to be sufficiently electrically conducting to avoid charging due to electron emission. For field emission, injection of electrons from an electrical contact into the semiconductor, transport of the electrons through the bulk to the emitting surface and the emission from the surface into vacuum contribute to the overall emission properties.

An e-beam evaporator has been employed to deposit Co or Zr films of 1, 2, 3, 6, 10 Å thickness onto the diamond (100), (111) and (110) surfaces. Before deposition the metal sources were melted to clean surface contaminants from the source material. The thickness was monitored by a quartz crystal oscillator. The growth rate was 0.1 Å/s up to 3 Å in thickness and 0.3 Å/s for 6 and 10 Å in thickness. The deposition was done at room temperature. The base pressure in the chamber was 1×10^{-10} Torr and the pressure rose to 5×10^{-9} Torr during deposition. The samples were characterized before and after metal deposition using angle-resolved ultraviolet photoemission spectroscopy (ARUPS), Auger electron spectroscopy (AES), low energy electron diffraction (LEED) and atomic force microscopy (AFM). The UPS measurements were also repeated following air exposure of the metallized diamond samples. This was done to examine whether the NEA characteristics were stable in air. Such an air stability would be of technological interest.

The presence of a zirconium or cobalt layer was confirmed by AES. AFM images of the diamond wafers used in this study clearly showed arrays of linear grooves parallel to each other. Typical depths of about 20 Å were observed for these grooves. This surface structure is due to the commercial surface polishing of the diamond samples. For metal thicknesses of 1 Å and 2 Å, the Zr layers replicated the surface morphology of the underlying diamond substrates as observed by AFM. For thicker layers nonuniform growth was detected. Similar characteristics were observed for Co.

C. Results

Diamond Surfaces. We first consider the properties of the diamond (100), (111) and (110) surfaces before Co or Zr deposition. Diamond (100) samples annealed to 500°C exhibited a 1×1 LEED pattern and an AES oxygen feature. An 1150°C anneal or a H plasma exposure resulted in 2×1 reconstructed surfaces and the removal of oxygen according to AES. As evidenced by UPS spectra the surfaces annealed to 500°C and 1150°C showed a positive electron affinity of 1.45 eV and 0.75 eV, respectively. A NEA was induced by the H plasma clean.

For diamond (111) surfaces annealing to 1150°C or exposure to a H plasma resulted in a 2×1 LEED pattern and caused the amount of surface oxygen contaminants to drop below the detection limit of the AES system. By means of UPS a positive electron affinity around 0.55 eV was measured for the 1150°C anneal and a NEA was determined for the H plasma clean.

A 700°C anneal or a H plasma removed the oxygen from the diamond (110) surfaces according to AES, and NEA characteristics as evidenced by UPS. Subsequent to a 1150°C anneal the NEA was removed and a positive electron affinity of 0.55 eV was determined. Another H plasma clean resulted in a NEA again.

Furthermore emission below the conduction band minimum was observed for (100), (111) and (110) surfaces following a H plasma treatment.

All these results are consistent with previous studies on surface cleaning and UPS measurements of diamond (100), (111) and (110) surfaces [1, 2, 24-27]. In particular, the effect of emission below the conduction band minimum for H terminated surfaces has been discussed in a recent report [27].

Zirconium on Diamond. The deposition of 1 Å of Zr onto clean diamond (100) surfaces resulted in an increase in the width of the photoemission spectrum consistent with a NEA. The energy between the bulk feature from the diamond (labeled B) and the valence band maximum did not change subsequent to 1 Å of Zr deposition (Fig. 3a). This energy is expected to remain constant for thicker Zr layers. Feature B is used as a point of reference to determine whether there is a shift in the spectra after metal deposition or other processing. This shift is indicative

of a change in Fermi level pinning in the gap. Thicker layers of Zr up to 10 Å still resulted in a NEA, however the intensity of the spectrum was reduced. A Schottky barrier height of $\Phi_B = 0.70$ eV was determined from the UPS spectra. This value stayed constant for the different thicknesses of the Zr films. The Fermi level pinning did not change with increasing thickness of the Zr layer. Also the bulk features of diamond became less intense with increased Zr coverage.

Zr deposition on H and O terminated (100) surfaces resulted in NEA characteristics, too (Fig. 3b and c). Schottky barrier heights of $\Phi_B = 0.75$ eV and $\Phi_B = 0.90$ eV were measured, respectively.

Subsequent to depositing Zr onto clean (111) surfaces a Schottky barrier height of $\Phi_B = 0.85$ eV and a NEA were measured (Fig. 3d). These characteristics did not change for increasing Zr thickness.

A NEA was still observed after growing Zr on the H terminated (111) surface, even for a 10 Å thick film. A Schottky barrier height of $\Phi_B = 0.95$ eV and a shift in the spectra of 0.6 eV were measured upon Zr deposition.

Corresponding to (100) and (111) surfaces a NEA was observed following Zr deposition on both the clean and H terminated (110) surfaces. A Schottky barrier height of $\Phi_B = 0.70$ eV was determined for both the clean and H covered surface. The low energy edge of the spectra extended to below the conduction band minimum.

In several cases an additional feature was observed at the low energy end of the spectrum, especially for 6 and 10 Å thick films. This peak may be attributed to emission from Zr. For Zr on the O terminated (100) and clean (111) surface the emission extended to 0.5 eV and 0.6 eV below the conduction band minimum, respectively. For several cases (see Fig. 3b for example) the emission below the conduction band minimum due to the NEA effect was so strong that it could not be determined whether there was also low energy emission due to the Zr or not.

All these results have been summarized in Table 1. After exposing the samples of Zr on clean, H and O terminated diamond surfaces to air the width of the UPS spectra still corresponded to a NEA. However the intensity of the spectra was reduced. Such a reduction in intensity may be consistent with the presence of physisorbed species. These are expected to be on the surface due to the air exposure. Indeed the presence of oxygen was detected by means of AES subsequent to air exposure. Overall the NEA characteristics proved to be stable following air exposure.

Cobalt on Diamond. A NEA and Schottky barrier heights of $\Phi_B = 0.35$ eV and $\Phi_B = 0.45$ eV were detected for Co on clean and H covered diamond (100) surfaces, respectively. However a positive electron affinity of $\chi = 0.80$ eV, and a Schottky barrier of $\Phi_B = 1.40$ eV were measured for Co on the oxygen terminated (100) surface.

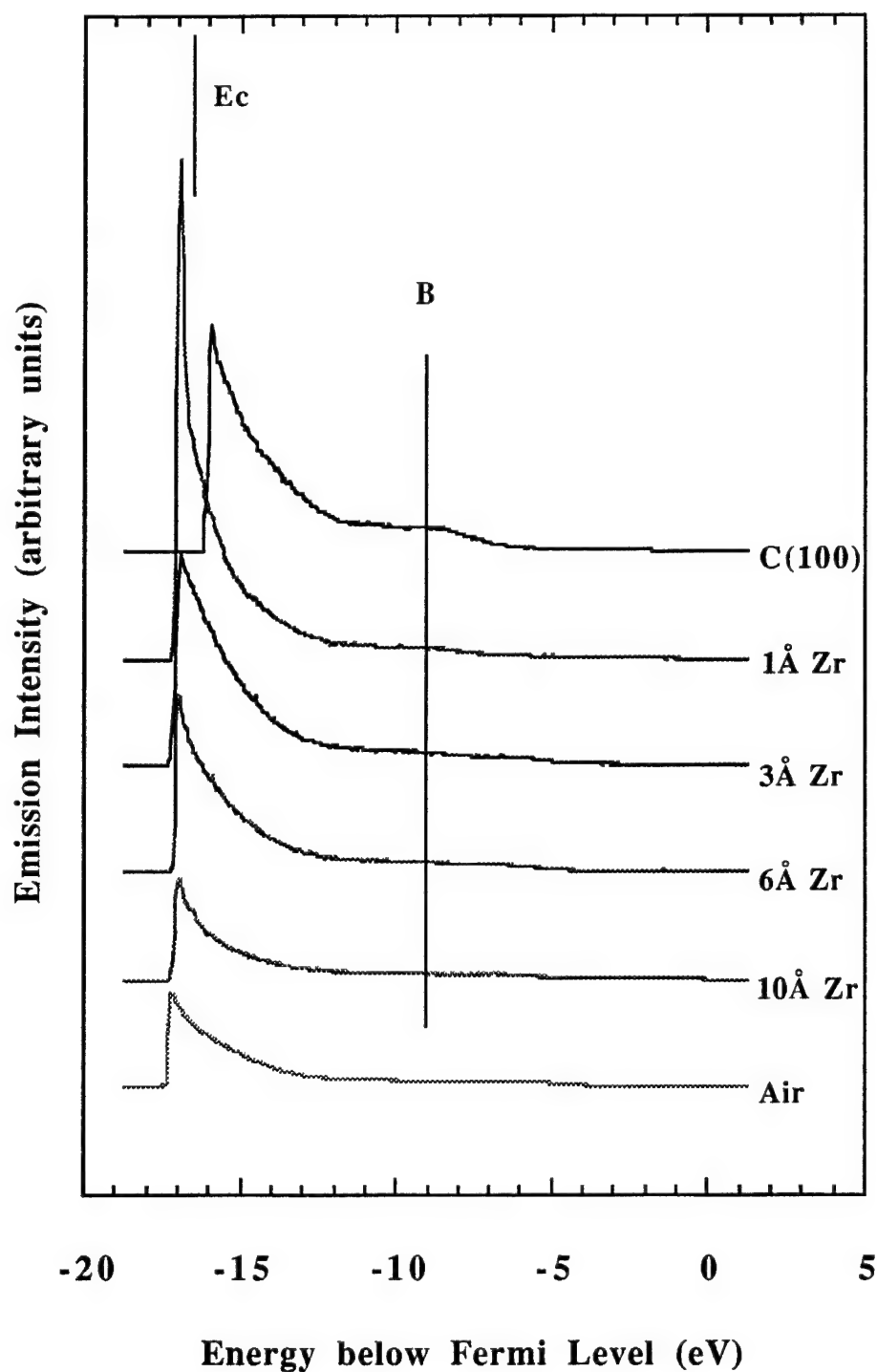


Figure 3a. UV photoemission spectra of Zr on a clean diamond (100) surface. The diamond surface exhibits a positive electron affinity before Zr deposition. Subsequent to Zr deposition, the width of the spectrum increases and a NEA is detected. Emission below E_c is observed. After air exposure, the NEA is still observed.

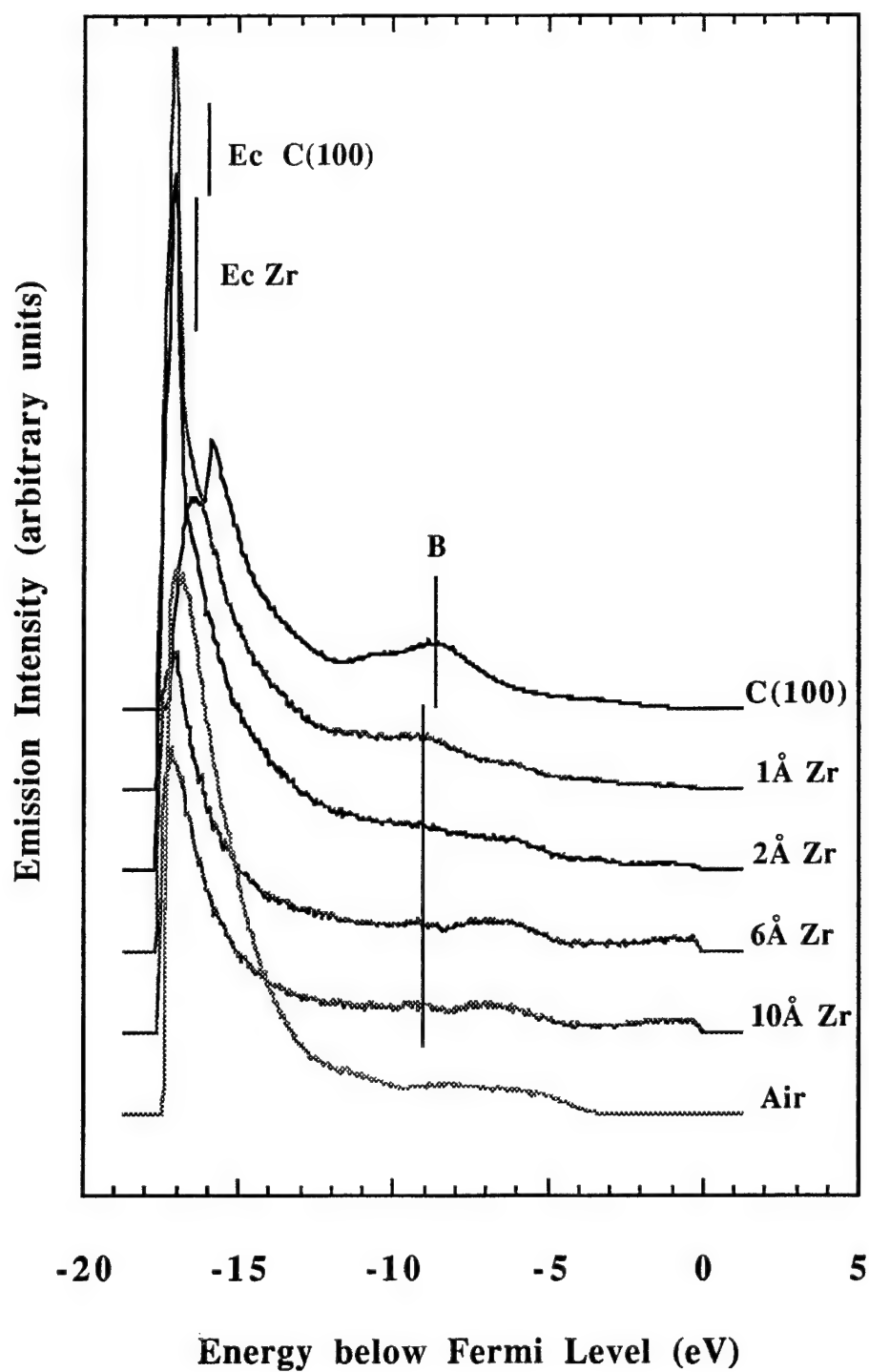


Figure 3b. UV photoemission spectra of Zr on a hydrogen terminated diamond (100) surface. The diamond surface exhibits a NEA before Zr deposition. Also, emission below E_c is detected. Following Zr deposition, the NEA is still observed, however the emission below E_c gets reduced with increasing thickness of Zr. After air exposure, the NEA is still detected.

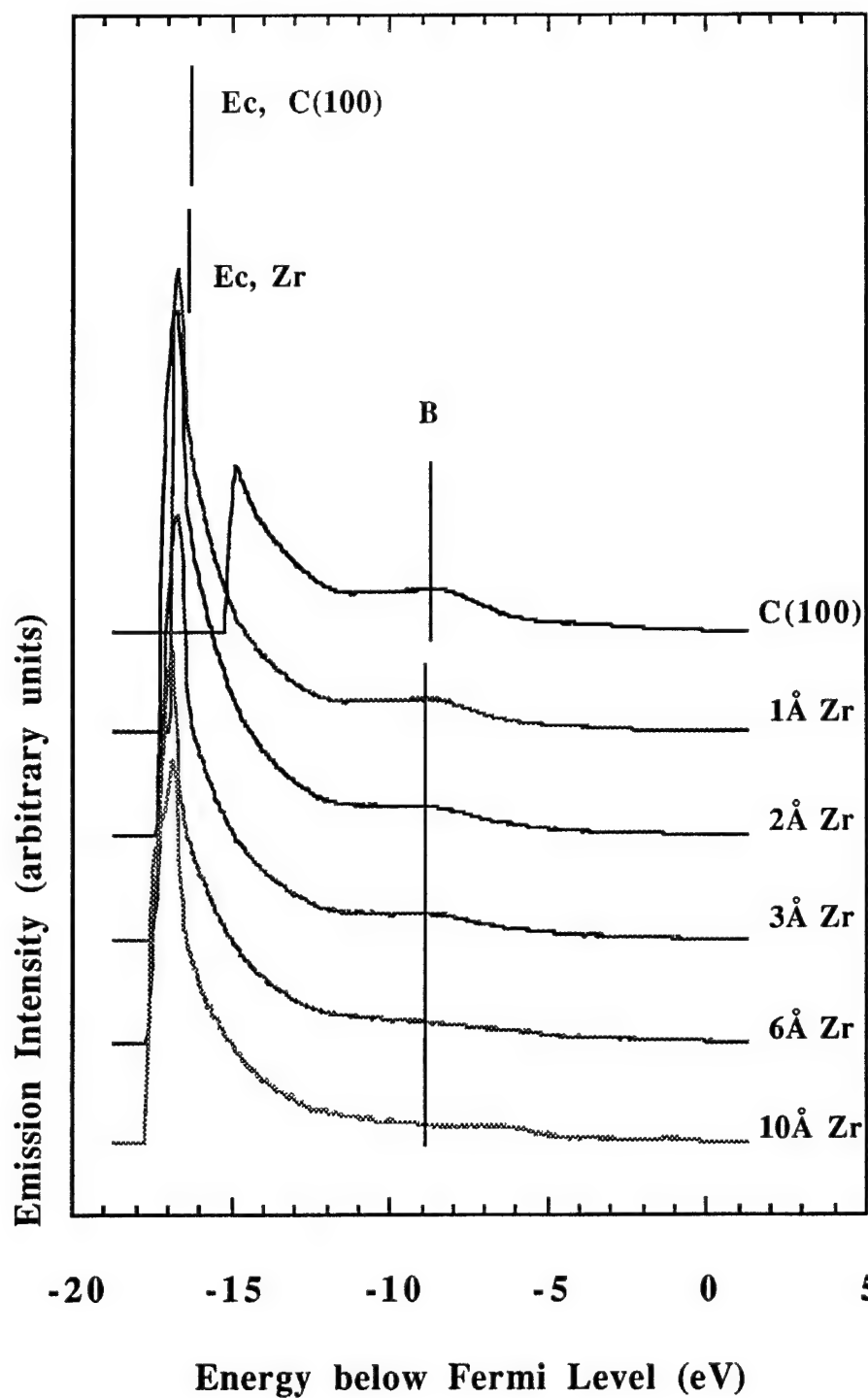


Figure 3c. UV photoemission spectra of Zr on an O terminated diamond (100) surface. The diamond surface exhibits a positive electron affinity before Zr deposition. Subsequent to Ar deposition, the width of the spectrum increases and a NEA is still detected.

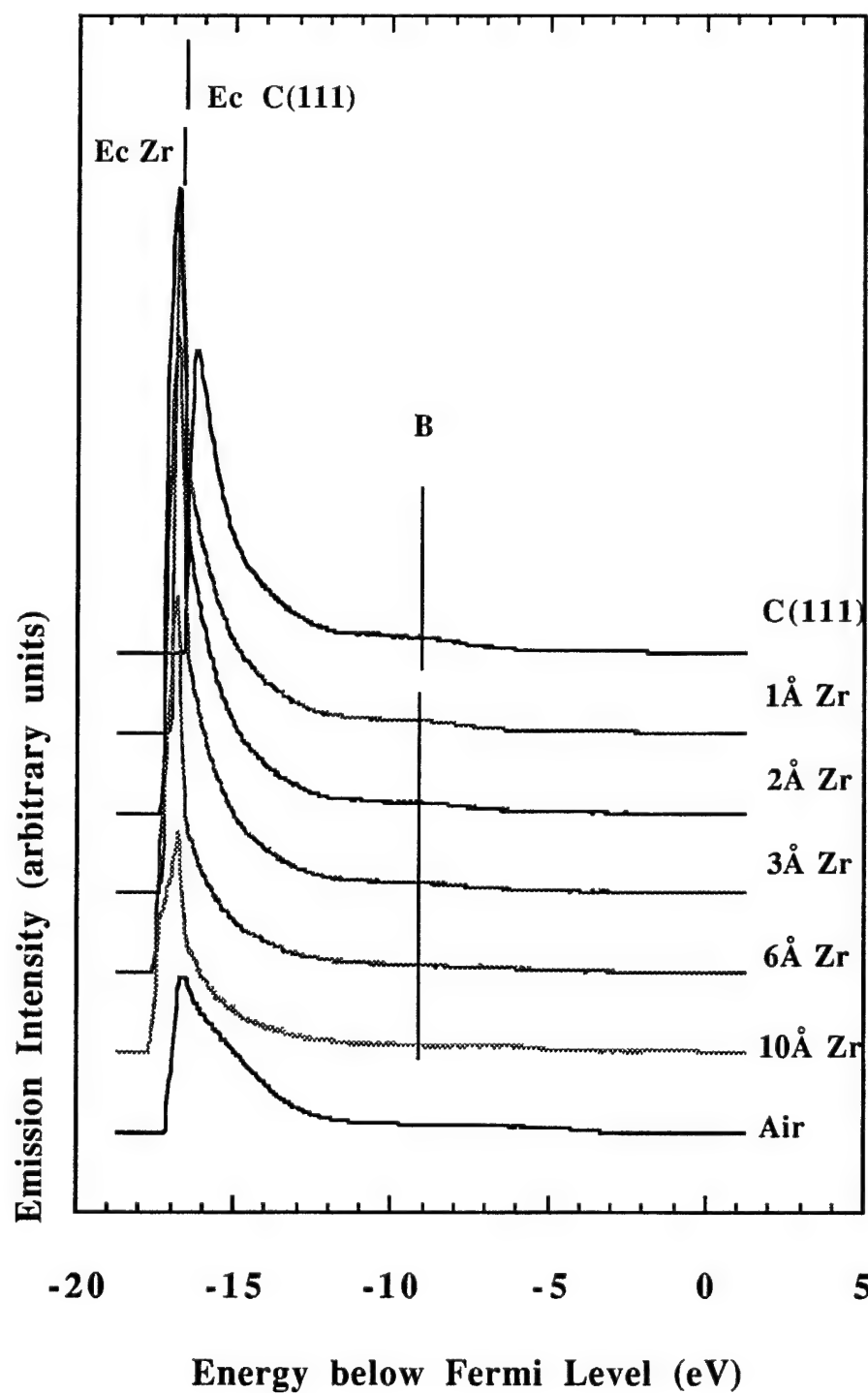


Figure 3d. UV photoemission spectra of Zr on a clean diamond (111) surface. The diamond surface exhibits a positive electron affinity before Zr deposition. Subsequent to Zr deposition, the width of the spectrum increases and a NEA is detected. After air exposure the NEA is still observed.

Table 1. Summary of the UPS measurements on diamond (100), (111) and (110) surfaces before and after Zr deposition. PEA: positive electron affinity, NEA: negative electron affinity. Also the values of the effective electron affinity χ_{eff} calculated according to equation (3). The experimental uncertainties are 0.1 eV.

| Sample UPS surface before Zr growth | UPS after Zr growth | NEA stable in air | calculated χ_{eff} |
|--|---------------------------------------|--|---------------------------------------|
| C(100) | | | |
| clean | PEA, $\chi = 0.75$ eV Ev-Ef=0.50eV | NEA, $\chi < 0$, $\Phi_B = 0.70$ eV, no shift | yes $\chi_{\text{eff}} = -0.7$ eV |
| H terminated | NEA, $\chi < 0$ Ev-Ef=0.50eV | NEA, $\chi < 0$, $\Phi_B = 0.75$ eV, 0.3 eV shift | yes $\chi_{\text{eff}} = -0.65$ eV |
| O terminated | PEA, $\chi = 1.40$ eV Ev-Ef=0.80eV | NEA, $\chi < 0$, $\Phi_B = 0.90$ eV, 0.1 eV shift | yes $\chi_{\text{eff}} = -0.5$ eV |
| C(111) | | | |
| clean | PEA, $\chi = 0.45$ eV Ev-Ef=0.60eV | NEA, $\chi < 0$, $\Phi_B = 0.85$ eV, 0.1 eV shift | yes $\chi_{\text{eff}} = -0.55$ eV |
| H terminated | NEA, $\chi < 0$ Ev-Ef=0.4eV | NEA, $\chi < 0$, $\Phi_B = 0.95$ eV, 0.6 eV shift | yes $\chi_{\text{eff}} = -0.45$ eV |
| C(110) | | | |
| clean | PEA, $\chi = 0.5$ eV Ev-Ef=0.50eV | NEA, $\chi < 0$, $\Phi_B = 0.70$ eV, 0.2 eV shift | yes $\chi_{\text{eff}} = -0.70$ eV |
| H terminated | NEA, $\chi < 0$ Ev-Ef=0.40eV | NEA, $\chi < 0$, $\Phi_B = 0.70$ eV, 0.4 eV shift | yes $\chi_{\text{eff}} = -0.70$ eV |

Similar to the (100) surface NEA characteristics were observed for Co on clean as well as H terminated (111) and (110) surfaces. Schottky barrier heights between $\Phi_B = 0.40$ eV and 0.50 eV were measured. In Figure 4 UPS spectra of Co on a H terminated (110) surface are shown as an example. The details of the measurements are listed in Table 2. Also the NEA of the Co - diamond interfaces proved to be stable following air exposure.

Field Emission Results. Field emission measurements were performed on diamond (100) samples as well as on 2Å and 10Å thick Zr or Co films deposited on clean, hydrogen or oxygen terminated diamond (100) surfaces. The measurements were used to determine the applied voltage per μm where detectable emission was observed. The voltage per μm is sometimes termed the average field. Since the measured current-voltage curves did not exhibit an absolute threshold it was necessary to define the emission threshold voltage per μm for a specific current and in this study a value of 0.1 μA was employed. The I-V data for Zr on the O terminated diamond surface are shown in Fig. 5. The average field emission threshold field was calculated from the values for different distances.

The results and the standard deviations for the different surface terminations are summarized in Table 3. Average threshold fields between 20 and 79 V/ μm were measured for the different surface preparations. The highest value of 79 V/ μm was determined for the diamond surface. In general, the threshold field was reduced for Zr or Co deposition. For both Zr and Co deposition the lowest threshold has been obtained for the clean surface, and here average field values of 20 V/ μm and 30 V/ μm have been determined for Zr and Co respectively. The next highest values of 23 V/ μm for Zr and 39 V/ μm for Co were measured on the hydrogen terminated surface. The clean and H terminated surfaces also exhibited a NEA as determined from UPS spectra. Higher threshold average field values were obtained for the Co and Zr on the oxygen terminated diamond. A value of 49 V/ μm was determined for Zr on the oxygenated surface, and this surface still exhibited a NEA. The Co on the oxygen terminated surface resulted in the highest average field value of 52 V/ μm for the different metal-diamond interfaces studied here. This surface exhibited a positive electron affinity.

The general trend of the results is that the threshold value decreased with decreasing electron affinity. The surfaces exhibiting a NEA also exhibited a lower field emission threshold than those with a positive electron affinity. Since the actual value of the electron affinity cannot be determined by UPS for a NEA one could correlate the threshold with the Schottky barrier height of the Zr diamond or Co-diamond interfaces. The threshold does decrease with declining values of the Schottky barrier height for both Zr and Co.

The values for the field emission threshold reported here are of the same order of magnitude as previously reported for diamond samples [28-30]. The data from the field emission measurements have been fitted to the Fowler-Nordheim equation [31]:

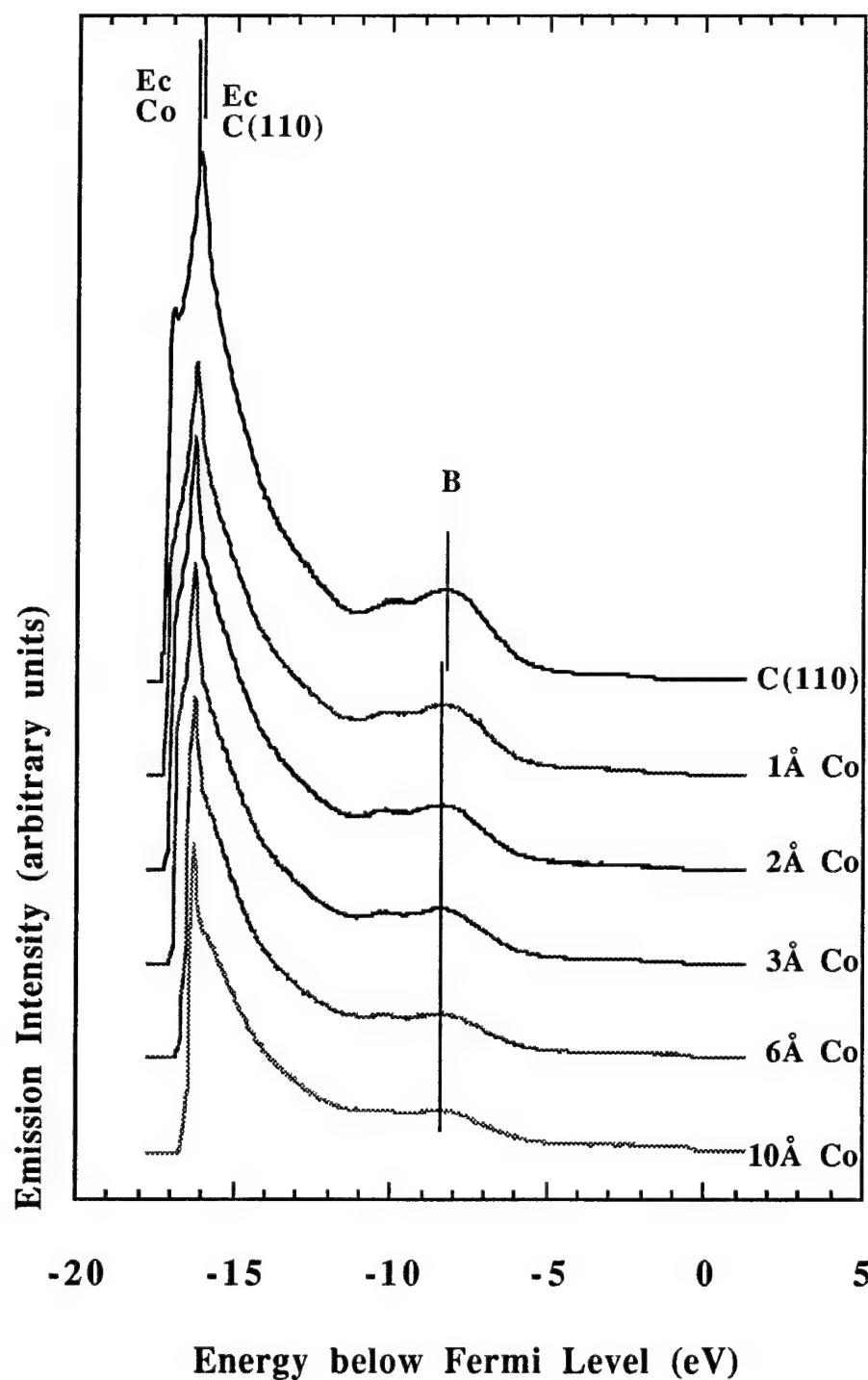


Figure 4. UV photoemission spectra of Co on a H terminated diamond (110) surface. The diamond surface exhibits a NEA before Zr deposition. Also, emission below E_c is detected. Following Zr deposition the NEA is still observed, however, the emission below E_c gets reduced with increasing thickness of Zr.

Table 2. Summary of the UPS measurements on diamond (100), (111) and (110) surfaces before and after Co deposition. PEA: positive electron affinity, NEA: negative electron affinity. Also the values of the effective electron affinity χ_{eff} calculated according to equation (3). The experimental uncertainties are 0.1 eV.

| Sample UPS surface before Co growth | UPS after Co growth | NEA stable in air | calculated χ_{eff} |
|-------------------------------------|--|--|---------------------------------------|
| C(100) | | | |
| clean | PEA, $\chi = 0.75$ eV Ev-Ef=0.50 eV | NEA, $\chi < 0$, $\Phi_B = 0.35$ eV, no shift | yes $\chi_{\text{eff}} = -0.2$ eV |
| H terminated | NEA, $\chi < 0$ Ev-Ef=0.55 eV | NEA, $\chi < 0$, $\Phi_B = 0.45$ eV, 0.15 eV shift | yes $\chi_{\text{eff}} = -0.1$ eV |
| O terminated | PEA, $\chi = 1.45$ eV Ev-Ef=0.80 eV | PEA, $\chi = 0.80$ eV, $\Phi_B = 1.40$ eV, 0.55 eV shift | $\chi_{\text{eff}} = 0.90$ eV |
| C(111) | | | |
| clean | PEA, $\chi = 0.50$ eV Ev-Ef=0.50 eV | NEA, $\chi < 0$, $\Phi_B = 0.40$ eV, no shift | yes $\chi_{\text{eff}} = -0.15$ eV |
| H terminated | NEA, $\chi < 0$ Ev-Ef=0.55 eV | NEA, $\chi < 0$, $\Phi_B = 0.50$ eV, 0.1 eV shift | yes $\chi_{\text{eff}} = -0.05$ eV |
| C(110) | | | |
| clean | PEA, $\chi = 0.6$ eV Ev-Ef=0.50 eV | NEA, $\chi < 0$, $\Phi_B = 0.40$ eV, 0.1 eV shift | yes $\chi_{\text{eff}} = -0.10$ eV |
| H terminated | NEA, $\chi < 0$ Ev-Ef=0.40 eV | NEA, $\chi < 0$, $\Phi_B = 0.45$ eV, 0.1 eV shift | yes $\chi_{\text{eff}} = -0.05$ eV |

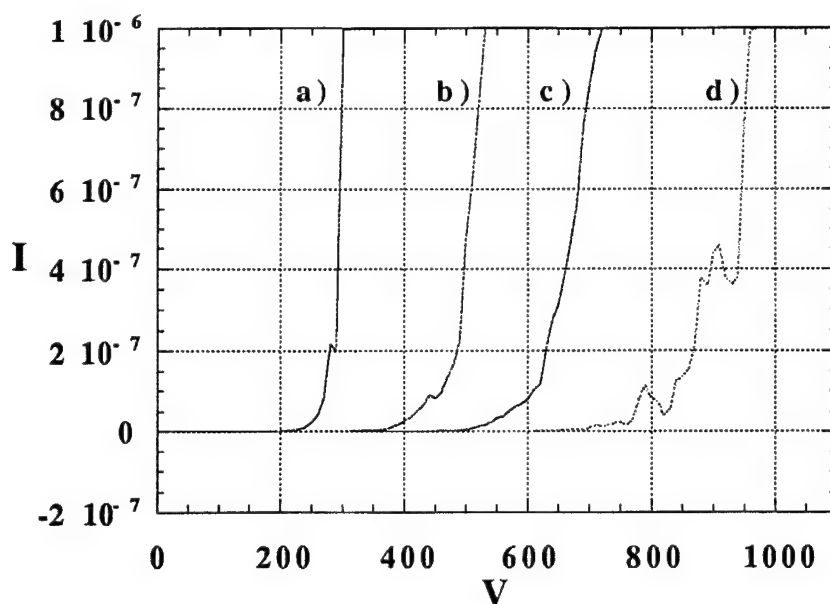


Figure 5. Field emission current-voltage curves for Zr on a oxygen terminated type IIb single crystal diamond (100) sample. Distances between the sample and the anode: a) 5.7 μm , b) 9.7 μm , c) 12.4 μm , d) 17.2 μm .

$$I = k \left(\frac{\beta V}{d} \right)^2 \exp \left(\frac{-6.530 d \phi^{3/2}}{\beta V} \right) \quad (2)$$

In this equation I is the current in amps, V is the bias in volts, d is the distance between the sample and the anode in μm , k is a constant, ϕ is the effective barrier height in eV and β is the field enhancement factor. For perfectly flat surfaces β is equal to 1 and can be neglected. It should be noted that different surface terminations could lead to changes in the actual workfunction and therefore give the appearance of different β values. In our case the RMS roughness of the diamond surfaces as well as the metal films on diamond was of the order of a few \AA . We therefore do not expect the surface roughness to have a significant impact on the field electron measurements. Based on this consideration a value of 1 has been assumed for β . The effective barrier heights ϕ were obtained by fitting the field emission data to equation (3). Figure 6 shows this fitting of the field emission data for Zr on the clean surface. The fitted graphs exhibit different slopes corresponding to different distances between the anode and the sample. They resulted in about the same value for the effective barrier height. The values and the standard deviations are listed in Table 3.

D. Discussion

It was found that the Schottky barrier height of Zr on H terminated surfaces was about the same or only 0.1 eV higher than for Zr on clean surfaces of the same orientation. In addition,

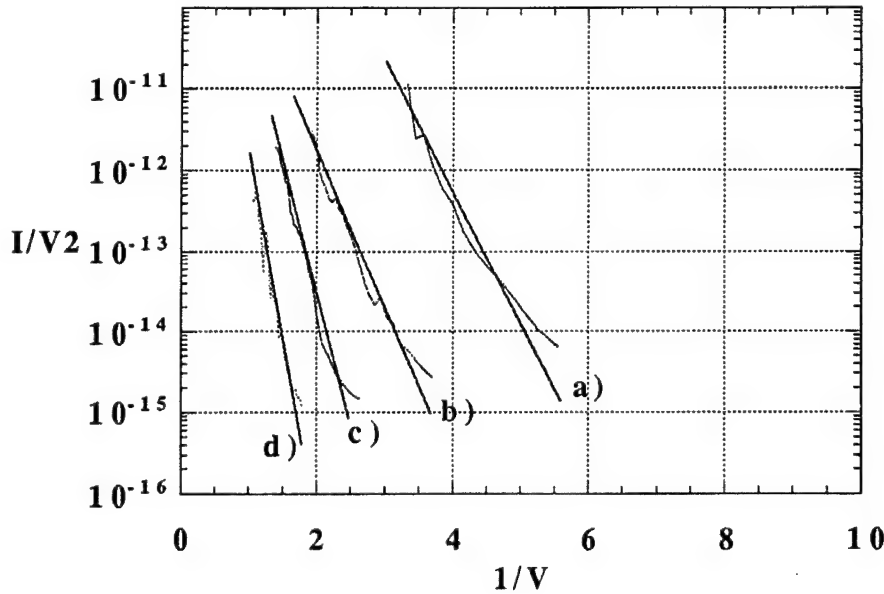


Figure 6. Field emission current-voltage curves (for Zr on a oxygen terminated type IIb single crystal diamond (100) sample) to Fowler-Nordheim equation. Distances between the sample and the anode: a) 5.7 μm , b) 9.7 μm , c) 12.4 μm , d) 17.2 μm .

the Schottky barrier height for Zr on the oxygenated (100) surface is only 0.2 eV larger than for the clean (100) surface. For Co on diamond the differences in Schottky barrier height for the H covered and clean surfaces are comparable to Zr. In contrast, for Co on the oxygen terminated (100) surface the Schottky barrier height was found to be larger by 1.05 eV than for the Co on the clean (100) surface.

The basic assumption in this study has been that it is necessary to consider both the metal-vacuum and metal-semiconductor interfaces to characterize the photoemission properties. With this in mind, the equation below gives an expression for the effective electron affinity for a thin metal overlayer on a semiconductor. The equation is a function of both the metal workfunction and the Schottky barrier height for the metal on the p-type semiconductor [32]. It is specific for photoemission of thin metal layers (less than the electron mean free path) on semiconductors:

$$\chi_{\text{eff}} = (\Phi_{\text{M}} + \Phi_{\text{B}}) - E_{\text{G}} \quad (3)$$

With the band gap of diamond $E_{\text{G}} = 5.47$ eV, the workfunction of Zr, $\Phi_{\text{M}} = 4.05$ eV or of Co, $\Phi_{\text{M}} = 5.00$ eV and the measured Schottky barrier height, the effective electron affinity can be calculated using Eq. 3. The results are listed for Zr in Table 1 and for Co in Table 2. In comparing with the photoemission measurements, the deduced effective electron affinity are consistent with the photoemission measurements. An NEA was observed for Zr on the clean,

Table 3. Results of electron emission measurements. PEA: positive electron affinity, NEA: negative electron affinity. The averages and standard deviations of the field emission measurements at different distances are shown as the field emission threshold and the barrier height. The threshold current is 0.1 μ A.

| Sample | UPS | Field Emission Threshold (V/ μ m) | Barrier Height (eV) |
|-----------------------|---|---------------------------------------|---------------------|
| C(100) | after 500°C anneal PEA, $\chi \cong 1.4$ eV | 79 ± 7 | 0.23 ± 0.01 |
| Zr/C(100) clean | NEA, $\chi < 0$, $\Phi_B \cong 0.70$ eV | 20 ± 3 | 0.09 ± 0.01 |
| Zr/C(100) hydrogen | NEA, $\chi < 0$, $\Phi_B \cong 0.75$ eV | 23 ± 3 | 0.11 ± 0.01 |
| Zr/C(100) oxygen | NEA, $\chi < 0$, $\Phi_B \cong 0.90$ eV | 49 ± 4 | 0.20 ± 0.01 |
| Co/C(100) clean | NEA, $\chi < 0$, $\Phi_B \cong 0.35$ eV | 30 ± 3 | 0.11 ± 0.01 |
| Co/C(100) hydrogen | NEA, $\chi < 0$, $\Phi_B \cong 0.45$ eV | 39 ± 4 | 0.16 ± 0.02 |
| Co/C(100) oxygen | PEA, $\chi \cong 0.75$ eV, $\Phi_B \cong 1.40$ eV | 52 ± 4 | 0.20 ± 0.02 |

H, and O terminated diamond surfaces as well as detecting a NEA for Co on clean and hydrogenated diamond surfaces and a positive electron affinity for the O terminated surface.

Other effects may contribute to the observations. For instance, it has been reported that carbon contamination can lower the workfunction of Ni [33]. The first layer of Ni deposited on diamond may have a different workfunction due to an interface reaction or inter-diffusion. This effect may also occur for Zr or Co on diamond. But such an effect could only lead to a stronger NEA for Zr on diamond and Co on the clean and H terminated diamond surfaces and would be consistent with our results. For Co on the oxygen terminated surface the measured and calculated values for the electron affinity are consistent with each other. Thus at least for the latter case this effect is not expected to be significant. Since all of the Zr-diamond interfaces investigated in our study exhibit a NEA we can not determine if such an effect could play a significant role for Zr. But one effect may give some clues on this issue: For Zr on the O terminated (100) and clean (111) surface emission is observed below the conduction band

extends to 0.5 eV and 0.6 eV below the conduction band minimum, respectively. These values are comparable to the calculated effective electron affinity χ of 0.5 eV for Zr on an oxygenated (100) and 0.55 eV for Zr on a clean (111) surface. From these considerations the workfunction of Zr does not appear to be changed.

From results here and previously, Eq. 3 has been used successfully to describe photoemission of Ti, Ni, Co, Cu and Zr deposited on diamond [3-6]. In these studies it has been found that the Schottky barrier height for clean surfaces was lower than for surfaces terminated by hydrogen or oxygen. Indeed, metal-diamond interfaces exhibiting a NEA have a lower Schottky barrier height than those exhibiting a positive electron affinity. The band schematic of the metal-diamond interface is shown in Fig. 7a). In Fig. 7a) the Schottky barrier height is sufficiently small to result in a NEA. Fig. 7b) shows the case for a larger Schottky barrier and a positive electron affinity. Surface preparation apparently has a significant impact on the properties of the interface subsequent to metal deposition [3-6].

There have been several recent theoretical studies of Schottky barriers on diamond. Studies by Erwin and Pickett [34-37] and Pickett, Pederson and Erwin [38] described two configurations with very similar values for the formation energy for Ni on clean (111) surfaces. One resulted in a Schottky barrier height of less than 0.1 eV, the other of 0.8 eV. Experimental results measured the Schottky barrier height to be 0.5 eV which is between the two calculated values [4]. It was suggested that both configurations exist on the surface resulting in the observed intermediate value. Considering copper on diamond (111) surfaces, Lambrecht [39] calculated a value for the Schottky barrier height of less than 0.1 eV for clean surfaces and greater than 1.0 eV for hydrogen terminated surfaces. Copper-diamond interfaces have been investigated previously by UPS [5]. The Schottky barrier heights were the lowest for clean surfaces and the highest for oxygen terminated surfaces. The values for H termination fell in-between. Furthermore, for thin Cu overlayers a NEA has been found for Cu on clean or H terminated diamond (100), (111) and (110) surfaces while a positive electron affinity was found for Cu on oxygenated diamond surfaces.

According to these results the surface termination prior to metal deposition appears to be have a significant effect on the Schottky barrier height. For metals deposited on clean surfaces lower values for the Schottky barrier height and a greater likelihood of inducing a NEA are expected than for metals on non adsorbate free surfaces. The Schottky barrier heights reported in our study for Zr and Co on diamond are consistent with this. Also the results of Ti, Ni or Cu on diamond [3-5] follow this pattern. In Fig. 8 the measured Schottky barrier heights of the different metal-diamond interfaces are plotted vs. the metal workfunction for Zr, Ti, Cu, Co and Ni. The data are experimental results from this study for Zr and Co as well as from previous publications for Ti, Cu and Ni [3-5]. Apparently the Schottky barrier height for Zr on

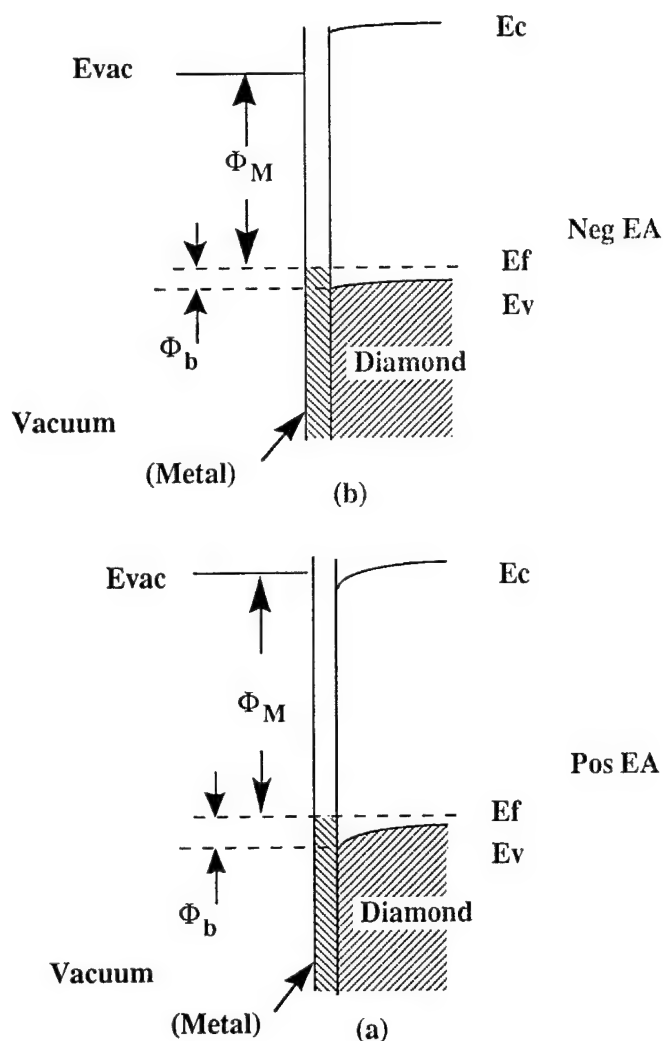


Figure 7. Band diagrams of the metal-diamond interface. (a) The sum of the Schottky barrier height and work function for metal on diamond is greater than the band gap of diamond resulting in a positive electron affinity (For Co on the oxygen terminated surface). (b) The Schottky barrier height added to the metal work function is less than the diamond band gap. This corresponds to a NEA. (Zr on clean, H and O terminated surfaces. Co on clean and H terminated surfaces.

diamond does not depend on the surface termination of the diamond substrate as strongly as is the case for Co, Cu or Ni.

The variations in the Schottky barrier for the different surface preparations may be due the reactivities of the metal layers with the diamond or the surface adsorbate. Zr, like Ti does react with C. In a prior study it was found that if a 30 Å thick Ti layer was annealed to $>400^\circ\text{C}$, a reaction with diamond was observed [3]. This reaction was not evident at room temperature, but it is likely that the reaction could affect the first few monolayers for Zr or Ti on diamond. In our experiments Zr may have also reacted with the oxygen from the oxygen terminated surface. In contrast, Co, Cu or Ni do not react as readily with C or O. Thus for the metal-diamond

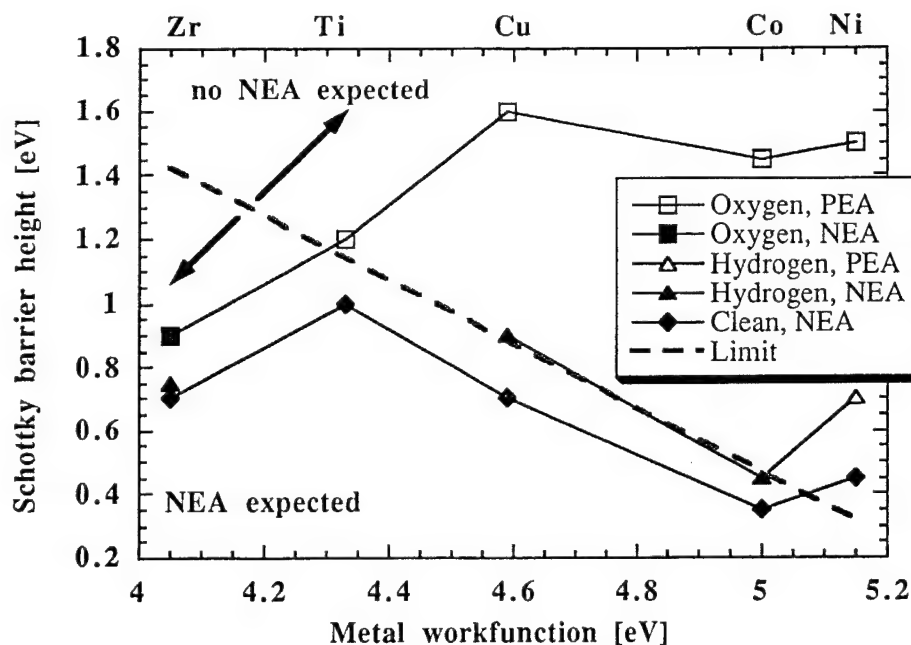


Figure 8. Diagram of the Schottky barrier height vs. metal workfunction for Ti, Zr, Cu, Co and Ni. The dashed line represents the limit for which a NEA is expected for metal-diamond interfaces according to Eq. (3). Thus, a NEA is expected for data points below this dashed line and a positive electron affinity for those above. The experimental data for Ti, Zr, Cu, Co and Ni are plotted. The filled markers correspond to an experimentally observed NEA and the empty markers indicate an experimentally observed positive electron affinity (labeled PEA in the figure).

interface structure for Co, Cu or Ni on the clean diamond surfaces is different than for the oxygen terminated surfaces. Consider now the Schottky barrier heights for a metal on H terminated diamond surfaces compared to clean surfaces. While relatively smaller differences were observed, the Schottky barrier changes were significant for Cu or Ni. Hardly any changes were detected for Zr, and the results for Co fall between the cases of Cu or Ni on the one hand and Zr on the other. Values for the Schottky barrier height of Ti on a H terminated surface were not available. But these values may be expected to be similar to the case of Ti on a clean surface due to the high reactivity of Ti. The overall trend seems to be that Zr and Ti will displace both oxygen and hydrogen, Co will displace hydrogen but not oxygen and both O and H will be present at the interface of Cu and Ni.

The dashed line in Fig. 8 represents the limiting value of the Schottky barrier for which a NEA is expected for metal-diamond interfaces according to Eq. 3. Thus a NEA is expected for data points below this dashed line and a positive electron affinity for those above. As evident from Fig. 8, the experimental results for the electron affinity agree with this model except for Ni. For this case an NEA has been observed for Ni on the clean diamond surface while a positive electron affinity would be expected for the measured Schottky barrier value of 0.5 eV. As discussed above the measured NEA may be indicative of the presence of two configurations

of Ni on the surface with Schottky barrier heights of 0.1 eV and 0.8 eV, respectively. The model would predict that the regions with a Schottky barrier of 0.1 eV would exhibit a NEA while the other regions would exhibit a positive electron affinity.

For Ti on diamond it has been found earlier that the intensity of the metal induced NEA peak in the photoemission spectrum was significantly reduced once the uniform metal film reached several Å in thickness. In particular the intensity was reduced by about 50% for an increase in the thickness of the Ti layer from 2 Å to 3 Å [3]. Only electrons from within a few scattering lengths of the surface will be emitted into vacuum and then be detected. In our study we have measured an emission reduction of ~10% for an increase in the Zr thickness from 2 Å to 3 Å. We have also observed nonuniform metal layers by AFM. This is consistent with a NEA peak still being more pronounced for thicker Zr or Co films than for the case of uniform Ti layers.

It is significant that the Zr or Co on diamond samples that exhibited a NEA retained this characteristic after air exposure. The air stability may be important for the development of cold cathode devices required to be stable in a technical vacuum. It has been reported that Ti as well as titanium oxide on diamond exhibit a NEA [40]. Zr has properties similar to Ti, and this may be indicative that Zr as well as zirconium oxide on diamond could exhibit a NEA. Similar stability to air exposure has been reported previously for Cu on diamond [5]. In this case it may be the reduced reactivity of Cu with O that results in the observation.

The field emission data indicate that depositing Zr or Co on clean, H and O terminated (100) surfaces leads to a lower field emission threshold than the oxygen terminated surfaces. The lowest values reported here were obtained for metal on clean diamond surfaces with 20 V/μm for Zr and 30 V/μm for Co, respectively. The field electron emission process is more complicated than photoemission because the process includes contributions from electron injection at the back interface, conduction through the bulk, and finally emission into vacuum. The last step could be the same for both photo- and field emission. Because of the added complexity, it is often difficult to attribute changes in the effective barrier height to specific differences in the samples. While field emission is often described by the Fowler-Nordheim expression, it should be noted that this expression was derived for emission from metal surfaces, assuming no field inside the bulk of the material. An equation for microscopic dielectric regions has been proposed [41], but this approach would not be a reasonable model for our case with a diamond substrate thickness of 0.25 mm.

The experiments presented here were on similarly prepared natural diamond surfaces with a low surface roughness particularly as compared to diamond films. The roughness of the surfaces before and after metal deposition was comparable and of the order of a few Å. The field enhancement factor, β , may not be expected to be significantly different for the various surfaces considered.

Simultaneous field emission and photoemission measurements from a (111) 1×1:H p-type natural diamond surface were reported by Bandis and Pate [42]. From these experiments it was found that the field emitted electrons originated from the valance band maximum. In contrast the photoemission process involved emission from the conduction band.

For a surface in which the vacuum level aligns in the band gap of the semiconductor (i.e. a NEA), electrons at the conduction band minimum can be freely emitted. In contrast, electrons emitted from the valence band edge would still have to overcome a significant energy barrier even for this NEA surface. Theoretical calculations have indicated that the electron affinity for some H-terminated diamond surfaces can be as low as -3.4 eV [43]. A NEA would then result in a reduced barrier at the surface even for valence band emission. For instance, we have found in this study a reduction of the electron affinity from +1.45 eV for the oxygenated diamond surface to +0.80 eV for Co on oxygen terminated diamond, and a corresponding reduction in the field emission threshold from 79 V/μm to 52 V/μm. An even lower value for the field emission threshold has been found for Co on the clean surface. The smallest value of 20 V/μm for the threshold has been determined for Zr on the clean surface. The NEA should also be the most negative for this case. In these studies, it appears that a decrease in the field emission threshold is correlated with a reduction of the electron affinity. The threshold values for each of the metals studied (Zr, Co, Cu [5]) decrease from oxygen to hydrogen terminated to clean surface. While affects due to the interface and transport through the bulk may be important in some instances, the results presented here suggest that the field emission from p-type diamond is most strongly affected by the surface preparation.

E. Conclusions

In this study, the Zr-diamond and Co-diamond (100), (111) and (110) interfaces were analyzed with UPS and field emission measurements. The metals were deposited on clean diamond surfaces as well as diamond terminated with oxygen or hydrogen. The results examined and correlated the Schottky barrier, the effective electron affinity and the field emission threshold.

The Schottky barrier value was found to depend on surface termination. The results were compared with previous studies on metal diamond interfaces. A general trend was that the barrier was greatest for metals on oxygen terminated surfaces and lowest on the clean surfaces. The Schottky barrier values for metal on H terminated surfaces were similar to or slightly higher than those from the clean surface. The Schottky barrier heights of Zr diamond interfaces were much less dependent on the surface termination before deposition than was the case for Co. We suggest that this is due to the higher reactivity of Zr which will displace either O or H from the interface.

The electron affinity was found to depend on both the metal and diamond surface preparation. NEA characteristics were observed for all metal-diamond interfaces except for Co on oxygen terminated diamond. The NEA was stable following air exposure which may prove to be a technologically relevant aspect. The effective electron affinity for a thin metal layer on the diamond was modeled in terms of two interfaces: the vacuum-metal and the metal-diamond. In this model a lower Schottky barrier height would result in a lower effective electron affinity, and this is consistent with the experimental results.

Metal deposition on the diamond resulted in a decrease in the field emission threshold as compared to the oxygen terminated diamond surface. The results of the field emission threshold and electron affinity showed a similar trend in which the field emission threshold decreased as the electron affinity decreased. The results showed that the emission threshold was dependent on the surface conditions.

F. Acknowledgments

This work has been supported in part by the Office of Naval Research (Contract No. N00014-92-J-1477).

G. References

1. F.J. Himpsel, J.A. Knapp, J.A. van Vechten, D.E. Eastman, Phys. Rev. B 20, 624 (1979).
2. B.B. Pate, Surf. Sci. 165, 83 (1986).
3. J. van der Weide and R.J. Nemanich, J. Vac. Sci. Technol. B 10 (1992) 1940.
4. J. van der Weide and R.J. Nemanich, Phys. Rev. B, 49 (1994) 13629.
5. P.K. Baumann and R.J. Nemanich, Phys. Rev. B, submitted for publication
6. P.K. Baumann and R.J. Nemanich, Appl. Surf. Sci. 104/105 (1996) 267.
7. P.K. Baumann and R.J. Nemanich, in *Diamond for Electronic Applications*, edited by C. Beetz, A. Collins, K. Das, D. Dreifus, T. Humphreys, P. Pehrsson, (Mater. Res. Symp. Soc. Proc. 416 MRS, Pittsburgh, PA 1996), 157 - 162.
8. P.K. Baumann, S.P. Bozeman, B.L. Ward and R.J. Nemanich, in *III-Nitride, SiC and Diamond Materials for Electronic Devices*, edited by D.K. Gaskill, C. Brandt, R.J. Nemanich: Mater. Res. Symp. Soc. Proc. 423, MRS, Pittsburgh, PA, 143 (1996).
9. P.K. Baumann, S.P. Bozeman, B.L. Ward and R.J. Nemanich, "Characterization of Metal - Diamond Interfaces": Proceedings of DIAMOND '96, the 7th European Conf. on Diamond, Diamond-like and Related Materials jointly with ICNDST-5, the 5th International Conf. on the New Diamond Science and Technology, edited by J.C. Angus, P.K. Bachmann, I.M. Buckley-Golder, O. Fukunaga, J.T. Glass, M. Kamo: accepted for publication in J. Diamond Rel. Mat. 6 (1997) 398-402.
10. P.K. Baumann and R.J. Nemanich, "Electron Affinity and Schottky Barrier Height of Metal - Diamond Interfaces": Proceedings of PCSI - 24, the 24th Conf. on Physics and Chemistry of Semiconductor Interfaces: J. Vac. Sci. Tech. B 15(4) (1997) accepted for publication
11. F.J. Himpsel, D.E. Eastman and J.F. van der Veen, J. Vac. Sci. Technol. 17 (1980) 1085.
12. C.A. Mead and T.C. McGill, Phys. Lett. 58A (1976) 149.
13. J.W. Glesener, A.A. Morrish and K.A. Snail, J. Appl. Phys. 70 (1991) 5144.

14. M.W. Geis, D.D. Rathman, D.J. Ehrlich, R.A. Murphy and W.T. Lindley, IEEE Electron Device Lett. **8** (1987) 341.
15. H. Shiomi, H. Nakahata, T. Imai, Y. Nishibayashi and N. Fujimori, Jpn. J. Appl. Phys. **28** (1989) 758.
16. T. Tachibachi, B.E. Williams and J.T. Glass, Phys. Rev. B **45** (1992) 11975.
17. M.C. Hicks, C.R. Wronski, S.A. Grot, G.S. Gildenblat, A.R. Badzian, T. Badzian and R. Messier, J. Appl. Phys. **65** (1989) 2139.
18. S.A. Grot, S. Lee, G.S. Gildenblat, C.W. Hatfield, C.R. Wronski, A.R. Badzian, T. Badzian and R. Messier, J. Mater. Res. **5** (1990) 2497.
19. M. Marchywka, P.E. Pehrsson, S.C. Binari and D. Moses, J. Electrochem. Soc., **140**, No. 2 (1993) L19.
20. P.K. Baumann, T.P. Humphreys and R.J. Nemanich, in *Diamond, SiC and Nitride Wide Band gap Semiconductors*, edited by C.H. Carter, G. Gildenblat, S. Nakamura, R.J. Nemanich, (Mater. Res. Soc. Proc. **339**, Pittsburgh, PA, 1994) 69-74.
21. T.P. Schneider, J. Cho, Y.L. Chen, D.H. Mahler and R.J. Nemanich, in *Surface Chemical Cleaning and Passivation for Semiconductor Processing*, edited by G.S. Higashi, E.A. Irene, T. Ohmi (Mater. Res. Soc. Proc. **315**, Pittsburgh, PA, 1993) pp.197-209.
22. M.H. Hecht, J. Vac. Sci. Technol. B **8**, 1018 (1990).
23. C. Bandis, B.B. Pate, Surf. Sci. Lett. **345**, L23 - L 27 (1996).
24. J. van der Weide and R.J. Nemanich, Appl. Phys. Lett. **62** (1993) 1878.
25. J. van der Weide, Z. Zhang, P.K. Baumann, M.G. Wensell, J. Bernholc and R.J. Nemanich, Phys. Rev. B **50** (1994) 5803.
26. P.K. Baumann and R.J. Nemanich, Proc. of the 5th European Conference on Diamond, Diamond-like and Related Materials, edited by P.K. Baumann, I.M. Buckley-Golder, J.T. Glass, M. Kamo: J. Diamond Rel. Mat., **4** (1995) 802.
27. P.K. Baumann, R.J. Nemanich, J. Appl. Phys., submitted for publication
28. W. Zhu, G.P. Kockanski, S. Jin and L. Siebels, J. of Appl. Phys. **78** (1995) 2707.
29. S.P. Bozeman, P.K. Baumann, B.L. Ward, M.J. Powers, J.J. Cuomo, R.J. Nemanich and D.L. Dreifus, Proc. of the 6th European Conference on Diamond, Diamond-like and Related Materials, edited by P.K. Baumann, I.M. Buckley-Golder, J.T. Glass, M. Kamo: J. Diamond Rel. Mat. **5**, (1996) 802.
30. P.K. Baumann, S.P. Bozeman, B.L. Ward and R.J. Nemanich, in *III-Nitride, SiC and Diamond Materials for Electronic Devices*, edited by D.K. Gaskill, C. Brandt, R.J. Nemanich: (Mater. Res. Symp. Soc. Proc. **423**, MRS, Pittsburgh, PA 1996) 143.
31. R. Gomer, *Field Emission and Field Ionization*, Cambridge, MA, (1961).
32. E.H. Rhoderick and R.H. Williams, *Metal-Semiconductor Contacts* Clarendon, Oxford, (1988).
33. C. Weiser, Surf. Sci. **20** (1970) 143.
34. S.C. Erwin and W.E. Pickett, Surf. Coat. Technol. **47** (1991) 487.
35. S.C. Erwin and W.E. Pickett, Solid State Commun. **81** (1992) 891.
36. W.E. Pickett and S.C. Erwin, Phys. Rev. B **41** (1990) 9756.
37. W.E. Pickett and S.C. Erwin, Superlatt. Microstruct. **7** (1990) 335.
38. W.E. Pickett, M.R. Pederson and S.C. Erwin, Mater. Sci. Eng. B **14** (1992) 87.
39. W.R.L. Lambrecht, Physica B **185** (1993) 512.
40. C. Bandis, D. Haggerty and B.B. Pate, in *Diamond, SiC and Nitride Wide Band Gap Semiconductors*, edited by C.H. Carter, G. Gildenblat, S. Nakamura, R.J. Nemanich, (Mater. Res. Soc. Proc. **339**, Pittsburgh, PA, 1994) 75.
41. R.V. Latham, Vacuum **32** (3) (1982) 137.
42. C. Bandis, B.B. Pate, Appl. Phys. Lett. **69** (1996) 366.
43. Z. Zhang, M. Wensell and J. Bernholc, Phys. Rev. B **51** (1995) 5291.

V. Electrical Characterization of Metal/AlN/6H-SiC(0001) Heterostructures

M.O. Aboelfotoh, R.S. Kern*, and R.F. Davis

*Department of Materials Science and Engineering, North Carolina State University
Raleigh, North Carolina 27695-7907*

*Present address: Hewlett Packard Corporation, Optoelectronics Division, San Jose, CA 95131

Abstract – Metal/AlN/n-type 6H-SiC (0001) (MIS) heterostructures have been prepared by epitaxially growing wurtzite AlN layers on both vicinal and on-axis 6H-SiC (0001) substrates using gas-source molecular beam epitaxy. The capacitance-voltage characteristics obtained for these MIS heterostructures are found to depend strongly on temperature in the range from 200 to 573 K, and to exhibit hysteresis effects consistent with the presence of slow interface traps. The amount of hysteresis is found to increase with decreasing temperature. This can be explained in terms of the shift of the Fermi level closer to the semiconductor conduction band with decreasing temperature, causing the emission rate of the trapped charge to be less dependent on temperature. Cross-sectional high-resolution transmission electron microscopy results show that the interface formed on the vicinal 6H-SiC (0001) substrate contains a higher density of defects than that on the on-axis substrate. However, these two interfaces are found to have a similar density of trapped negative charge of $3 \times 10^{11} \text{ cm}^{-2}$ at room temperature, which decreases with increasing temperature. These results indicate that the interface between AlN and Si-terminated 6H-SiC (0001) is of a high quality suitable for device application.

I. Introduction

Recently, there has been increasing interest in the electrical properties of silicon carbide (SiC) metal-oxide-semiconductor (MOS) structures because of their applications in high-power and high-temperature devices[1]. The fabrication of these structures is made possible, in part, by the fact that SiC is unusual among wide band gap semiconductors in that it can be thermally oxidized to form silicon oxide (SiO_2) layers with relatively low oxide charge and interface state densities[2]. However, several authors[3]-[5] have reported electrical instabilities in the SiO_2/SiC system. Furthermore, the transconductances of SiC MOS field-effect transistors (MOSFETs) are presently limited by the carrier surface mobility which is degraded by surface roughness and charged interface states[1]. The problems associated with thermally grown oxides, however, may be alleviated by the use of deposited dielectrics[6]. Because of its wide band gap (6.2 eV at 300 K) and low dielectric constant ($\epsilon_0 = 8.5$)[7], aluminum nitride (AlN) represents an attractive alternative to oxides as a dielectric for SiC-based devices. In addition, AlN normally forms in the hexagonal wurtzite structure and is rather closely lattice-matched to SiC allowing the growth of high-quality epitaxial layers[8].

It has been theoretically shown that for the nonpolar (110) interface between cubic AlN and cubic SiC, the energetically favorable bonding configuration is Si-N and Al-C which corresponds to cation-anion bonding across the interface[9]. It has also been shown that for this bonding configuration, no interface localized states occur in the main band gap, and that dangling

bonds existing at the SiC (110) surface are almost completely healed at the interface[9]. On the other hand, for nonisovalent systems such as AlN/SiC, abrupt polar interfaces would be characterized by the occurrence of either oversaturated or undersaturated bonds. It is well known[10] from semiconductor interface studies of similar nonisovalent systems (e.g., Ge/GaAs), that this situation would place the system in an unstable state. This has led to the suggestion that atomic intermixing occurs at the interface in such a way as to compensate III-IV and IV-V bonds, thereby avoiding the occurrence of strong electric fields in the system[11]. In fact, Ourmazd et al.[12] showed that atomic intermixing even exists for isovalent systems such as $\text{Al}_x\text{Ga}_{1-x}\text{As}/\text{GaAs}$ and depends strongly on the growth temperature. From results of high-resolution transmission electron microscopy (HRTEM) studies, Ponce et al.[13] concluded that the most favorable atomic arrangements at the abrupt polar interface between AlN and (0001) Si-terminated 6H-SiC are the intermixed configurations of Si-N and Al-C bonds, which produce no significant changes in the Si-C or Al-N back-bond lengths. Recently, we have shown[14] that the interface formed on n-type 6H-SiC (0001) has a density of trapped negative charge of $1 \times 10^{11} \text{ cm}^{-2}$ at room temperature. In this paper, we show that the capacitance-voltage (C-V) characteristics of metal/AlN/n-type 6H-SiC (0001) (MIS) heterostructures depend strongly on temperature and exhibit hysteresis effects consistent with the presence of slow interface traps. We also show that the amount of hysteresis is dependent upon temperature. It has been shown[15] that the presence of particular Si-terminated steps on the vicinal 6H-SiC (0001) surface causes the introduction of defects in the AlN layer that originate at the interface. However, we find that the interfaces formed on both vicinal and on-axis 6H-SiC (0001) substrates have a similar density of trapped negative charge at room temperature, which decreases with increasing temperature.

II. Experimental Procedure

The AlN layers (100 nm thick) were grown on (0001) Si-terminated 6H-SiC substrates at 1373 K using gas-source molecular beam epitaxy (GSMBE)[16]. Sources were Al (99.999 % pure), evaporated from standard effusion cell, and 3.0 sccm ammonia (99.999 % pure). Nitrogen-doped ($2 \times 10^{18} \text{ cm}^{-3}$) 6H-SiC wafers containing 0.8- μm -thick epitaxial layers [N-doped to $(2-4) \times 10^{16} \text{ cm}^{-3}$] deposited via chemical vapor deposition and thermally oxidized to a depth of 75 nm were used as substrates in this work. The substrates were chemically cleaned in a 10% hydrofluoric acid solution to remove the oxide immediately before they were inserted into the growth chamber. To remove any residual hydrocarbons and oxide prior to deposition, the substrates were further cleaned using a 1-min silane exposure at 1273 K followed by a 10-min anneal at 1523 K in ultrahigh vacuum (1×10^{-9} Torr) until a 1×1 reconstruction pattern became visible in the reflection high-energy electron diffraction (RHEED) pattern of the 6H-SiC (0001) surface[17]. In order to investigate the effect of the interfacial defect structure on the C-V characteristics, the AlN layers were grown simultaneously on vicinal ($3-4^\circ$ off (0001) toward $[11\bar{2}0]$) and on-axis substrates at a rate of 100 nm/h. The AlN/SiC interface was examined by cross-sectional HRTEM using 200 KV Topcon 002 B electron microscope. Depth profiles of impurities in the AlN layers were determined by secondary ion mass spectrometry, with a C_s^+ primary ion beam.

The doping profile of uncompensated donors in the epitaxial layers was uniform and their concentration was $2 \times 10^{16} \text{ cm}^{-3}$, as determined from the C-V measurements reported below. The MIS heterostructures were prepared by deposition of circular Al contacts with an area of $5.4 \times 10^{-3} \text{ cm}^2$ on the AlN through a metal mask. Blanket deposition of Al was made on the backside of the wafers to form a large area ohmic contact. The C-V measurements were performed at frequencies between 1 kHz and 1 MHz and at temperatures ranging from 200 to 573 K. The measurements were carried out in the dark with a voltage sweep rate of 100 mV/s. Measurements were also performed as follows: the device was illuminated with light from a halogen lamp while biased in deep depletion, making possible the modulation of the interface trap population. When a stable capacitance value was reached, the bias voltage was swept in the dark into accumulation and back to deep depletion at a sweep rate of 100 mV/s.

III. Results and Discussion

Figure 1 shows cross-sectional HRTEM images of the AlN layer on the on-axis and vicinal 6H-SiC (0001) substrates. The AlN layer grows in a two-dimensional growth mode with a hexagonal wurtzite structure and has an abrupt interface with the 6H-SiC (0001) substrate [Fig. 1 (a)].

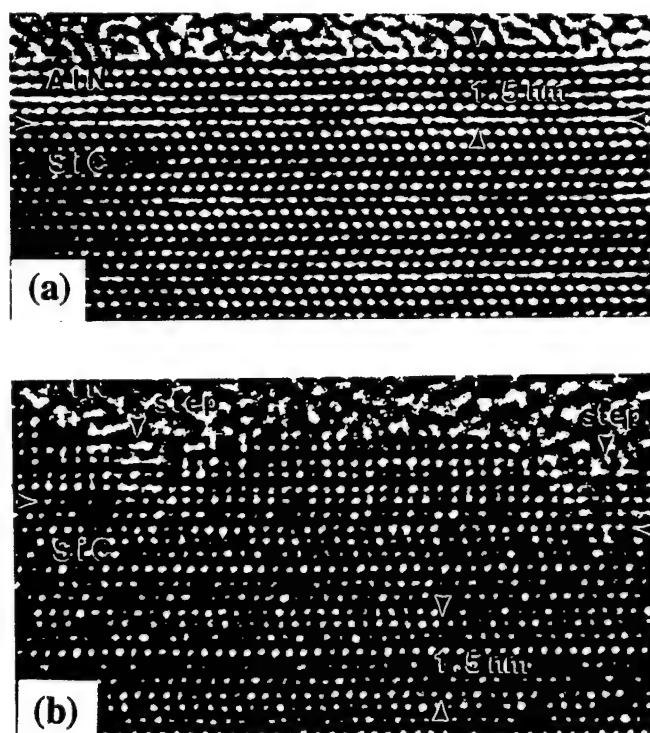


Fig. 1 High-resolution TEM images of the AlN/6H-SiC (0001) interface formed on (a) an on-axis substrate and (b) a vicinal substrate. The arrows shown in (b) indicate the step positions.

However, the misalignment of coalescing AlN island-like areas at steps on the vicinal 6H-SiC surface due to the difference in stacking sequences of the AlN and the SiC results in the introduction of inversion domain boundaries (IDBs) in the AlN layer[15]. The presence of IDBs and the abrupt nature of the interface are revealed in Fig. 1 (b). For the layers used here with a thickness exceeding the equilibrium critical thickness for hexagonal AlN (~ 4.6 nm), threading dislocations that arise from the strain associated with these planar defects and with lattice mismatch are also observed[17].

A typical high-frequency (1 MHz) C-V curve obtained at room temperature for MIS heterostructures formed on a vicinal, n-type 6H-SiC (0001) substrate is shown in Fig. 2. Also shown in Fig. 2 is a theoretical curve calculated[18] for a 100 nm AlN layer on an n-type ($2 \times 10^{16} \text{ cm}^{-3}$) 6H-SiC (0001) substrate. No frequency dispersion of the capacitance is observed in the frequency range studied here. The C-V curve exhibits no appreciable hysteresis and shows deep depletion for negative gate voltages with no inversion capacitance characteristics observed due to the extremely low minority-carrier generation rate[19]. Figure 3 shows the behavior of the C-V curve when the device is illuminated with light from a halogen lamp while biased in deep depletion. It can be seen that hysteresis now appears in the deep-depletion portion of the curve consistent with the presence of slow interface traps that are not in equilibrium with the Fermi level in our experiment. Illumination results in a reduction of the charge occupancy of these interface traps and as a consequence, for a given bias voltage there is less negative charge in the interface traps on the positively going than on the negatively going voltage sweep. This results in the device capacitance being smaller on the negatively going than on the positively going voltage sweep.

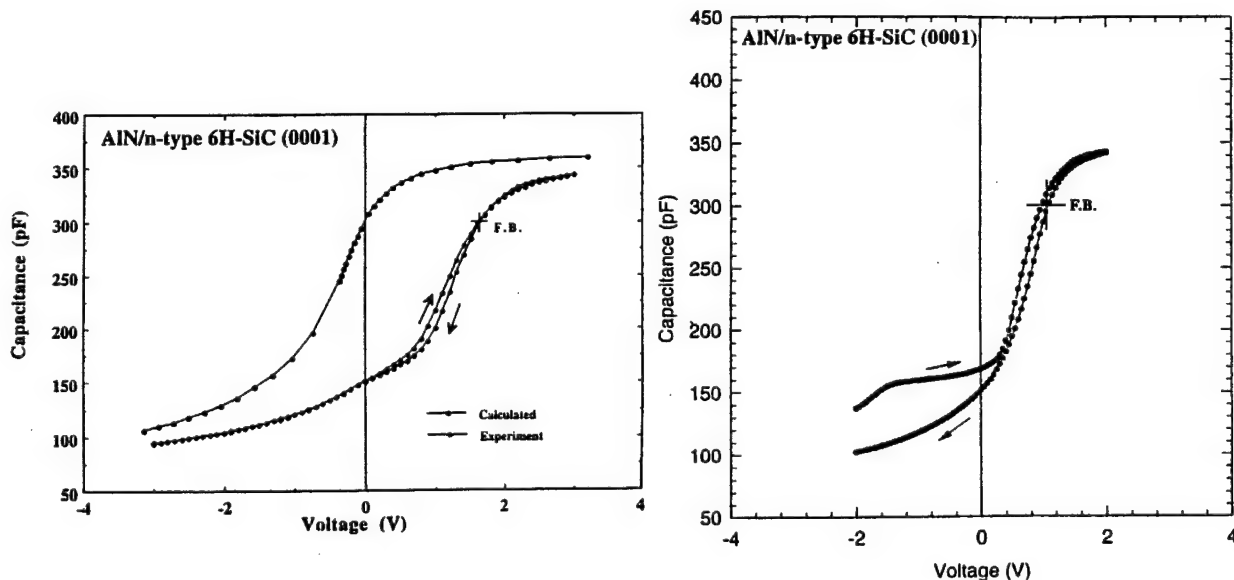


Fig. 2 High-frequency (1 MHz) C-V curve measured at room temperature in the dark with a voltage sweep rate of 100 mV/s and a theoretical curve calculated for a 100 nm AlN layer on an n-type ($2 \times 10^{16} \text{ cm}^{-3}$) 6H-SiC (0001) substrate.

Fig. 3 Effect of illuminating the MIS device with light from a halogen lamp while biased in deep depletion on the C-V behavior.

Similar hysteresis effects were also observed in silicon MIS structures at low temperatures (≤ 160 K), where the generation of minority carriers is very small and the time constant for the charge emission from interface traps is very long[20].

From Fig. 2, using 4.2 eV for the work function of Al and 3.7 eV for the electron affinity of 6H-SiC (0001)[21], the flatband voltage, V_{FB} , of +1.2 V (determined from the sweep from accumulation to deep depletion) represents a shift of +0.85 V from ideal, for a negative interface charge density of $3 \times 10^{11} \text{ cm}^{-2}$ at room temperature. Note that interface trap stretchout is not observed in the experimental C-V curve when compared to the ideal curve in Fig. 2. This charge must then reside largely in such slow interface traps.

Figure 4 illustrates the effect of temperature on the C-V characteristics. It can be seen that increasing the temperature has the effect of shifting the curves to less positive gate voltages (or the capacitance to higher values). This shift indicates that less negative charge is trapped at the interface for a given bias voltage as a consequence of the movement of the Fermi level to lower energies with increasing temperature[22]. This behavior is consistent with the presence of acceptor-type traps. At 473 K V_{FB} is almost dominated by the work function difference between Al and 6H-SiC (0001). Note also that as the temperature is lowered below 300 K, the portions of the curves that correspond to depletion exhibit a pronounced hysteresis. It is observed that the amount of hysteresis increases with decreasing temperature, yet one would have thought that the emission rate of the trapped charge would decrease drastically with decreasing temperature and hence, that no substantial hysteresis effects would be manifested in the C-V characteristics. The movement of the Fermi level closer to the bottom of the semiconductor conduction band (note that the interface traps are now filled to a higher level) must then have the effect of causing the emission rate to be less dependent on temperature[22]. The emission rate must also be less than the rate of change of the gate charge in our experiment as evidenced by the hysteresis effects.

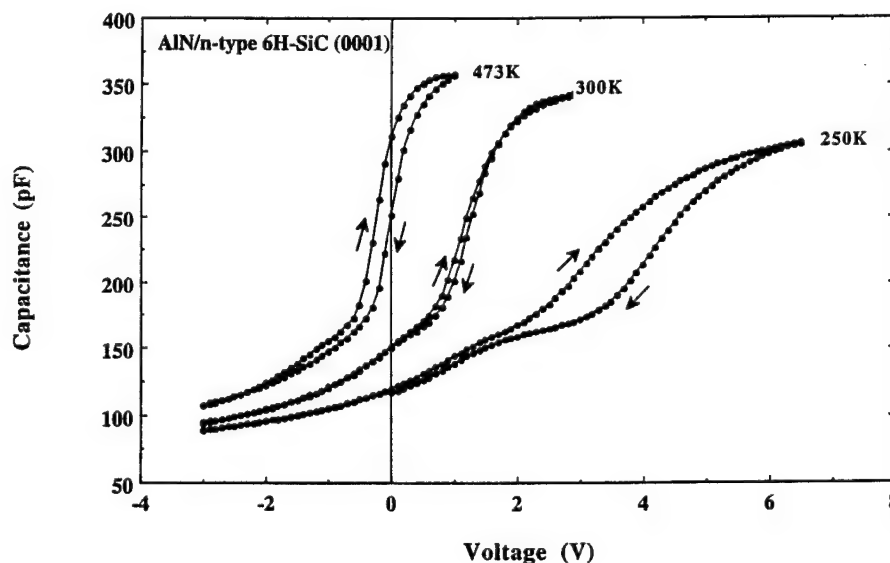


Fig. 4 A set of C-V curves measured at different temperatures in the dark with a voltage sweep rate of 100 mV/s.

Furthermore, the reduction of the slopes in the C-V characteristics from the ideal ones with decreasing temperature suggests that charge emission takes place from a continuum of interface traps[22].

It should be emphasized here that regardless of whether the MIS heterostructures are formed on vicinal or on-axis 6H-SiC (0001) substrates, almost identical C-V characteristics are obtained (Figs. 2 and 4). These results are in marked contrast to those reported for thermally grown and deposited oxides on n-type 6H-SiC (0001)[6], [19], which show increased hysteresis, and a shift in the C-V curves to more positive gate voltages as the temperature is increased from 300 to 573 K. This shift indicates that in this case, more negative charge is trapped at the interface due presumably to a larger number of slow interface traps being thermally excited[19].

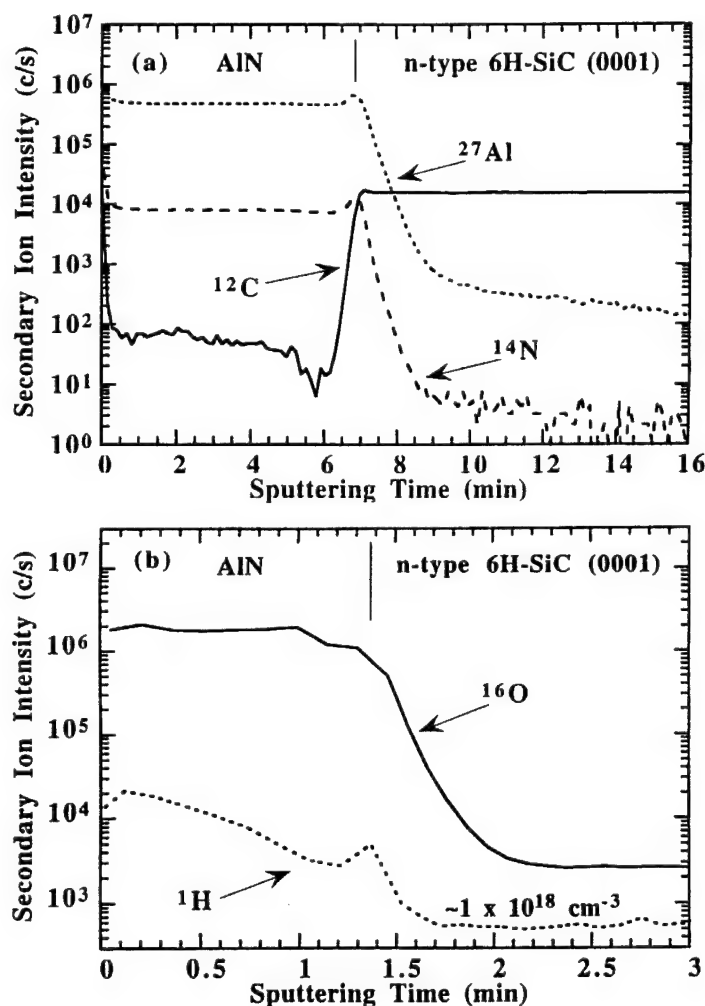


Fig. 5 SIMS depth profiles of (a) carbon, (b) oxygen and hydrogen in an AlN/6H-SiC (0001) heterostructure. The carbon concentration in the AlN layer is estimated to be about $10^{16} \text{ atoms/cm}^3$. The oxygen and the hydrogen concentration is estimated to be about $10^{19} \text{ atoms/cm}^3$ using the background signals in the 6H-SiC substrate. The apparent Al signal in the substrate is due to the interference of the NC signal and does not indicate the diffusion of Al into the 6H-SiC substrate.

Although high-resolution TEM images show that the interface formed on the vicinal 6H-SiC (0001) substrate contains a higher density of defects than that on the on-axis substrate (Fig. 1), both interfaces are found to have a similar density of trapped negative charge.

The SIMS depth profiles shown in Fig. 5, however, reveal that oxygen, hydrogen and carbon atoms are incorporated into the AlN and at the interface during growth. The drift of such impurity ions under the applied electric fields and at the low temperatures used here is not expected, but their presence at the interface can alter the nature of the local chemical bonds which can be at the origin of the interface traps[9]. However, more studies are currently underway to further clarify their role in determining the electrical characteristics of the interface.

IV. Summary

Metal/AlN/n-type 6H-SiC (0001) (MIS) heterostructures have been prepared by epitaxially growing wurtzite AlN layers on both vicinal and on-axis 6H-SiC (0001) substrates using GSMBE. The C-V characteristics obtained for these MIS heterostructures depend strongly on temperature in the range from 200 to 573 K, and exhibit hysteresis effects consistent with the presence of slow interface traps. The amount of hysteresis increases with decreasing temperature as a consequence of the shift of the Fermi level closer to the semiconductor conduction band, causing the emission rate to be less dependent on temperature. Despite the higher density of defects at the interface formed on the vicinal 6H-SiC (0001) substrate, both the interfaces on the vicinal and on-axis substrates are found to have a similar density of trapped negative charge of $3 \times 10^{11} \text{ cm}^{-2}$ at 300 K, which decreases with increasing temperature. These results indicate that the interface is of a high quality suitable for device application.

Acknowledgments

The authors express their appreciation to the Office of Naval Research for support of this research under Grant Nos. N00014-92-J-1477 and N00014-95-J-1080 and to Cree Research, Inc., for the 6H-SiC wafers. Appreciation is also expressed to Dr. B.G. Svensson for the SIMS analysis.

References

- [1] H. Morkoc, S. Strite, G.B. Gao, M.E. Lin, B. Sverdlov, and M. Burns, *J. Appl. Phys.* 76, 1363 (1994).
- [2] J.N. Shenoy, G.L. Chindalore, M.R. Melloch, J.A. Cooper, Jr., J.W. Palmour, and K.G. Irvine, *J. Electron. Mater.* 24, 303 (1995).
- [3] C. Raynaud, J.-L. Autran, B. Balland, G. Guillot, C. Jaussaud, and T. Billon, *J. Appl. Phys.* 76, 993 (1994).
- [4] E. Bano, T. Quisse, L. DiCioccio, and S. Karmann, *Appl. Phys. Lett.* 65, 2723 (1994).
- [5] C. Raynaud, J.-L. Autran, J.B. Briot, B. Balland, N. Becourt, T. Billon, and C. Jaussaud, *Appl. Phys. Lett.* 66, 2340 (1995).

- [6] S. Sridevan, V. Misra, P.K. McLarty, B.J. Baliga, and J.J. Wortman, in Technical Digest of the International Conference on Silicon Carbide and Related Materials, 1995, p. 213; IEEE Electron Dev. Lett. 16, 524 (1995).
- [7] S. Strite and H. Morkoc, J. Vac. Sci. Technol. B10, 1237 (1992).
- [8] L.B. Rowland, R.S. Kern, S. Tanaka, and R.F. Davis, Appl. Phys. Lett. 62, 3333 (1993).
- [9] W.R.L. Lambrecht and B. Segall, Phys. Rev. B43, 7070 (1991).
- [10] G.A. Braraff, J.A. Appelbaum, and D.R. Hamann, Phys. Rev. Lett. 38, 237 (1977).
- [11] W.A. Harrison, E.A. Kraut, J.R. Waldrop, and R.W. Grant, Phys. Rev. B18, 4402 (1978).
- [12] A. Ourmazd, D.W. Taylor, J. Cunningham, and C.W. Tu, Phys. Rev. Lett. 62, 933 (1989).
- [13] F.A. Ponce, C.G. Van de Walle, and J.E. Northrup, Phys. Rev. B53, 7473 (1996).
- [14] M.O. Aboelfotoh, R.S. Kern, S. Tanaka, R.F. Davis, and C.I. Harris, Appl. Phys. Lett. 69, 2873 (1996).
- [15] R.F. Davis, S. Tanaka, L.B. Rowland, R.S. Kern, Z. Sitar, S.K. Ailey, and C. Wang, J. Crystal Growth 164, 132 (1996).
- [16] L.B. Rowland, S. Tanaka, R.S. Kern, and R.F. Davis, in Amorphous and Crystalline Silicon Carbide IV, edited by C.Y. Yang, M.M. Rahman, and G.L. Harris (Springer, Berlin, 1992), p. 84.
- [17] R.S. Kern, Ph.D. thesis, North Carolina State University, Raleigh, NC, 1996.
- [18] E.H. Nicollian and J.R. Brews, MOS (Metal Oxide Semiconductor) Physics and Technology (Wiley, New York, 1982), p. 96.
- [19] P. Neudeck, S. Kang, J. Petit, and M. Tabib-Azar, J. Appl. Phys. 75, 7949 (1994).
- [20] L.S. Wei and J.G. Simmons, Solid-State Electron. 17, 1021 (1974).
- [21] D. Alok, P.K. McLarty, and J. Baliga, Appl. Phys. Lett. 64, 2845 (1994).
- [22] J.G. Simmons and L.S. Wei, Solid-State Electron. 16, 53 (1973).

Nitrogen-based Materials

VI. Analysis of Reactor Geometry and Diluent Gas Flow Effects on the Metalorganic Vapor Phase Epitaxy of AlN and GaN Thin Films on α (6H)-SiC Substrates

A. Introduction

Over the last few years extensive world-wide research has resulted in significant advances in the quality of the III-V nitride materials: AlN, GaN, InN, and their alloys. As a result of these advances, short-wavelength optoelectronic devices such as blue and green light emitting diodes (LEDs) are now commercially available [1]. In addition, the fabrication and room temperature continuous wave (CW) operation of the first nitride-based short wavelength injection laser diodes have recently been reported [2]. Also, microelectronic devices for high-temperature, high-frequency, and high-power applications are being actively pursued [3]. These and other applications for the III-V nitride materials represent large potential markets which provide the driving force for the research of these materials.

Many growth processes have been developed for depositing thin nitride films, including molecular beam epitaxy (MBE), hydride vapor phase epitaxy (HVPE), reactive magnetron sputtering, and metalorganic vapor phase epitaxy (MOVPE) (also known as organometallic chemical vapor deposition), among others. Metalorganic vapor phase epitaxy has become the main technique for growing high-quality epitaxial films and heterostructures. It is a growth method which provides high purity sources, a high degree of compositional control and areal uniformity, high growth rates, and the ability to grow abrupt junctions. It is a complicated process, requiring an understanding of fluid flow, gas phase and surface reactions, and transport processes.

Successful MOVPE reactor design involves a detailed analysis of the coupled transport phenomena that affects the film deposition process. The reactor geometry and operating conditions determine the fluid flow structure which, in turn, determines the heat and mass transfer characteristics in the deposition chamber. Complex flow structures can develop in vertical MOVPE reactors due to large thermal gradients between the heated substrate and the cold walls. This leads to buoyancy-driven recirculation flows that can greatly influence the thickness uniformity of deposited films. Inverting the reactor (bottom-up flow) so the buoyancy and inlet flow directions are aligned greatly reduces the major cause of thermal convection. However, proper design and operation are necessary to achieve stagnation point flow which enables the growth of uniform films. In this work, presented are results of applying a computational fluid dynamic model to the gas inlet and inverted MOVPE reactor. The results of the computer model which predict the heat and mass transfer gradients present in the reactor are analyzed. These results were applied to the deposition of high-quality AlN and GaN thin films on SiC substrates.

In addition to examining the MOVPE reactor design and flow structure, the influence of the diluent gas on the deposition process was investigated. The diluent gas plays an important role in the MOVPE process, as it can constitute over 50% of the gas phase in the reactor. In addition to determining the flow structure in the reactor, it can affect the decomposition of the source species. The thermal conductivity and viscosity of the gas phase, and molecular diffusivity of species through the gas are also important parts of the MOVPE process. Hydrogen is the typical diluent gas used in MOVPE deposition of AlN, GaN, and AlGaIn compounds. Hydrogen, however, has been shown to have deleterious effects on the growth of indium-containing nitride thin films [4,5]. This necessitates the use of nitrogen as the diluent gas for these compounds, and requires stopping the growth process to switch diluent gas sources when hydrogen is used otherwise. The use of nitrogen as the diluent gas for the growth of all nitride thin films would simplify the growth process. This work presents a comparison of AlN and GaN thin films grown using hydrogen and nitrogen as the diluent gas. The electrical, optical, and microstructural properties of the thin films are presented.

B. Reactor Model and Design

Model Description. The production of advanced semiconductor device structures such as quantum wells and superlattices requires control at the atomic level. Researchers have recognized the potential of the stagnation point flow reactor geometry to produce large area films that are uniform in both thickness and composition [6,7]. Under ideal conditions a flow field is obtained that results in uniform heat and mass transfer gradients across the deposition radius. However, the effects of buoyancy and finite geometries lead to the development of thermal recirculation flows that disrupt the ideal transport conditions. These effects were observed in preliminary GaN deposition experiments in the MOVPE system when the source gases entered the bottom of the reactor under consideration here through a straight 0.635 cm (1/4") tube. The resulting films were not homogenous.

To alleviate these problems, a computational fluid dynamic model was developed to redesign the inlet and determine the optimum operating conditions. The model was developed using FIDAP, a commercial package that employs the finite element method. The velocity and temperature fields were calculated by solving the following coupled conservation equations in cylindrical coordinates:

$$\nabla(\rho v) = 0 \quad \text{Continuity Equation} \quad (1)$$

$$\rho(v \cdot \nabla v) = -\nabla P + \mu \nabla^2 v + \rho g \quad \text{Conservation of Momentum} \quad (2)$$

$$\rho C_p (v \cdot \nabla T) = \nabla \cdot (k \nabla T) \quad \text{Conservation of Energy} \quad (3)$$

The simplified energy balance neglects contributions from Dufour effects, viscous dissipation, radiation, and heat generated by reactions. Previous work [6,8] has shown that it

is safe to ignore these effects at low pressure MOVPE conditions. The temperature-dependence of the physical properties were abstracted from the Sandia database [9,10] and included in the simulations. The calculations were performed for a binary mixture of ammonia and the diluent gas (hydrogen or nitrogen). The viscosity and thermal conductivity of the mixture were determined using the semiempirical formula developed by Wilke [11]. It is appropriate to neglect contributions of the metalorganic precursors they constitute less than 0.01% of the mixture. Buoyancy effects were included in the momentum balance.

The reactor geometry shown in Fig. 1 was simulated (excepting the exclusion of two viewports to make the system perfectly axisymmetric) in the computer model. The velocity boundary conditions include a zero velocity condition at all surfaces, no radial gradient at the centerline, and no axial gradient at the outlet. Two inlet velocity conditions were examined: (i) a parabolic profile that corresponds to fully developed flow in a pipe, and (ii) a uniform axial velocity across the inlet. Analogous temperature boundary condition included were fixed temperatures at the inlet, reactor walls and susceptor, no radial gradient at the centerline, and no axial gradient at the outlet. A nonuniform mesh employing nine-node biquadratic elements was used to discretize the reactor geometry. A typical mesh included xx elements which produced yy equations and unknowns that were solved using a combination of successive substitution and Newton Raphson techniques. All calculations were performed at the North Carolina Supercomputing Center.

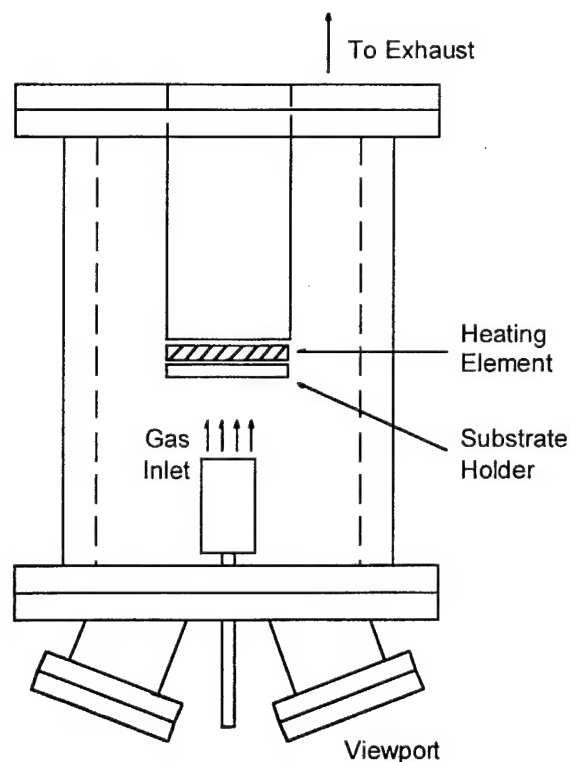


Figure 1. Schematic of deposition chamber for flow dynamics model.

Model Results. Figure 2 shows the velocity field and the associated temperature gradients for the original reactor configuration using the 0.635 cm inlet. Strong recirculation cells were predicted, resulting in nonuniform temperature gradients above the substrate. Using the classical analogy between heat and mass transfer [12] the general conclusions can be extended from heat to mass transfer, especially when deposition is limited by mass-transfer. Houtman and coworkers [6] have been shown that the inlet dimension, and also its relation to the substrate radius and separation, are critical to the achievement of uniformity. The insights of their study were used as guidelines in the redesign of our particular reactor. The results are shown in Fig. 3. The major changes were an increase in the inlet diameter from 0.635 to 2.54 cm, and a reduction of the nozzle to substrate distance from ~8 cm to ~4 cm. Simulations showed that much better uniformity was achieved using a flat velocity profile than with a parabolic profile. Experimentally a flat velocity profile was achieved following the approach used to generate flat flames for combustion studies [13]. After passing the reactants through a packed bed to ensure good mixing, the uniform velocity profile was created by flowing the reactants through a 1 inch long honeycomb structure created by a packed array of thin wall, 1 mm diameter silica tubes. The structure shown in Fig. 1 produced uniform temperature contours for total gas flows between 3 and 6 slm. The profiles were similar for both nitrogen and hydrogen diluent gases.

C. Experimental Procedure

The AlN and GaN thin films presented in this work were grown on SiC substrates (Cree Research, Inc.) in an inverted flow, vertical cold wall MOVPE reactor. The as-received on-axis, Si-Face $\alpha(6H)$ -SiC(0001) wafers were cleaved into the desired size and degreased in sequential ultrasonic baths of trichloroethylene, acetone, and methanol, followed by a deionized water rinse. The substrate was then dipped in a 10% HF solution to remove the thermally grown protective oxide and blown dry with nitrogen before mounting on a molybdenum substrate carrier. The carrier was mounted in the deposition system and the deposition chamber was evacuated to less than 5.0×10^{-6} Torr before beginning the deposition process. The system was operated under computer control using a LabVIEW (National Instruments) control program developed in-house. The substrate was heated to the deposition temperature under a diluent flow of either hydrogen or nitrogen. A flow of 2.2 slm was used for the nitrogen diluent, while a flow of 2.5 slm was used for the hydrogen diluent. The deposition pressure was 45 Torr. The substrate was rotated continuously at approximately 30 RPM during deposition. The substrate heater temperature was monitored by the computer using a thermocouple and calibrated with the temperature of the substrate using an Iacon Ultimax Infrared Thermometer. While the growth temperature was being obtained, the flow of

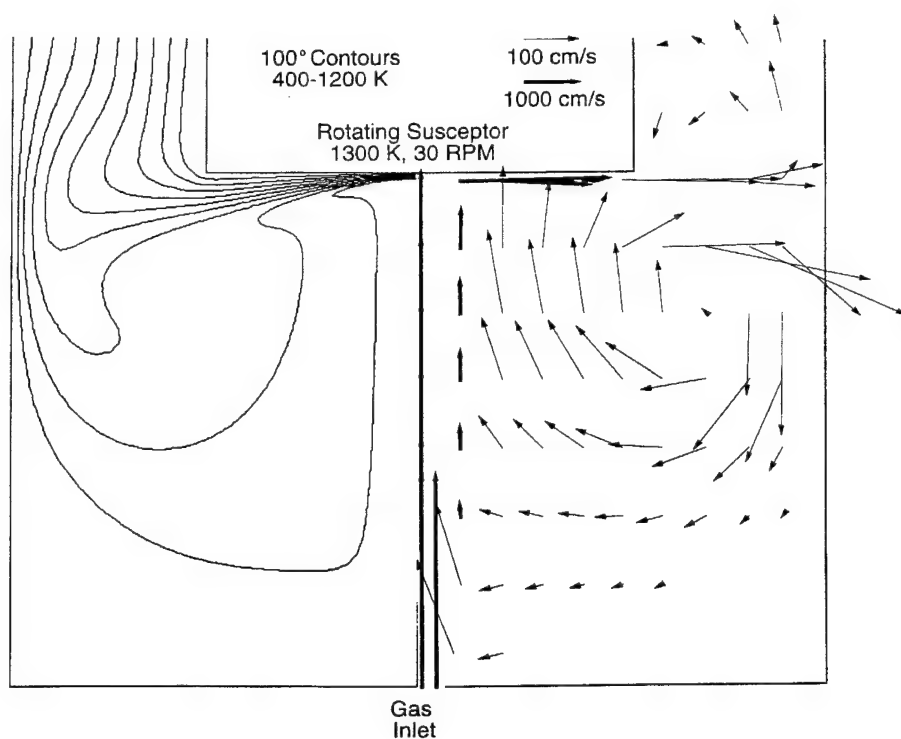


Figure 2. Temperature gradients and gas velocity vector field for reactor configuration with 0.635 gas inlet.

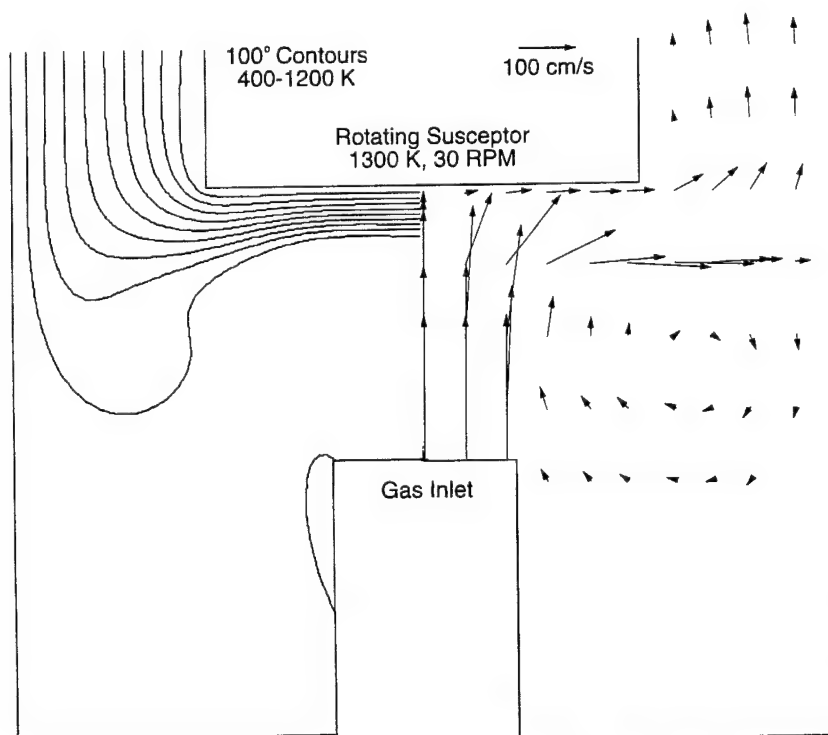


Figure 3. Temperature gradients and gas velocity vector field for reactor configuration with 2.54 gas inlet.

the carrier gas through the metalorganic bubblers was established using a run/vent configuration. The temperature and pressure of each metalorganic bubbler were independently controlled. Nitrogen only was used as the carrier gas for the metalorganic precursors. Trimethylaluminum (TMA) and triethylgallium (TEG) were the group III sources, and ammonia (NH_3) was the nitrogen source. Silane (SiH_4) diluted in hydrogen was the silicon source for the n-type dopant, and bis-(cyclopentadienyl) magnesium (Cp_2Mg) was the magnesium source for the p-type dopant.

All GaN films were grown on a high temperature AlN buffer layer that was approximately 1000 Å thick. The growth temperature for the AlN buffer layer was 1110°C. When the AlN deposition temperature was reached, TMA was introduced into the system at a rate of 4.0 $\mu\text{mol/min}$ with an NH_3 flow of 1.8 slm for 20 minutes. After the growth of the buffer layer the substrate was cooled to approximately 1025°C to deposit the GaN film. The GaN deposition conditions were optimized for each diluent. In both diluent gases the flow rate of TEG was 20.0 $\mu\text{mol/min}$ and the flow rate of NH_3 was 1.8 slm. For Si doping, SiH_4 was introduced into the reactor at flow rates varying between 0.15 and 3.75 nmol/min. For Mg doping, Cp_2Mg was introduced into the reactor at a flow rate of 0.13 $\mu\text{mol/min}$. After terminating the GaN growth the substrate was cooled to room temperature under flowing diluent and NH_3 at a controlled rate.

The photoluminescence (PL) properties of the films were determined at room temperature and 4.2 K using a 15 mW He-Cd laser ($\lambda=325$ nm) as the excitation source. Scanning electron microscopy (SEM) was performed on a JEOL 6400 FE operating at 5 keV. Transmission electron microscopy (TEM) was performed at 200 keV using standard sample preparation techniques. Atomic force microscopy (AFM) was performed on a Digital Instruments Dimension 3000 Nanoscope IIIa with a Si tip in tapping mode. Capacitance-voltage (CV) measurements were made using a mercury (Hg) probe and a computer controlled Hewlett-Packard 4284A LCR meter. Contacts for Hall-effect measurements were made using an annealed, electron-beam deposited Ti/Au bilayer with thicknesses of 500 and 1500 Å, respectively. X-ray diffraction measurements were made using a Phillips X'Pert MRD diffractometer in the triple axis mode. The incident beam optics were a Bartels-type four crystal Ge(220) monochromator and the diffracted beam optics were a triple bounce Ge(220) analyzer crystal. The angular divergence of the Cu $\text{K}\alpha_1$ source using this configuration was ≤ 10 arcsec.

D. Results and Discussion

AlN Thin Films. The AlN films characterized were grown under the same conditions as the buffer layers used in the GaN growth described above. The as-grown AlN films had highly reflective mirror-like surfaces. SEM analysis revealed a smooth surface with small pinholes

less than 100 nm in size as shown in Fig. 4. The pinholes in areas appeared to be oriented along lines for several microns across the surface of the sample. The source of these pinholes may be due to nucleation of defects at surface imperfections on the substrate, such as polishing scratches. AFM analysis of the AlN films verified this, as it showed a large number of linear features as seen in Figure 5. This would suggest the thin (1000Å) AlN films mimic the features of the SiC substrate, and the quality of the film is a function of the condition of the substrate surface. AlN films grown in a nitrogen diluent had an RMS surface roughness of approximately 18Å (10×10 μm AFM scan), while films grown in hydrogen had an RMS surface roughness of approximately 15Å. As a result, AlN buffer layers used in the growth of GaN thin films were grown in a hydrogen diluent.

Figure 6 shows a typical cross-sectional TEM of an AlN buffer layer which reveals a high density of dislocations in the AlN film. The selective area diffraction (SAD) pattern shows monocrystalline growth, with no evidence of domain growth or low angle grain boundaries, which is consistent with previously reported high-temperature growth of AlN on SiC substrates [14]. The average full width at half maximum (FWHM) of X-ray rocking curve measurements (2θ-ω scan) of the AlN films was 190 arcsec (0002 reflection).

GaN Thin Films: Crystal Quality. Table I lists the FWHM values for GaN films grown in both hydrogen and nitrogen diluents. Both the 002 (symmetric) and 012 (asymmetric) reflections were measured to obtain a better notion of film quality. Quantitative defect analysis has shown edge dislocations to be the prevalent threading dislocation type in heteroepitaxially grown GaN thin films [15], with the remainder being either of mixed type or pure screw. In GaN, the crystal distortion effects of pure edge dislocations do not show up in symmetric (002 in this case) XRD reflections [16]. As a result, an asymmetric reflection such as the 012 gives a better indication of overall film quality, as all types of dislocations distort the planes used in the XRD measurement. For films grown in both diluents the ω and 2θ-ω scan widths are broader for the asymmetric 012 reflections compared to the symmetric 002 reflections. This asymmetric reflection broadening is indicative of a defect structure in the film containing pure edge threading dislocations which were not seen in the symmetric reflection measurement. The 2θ-ω FWHM values for the nitrogen diluent GaN films are more narrow than the corresponding values for films grown in a hydrogen diluent.

Figure 7 is a cross-sectional TEM picture of a 1 μm GaN films grown in a nitrogen diluent on an AlN buffer layer. The GaN has a high concentration of defects near the AlN-GaN interface, which decreases with increasing distance away from the interface. The microstructure of films grown in both diluents was very similar. Figure 8 is a plan-view TEM of a GaN films grown in hydrogen showing the distribution of threading dislocations in the film. The measured dislocation density is $1 \times 10^9 \text{ cm}^{-2}$.

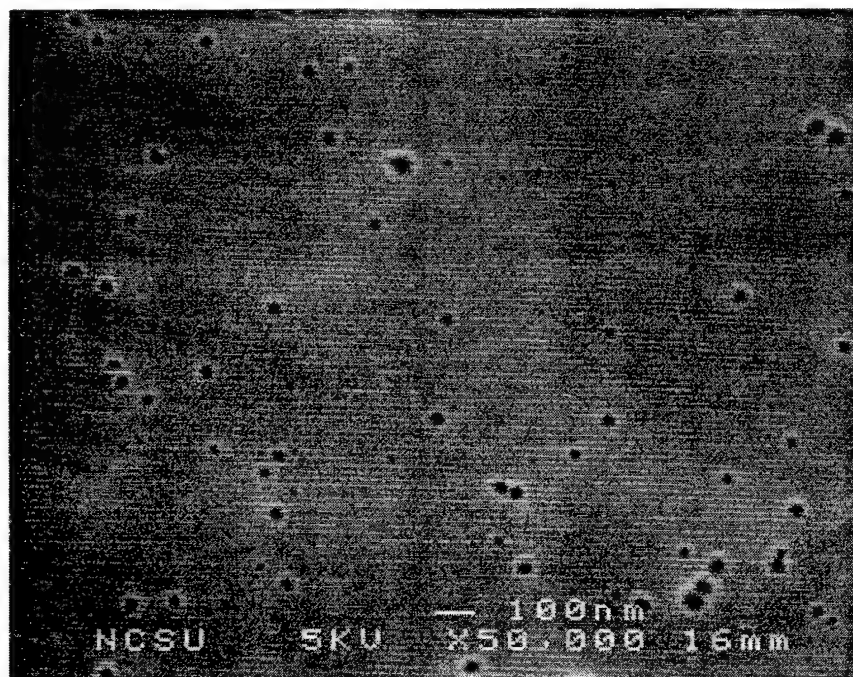


Figure 4. SEM of 1000Å AlN thin film grown directly on SiC.

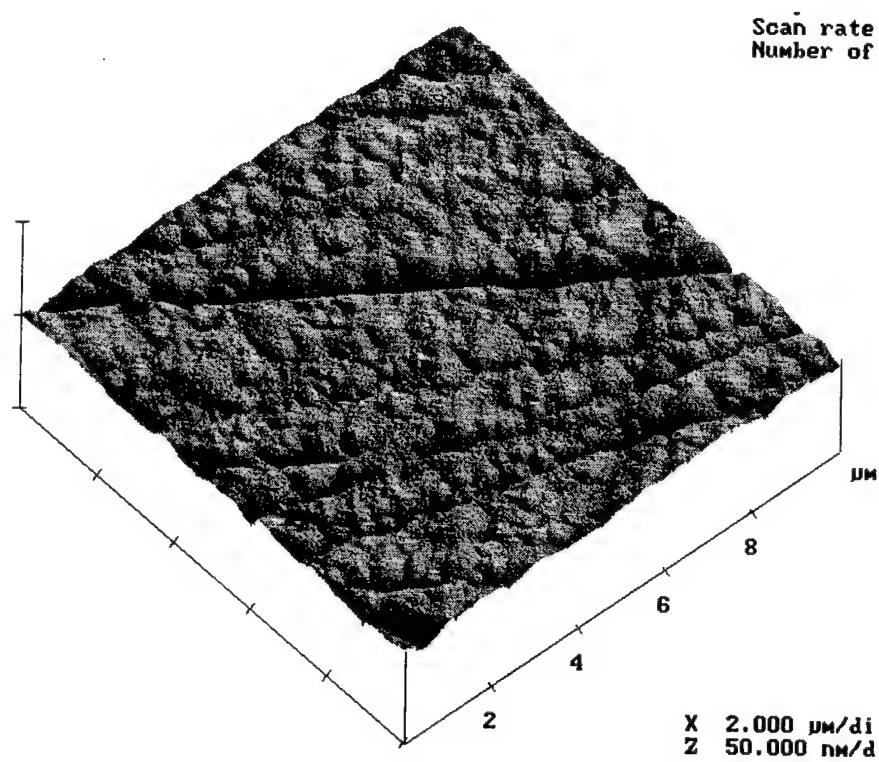


Figure 5. AFM of 1000Å AlN thin film grown directly on SiC. z scale is 50 Å.

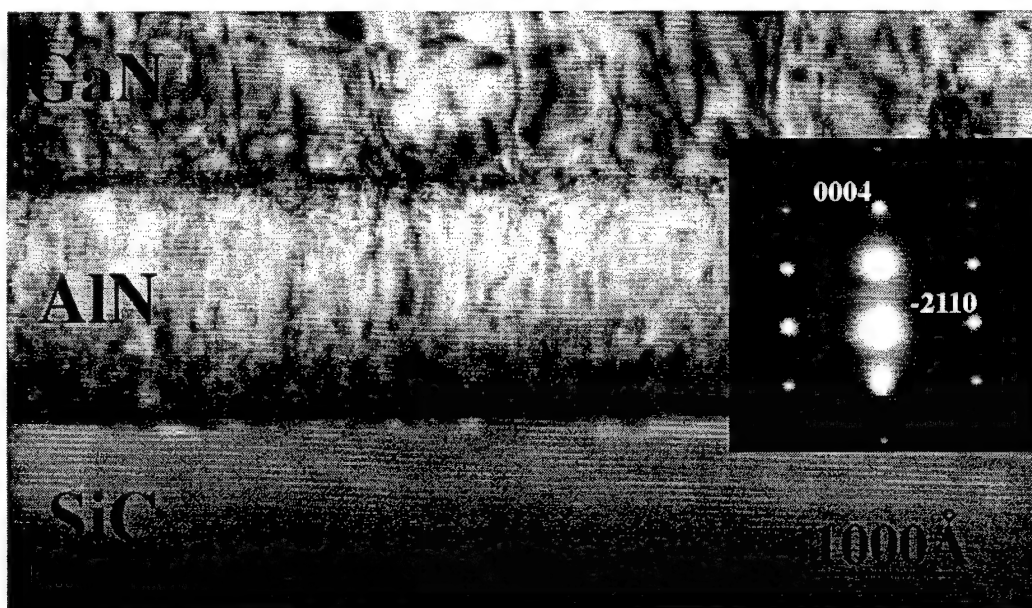


Figure 6. Cross-sectional TEM of AlN buffer layer. Sample orientation is $[01\bar{1}0]$.

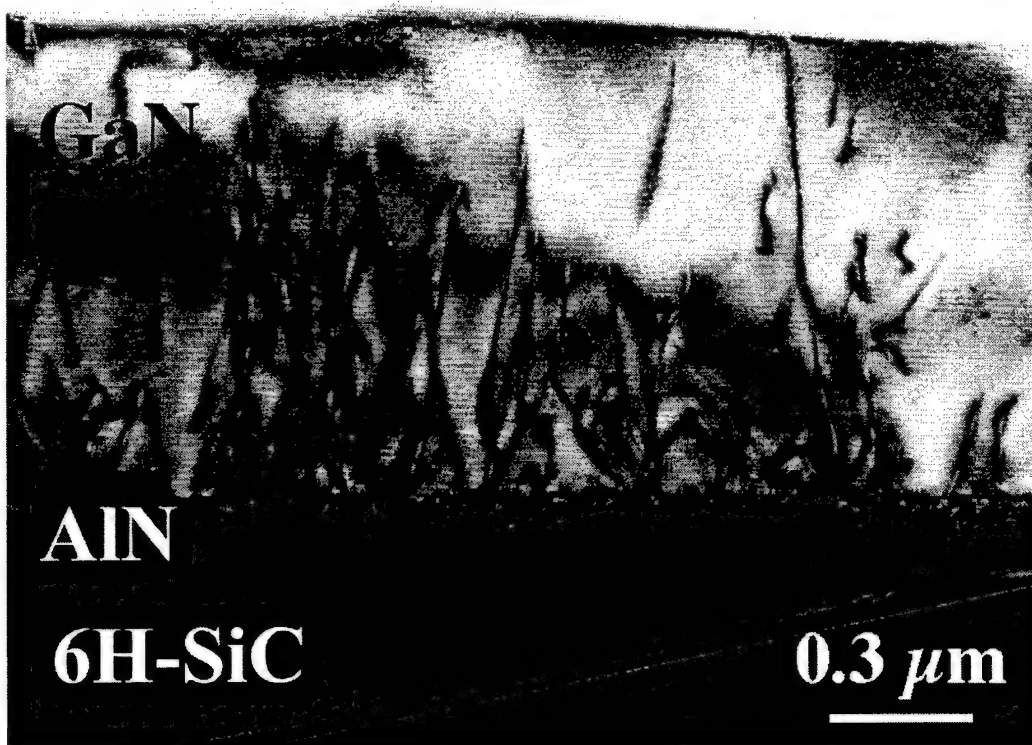


Figure 7. Cross-sectional TEM of GaN film on AlN buffer layer.

Table I. GaN X-ray Diffraction Measurements

| Diluent | | 002 FWHM (arcsec) | 012 FWHM (arcsec) |
|----------|------------------|----------------------|----------------------|
| Nitrogen | ω | 235.1 | 346.6 |
| | $2\theta-\omega$ | 100.8 | 128.4 |
| Hydrogen | ω | 219.4 | 502.1 |
| | $2\theta-\omega$ | 138.1 | 191.1 |

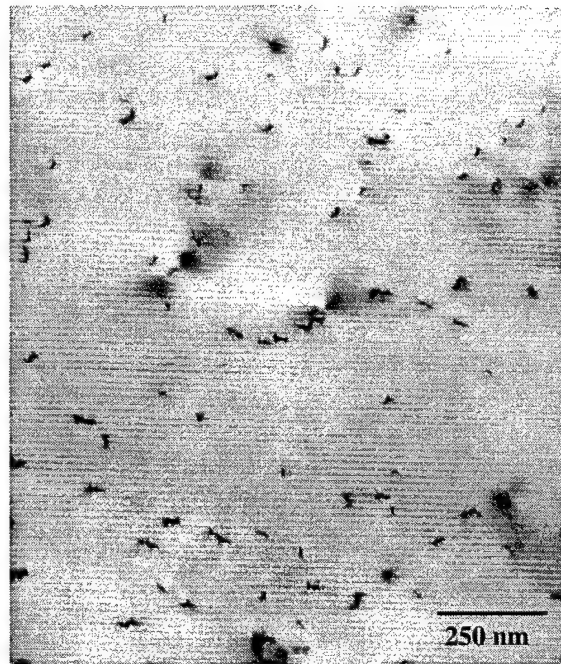


Figure 8. Plan-view TEM of 1 μm GaN film grown in hydrogen diluent. Measured dislocation density of $1 \times 10^9 \text{ cm}^{-2}$.

GaN Thin Films: Photoluminescence. Low temperature (12 K) PL measurements were made on GaN films grown in both diluents. Figures 9 and 10 show the PL spectra for undoped GaN films grown in nitrogen and hydrogen diluents, respectively. The spectra for the nitrogen diluent film is characterized by strong near band edge emission with a FWHM of 6.90 meV, and low “yellow” emission. The yellow emission levels are three orders of magnitude lower than the near band edge emission. The single feature of the near band edge emission at 358.4 nm (3.460 meV) is attributed to an exciton bound to a neutral donor (I_2) [17]. The PL spectra for the hydrogen film is characterized by weaker band edge emission and stronger yellow emission levels. The near band edge emission is characterized by two features, centered

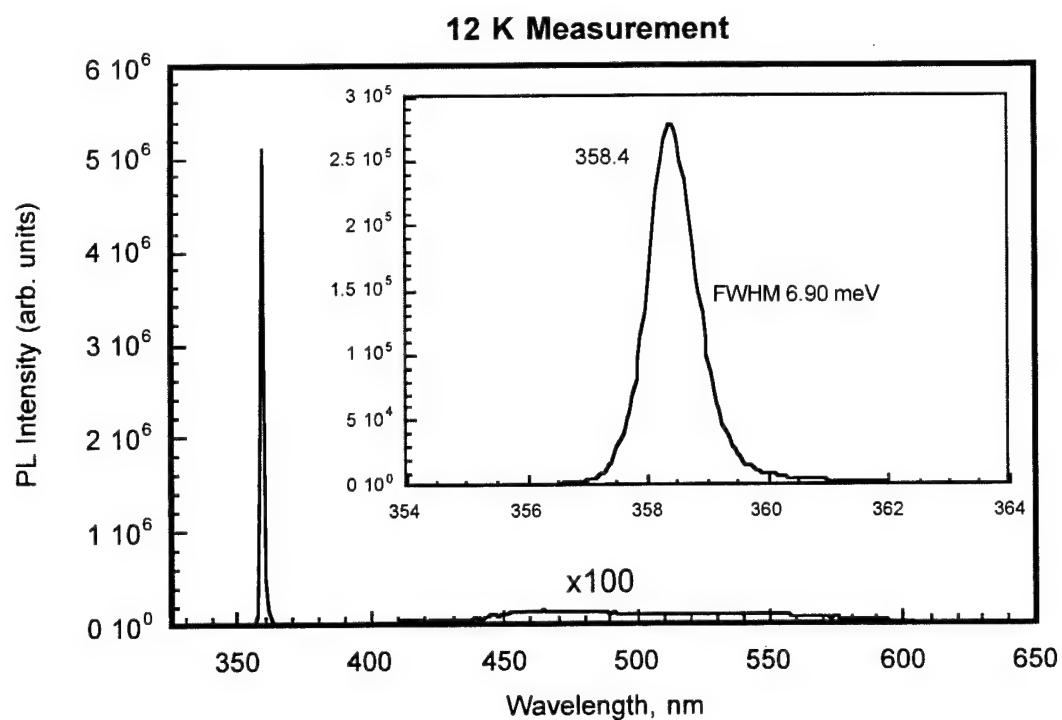


Figure 9. 12 K photoluminescence of GaN film grown in nitrogen diluent.

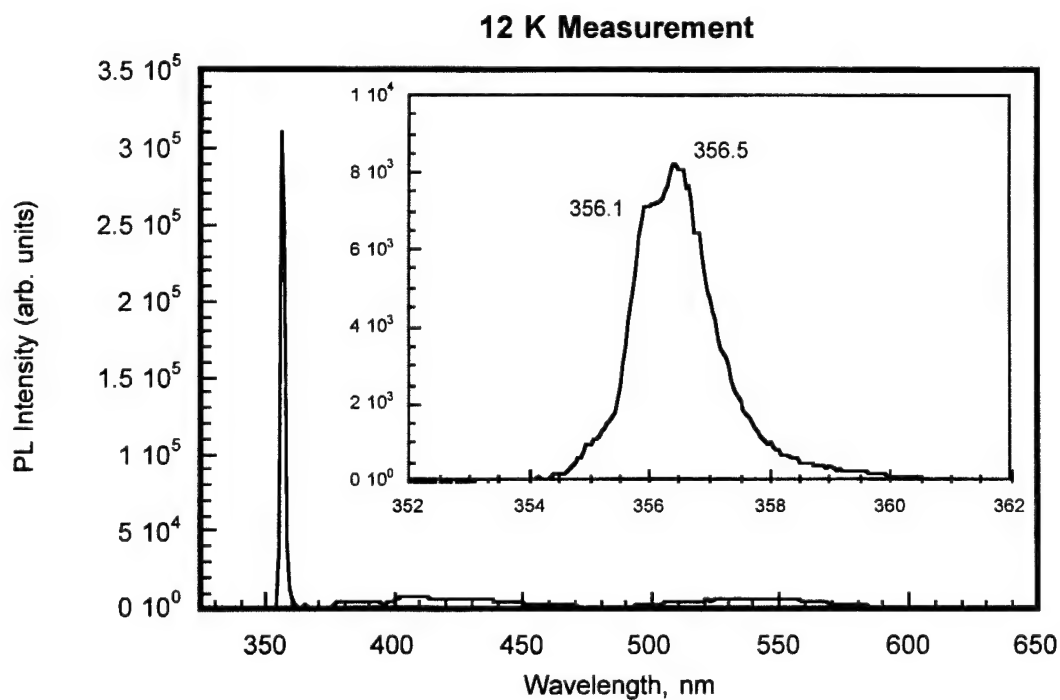


Figure 10. 12 K photoluminescence of GaN film grown in hydrogen diluent.

at 356.5 nm (3.478 eV) and 356.1 nm (3.482 eV). These peaks are attributed to I_2 emission and free exciton (A) emission [17,18].

GaN Thin Films: Electrical Measurements. Undoped GaN films grown in both hydrogen and nitrogen had background free carrier concentrations of $3 \times 10^{16} \text{ cm}^{-3}$ as measured by CV. Hall measurements of these films yielded no information, as they were too resistive to obtain a good measurement. N-type films were achieved through the introduction of SiH_4 during film growth. Si doping levels were demonstrated from the mid 10^{16} s to the mid 10^{18} s. Hall measurements on 1 μm thick Si-doped films were taken at room temperature and the Hall mobility versus carrier concentration is depicted in Figure 11. The maximum Hall mobility was $275 \text{ cm}^2/\text{V}\cdot\text{s}$ at a carrier concentration of $1 \times 10^{17} \text{ cm}^{-3}$.

P-type behavior of GaN was investigated using bis-(cyclopentadienyl) magnesium as the source of magnesium. Mg-doped GaN films grown in a nitrogen diluent have repeatably shown p-type behavior as-grown, as determined by CV measurements. As-grown hole concentrations have been achieved between $3 \times 10^{17} \text{ cm}^{-3}$ and $8 \times 10^{18} \text{ cm}^{-3}$. Films grown in hydrogen typically require a post-growth thermal anneal to activate the hydrogen-passivated magnesium acceptors [19, 20]. Annealing (RTA) of the Mg-doped films showed no change in acceptor levels with short anneal times (30 seconds) between 400 and 800°C , however, a

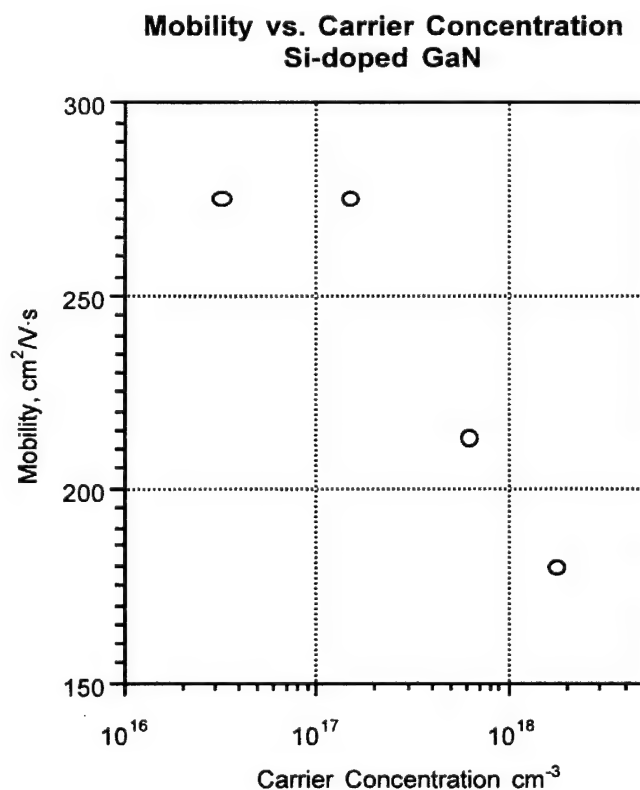


Figure 11. Room temperature Hall mobility measurements of Si-doped GaN films grown in nitrogen diluent.

5 minute anneal at 800°C increased acceptor levels by approximately half an order of magnitude for a sample which initially measured $3 \times 10^{17} \text{ cm}^{-3}$. Further annealing studies and Hall measurements are currently underway.

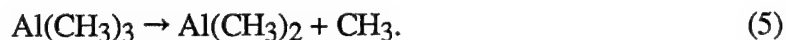
GaN Thin Films: Effect of Diluent on Growth Rates. It was found that the growth rates of both AlN and GaN with nitrogen as the diluent were ~35% less than when using hydrogen. The growth of the GaN films in both diluents was found to be in the mass transport limited regime, as the growth rate of the GaN films was relatively independent of the growth temperature over the temperature range investigated. The reactor model was used to investigate differences in mass transfer characteristics in the two diluents.

The velocity profiles were nearly identical in both mixtures which indicated that the differences were not related to convective transport. However, it was found that hydrogen enhanced diffusion across the substrate boundary layer relative to nitrogen through two mechanisms. First, being a smaller molecule the diffusivity of the metalorganic species through the $\text{H}_2\text{-NH}_3$ mixture is about three times greater than in $\text{N}_2\text{-NH}_3$. Second the thermal diffusivity of the H_2 mixture is about twice that of N_2 , which created a thicker temperature boundary layer below the substrate ($\delta_T \approx 7 \text{ mm}$ for H_2 vs. $\delta_T \approx 4 \text{ mm}$ for N_2). Gas phase diffusivities increase with temperature as described by the following power law expression:

$$D(T) = D_o \left(\frac{T}{T_o} \right)^m \text{ where } m \approx 1.7 \quad (4)$$

Based on the calculated temperature fields the diffusivity of TEG was determined as a function of position below the substrate for both gases which is shown in Fig. 12. Far from the substrate ($z > 1 \text{ cm}$) the gas is cold and the ratio of the diffusivities is constant. Approaching the substrate the gas is hotter in the case of hydrogen due to its thermal diffusivity. As a result the mass diffusivity increases more rapidly in hydrogen, becoming as much as 9X greater than in nitrogen in the boundary layer. The diffusivity of TMA is nearly identical to what is shown in Fig. 12.

An alternative mechanism for the growth rate enhancement is accelerated gas-phase decomposition. For TMA, it is known that pyrolysis is enhanced by the presence of hydrogen [21]. Decomposition of TMA begins by homolytic fission, producing methyl radicals as expressed by Eq. 5:



In the presence of hydrogen the methyl radicals produce atomic hydrogen through the fast, reversible reaction:



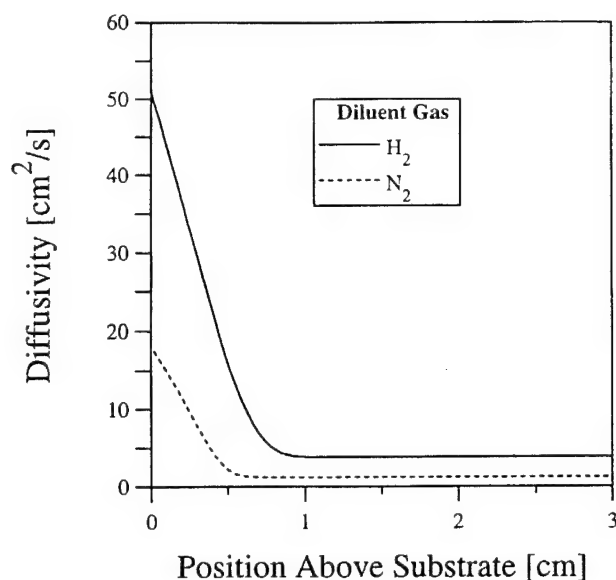
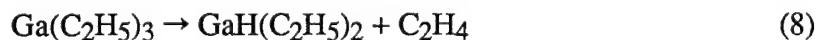


Figure 12. Calculated diffusivity of TEG in diluent gas/NH₃ mixture.

This creates a second decomposition pathway:



This hydrogenolysis reaction has been shown to reduce the decomposition temperature of metalorganics by as much as 100 °C [22]. Although this chemistry undoubtedly occurs, it is not believed to be responsible for the observed differences in growth rate for a number of reasons. First, the decomposition temperatures of both TMA and TEG are < 500 °C regardless of diluent gas [21,22]. At the substrate temperatures employed both organometallics should be fully decomposed by the time they reach the substrate surface. In addition, the growth rates were insensitive to substrate temperature which indicates that decomposition was complete. Furthermore the growth rate enhancement in H₂ was similar for both AlN and GaN. In contrast to TMA the thermal decomposition pathway for TEG proceeds through the β-hydride elimination reaction [22] expressed in Eq. 8:



As no radicals are produced by this reaction, the decomposition process is nearly insensitive to the nature of the carrier gas [22]. Thus, it is concluded that the higher growth rates observed in hydrogen diluent are primarily due to the enhancement of the diffusivity across the boundary layer as outlined above, and not related to differences in gas-phase chemistry.

E. Conclusions

The MOVPE growth process for the deposition of AlN and GaN thin films was investigated. The effects of flow structures in the deposition chamber and the influence of the physical properties of hydrogen and nitrogen diluent gases were considered, and a computational fluid dynamic model was developed to examine the fluid flow structure in the deposition chamber. AlN thin films grown in nitrogen diluent gases were shown to have slightly rougher surfaces than those grown in hydrogen. Measurements (TEM and XRD) of GaN films were examined. Low temperature (12 K) photoluminescence measurements of GaN films grown in a nitrogen diluent had peak intensities and full widths at half maximum equal to or better than those films grown in an hydrogen diluent. Hall measurements of n-type (Si doped) GaN were made with a maximum Hall mobility of $275 \text{ cm}^2/\text{V}\cdot\text{s}$ at $1 \times 10^{17} \text{ cm}^{-3}$ for a $1 \text{ }\mu\text{m}$ film. P-type behavior of GaN (Mg doped) was repeatably obtained without post-growth anneal by growing in nitrogen. Examination of the molecular diffusivity of the growth species explained the difference in the growth rates of AlN and GaN films in hydrogen and nitrogen diluents. Nitrogen is shown to be a feasible alternative to hydrogen as a diluent gas for the growth of AlN and GaN thin films.

F. Future Research

Future research will include further investigation of the as-grown p-type behavior of Mg-doped GaN films grown in a nitrogen diluent. Annealing and Hall mobility measurement studies will be performed. In addition, further optimization of undoped GaN films will be examined, with the goal to improve the XRD and PL measurements. Additionally, the difference in PL of GaN films grown in the two diluents will be investigated. Other work includes growth and characterization of InGaN and AlGaIn films, doping of these films, and their application in microelectronic and optoelectronic devices. Simple diode devices will be fabricated and tested, as well and FET-type devices.

G. References

1. S. Nakamura, M. Senoh, N. Iwasa, S. Nagahama, *Jpn. J. Appl. Phys.* **34** (1995) L797.
2. S. Nakamura, *J. Cryst. Growth*, **170** (1997) 11.
3. J. Burm, W. J. Schaff, L. F. Eastman, H. Amano, I. Akasaki, *Appl. Phys. Lett.* **68** (20) 2849.
4. M. V. Weckwerth, K. P. Killeen, R. Biefeld, T. Drummond, M. H. Crawford, J. C. Zolper, *Electronic Materials Conference*, Santa Barbara, June 1996.
5. E. L. Piner, M. K. Behbehani, N. A. El-Masry, F. G. McIntosh, J. C. Roberts. K. C. Boutros, S. M. Bedair, *Appl. Phys. Lett.* **70** (4) 461.
6. C. Houtman, D. B. Graves, K. F. Jensen, *J. Electrochem Soc.*, **133**, 961 (1986).
7. G. Evans, R. Grief, *Trans. ASME*, **109**, 928, (1987).
8. J. P. Jenkinson, R. Pollard, *J. Electrochem. Soc.*, **131**, 2911, (1984).
9. R. J. Kee, F. M. Rupley, J. A. Miller, Sandia National Laboratories Report SAND87-8215, (1994).

10. R. J. Kee, G. Dixon-Lewis, J. Warnatz, M. E. Coltrin, J. A. Miller, Sandia National Laboratories Report SAND86-8246, (1995).
11. C. R. Wilke, J. Chem. Phys. **18**, 517 (1950).
12. See Chapter 21 of R. B. Bird, W. E. Stewart, and E. N. Lightfoot, *Transport Phenomena*, John Wiley and Sons, New York, (1960).
13. C. A. Wolden, Z. Sitar, R. F. Davis, J. T. Prater, Appl. Phys. Lett. **69**, 2258 (1996).
14. T. W. Weeks, M. D. Bremser, K. S. Ailey, E. Carlson, W. G. Perry, R. F. Davis **67**, (3) 401.
15. D. Kapolnek, X. H. Wu, B. Heying, S. Keller, U. K. Mishra, S. P. Denbaars, J. S. Speck, Appl. Phys. Lett. **67**, 1541 (1995).
16. B. Heying, X. H. Wu, S. Keller, Y. Li, D. Kapolnek, B. P. Keller, S. P. DenBaars, J. S. Speck, Appl. Phys. Lett. **68**, 643 (1996).
17. R. Dingle, D. D. Sell, S. E. Stokowski, M. Ilegems, Phys. Rev. B **4**, 1211 (1971).
18. B. Monemar, I. A. Buyanova, J. P. Bergman, H. Amano, I. Akasaki, Mat. Sci. Eng. B43 (1997) 172.
19. H. Amano, M. Kito, K. Hiramatsu, I. Akasaki, Jpn. J. Appl. Phys. **28**, L2112 (1989).
20. S. Nakamura, N. Iwata, M. Senoh, T. Mukai, Jpn. J. Appl. Phys. **31**, 1258 (1992).
21. T. F. Kuech, Mat. Sci. Rep. **2** (1987).
22. M. Yoshida, H. Watanabe, F. Uesgi, J. Electrochem. Soc. **132**, 677 (1985).

VII. Effect of Hydrogen on the Indium Incorporation in InGaN Epitaxial Films

Significant strides in the growth of III-nitride semiconductor films have led to the recent achievement of extremely bright blue and green light-emitting diodes (LEDs) [1] and blue lasing in InGaN/GaN/AlGaIn-based heterostructures [2]. These developments have occurred in spite of the fact that there is still much that is not understood in the growth and properties of these compounds. This lack of understanding is most apparent in the indium-based nitrides as indicated by the limited number of reports currently being presented and published. The problems impeding the progress in the growth of InGaN and AlInGaIn include poor optical properties, low percentages of indium incorporation in the films, and the formation of indium metal on the film surfaces.

Hydrogen is currently being used for many diverse activities in the growth and processing of III-nitride films. For example, hydrogen has been shown to passivate Ca and Mg acceptors in GaN [3-6] and a difference in the behavior of hydrogen between p-type and n-type materials has been identified using energetics calculations [7]. Also, the addition of hydrogen to nitrogen during the growth of GaN by metalorganic chemical vapor deposition (MOCVD) results in changes in the gas flow pattern and decreases the growth rate [8]. Most of the work reported in the literature to date uses hydrogen as the precursor carrier gas. This is particularly true for the growth of GaN, AlN, and AlGaIn, however, for the limited amount of work involving indium related nitrides, nitrogen becomes the predominantly used carrier gas. The question then arises, if the growth of other nitrides is so successful using hydrogen, why is it not also useful for the growth of InN and InGaIn? Part of the answer lies in the role of hydrogen during the growth of indium containing nitrides. In this section, the effect of hydrogen on the InN percent in InGaIn is presented with the dramatic result that the indium incorporation varies with hydrogen flow holding all other growth conditions constant. This result has not been reported before in the growth of III-nitrides nor in the growth of any other III-V compound previously studied.

The films were grown on (0001) sapphire substrates at atmospheric pressure using a specially designed reactor that has been described elsewhere [9,10]. The sapphire substrates were solvent cleaned prior to loading in the growth reactor. The pre-growth treatment included annealing under nitrogen and passivating under ammonia at 1050°C for 15 and 1 minute, respectively. An AlN buffer layer grown by atomic layer epitaxy (ALE) was then deposited at 700°C and 100 Torr, followed by a MOCVD grown AlGaIn graded to GaIn prelayer at 950°C and 750 Torr for 15 and 10 minutes, respectively, with a 2.5 minute grading period in between. The details of the growth conditions for the buffer layer are described elsewhere [11].

The InGa_N layer was grown for 1 hour either by MOCVD in the temperature range 710-780°C or by ALE in the range 650 and 700°C. Trimethylgallium (TMGa), trimethyl-aluminum (TMAI), and ethyldimethylindium (EDMIn) were used as the precursors with a nitrogen/hydrogen mixed carrier gas. High purity ammonia was used as the nitrogen source. The quality and InN percent of the films were characterized by q-2q x-ray diffraction (q-2q XRD) and x-ray rocking curve (XRC).

Figure 1 plots the InN percent, as determined by q-2q XRD, in InGa_N as a function of the hydrogen flow injected with the nitrogen carrier gas. All of the samples were grown by MOCVD using 1 sccm of TMGa (-10°C), and 90 sccm of EDMIn (+10°C) in 5 slm of nitrogen carrier gas and 5 slm of ammonia at the temperatures and hydrogen flows indicated. The figure indicates that the InN percent in the films dropped significantly as the hydrogen flow increased. This trend occurred at all four temperatures investigated with very good consistency. The general trend of Fig. 1 showed a fairly rapid decrease in the InN percent as the hydrogen flow increased from 0 to 20 sccm, followed by a more gradual decrease upon further increased hydrogen flow from 20 to 100 sccm. All films were single crystalline, good quality, and without indium metal as-grown, as indicated in Figs. 2(a) and (b). The q-2q XRD pattern for the sample grown at 710°C with no hydrogen, shown in Fig. 2(a), indicated 40% InN in the ternary film. The scan showed the (0002) plane of InGa_N and GaN along with the (0006) c-plane of the sapphire substrate. The scan also showed the absence of any pure indium peaks such as the (002) plane at 36.33° or the (110) plane at 39.17°, as well as no other InGa_N planes, which indicated that the film was free of indium metal and single crystalline as-grown. Fig. 2(b), which gave an indication of the good quality of the films, was an XRC pattern of the sample grown at 750°C with 50 sccm hydrogen. The peak on the left corresponded to the (0002) plane of the ternary film while the peak on the right was the (0002) plane of GaN. The

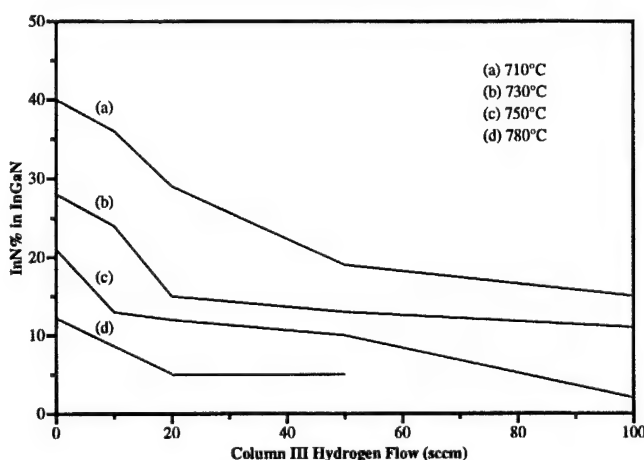


Figure 1. InN percent in InGa_N as determined by q-2q XRD as a function of the hydrogen flow at the growth temperature (a) 710, (b) 730, (c) 750, and (d) 780°C.

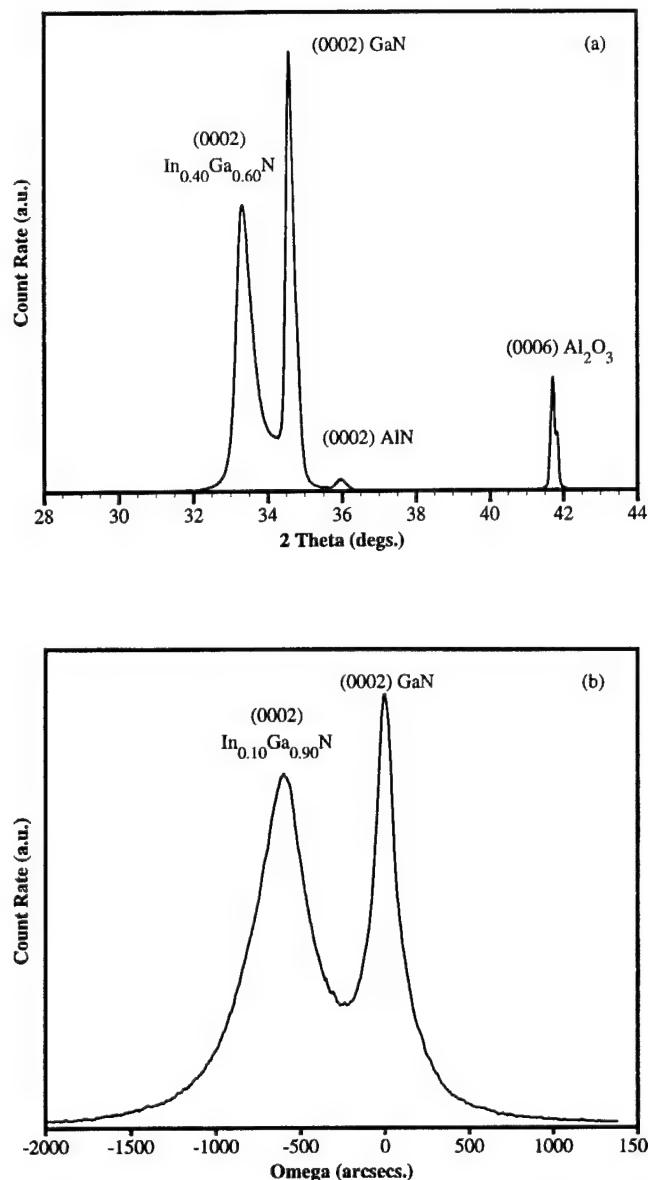


Figure 2. (a) q-2 θ XRD pattern for In_{0.40}Ga_{0.60}N grown at 710°C with no hydrogen and (b) XRC pattern for In_{0.10}Ga_{0.90}N grown at 750°C with 50 sccm hydrogen.

full width at half maximum (FWHM) of these planes was 416 and 159 arcsecs., respectively. The splitting between the peaks indicated 10% InN in the InGaN film which was in agreement with the value obtained by q-2 θ XRD. The GaN FWHM was slightly larger than the previously reported value of 130 arcsecs [11], however, this GaN layer was much thinner and was being used as a prelayer for the InGaN growth. The FWHM of the ternary film was quite good compared to previously reported values for InGaN at this growth temperature [9,12]. The general trend was that as the InN percent in the ternary increased, the FWHM of the films also increased. This is to be expected since, as the InN percent increased, the lattice mismatch

between the ternary and the underlying GaN prelayer increased causing an increase in the dislocation density in the film.

The effect of hydrogen on In incorporation was also observed for InGa_N grown by ALE. The main characteristic of this growth technique was reactant gas separation thereby eliminating the possibility for gas phase reactions as described elsewhere [9,10]. In the growth temperature range of 650 to 700°C, a consistent reduction in the InN percent was observed with increasing amounts of hydrogen. For example, at 650°C with hydrogen flowing at 2 sccm with the organometallics and 100 sccm with the ammonia gas stream, 17% InN in InGa_N was observed. When the hydrogen flow was increased to 4 and 200 sccm, respectively, the indium incorporation dropped to 11%.

In an effort to determine the effect on the InN percent due to the hydrogen generated during the decomposition of ammonia, a series of experiments was performed in which the overall ammonia flow was varied while keeping all other parameters constant. The results of that study are shown in Fig. 3 in which the ammonia flow was varied from 0.3 to 5 slm while using nitrogen as a make-up gas to keep the overall column V flow constant at 5 slm. The samples representing curve (a) in Fig. 3 were grown at 730°C with no hydrogen while those on curve (b) were grown at 780°C with 50 sccm hydrogen. Both were deposited by MOCVD with the same TMGa and EDMIn flows as those in Fig. 1. Both curves showed little change in InN percent for ammonia flows greater than 1 slm indicating a sufficient supply of reactive nitrogen species at the growing surface with little effect from the hydrogen being generated by the decomposition of ammonia. This was an indication that the decomposition of ammonia into nitrogen and hydrogen at these temperatures was extremely low. If the decomposition were occurring at a higher rate, the increased hydrogen being generated from the ammonia would result in a decrease in the InN percent similar to that observed in Fig. 1. Using a ± 1 InN% error associated with the points on curve (a) of Fig. 3 and comparing this number to the zero hydrogen point on curve (b) of Fig. 1 indicates that 5 sccm of hydrogen, at most, was being generated from the ammonia. Assuming 5 slm of ammonia, 15 sccm of liberated hydrogen would result from 0.1% decomposition of the ammonia at the temperature range studied. Therefore, the data from Figs. 1 and 3 suggest an ammonia decomposition rate of less than 0.1%. The drop in InN percent when lowering the ammonia flow to 0.3 slm in curve 3(a) was accompanied by indium metal on the sample as indicated by q-2 θ XRD, although the drop in curve 3(b) was not accompanied by an indication of indium metal on the sample. This indicates that at this low ammonia flow, the reactive nitrogen species concentration from ammonia was limiting the growth of the ternary film and for curve 3(a), the temperature was sufficiently low enough to allow the excess indium to form indium metal, while for curve 3(b) the excess indium was desorbing from the film surface.

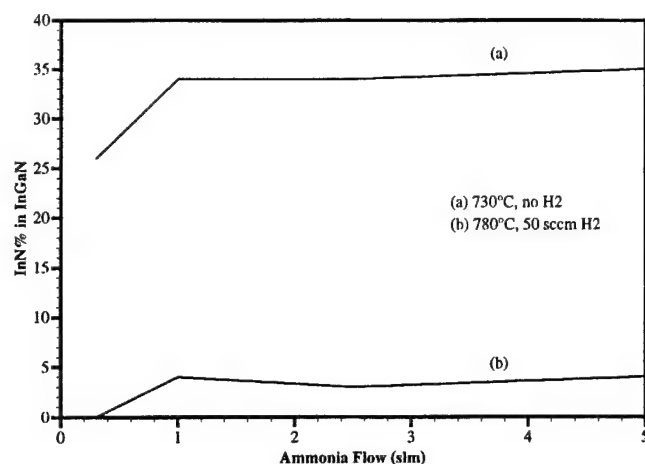


Figure 3. InN percent in InGaN as determined by q-2q XRD as a function of the ammonia flow at (a) 730°C and no hydrogen, and (b) 780°C and 50 sccm hydrogen.

At this time, any effort to explain why hydrogen effects indium incorporation would be speculation. However, hydrogen may have an effect on the lifetime of the reactive indium species at the film surface [13,14]. If hydrogen were to reduce the lifetime, the concentration of reactive indium species at the surface would be reduced with increased hydrogen flows, thereby reducing the amount of indium being incorporated into the growing film. Another possibility is that hydrogen somehow affects the concentration of contaminants, such as carbon, in the near surface region which could, in turn, affect the incorporation of indium.

In summary, flowing small amounts of hydrogen has been shown to have a profound effect on the InN percent in III-nitride compounds, as well as on the crystalline quality of these films. This result has never before been reported for any III-V compound semiconductor and represents a new and interesting avenue of investigation into the understanding of the growth of nitride films. An increase of up to 25% InN in InGaN, depending on the growth temperature, can be obtained by reducing the hydrogen flow from 100 to 0 sccm. The amount of hydrogen being generated by the ammonia at these temperatures does not appreciably change the InN percent in the films, indicating a very low decomposition rate (less than 0.1%) of the available ammonia. Further characterization of these films is underway to help fully understand the exact nature of the mechanisms responsible for the phenomena presented in this letter. Studies aimed at identifying any correlation between the impurities and hydrogen flow in these films to aid in the improvement of the optical and electrical properties of InGaN are also being investigated.

References

1. S. Nakamura, M. Senoh, N. Iwasa, and S. Nagahama, *Jpn. J. Appl. Phys.* **34**, L797 (1995).

2. S. Nakamura, M. Senoh, S. Nagahama, N. Iwasa, T. Yamada, T. Matsushita, H. Kiyoku, and Y. Sugimoto, *Jpn. J. Appl. Phys.* **35**, L74 (1996).
3. J. W. Lee, S. J. Pearton, J. C. Zolper, and R. A. Stall, *Appl. Phys. Lett.* **68**, 2102 (1996).
4. P. Perlin, I. Gorczyca, N. E. Christensen, I. Grzegory, H. Teisseyne, and T. Suski, *Phys. Rev. B* **45**, 13307 (1992).
5. R. F. Davis, *Physica B* **185**, 1 (1993).
6. S. Nakamura, T. Mukai, and M. Senoh, *Appl. Phys. Lett.* **64**, 1687 (1994).
7. J. Neugebauer, and C. G. Van de Walle, *Appl. Phys. Lett.* **68**, 1829 (1996).
8. H. Hashimoto, H. Amano, N. Sawaki, and I. Akasaki, *J. Crystal Growth* **68**, 163 (1984).
9. K. S. Boutros, F. G. McIntosh, J. C. Roberts, S. M. Bedair, E. L. Piner, and N. A. El-Masry, *Appl. Phys. Lett.* **67**, 1797 (1995).
10. N. Karam, T. Parados, W. Rowland, J. Schetzina, N. El-Masry, and S. M. Bedair, *Appl. Phys. Lett.* **67**, 94 (1995).
11. E. L. Piner, Y. W. He, K. S. Boutros, F. G. McIntosh, J. C. Roberts, S. M. Bedair, and N. A. El-Masry, *Mater. Res. Soc. Symp. Proc.* **395**, 307 (1996).
12. S. Nakamura, *Microelect. J.*, **25**, 651 (1994).
13. S. M. Bedair, F. G. McIntosh, J. Roberts, E. Piner, K. Boutros, and N. A. El-Masry, accepted for publication in *J. Crystal Growth*.
14. Y. Horikoshi, H. Yamaguchi, F. Briones, and M. Kawashima, *J. Crystal Growth* **105**, 326 (1990).

VIII. Impurity Dependence on Hydrogen and Ammonia Flow Rates in InGaN Bulk Films

The effect of small amounts of hydrogen on the InN percent in InGaN epitaxial films were recently reported [1] with the result that the In incorporation was controlled by the hydrogen flow rate while holding all other growth conditions constant. Due to the effect of hydrogen in reducing the InN incorporation rate, most of the work reported on the growth of InGaN was carried out under nitrogen carrier gas flows. Another source of hydrogen was derived from NH_3 , however, at the growth temperatures used to grow InGaN, the NH_3 cracking efficiency was less than 0.1%. Hydrogen had also been shown to effect other aspects of III-V film growth. For example, hydrogen can passivate Ca and Mg acceptors in GaN [2-5]. By substituting hydrogen in place of nitrogen as the carrier gas, different reactant gas flow patterns were obtained due to the different thermal properties of nitrogen and hydrogen [6]. Hydrogen was also shown to enhance the step flow growth of GaAs by gas-source migration enhanced epitaxy [7], as well as the Ga surface-diffusion length on GaAs during molecular-beam epitaxy [8]. In this section, the influence of hydrogen and NH_3 on the H, C, and O impurity levels in bulk InGaN epitaxial films grown by metalorganic chemical vapor deposition (MOCVD) are reported. Secondary ion mass spectrometry (SIMS) analysis indicated a significant decrease in the H, C, and O impurity levels as the hydrogen flow rate was increased while increasing the NH_3 flow rate results in a decrease in the C and an increase in the H and O holding all other growth conditions constant.

Bulk InGaN films were grown on (0001) sapphire substrates at atmospheric pressure using a specially designed reactor that has been described elsewhere [9,10]. Trimethylgallium (TMGa), trimethylaluminum (TMAI), and ethyldimethylindium (EDMIn) were used as the precursors with a nitrogen/hydrogen mixed carrier gas. High purity ammonia was used as the nitrogen source. The pre-growth treatment including the buffer layer and prelayer growth has been described elsewhere [1,11]. The InGaN layer was grown for 1 hour by MOCVD in the temperature range 710 to 780°C resulting in a thickness of 0.3 μm for the bulk ternary alloy as determined by transmission electron microscopy and SIMS. All films were single crystalline, good quality, and without indium metal as indicated by θ -2 θ x-ray diffraction (θ -2 θ XRD) and x-ray rocking curve (XRC) [1]. All measurements were taken using a Cameca IMS-6F SIMS instrument. H (1), C (12), O (16), Ga (69), and In (115) measurements were performed using Cs^+ bombardment and monitoring negative secondary ions. Atomic ions were measured for all elements.

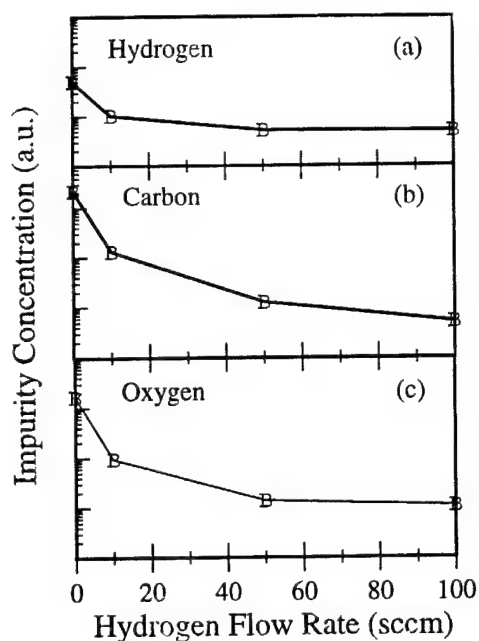


Figure. 1. (a) Hydrogen, (b) carbon, and (c) oxygen impurity concentrations determined by SIMS and normalized to the Ga signal as a function of the hydrogen flow rate for bulk InGa_N films grown at 730°C by MOCVD.

Figure 1 plots the (a) H, (b) C, and (c) O impurity concentrations from SIMS as a function of the hydrogen flow injected with the nitrogen carrier gas. These samples were grown at 730°C using 1 sccm of TMGa (-10°C), and 90 sccm of EDMin (+10°C) in 5 slm of nitrogen carrier gas and 5 slm of NH₃. Due to the unavailability of InGa_N calibration standards, absolute impurity concentrations in atoms/cm³ cannot be determined. The H, C, and O levels were normalized to the Ga signal, factoring in the Ga content determined by q-2q XRD. This method of SIMS data analysis produces the most self-consistent data. Figure 1 shows the impurity levels dropped significantly as the hydrogen flow rate increased. Figure 1(a) indicates approximately a ten-fold decrease in the H impurity level as the hydrogen flow rate increased from 0 to 50 sccm. There is greater than an order of magnitude decrease in both the C and O concentrations as the hydrogen flow rate was increased from 0 to 10 sccm. There was a further decrease by another order of magnitude as the hydrogen flow rate was increased from 10 to 100 sccm, however, the decrease in the impurity levels seemed to level off between 50 and 100 sccm. Similar trends were observed for bulk InGa_N samples grown at 710 and 780°C.

The decrease in the impurity levels with hydrogen flow rate was also accompanied by a decrease in the InN percent in the ternary alloy. The In incorporation decreased from 28 to 11% as a result of increasing the hydrogen flow rate from 0 to 100 sccm as previously reported [1]. To show the decrease in the impurity levels was mainly a function of the hydrogen flow rate rather than the change in InN percent, films grown with varied hydrogen flow rates yielded the same InN percent are shown in Table I. The data shown in Table I represents three different

Table I. Comparison of the Impurity Concentrations to the Hydrogen Flow Rate for Three Different Growth Temperature Conditions Yielding Constant InN Percentages

| Group | Temp. (°C) | Growth H ₂ (sccm) | InN% | Relative Impurity Levels | | |
|-------|------------|---------------------------------|------|--------------------------|-----|-----|
| | | | | H | C | O |
| A | 780 | 20 | 5 | 2.0 | 3.7 | 4.5 |
| | 780 | 50 | 4 | 1.0 | 1.0 | 1.0 |
| B | 730 | 0 | 28 | 1.7 | 2.2 | 3.3 |
| | 780 | 20 | 29 | 1.0 | 1.0 | 1.0 |
| C | 780 | 0 | 12 | 0.4 | 33 | 9.1 |
| | 730 | 50 | 13 | 1.0 | 2.5 | 1.2 |
| | 730 | 100 | 11 | 1.0 | 1.0 | 1.0 |

growth temperature conditions. For each condition, labeled A, B, and C in the first column of Table I, the impurity concentrations were normalized to the sample with the highest hydrogen flow rate to facilitate comparisons. In Group A, the growth temperature was constant as the hydrogen flow rate increased, in Group B, the temperature increased as the hydrogen flow rate increased, and in Group C, the temperature decreased as the hydrogen flow rate increased. In all cases, the C and O impurity levels increased with decreased hydrogen flow rate and indicated that the hydrogen flow rate was affecting the impurity concentrations irrespective of the InN percent in the films. Additionally, the hydrogen flow rate was shown to have a more pronounced effect on the C and O impurity concentrations than changes in the growth temperature. For example, from Group C, films grown at 780°C without hydrogen had higher C concentrations, over thirty times higher, than the corresponding films grown at 730°C with 100 sccm of hydrogen. The data shown in Table I was consistent with the trends shown in Fig. 1 except for the H impurity incorporation at the relatively high temperature in Group C. In this case, the H impurity concentration decreased by a factor of 2.5 as the temperature increased and the hydrogen flow rate decreased. This could indicate that the growth temperature played a critical role on the impurity H incorporation in this ternary alloy.

The most probable source of C contamination was the OM precursors. During InGaN growth, TMGa [(CH₃)₃Ga] and EDMin [(CH₃)₂C₂H₅In] were continuously flowing into the growth reactor. The decomposition of these OMs typically resulted in the liberation of methyl radicals (CH₃) and, to a lesser extent, other hydrocarbons such as CH₂ and CH [12]. These hydrocarbon radicals could attach to the growing surface leading to their incorporation in the InGaN film. Additionally, the final hydrocarbon attached to the Ga and In species during their surface decomposition process could be difficult to remove and become incorporated into the film as the Ga and In species are incorporated. This will result in a relatively high C and H impurity content since inclusion of a methyl radical, for example, will lead to the simultaneous

incorporation of C and H. This is consistent with the previous finding using high-resolution infrared absorption spectroscopy showing the presence of carbon-hydrogen defect complexes [13]. Hydrogen can interact with a CH_3 radical either in the gas phase or, more likely, at the InGa N surface to form a more stable CH_4 molecule that is less likely to react with the growing surface. A very small amount of hydrogen in the carrier gas, 10 sccm for example, seems to be very effective in reducing both C and H impurity levels in the bulk ternary film. Even though the ratio of hydrogen to nitrogen in the carrier gas is very low, the mole fraction ratio of hydrogen to the OM is quite large. For example, the hydrogen to OM mole fraction ratio is ~ 100 at a hydrogen flow rate of 10 sccm. Thus, the mole fraction of hydrogen to hydrocarbons from the OM is ~ 33 at a 10 sccm hydrogen flow rate.

The source of O contamination in the growth reactor was not as apparent as the C source. Although high purity ammonia (99.999%), which was further purified by an OM resin filter, was being used as the nitrogen supply, it was still suspected as being a possible candidate for the O source. A set of experiments in which the NH_3 ratio in the column V nitrogen carrier gas was varied while holding all other growth parameters constant was performed. The samples were grown at 730°C with no hydrogen and with the same TMGa and EDMIn flow rates as the samples shown in Fig. 1. The NH_3 flow rate was varied from 1 to 5 slm while nitrogen was used as a make-up flow to keep the overall column V flow rate a constant 5 slm. q-2q XRD showed no appreciable change in the InN percent for these samples indicating a sufficient supply of reactive nitrogen species at the growing surface and a lack of enough hydrogen liberated from the NH_3 to reduce the In incorporation as we had previously reported [1]. SIMS analysis of the H, C, and O impurity levels in these samples are shown in Fig. 2(a), (b), and (c), respectively. Figure 2(c) shows there was, in fact, an increase in the O impurity level by about a factor of four as the NH_3 flow rate increased from 2.5 to 5 slm giving a good indication that O was appreciably present in the NH_3 supply. However, the O concentration did not significantly change while increasing the NH_3 flow rate from 1 to 2.5 slm. This may be an indication that the effectiveness of the OM resin purifier, while stable at lower NH_3 flow rates, diminished at higher flow rates. Additionally, the H impurity level in Fig. 2(a) was seen to also increase by the same amount as the O. This could indicate that hydroxyl radicals were being incorporated as oxygen-hydrogen defect complexes into the film and, in a similar fashion as with the hydrocarbon radicals discussed earlier, the hydrogen in the carrier gas could interact with an OH radical at the surface to form H_2O which is more stable and less likely to react with the nitride film surface. What is also interesting is the observation that the C concentration shown in Fig. 2(b) decreased by an order of magnitude as the NH_3 flow rate increased from 1 to 2.5 slm. This may be an indication of a surface enhanced reaction between NH_3 and the hydrocarbon radicals [12] such that NH_3 decomposed to NH_2 and H and the H atom bonds

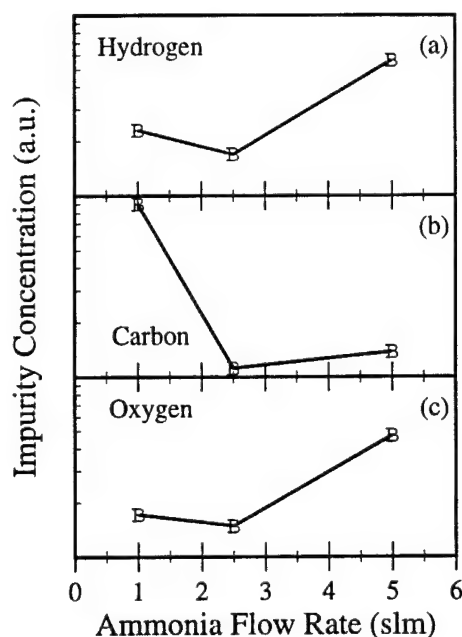


Figure 2. (a) Hydrogen, (b) carbon, and (c) oxygen impurity concentrations determined by SIMS and normalized to the Ga signal as a function of the ammonia flow rate for bulk InGa_N films grown at 730°C with no hydrogen by MOCVD.

with CH₃ to form CH₄ which was stable thereby reducing the C impurity level at higher NH₃ flow rates. However, this effect seemed to saturate upon further increase in NH₃ flow rate as seen in Fig. 2(b).

In addition to the previously discussed mechanism for the decrease in the impurity levels associated with an increase in the hydrogen flow rate, it has also been proposed [14] that due to the differences in thermal properties of hydrogen and nitrogen, increasing the hydrogen to nitrogen ratio will reduce the thickness of the gaseous thermal boundary layer above the substrate. Reducing the boundary layer can lead to less parasitic gas phase reactions that can be partially responsible for the impurities in the growing film. However, in the present experiment, the hydrogen to nitrogen ratio in the carrier gas is much lower than the flow rates used by Scholz *et al* [14] and, therefore, should not substantially affect the thermal boundary layer. Another possible explanation is that hydrogen partially passivates the InGa_N surface in a similar fashion as in the growth of GaAs [15]. When the carbon- and oxygen-containing radicals come in contact with the film surface they can interact with the hydrogen on the surface and form CH₄ and H₂O, respectively, in two possible scenarios as described earlier. However, the dissociation of hydrogen from the nitride surface at the presently used growth temperatures has not been studied.

To aid in further understanding the overall effect on the impurity levels as the amount of InN in the InGa_N ternary alloy is increased, the impurity concentrations are plotted as a function of the InN percent and shown in Fig. 3 for the (a) H, (b) C, and (c) O impurity levels.

The impurity level signals are normalized to the Ga signal as in Figs. 1 and 2. Figure 3 represents data collected under several different growth conditions: B-710°C, J-730°C, P-780°C, with varied hydrogen flow rates, and H-varied NH₃ flow rates at two different temperatures which can account for much of the spread in the data. There is a general trend in Fig. 3 that indicates as the InN percent in the bulk films increase the impurity levels increase. This suggests that, regardless of changes in the growth conditions, increasing the InN percent will result in greater concentrations of impurities in the film. For example, increasing the In incorporation from 10 to 40% can result in approximately three orders of magnitude increase in the C and O impurity levels.

In summary, flowing small amounts of hydrogen has been shown by SIMS to have a significant effect on the H, C, and O impurity concentrations in InGaN bulk films. A decrease of over two orders of magnitude in both the C and O levels results from increasing the hydrogen flow rate from 0 to 100 sccm while the H impurity level drops by a factor of ten over the same range. The NH₃ flow rate was shown to affect the H, C, and O concentrations as well. The H and O increases and the C decreases as the NH₃ flow rate increases indicating that even high purity NH₃ (99.999%) can be a source of oxygen. Further studies indicate that when the InN percent in InGaN increases, the impurity levels increase regardless of changes in the growth conditions. More work is needed to fully understand the origin of these results.

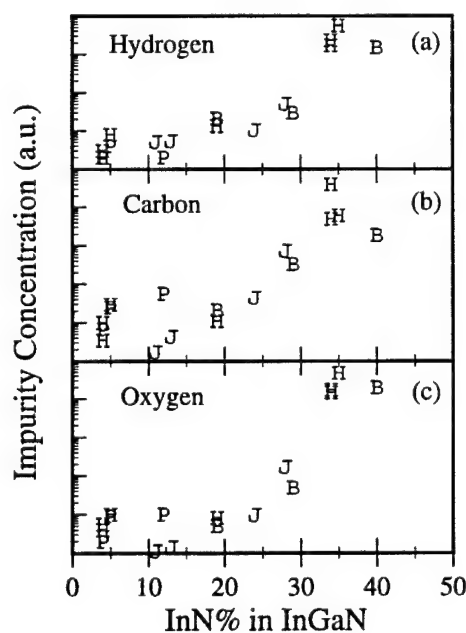


Figure 3. (a) Hydrogen, (b) carbon, and (c) oxygen impurity concentrations determined by SIMS and normalized to the Ga signal as a function of the InN percent for bulk InGaN films grown under varied growth conditions by MOCVD: Varied hydrogen flow rate at; B - 710°C, J - 730°C, and P - 780°C, and H - varied ammonia flow rate at two different temperatures.

We would like to thank Drs. Dieter P. Griffis and David A. Ricks of NCSU Analytical Instrumentation Facility for their assistance with the SIMS data. This work is supported by ONR (The University Research Initiative) under grant number N00014-92-J-1477 and ARO/ARPA under grant number DAAH04-96-1-0173. E. L. Piner would also like to thank the U. S. Department of Education GAANN Electronic Materials Fellowship Program for their support.

References

1. E. L. Piner, M. K. Behbehani, N. A. El-Masry, F. G. McIntosh, J. C. Roberts, and S. M. Bedair, *Appl. Phys. Lett.* **70**, 461 (1997).
2. J. W. Lee, S. J. Pearton, J. C. Zolper, and R. A. Stall, *Appl. Phys. Lett.* **68**, 2102 (1996).
3. P. Perlin, I. Gorczyca, N. E. Christensen, I. Grzegory, H. Teisseyne, and T. Suski, *Phys. Rev. B* **45**, 13307 (1992).
4. R. F. Davis, *Physica B* **185**, 1 (1993).
5. S. Nakamura, T. Mukai, and M. Senoh, *Appl. Phys. Lett.* **64**, 1687 (1994).
6. H. Hashimoto, H. Amano, N. Sawaki, and I. Akasaki, *J. Crystal Growth* **68**, 163 (1984).
7. H. Asahi, T. Hisaka, S. G. Kim, T. Kaneko, S. J. Yu, Y. Okuno, and S. Gonda, *Appl. Phys. Lett.* **61**, 1054 (1992).
8. Y. Morishita, Y. Nomura, S. Goto, and Y. Katayama, *Appl. Phys. Lett.* **67**, 2500 (1995).
9. K. S. Boutros, F. G. McIntosh, J. C. Roberts, S. M. Bedair, E. L. Piner, and N. A. El-Masry, *Appl. Phys. Lett.* **67**, 1797 (1995).
10. N. Karam, T. Parados, W. Rowland, J. Schetzina, N. El-Masry, and S. M. Bedair, *Appl. Phys. Lett.* **67**, 94 (1995).
11. E. L. Piner, Y. W. He, K. S. Boutros, F. G. McIntosh, J. C. Roberts, S. M. Bedair, and N. A. El-Masry, *Mater. Res. Soc. Symp. Proc.* **395**, 307 (1996).
12. Y. Park, and D. Pavlidis, *J. Elect. Mat.* **25**, 1554 (1996).
13. G.-C. Yi, and B. W. Wessels, *Appl. Phys. Lett.* **70**, 357 (1997).
14. F. Scholz, V. Härle, F. Steuber, H. Bolay, A. Dörnen, B. Kaufmann, V. Syganow, and A. Hangleiter, *J. Crystal Growth* **170**, 321 (1997).
15. Y. Horikoshi, H. Yamaguchi, F. Briones, and M. Kawashima, *J. Crystal Growth* **105**, 326 (1990).

IX. Optical Memory Effect in GaN Epitaxial Films

During the last 25 years, considerable effort has been devoted to the design of optical data storage devices [1-6]. Despite the commercial success of high-density magneto-optical data storage systems, vigorous research activity continues regarding the development of non-magnetic, all-optical storage media. Most of these investigations are based on materials that trap electrons at deep defects. Read and write data transfer rates in electron trapping media should be fast because the process is photon-electronic rather than thermal in nature. One of the most promising technologies is based on electron trapping in alkaline earth crystals doped with rare earth elements [7-9]. A number of investigators have also studied the optical memory effect in AlN ceramics [10] and AlGaAs alloys [11]. In these technologies, information is written when photoionization of deep electron traps effectively sensitizes these materials by creating metastable states that modulate their electrical and/or optical properties. The written information can be retrieved from these sensitized crystals in various ways. For example, when the sensitized areas of the crystal are exposed to a "reading" laser beam, electrons can escape from the traps and produce photons with near band edge energy [7-10] or the beam can be diffracted by a locally varying refractive index due to variations in space charge [11]. Another effect related to electron trapping in epitaxial GaN and AlN that also has potential to be used for optical data storage systems has been observed.

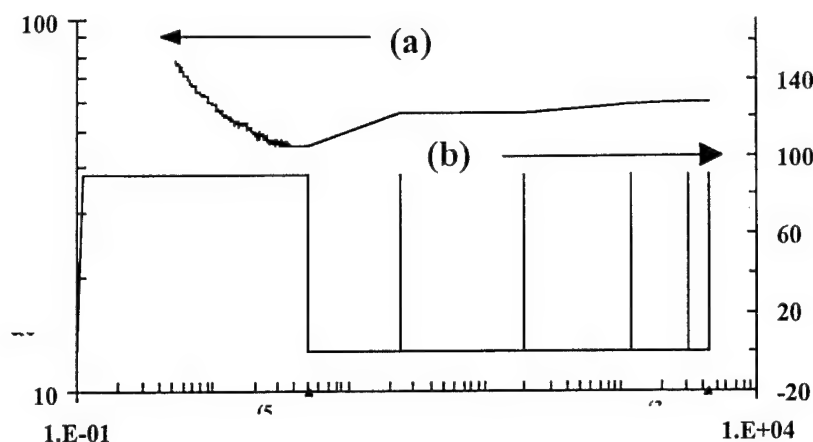
Researchers at NC State University report that the intensity of room temperature (RT) near band edge photoluminescence (PL) of GaN is significantly decreased at areas that have been exposed to a sufficient dose of ultraviolet (UV) radiation, and that this effect can be reversed i.e., "erased" with illumination of these areas with longer wavelength laser light.

The investigated films were grown by atmospheric pressure metalorganic chemical vapor deposition (MOCVD) at 950 °C on (0001) sapphire substrates. Trimethylgallium (TMG, -10 °C) and trimethylaluminum (TMA, +18 °C) were used as the column III sources, ammonia (NH₃, 100%) was used as the column V source, and nitrogen was used as the carrier gas. Following the initial deposition of a ~100 Å AlN buffer layer grown at 700 °C by atomic layer epitaxy (ALE), a ~0.3 mm Al_{0.1}Ga_{0.9}N lower cladding layer and the 1 mm GaN layer were grown at 950 °C. The surfaces of these films have pyramid-like hillocks, that are similar to results of investigations of GaN grown by MOCVD in a nitrogen ambient reported by Sasaki *et al.* [12]. The resistivity of these films have been estimated to be ~1 Wxcm and the films exhibit double crystal x-ray diffraction (DCXRD) rocking curves of the (0002) plane that have a full width at half maximum (FWHM) of ~100 arc sec. This optical memory effect in AlN films grown directly on sapphire by ALE at 700 °C has also been investigated.

The RT PL spectra of these films have been studied using a 10 mW He-Cd laser (325 nm), which was focused to a spot size ~ 100 μm in diameter. The He-Cd laser was used not only for PL excitation but also for longer UV exposures of the sample that induced the optical memory effect. A 4 mW He-Ne laser operating at 632.8 nm with a ~ 1 mm diameter spot size (unfocused) was used to reverse i.e., “erase” the optical memory effect that was induced by the He-Cd laser beam. The samples were mounted on a motorized linear translation stage. For studying the optical memory effect, PL measurements were typically performed by keeping the He-Cd laser beam focused at a fixed position and moving the sample through the beam at a controlled rate, thereby obtaining a spatial record of emitted PL at the near band edge transition energy (~ 3.4 eV for GaN). Conventional PL spectra i.e., intensity vs wavelength, can also be measured with this setup by keeping the sample stationary and scanning the monochromator over wavelength.

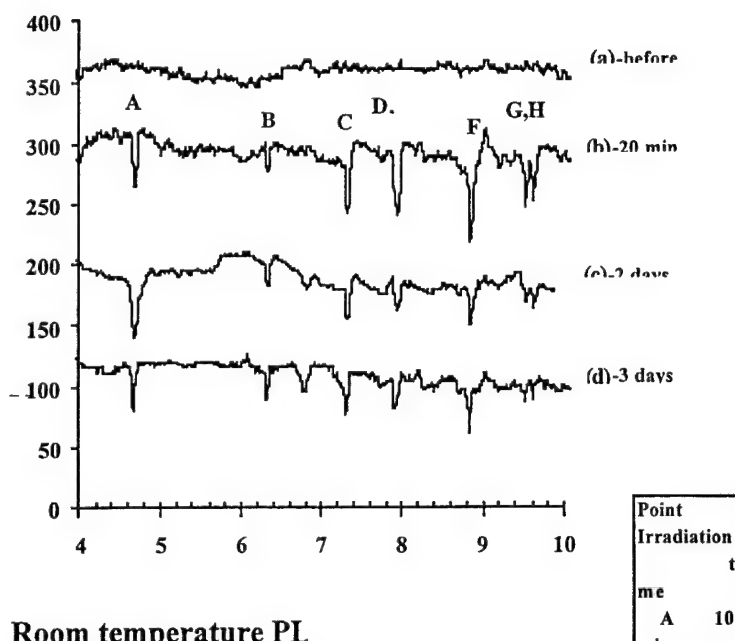
The RT PL spectra of the GaN films exhibits intense near band edge emission at 3.4 eV and very weak yellow emission at 2.3 eV. It has been observed that prolonged UV excitation of some GaN samples results in a marked decrease of their PL emission intensity with time, and this effect persists long after removal of the UV excitation. This memory effect is illustrated in curve a of Fig. 1, which shows the decrease of near band edge (~ 3.4 eV) PL emission intensity versus time of He-Cd laser excitation. Curve b of Fig. 1 illustrates the timing and duration of the sample excitation. The sample was initially illuminated for 5 minutes with the He-Cd laser, and the PL emission decreased appreciably, saturating at an intensity less than half of the initial measured intensity. The ~ 20 second delay of measuring the PL emission (curve a) from the GaN sample is related to the stabilization time of our lock-in amplifier after the initial exposure of the sample to the He-Cd beam. After 5 minutes of irradiation, the He-Cd laser was switched off and the sample was allowed to “recover” at RT in ambient light. The He-Cd laser was switched on to make five more measurements over a 3 day period to measure the PL intensity in the recovering film. The laser was turned on only long enough to obtain a stable reading of PL emission, and then immediately turned back off to minimize further degradation of PL emission intensity. After a three-day period, the PL emission was still not fully recovered with respect to the initial measured intensity.

The long lifetime of the PL intensity recovery in these films constitutes a memory effect that can be used to record information over the areal extent of the material. By exposing selected points to various doses of UV radiation, their subsequent emission to optical excitation can be modulated compared to unirradiated areas. Figure 2 illustrates a demonstration of this concept where 8 points, A - H, all known distances from one another and lying on the same line, have been irradiated by focused He-Cd laser light for durations of 10, 5, 10, 2, 2, 5, 1, and 1 min. respectively. A baseline measurement of PL emission (3.4 eV) was made along this line before



Time dependence of room
temperature PL intensity at

Figure 1. (a) Time dependence of PL emission intensity at 3.4 eV.
(b) Timing and duration of He-Cd laser excitation for the PL measurement of (a).



Room temperature PL
intensity variation

Figure 2. (a) PL emission intensity (@ 3.4 eV) vs. distance along the sample prior to UV "writing" exposure.
(b) PL emission intensity (@ 3.4 eV) vs. distance along the sample immediately after "writing" at points A-H with He-Cd nm laser light for various durations.
(c) PL scan similar to (b) made two days after writing at points A-H.
(d) PL scan similar to (d) made three days after writing at points A-H.

irradiating these points, as shown in curve a, Fig. 2. It should be noted that points D and E are separated by ~ 50 mm, points G and H are separated by ~ 100 mm, while the other points have spatial separations of ~ 1 mm or more. Immediately following the UV exposure of these isolated points, the sample was scanned at a rate of ~ 1.5 mm/min from a location just before point A through point H and PL emission was collected at the near band edge energy of 3.4 eV. The results of this measurement are shown in curve b, Fig. 2 and indicate that the $\sim 20\%$ decrease in PL emission intensity can be effectively "read" at each point of this scan. Subsequent PL scans made after a period of two and three days, as shown in Fig. 2 curves c and d respectively, demonstrate the persistence of this memory effect at RT. Since points G and H (~ 100 mm spacing) can be spatially resolved, while points D and E (~ 50 mm spacing) cannot, our spatial resolution is apparently limited by our He-Cd laser spot size (~ 100 mm). It should also be mentioned that when conventional PL spectra are measured at irradiated points A - H, we observed no shift in peak emission energy (3.4 eV) and no change in the FWHM of the PL spectra.

A preliminary investigation has been made of whether or not longer wavelength radiation has an influence on this optical memory effect. First, a GaN sample (~ 1 mm thick) was written to at two different points, separated by about 150 mm, by exposing the sample to He-Cd laser light. The PL intensity (measured at 3.4 eV) was measured along this linear region to confirm that the PL intensity was diminished at these two points, as shown in Fig. 3, curve a. Next, a 4 mW He-Ne laser (632.8 nm) with a 1 mm (defocused) spot size was used to simultaneously irradiate these two closely spaced points for 30 minutes. Within 3 minutes of the He-Ne irradiation, another linear scan of PL emission intensity was performed that exhibited little apparent change, as shown in Fig. 3, curve b. However, 6 hours after the He-Ne irradiation, a second linear scan of PL emission exhibited a nearly uniform intensity profile, shown in Fig. 3, curve c, indicating that the optical memory effect had been effectively erased.

This optical memory effect has also been observed in a thin AlN film grown by ALE at 700 °C. Because the reduction in PL emission intensity with irradiation time is even more pronounced than in the aforementioned GaN films, a slight variation in our measurement method was used to measure the effect in the AlN film. To avoid overexposing the film and lose the PL signal completely, an initial scan was made by moving the AlN sample through the He-Cd beam at a rate of ~ 1.5 mm/min while acquiring the emission intensity vs wavelength data. This measurement approach limits the UV exposure of each point on the sample to approximately 9 seconds, assuming a laser spot size of 100 mm, and the resulting spectra is displayed in curve a of Figure 4. Curve b of Figure 4 shows the PL emission measured with the sample held at a fixed position during the 10 minute monochromator scan. While both spectra exhibit a deep level peak at ~ 3.1 eV, the second scan with the prolonged UV exposure

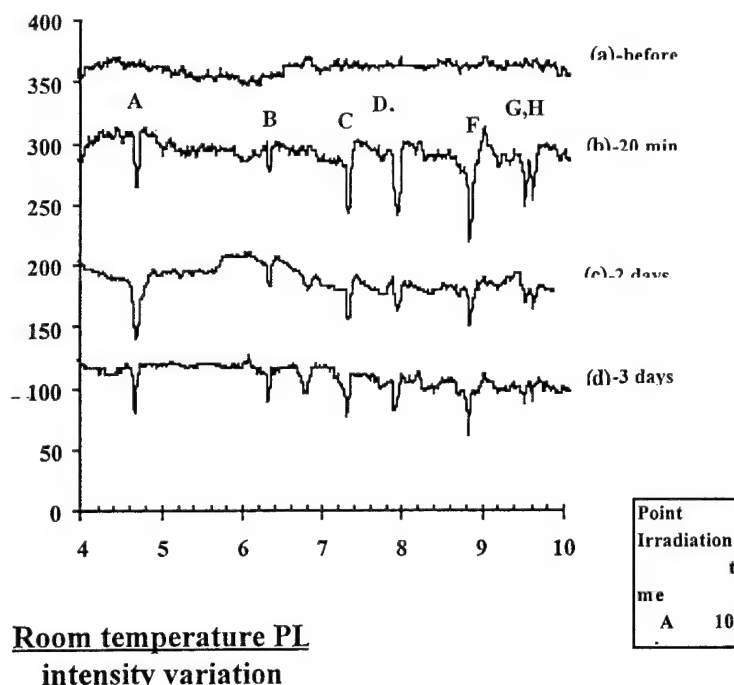


Figure 3. PL emission intensity (@ 3.4 eV) vs. distance along sample:
 (a) After "writing" at two points along the line with He-Cd laser light.
 (b) Three minutes after irradiating the points with He-Ne laser light.
 (c) Six hours after irradiating the points with He-Ne laser light.

is 30 times less intense than that of curve a. The yellow emission at 2.25 eV was not diminished by the prolonged UV exposure. It should be noted that similar deep level emission near 3.1 eV has been observed previously from AlN and been attributed to oxygen impurities [13].

To explain the phenomena we suggest that the effect is related to donor-like states, probably due to oxygen. One of these states is the fundamental state near the conduction band of GaN. The other, charged metastable state (or states) with their accompanied large lattice distortion, can produce nonradiative recombination of excitons [14]. This metastable state can be created from the fundamental state by trapping of an electron during the He-Cd laser exposure. The "lifetime" of this metastable state seems to be long, retaining its charge for days. The increasing of the density of metastable states during He-Cd laser exposure results in the reduction of near band edge emission as shown in Fig. 2. We feel more work is needed to have a better understanding of not only the fundamental nature of these defect levels, but also the role that supposed oxygen impurities and strain have in their creation and their relaxation.

In conclusion, a long term optical memory effect in GaN epitaxial films having structured, grainy surfaces has been observed. This effect has been demonstrated by "writing" at spatially resolved points with UV laser energy and then "reading" these points by monitoring a decrease in near band edge PL emission compared to the unirradiated area between the points.

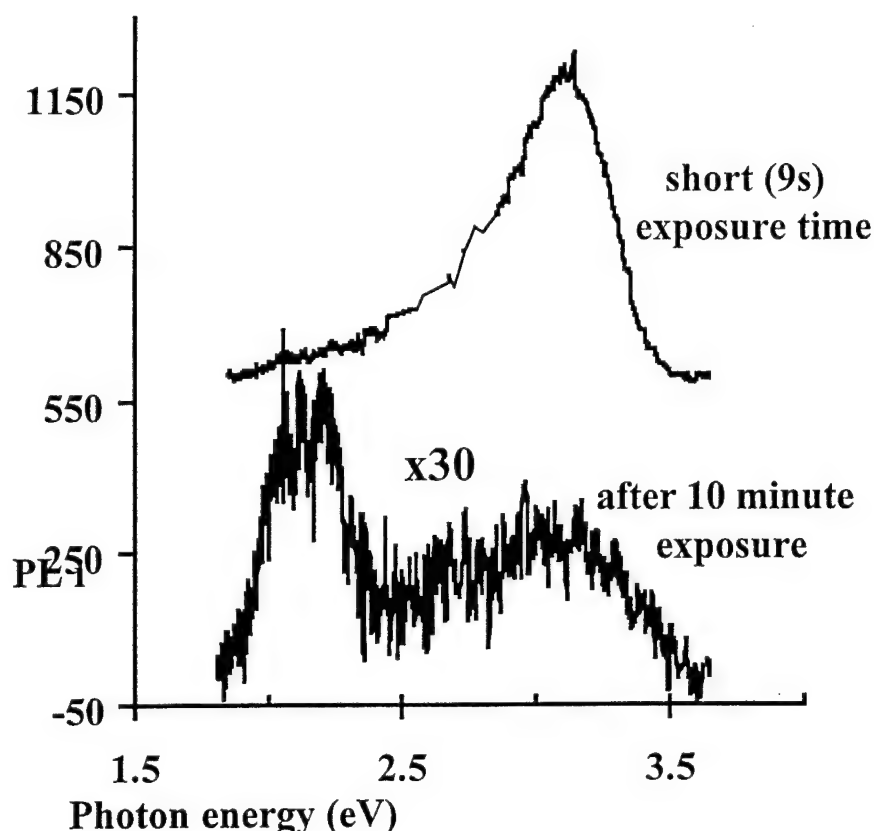


Figure 4. PL intensity vs. wavelength of an ALE grown AlN film:
 (a) Data taken by translating sample at 1.5 mm/min. under the He-Cd laser beam (9 sec. of UV exposure per point).
 (b) "Standard" PL measurement of the same AlN film, where the total exposure time was 10 minutes during the scan at a single point on the film.

Subsequent irradiation of written points with red light appears to erase the optical memory effect after a sufficient delay. The potential applications of this phenomenon toward optical recording of information have been highlighted.

This work has been supported in part by the Office of Naval Research (ONR), University Research Initiative (URI) N00014-92-J-1477.

References

1. R. A. Bartolini, H. A. Weakliem, and B. F. Williams, *Review and Analysis of Optical Recording Media*, Selected Papers on Optical Storage, ed. G. T. Sincerbox and J. M. Zavislan, SPIE Milestone Series MS 42, 488-497.
2. D. Smith, *Magnetic Films and Optics in Computer Memories*, Selected Papers on Optical Storage, ed. G. T. Sincerbox and J. M. Zavislan, SPIE Milestone Series MS 42, 528-547.
3. D. Psaltis and F. Mok, *Scientific American*, Nov. 1995, 70-76.
4. K. A. Rubin and M. Chen, *Progress and Issues of Phase-change Erasable Optical Recording Media*, Selected Papers on Optical Storage, ed. G. T. Sincerbox and J. M. Zavislan, SPIE Milestone Series MS 42, 621-629.

5. E. Udd, Optical Information Processing, ed. S. Jutamulia and J. Tsujiuchi, Part 2, Proc. IEEE, **84**, 884 (1996).
6. S. Jutamulia, G. M. Storti, W. Seiderman and J. Lindmayer, Optical Data Storage Technologies, ed. S.-J. Chua and J. C. McCallum **1401**, 113 (1991).
7. J. Lindmayer, P. Goldsmith and K. Gross, Optical Data Storage Technologies, ed. S.-J. Chua and J. C. McCallum **1401**, 103 (1991).
8. D. T. Brower and R. E. Revay, Optical Data Storage, ed. D. B. Carlin and D. B. Kay **1663**, 867 (1992).
9. S. Chen, C. Qi, F. Dai and F. Gan, 3rd International Symposium on Optical Storage, ed. F. Gan, SPIE **2053**, 114 (1993).
10. J. H. Harris and R. A. Youngman, Wide Band Gap Semiconductors, ed. T. D. Moustakas, J. I. Pankove and Y. Hamakawa, Mat. Res. Soc. Symp. Proc. **242**, 451 (1992).
11. P. Mortensen, Laser Focus World, p. 38, Aug. 1995.
12. T. Sasaki and T. Matsuoka, J. Appl. Phys. **77**, 192 (1995).
13. J. H. Harris and R. A. Youngman, Photoluminescence and Cathodoluminescence of AlN, Properties of Group III Nitrides, ed. J. H. Edgar, EMIS Datareviews Series No. 11, P. 203 (1994).
14. K. J. Malloy and K. Khachaturyan, *Imperfections in III/V Materials* (ed. E. R. Weber), Semiconductors and Semimetals **38**, 235 (1993).

X. Dry Etching of Gallium Nitride

A. Introduction

Gallium nitride (GaN) is a wide band gap semiconductor which has applications such as short wavelength light emitters and detectors, high-temperature, high-frequency, and high-power electronics [1,2]. A crucial step in creating these devices is to etch anisotropic features in the GaN. Wet etching has been employed in many semiconductor processes. Thus far, wet etching has produced poor results on GaN, such as slow etch rate and isotropic etch profiles [3]. Both of these characteristics are undesirable for commercial applications. As technology advances, the need for anisotropic etch profiles increases to accommodate a smaller, more densely packed network of devices. Dry etching is an attractive alternative to wet etching. Varying degrees of anisotropy along with high etch rates can be achieved using different dry etch techniques.

There are four primary dry etch techniques that have been employed on GaN. They are reactive ion etching (RIE), electron cyclotron resonance etching (ECR), magnetron enhanced reactive ion etching (MIE), and inductively coupled plasma etching (ICP). Out of the four techniques, RIE produces the slowest etch rates and lowest degree of anisotropy [4-6]. ECR, which has had much attention from Pearson *et al.* [1,3,7-8], produces significantly better results than RIE. MIE, was employed by McLane *et al.* [2], and produced results comparable to that of ECR etching. ICP is the newest addition to the dry etching techniques of GaN. Shul [9] has shown that ICP can produce etch characteristics similar to that of ECR.

This report discusses recent advances in etching GaN with the three techniques of dry etching. In the following sections, each of the etching techniques will be discussed and compared, along with a discussion of the work on etching GaN and the results to date.

B. Etching Overview

As previously stated, each of the three primary dry etch techniques will be discussed. They will be presented individually, and then compared at the end of this section.

Reactive Ion Etching. As the III-V nitride technology advances, the need for commercially viable processes is getting more important. In this case, a commercially viable etching process would be one that produces the fastest controllable etch rate along with etch profiles that are suitable for the desired electronic device. RIE is lacking in both of these areas. The reason for these shortcomings are the parameters that are involved in the process. RIE is generally performed at pressures between 10 and 100 mTorr [4-6]; at these pressures the mean free path of the bombarding ions is between 5 and .5 mm, respectively. With mean free paths this small, the bombarding ions will hit other ions and scatter. This scattering will result in the ions not hitting the GaN surface at 90° angles, resulting in a lesser degree of anisotropy than is usually

desired. There are some cases where isotropic etch profiles are desired, but for the most part, anisotropic etch profiles are desired.

Etch rate is another area where RIE has fallen behind the other two methods. Lin *et al.* [4] have reported the highest etch rate to date via RIE of 105 nm/min in a BCl₃ plasma. This is actually a fairly high etch rate, but at what cost? The parameters were 15 sccm BCl₃, 10 mTorr pressure, 150 w RF power, and -600 v dc bias. The etch rate is in part a function of the dc self bias and the energy of the bombarding ions is also a function of the dc self bias. As the ion energy increases, there is a better the chance of etch induced damage to the surface of the material. There have been no etch induced surface damage studies on GaN reported to date. Murtagh *et al.* [10] showed via photoreflectance spectroscopy that the larger the dc self bias, the greater the surface damage to GaAs. Even though GaN is a much stronger material than GaAs, it could still undergo the same damage as GaAs, just to a lesser extent.

Electron Cyclotron Resonance Etching . Out of the major types of etching GaN, ECR has the most widespread use in the research field. Shul *et al.* [9] have obtained etch rates of 900 nm/min in a Cl₂/H₂/ Ar plasma using ECR etching. One of the reasons for the high etch rates is that ECR produces a high density plasma, which results in higher etch rates as compared to RIE. The plasma in an RIE is everywhere in the chamber between the source and ground. In an ECR etching system, the plasma is magnetically confined by permanent magnets on the outside of the chamber.

The potential for surface damage to the material is reduced in an ECR etcher. ECR etching uses a microwave source instead of a RF source to produce the plasma, and a separate RF source on the substrate to bias the substrate. Since the microwave source produces a high density plasma, a lower bias is required to etch the material. With a lower dc bias on the substrate, the energies of the ions bombarding the surface of the material are in turn lowered. This reduces the risk of producing etch induced surface damage.

Magnetically Enhanced Reactive Ion Etching. The major difference between RIE and MIE is that the plasma is magnetically confined in an MIE etcher. The magnetic field confines the plasma around the cathode that the sample is on. This in turn increases the etch rate and lowers the dc bias. Along with other things, the dc bias is a function of the surface area of the ground. Since the plasma is confined, the surface area of the ground that the plasma is exposed to is significantly reduced. McLane *et al.* [2] have reported etch rates of 350 nm/min using a BCl₃ plasma which is the highest reported to date.

Inductively Coupled Plasma Etching. A newcomer to etching GaN, ICP has already proven to have much potential as the best etching technique for GaN. Etch rates over 7000Å/min have been achieved by Shul [9] using Cl₂/H₂/Ar chemistries in a commercial ICP system. Like ECR, ICP produces a high density plasma and has a separate RF source on the substrate to control the dc bias. ICP has some distinct advantages over ECR etching, such as better control

of plasma density, higher operating pressures, more economical, and more easily scaled up to production.

The above has been a brief description of the four primary dry etch techniques for GaN. The ICP, ECR, and MIE improve upon three major faults of RIE; namely the slow etch rate, surface damage, and isotropic etch profiles. Table I is a summary of the 4 different etching methods and some typical etching parameters along with the corresponding etch rates.

Table I. Etch Rate Parameters for Dry Etching of GaN

| Maximum Etch Rate (nm/min) | Plasma Gasses | Pressure (mTorr) | Power (watts) | DC Bias (- volts) | Reference |
|----------------------------|--|------------------|-----------------|-------------------|-----------|
| 700 | Cl ₂ /H ₂ /Ar | 1 | 750 | 280 | [9] ICP |
| 900 | NM [#] | 1 | 1000 | 290 | [9] ECR |
| 285 | Cl ₂ /H ₂ /CH ₄ /Ar | 2 | 275 | NM [#] | [11] ECR |
| 110 | Cl ₂ /H ₂ | 1 | 1000 | 150 | [1] ECR |
| 110 | HI/H ₂ /Ar | 1 | 1000 | 150 | [8] ECR |
| 90 | HBr/H ₂ /Ar | 1 | 1000 | 150 | [8] ECR |
| 350 | BCl ₃ | 7 | NM [#] | 100 | [2] MIE |
| 105 | BCl ₃ | 10 | 150 | 231 | [4] RIE |
| 60 | HBr/Ar | 50 | NM [#] | 350 | [6] RIE |
| 50 | SiCl ₄ /Ar | 20 | NM [#] | 400 | [5] RIE |

NM[#] designates a parameter that was not mentioned in the reference.

C. Experimental Procedure

Experimental Apparatus. Figure 1 shows the basic etching setup. It consists of an inductively coupled plasma etcher, gas handling/storage, gas scrubber, optical emission spectrometer, laser reflectance interferometer, and a residual gas analyzer. The etcher consists of a custom designed and built stainless steel chamber with a loadlock, with a water cooled anodized aluminum cathode. A 2000w 13.56 MHz power generator and autotuning matching network provide power to the inductive source antennae for plasma generation. Pressure in the chamber is monitored by an MKS 627A Capacitance Manometer. A Leybold mechanical pump and an Alcatel turbomolecular pump maintain the proper level of vacuum required for processing with a base pressure of 1E-7 Torr.

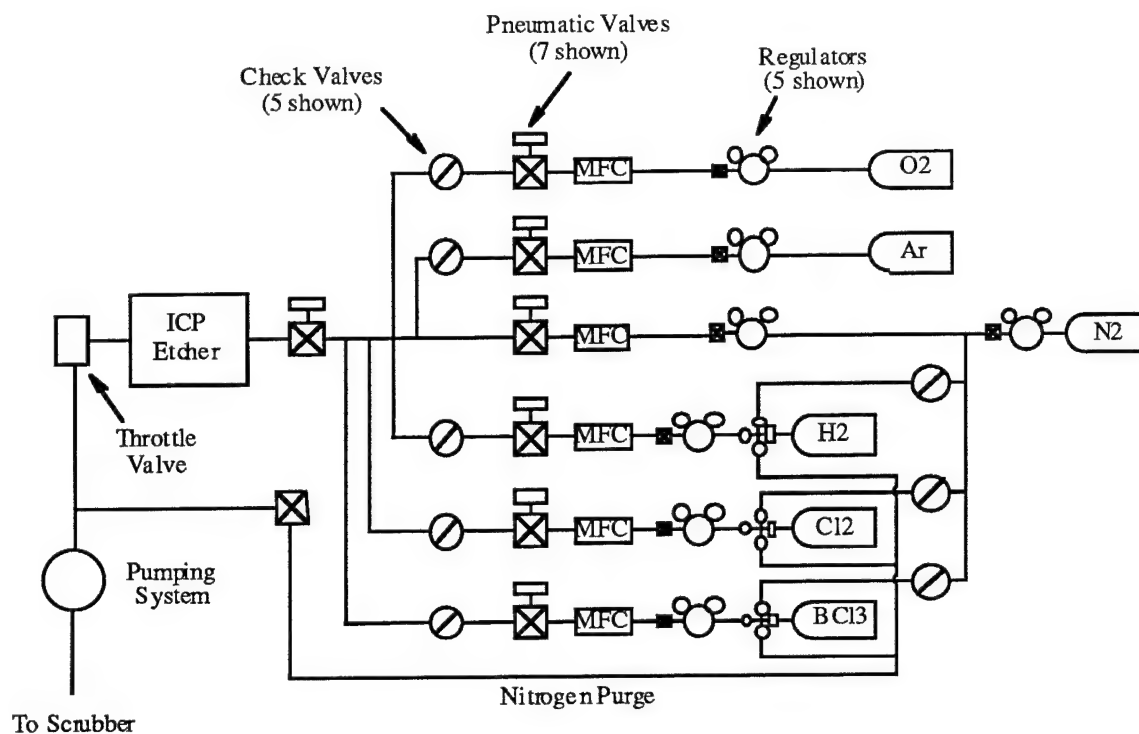


Figure 1. ICP schematic diagram.

Choice of Process Gasses. The gasses that the etching system will be capable of using are BCl₃, Cl₂, H₂, O₂, N₂, and Ar. Chlorides have proven to be effective gasses to etch GaN [1,2,4,8,11].

Etching Procedure. Prior to etching, the samples are masked using JSR 10cp photoresist or nickel. The thickness of the resist must be greater than 1.5 μm due to erosion of the resist. Once patterned, the samples are mounted to an anodized aluminum disk via vacuum grease and inserted into the loadlock. When sufficient vacuum is reached, the disk is loaded onto the waferchuck in the chamber via a magnetically coupled transfer arm. The waferchuck, which is mounted on a z-stage, is then raised into the process zone. Etching is then performed and the sample is removed from the chamber.

The analytical tools that are used to characterize the etch are a profilometer for the step height, an SEM for the slope of the step, AFM for the surface roughness, and AES/XPS to observe the residual gas species on the sample surface. Schottky contacts are also going to be deposited to see how etching affects the barrier height, ideality factor, and leakage current [12].

D. Results and Discussion

The etch selectivity of GaN relative to AlN and Al_xGa_{1-x}N is of significant interest for the fabrication of Al_xGa_{1-x}N based heterostructure devices. One example is the etch penetration through a GaN capping layer to the Al_xGa_{1-x}N recessed gate in a high electron mobility transistor. Etching of the latter material should be minimal. Selective etching was achieved at

low DC biases. The selectivity is plotted in Fig. 2 for GaN relative to $\text{Al}_{1.28}\text{Ga}_{0.72}\text{N}$ and AlN over the range of $-(20\text{--}50\text{ V})$. The selectivity is the ratio of the etch rate of GaN to the AlN or $\text{Al}_x\text{Ga}_{1-x}\text{N}$. At -50 V , the selectivity between GaN and AlN is 8.5; whereas, it is only 1.2 between the GaN and $\text{Al}_{1.28}\text{Ga}_{0.72}\text{N}$. The greatest selectivities for GaN were found at a bias of -20 V , a factor of 38 over AlN and approximately 10 over $\text{Al}_{1.28}\text{Ga}_{0.72}\text{N}$. The difference in etch rates are consistent with the different bond energies between Ga-N and Al-N, 8.92 eV/atom and 11.52 eV/atom respectively. A second factor is the lower volatility of AlCl_x relative to GaCl_x . Since lower DC biases were used to attain the selective etching, there is a tradeoff between the selectivity and the total etch rate.

The strong dependence of the etch rate on DC bias indicates that ion bombardment plays a significant role in the etching of these materials. Ion bombardment can enhance etching via damaging the surface to make it more reactive, stimulating desorption of the etch products, and direct physical sputtering. The existence of a threshold bias indicates that breaking Ga-N or Al-N bonds by ion bombardment may be the rate-limiting step. It is presumed that ion damage increases the reactivity of these ordinarily inert materials. The ion-induced damage may be necessary to form the volatile $\text{GaCl}_x/\text{AlCl}_x$ etch products.

E. Future Research

Optical emission spectroscopy (OES) and mass spectroscopy (MS) studies are underway to determine the underlying mechanisms responsible for the etching of GaN. A comprehensive etch induced damage study is also underway which will utilize Schottky contacts, TEM, AFM, CL, and XPS to quantify the damage.

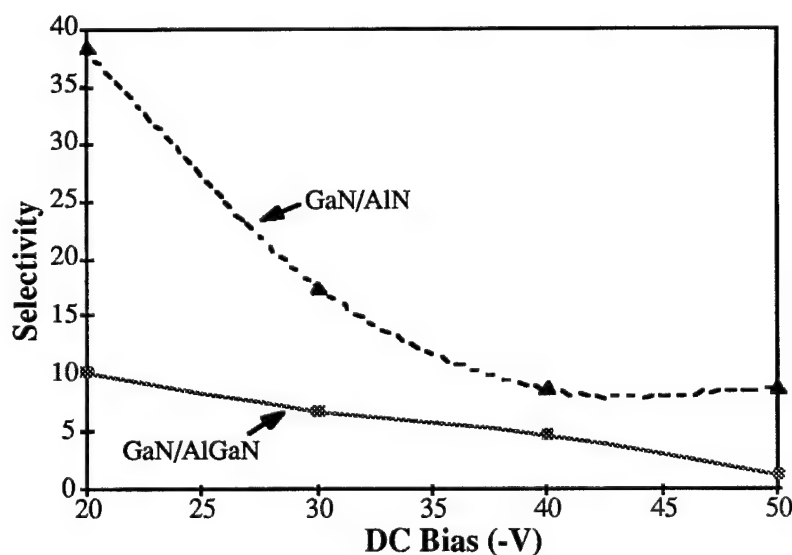


Figure 2. Selectivity.

F. References

1. S. J. Pearton, C. R. Abernathy, F. Ren, Appl. Phys. Lett. **64**, 2294 (1994).
2. G. F. McLane, L. Casas, S. J. Pearton, C. R. Abernathy, Appl. Phys. Lett. **66**, 3328 (1995).
3. S. J. Pearton, C. R. Abernathy, F. Ren, J.R. Lothian, P.W. Wisk, A. Katz, J. Vac. Sci. Technol. A **11**, 1772 (1993).
4. M. E. Lin, Z. F. Fan, Z. Ma, L. H. Allen, H. Morkoc, Appl. Phys. Lett. **64**, 887 (1994).
5. I. Adesida, A. Mahajan, E. Andideh, Appl. Phys. Lett. **63**, 2777 (1993).
6. A. T. Ping, I. Adesida, M. Asif Khan, J. N. Kuznia, Electronics Letters **30**, 1895 (1994).
7. S.J. Pearton, C. R. Abernathy, F. Ren, J. R. Lothian, P. W. Wisk, A. Katz, C. Constantine, Semicond. Sci. Technol. **8**, 310 (1993).
8. S. J. Pearton, C. R. Abernathy, C. B. Vartuli, Electronics Letters **30**, 1985 (1994).
9. R. J. Shul, Presentation Viewgraphs
10. M. Mortagh, P. V. Kelly, P. Herbert, M. O'Connor, G. Duffy, G.M. Crean, Applied Surface Science **63**, 158 (1993).
11. R. J. Shul, A. J. Howard, S. J. Pearton, C. R. Abernathy, C. B Vortuli, P. A. Barnes, M. J. Bozack, J. Vac. Sci. Technol. B **13**, 2016 (1995).
12. G. F. McLane, W. R. Buchwald, Mat. Res. Soc. Symp. Proc. **340**, 221 (1994).

XI. Platinum Schottky Contacts on Etched and Unetched n-type GaN

A. Introduction

In the past few years, there has been a resurgence in the interest of using wide band gap nitride based semiconductors for device applications. One of these wide band gap materials is GaN, which has a band gap of 3.45 eV. This renewed interest in gallium nitride stems from its physical properties such as its excellent thermal and chemical stability. Growth of GaN has improved over the years thanks in part to new and improved substrate materials. As a result, researchers are studying GaN for device applications in high-temperature electronics, optoelectronics, and high-power devices. Device applications mentioned for GaN include blue light emitting diodes, blue lasers, detectors, and high-frequency, high-power and high-temperature transistors. Accordingly, for such devices to be fabricated and marketed, the properties of metal-GaN junctions must be studied. This report summarizes Schottky barrier studies on virgin and etched GaN surfaces.

B. Experimental Procedure

The GaN used for this experiment was grown on a 6H-SiC substrate using a 1000Å thick AlN buffer layer. The orientation of the SiC was (0001) on-axis. Cree Research, Inc. supplied the SiC wafer. Silicon doped GaN film was grown in an OMVPE reactor. Capacitance-voltage techniques were used to measure the doping characteristics of the GaN film. The result of capacitance-voltage testing indicated an electronic doping level ($N_d - N_a$) of $1E17 \text{ cm}^{-3}$. The thickness of the GaN was 2 μm and the size of the samples ranged from 1.5 cm by 1.5 cm for the unetched GaN to .5 cm by .5 cm for the etched samples.

The cleaning for all the samples was identical. First, the samples were degreased in acetone and methanol for one minute each. They were then placed in a HCl bath for 15 minutes to remove oxides. Following the HCl bath, the samples were mounted on molybdenum sample holders and placed into a UHV transfer line system. The transfer line system connected nine different growth and surface characterization chambers. The base pressure of the transfer line was $1E-9$ Torr.

Once in the transfer line, the samples were placed in a 5-target e-beam evaporator. Once in the e-beam, the samples were thermally desorbed at 700°C for 15. It has been shown that the thermal desorption removes the C and most of the O on the surface of the GaN [1].

After the thermal desorption of C and O, a 1000Å-blanket layer of platinum was deposited on the surface of the GaN. The deposition of the Pt occurred while the sample temperature was 23°C. Following the Pt deposition, a two-step photolithography process was employed to fabricate the Schottky diodes. The first step involved spinning photoresist pads covering the Pt not to be etched. The extraneous Pt was etched using a mixture of HCl, HNO₃ and H₂O at

85°C with the ratios 8:1:7, respectively. The Pt etch rate of this compound was about 500Å/minute. The result was an array of cylindrical Pt pads 1000Å thick with diameters of 50, 100, 150 and 200 μm, see Fig. 1. The next processing step involved spinning photoresist to form the Al ohmic contacts. The ohmic contacts were rings surrounding individual Pt Schottky contact pads. The ohmic contacts were fabricated using a process called liftoff. Photoresist was patterned on the GaN/Pt to form annular wells. The GaN surface formed the bottom of the well and the sides consisted of the patterned photoresist. Al was then deposited on the GaN and photoresist. The photoresist was then removed using acetone. The resulting structure contained the Pt Schottky contact pad surrounded by an annulus of Al. The separation distance between the Pt and Al ranges from 10 to 30 μm, Fig. 1.

After the fabrication of the contacts, testing of the samples consisted of collecting electrical data using current-voltage (I/V) techniques. The data collection was achieved by using a computer-controlled Keithley Source Measure Unit Model 236. The unit was connected to the devices by using tungsten probe tips.

C. Results and Discussion

Most of the I/V data collected can be analyzed using thermionic emission theory to find the values of the ideality factor n and the Schottky barrier height ϕ_b . Current-voltage characteristics of a forward biased Schottky diode follow the equation [2],

$$I = I_s \exp\left(\frac{qV}{nkT}\right) \cdot \left[1 - \exp\left(-\frac{qV}{kT}\right)\right],$$

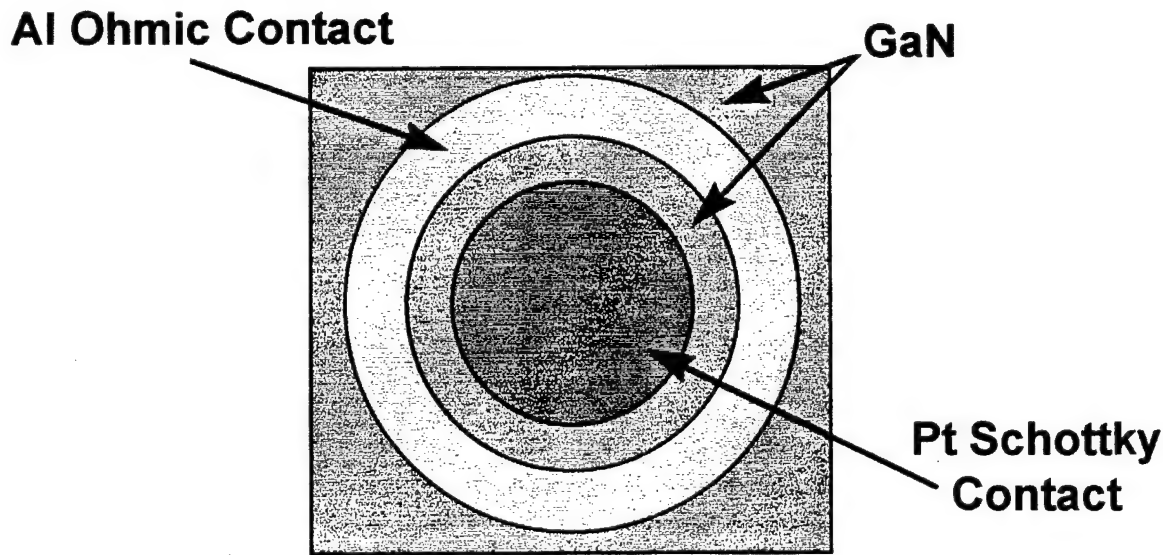


Figure 1. Schottky contact pattern.

where n is the ideality factor, I_s is the saturation current and V is the applied voltage. However, if the voltage is greater than $3kT/q$ (.075 eV), then the equation can be simplified [1],

$$I = I_s \exp\left(\frac{qV}{nkT}\right).$$

The rest of the terms have their usual meanings. The data can be plotted with axes of $\ln(I)$ vs. V for the forward biased values. For high-quality diodes, the resulting plot should have a linear region for low forward voltages [2].

This linear region should span many decades on a semilog plot. By curve fitting this linear region, the ideality factor can be calculated from the simplified equation above. The barrier height ϕ_b can then be determined by using the following equation,

$$I_s = AA^*T^2 \exp\left(\frac{-\phi_b}{kT}\right),$$

where A^* is the Richardson constant for GaN, A is the area of the contact, and T is the temperature and k is Boltzmann's constant. A reported value for A^* is $26.4 \text{ A cm}^{-2} \text{ K}^{-2}$ [3]. The calculated value of ϕ_b from the above equation includes the image force lowering of the barrier.

For the unetched GaN, the calculated barrier height and ideality factor for different-sized Pt contacts are displayed in Table I. For each of the contact sizes, 10 devices were tested with the average results tabulated in Table I. The 50 and 100 μm diameter contacts appeared to have high barrier heights and low ideality factors. These devices were also the most consistent. Out of the ten devices tested, all but one device displayed rectifying behavior. The $\ln(I)$ vs. V plot displayed linear regions that spanned 5 to 6 decades, see Fig. 2. This behavior was consistent for all of the rectifying contacts. The reverse bias leakage currents for all of the working contacts tested were less than -1nA , see Fig. 3. The divergence of the ideality factors from unity is most likely due to recombination in the depletion region [2]. The breakdown for these contacts can be seen in Fig. 4.

Table I. Electrical Characteristics of Pt Schottky Contacts on N-type GaN

| | 50 μm dia contacts | 100 μm dia contacts | 150 μm dia contacts | 200 μm dia contacts |
|--------------------------------|----------------------------------|-----------------------------------|---|-----------------------------------|
| ϕ_b (eV) | 1.09 | 1.01 | 0.92 | .8 |
| Ideality Factor n | 1.13 | 1.13 | 1.5 | 1.9 |
| Leakage Current at -10V (A) | $< -1 \times 10^{-9}$ | $< -1 \times 10^{-9}$ | $< -1 \times 10^{-9}$ to -1×10^{-3} | -6×10^{-3} |

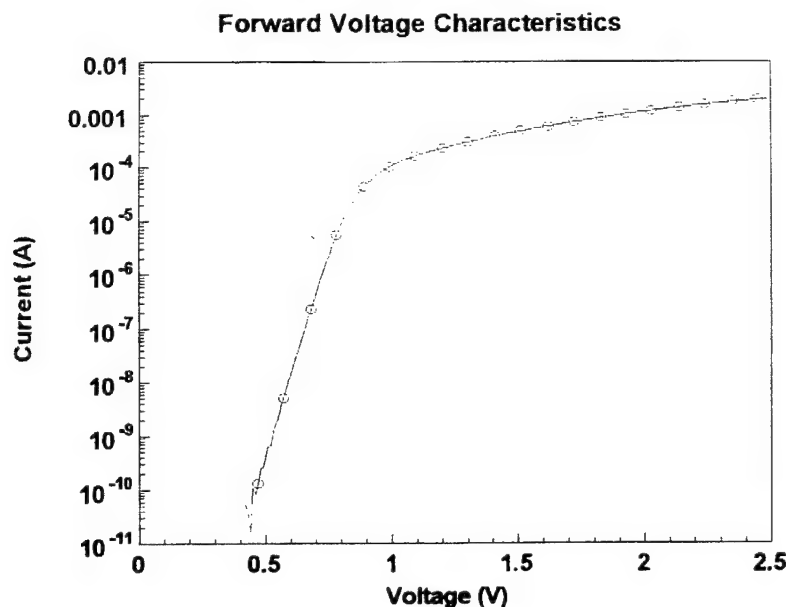


Figure 2. Forward bias voltage characteristics for a 50 μm contact.

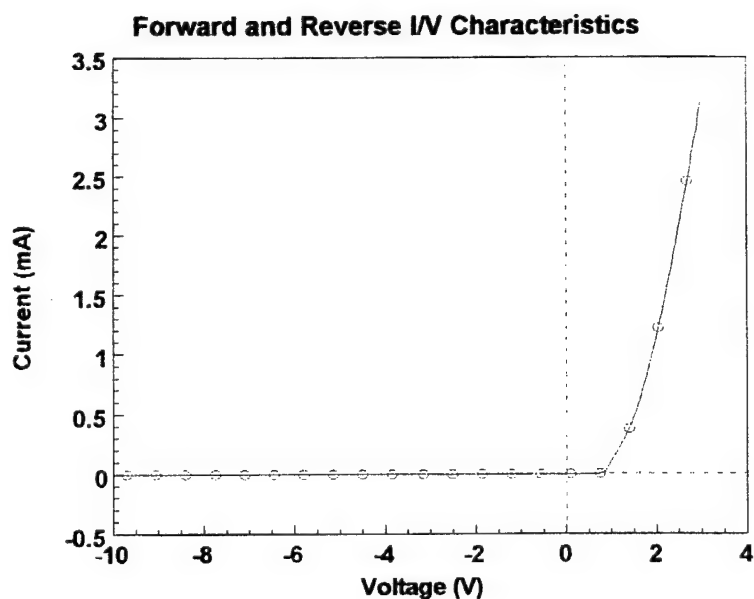


Figure 3. Forward and reverse I/V characteristics for a 50 μm contact.

For the 150 μm contacts, half the contacts tested could be considered good Schottky contacts. They displayed good ideality factors, low leakage currents and high barrier heights, similar to those values for the smaller contacts. However, half the contacts were bad rectifiers. These contacts had higher ideality factor, low barrier heights and were very leaky in the reverse bias region. Meanwhile for the 200 μm contacts, all of the devices tested could be considered

bad Schottky contacts, see Fig. 5. These were extremely leaky with high ideality factors and very low barrier heights. The non-ideal behavior of the larger contacts might be attributed to the high defect density in GaN. It is believed that the defect density of the GaN played a role in the behavior of these contacts.

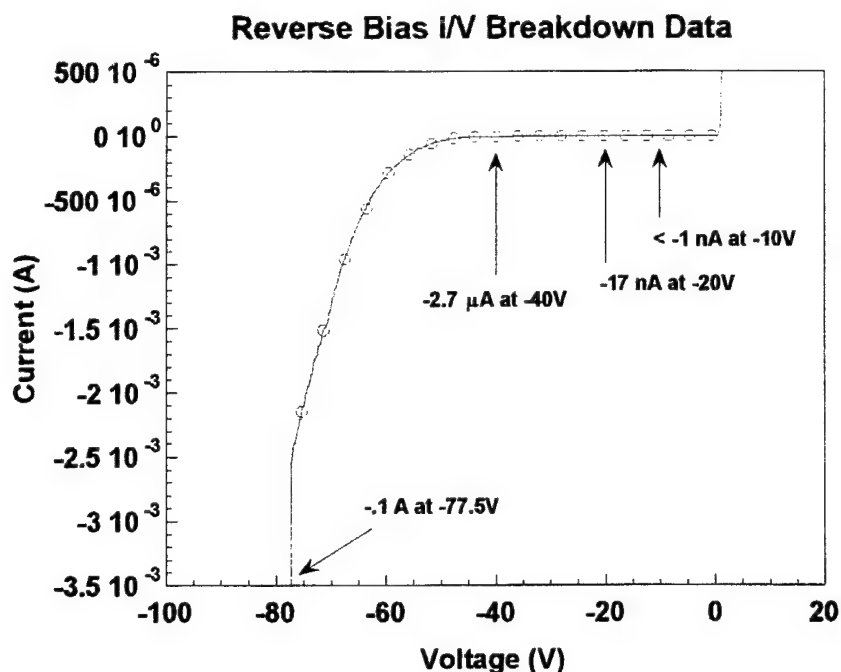


Figure 4. Breakdown of a 100 μm contact.

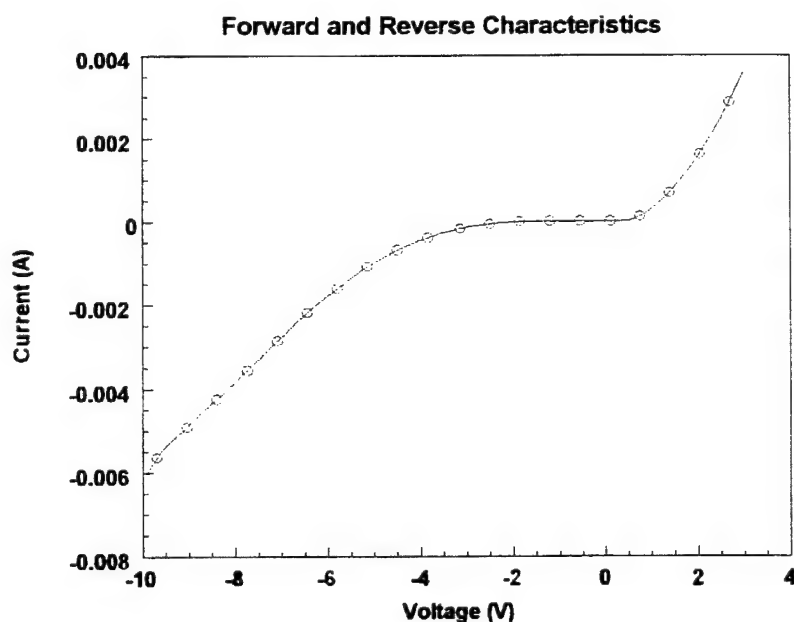


Figure 5. 200 μm diameter contact characteristics.

There were two etched GaN samples used in this study. One of the samples was etched at low power. The etching parameters for this sample were 200W ICP power, 75V DC bias, system pressure of 5 mTorr and etch time of 90 sec. The other sample was etched at high power. Parameters for this sample are the same as the low power sample with the exception of the ICP power, which was set to 500W. The size of the contacts fabricated on these samples were 100 μm diameter Pt contacts surrounded by Al annular rings. The separation distances between Pt and Al were 10 to 30 μm . These contacts are identical to those used on the unetched GaN. Having contacts of only 100 μm diameter was based on the size of the samples.

The Schottky diodes fabricated on the low etch power sample displayed characteristics similar to that of the unetched sample. The average barrier height was around 1.0 eV and the average ideality factor was 1.1. The forward bias characteristics of these diodes are shown in Fig. 6. From the forward bias characteristics, the current was linear on a semilog scale spanning about 7 decades. The reverse current at -10V bias was less than -1nA , which was seen with the unetched material, see Fig. 7. These diodes broke down at lower reverse biases than the unetched material. For the etched GaN, avalanche breakdown was reached at -45V compared to -80V breakdown for the unetched GaN.

For the high-power etched material, the barrier heights and the ideality factors mirrored that of the 150 to 200 μm diameter contacts. The barrier heights were low, 0.8 eV, and the ideality

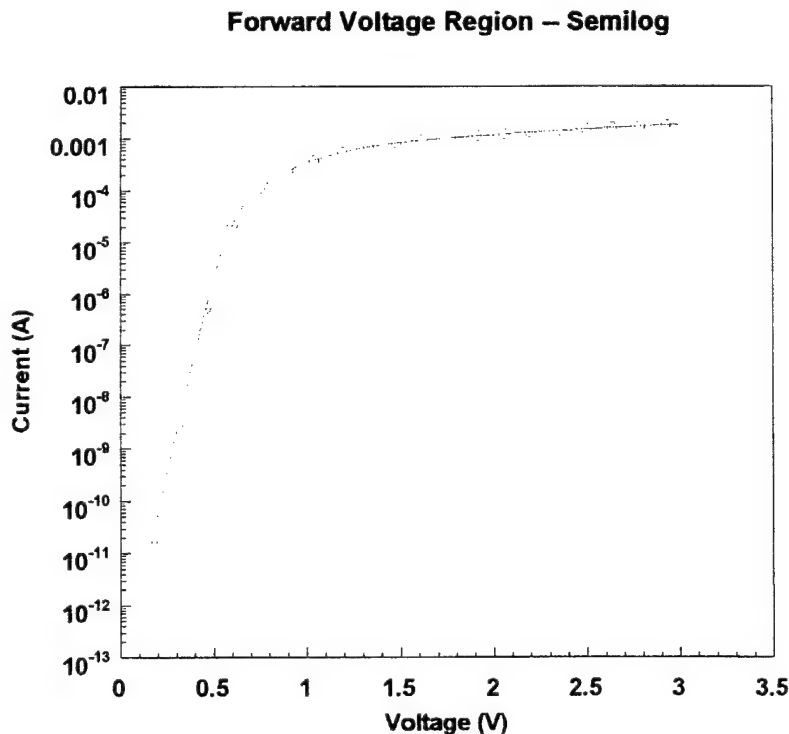


Figure 6. Forward bias of etched GaN Pt Schottky diode.

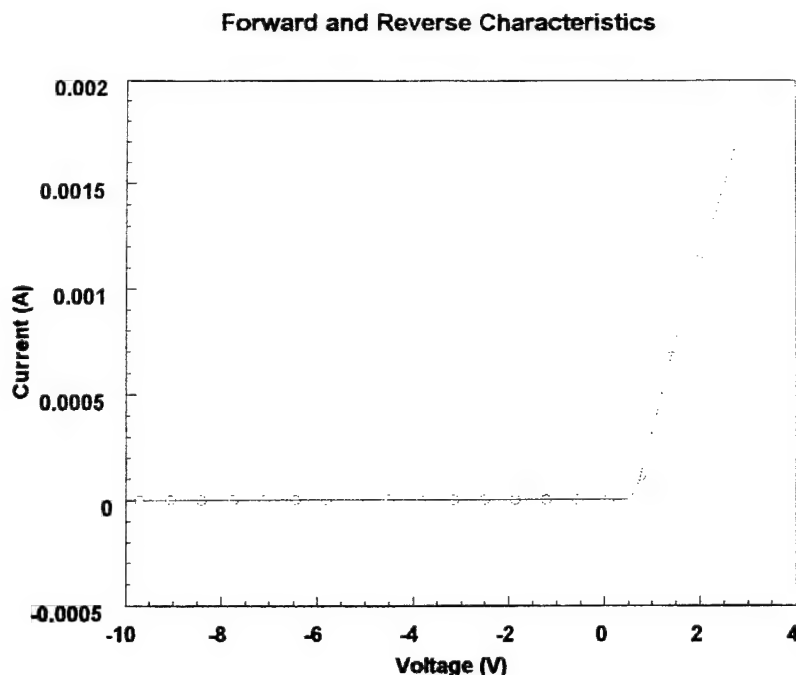


Figure 7. Forward and reverse bias for low power etched GaN.

factors were greater than 1.5. The leakage currents for these devices at -10V reverse bias were in the μA -mA range. Avalanche breakdown occurred between -20 to -25V for these diodes. The high-power etch seems to create electrically active surface defects that effect the rectifying behavior of the Pt on GaN. More experiments are planned to look at the effect of etch power on the rectifying properties of Pt on GaN.

D. Conclusion

Platinum Schottky contacts on unetched and etched GaN were investigated. There was virtually no difference between the Schottky barrier height of low power etched and unetched GaN contacts. The reverse bias currents, however, appeared to be different. The diodes on the unetched material broke down at higher reverse biases than the low power etched material. As for the high-power etched material, these diodes did not display optimal behavior for reverse or forward bias. These contacts were leaky with low barrier height and high ideality factors. More detailed experiments are planned to study in depth the effect of etching in the surface characteristics of GaN.

E. References

1. Sean W. King, Ph.D. Thesis (1997).
2. E. H. Rhoderick and R. H. Williams, *Metal Semiconductor Contacts Second Ed.*, (Oxford 1988).
3. B. L. Sharma, *Metal Semiconductor Schottky Barrier Junctions and Their Applications*, (Plenum 1984).
4. A. T. Ping, A. C. Schmitz, M. Asif Khan and I. Adesida, *Electronic Letters* **29** (1996).

XII. Theory of Group-IV Impurities in Wide Gap Nitrides

P. BOGUSŁAWSKI

Institute of Physics PAN, 02-668 WARSAW

02-668 Warsaw, Poland

E-mail: bogus@ifpan.edu.pl

and

J. BERNHOLC

Dep. of Physics, NC State University, Raleigh, NC 27695-8202, USA

ABSTRACT

Doping properties of substitutional C, Si, and Ge impurities in hexagonal GaN and AlN were studied by quantum molecular dynamics. Si and Ge are effective-mass donors, and C is an effective-mass acceptor. However, under certain conditions of growth, doping efficiency of these impurities is severely limited by self-compensation and formation of nearest-neighbor pairs.

1. Introduction

Wide band-gap nitrides are of considerable interest due to possible applications in blue/UV light-emitting diodes and lasers.^{1,2} To exploit fully the potential of these materials, understanding and control of doping needs to be achieved. In the present work we study substitutional group-IV impurities ($X=C$, Si, and Ge) in wurtzite GaN and AlN. We have recently shown that C_N is a promising effective-mass acceptor in GaN, and somewhat deeper in AlN, while C_N is an effective-mass donor in GaN, and a deep one in AlN.³ Si and Ge on the cation site are effective-mass donors, but are deep acceptors (with energy levels at about 1.3 eV above the valence band top) in both GaN and AlN.⁴ However, the doping efficiency of Si and Ge in AlN is quenched due to the stability of DX^- states.⁴ Here, we focus on the problem of self-compensation by the dopant itself, *i.e.*, its simultaneous incorporation on both the cation and anion sublattices. This may severely limit its doping efficiency. The tendency towards self-compensation may be further increased by the formation of donor-acceptor pairs, studied in the last part of this paper. The calculations were performed using quantum molecular dynamics,⁵ with atoms moving according to Newton equations.⁶ Soft pseudopotentials for N and C were used,⁷ which allowed for a relatively low plane wave cutoff of 30 Ry. The pseudopotential of Ge was generated according to Ref. 7. Large supercells, corresponding to 72 atoms in the perfect crystal, were used. Other

details may be found in Ref. 3.

2. Formation energies and compensation effects

The concentration of an impurity at thermodynamic equilibrium is given by

$$[conc] = N_{sites} \exp(S_{form}/k_B - E_{form}/k_B T), \quad (1)$$

where N_{sites} is the concentration of atomic sites and S_{form} is its formation entropy, which typically assumes a value of about $6 k_B$. The formation energy of, *e.g.*, Si in GaN in the charge state q is⁹

$$E_{form}(q) = E_{tot}(q) - n_{Ga}\mu_{Ga} - n_N\mu_N - \mu_{Si} + qE_F, \quad (2)$$

where E_{tot} is the total energy of the supercell with the impurity, n_{Ga} and n_N are the numbers of Ga and N atoms in the supercell, μ is the chemical potential, and E_F is the Fermi energy. The chemical potentials depend on the source of atoms involved in the process, and therefore on the actual experimental situation. The highest possible concentration of a given dopant is obtained for its lowest formation energy, *i.e.*, for the highest chemical potential of the source of dopant atoms. For C doping, we have assumed that the source is an elemental solid, *i.e.*, diamond. For Si and Ge doping, we have also taken into account the possible formation of Si_3N_4 and Ge_3N_4 alloys.

Table 1. Calculated formation energies (in eV) for cation-rich and N-rich conditions.

| dopant | cation-rich | N-rich |
|-----------|-------------|--------|
| GaN | | |
| C_{Ga} | 5.7 | 4.0 |
| C_N | 1.1 | 2.8 |
| Si_{Ga} | 1.6 | 2.0 |
| Si_N | 4.4 | 7.0 |
| Ge_{Ga} | 1.6 | 1.8 |
| Ge_N | 3.1 | 5.5 |
| AlN | | |
| C_{Al} | 5.2 | 1.9 |
| C_N | 0.4 | 3.7 |
| Si_{Al} | 2.7 | 2.0 |
| Si_N | 5.1 | 11.0 |
| Ge_{Al} | 3.4 | 1.4 |
| Ge_N | 4.1 | 8.7 |

The calculated formation energies are given in Table 1.¹⁰ They were obtained using experimental heats of formations of the considered compounds. As follows from the Table, C is preferentially incorporated on the anion sublattice, while both Si and Ge

substitute for cations. These results are simply explained by the presence of excess strain energy when the mismatch between the host and the impurity atom is large.

The values quoted in Table 1 are for neutral impurities. Formation energies of charged impurities may be reduced by electron transfer to/from the Fermi level according to Eq. (2). Since the energy gain may be of the order of the band gap (equal to 3.5 eV for GaN, and 6.5 eV for AlN), electron transfer effects may overcome the strain-driven preference of the impurity to substitute for the component of the similar size. Consequently, the self-compensation of the dopant by itself becomes possible, depending on the conditions of growth.

As it follows from Table 1, for Si and Ge doping under N-rich conditions, the difference of formation energies between X_N and X_{cation} exceeds the value of the band gap. Thus, in this limit, the strain-driven effects are dominant, the concentration of X_{cation} is always higher than that of X_N , and the self-compensation is negligible. These growth conditions should lead to the highest efficiencies of n -type doping with Si and Ge. Analogous arguments hold for doping of GaN with carbon, which under cation-rich conditions is a non-self-compensated acceptor. However, under the opposite conditions of growth, *i.e.*, in the cation-rich limit for Si and Ge, and N-rich limit for C, self-compensation may play a dominant role. In all the considered cases, with the exception of GaN:Si, a value of the Fermi level exists for which $E_{form}(X_{cation}^+)$ is equal to $E_{form}(X_N^-)$, and strong self-compensation effects are likely.

3. Formation of NN donor-acceptor pairs

The self-compensation can be further increased by the formation of donor-acceptor nearest-neighbor (NN) pairs. The concentration of NN pairs is given by Eq. (1), with N_{sites} in the low solubility limit being four times bigger than that for point defects, and the formation energy is

$$E_{form}(XX) = E_{form}(X_{cation}^+) + E_{form}(X_N^-) + E_{pair}, \quad (3)$$

where E_{pair} is the binding energy of the pair, relative to ionized distant X_{cation}^+ and X_N^- . According to our results, the coupling between a second-neighbor, or a more distant pair is essentially the Coulomb interaction between two point charges embedded in a medium with the appropriate dielectric constant. However, the coupling of a NN pair deviates from the purely Coulombic character. The additional short-range interaction is $E_{sr} = E_{pair} - E_{Coul}^{NN}$, where E_{Coul}^{NN} is the Coulomb energy of pair of point charges separated by the theoretical NN distance.

The calculated pairing energies E_{pair} are about 1 eV, see Table 2. This is higher than the Si-Si binding in GaAs,^{11,12} due to a smaller NN distance and a smaller dielectric constant. The additional short-range coupling ranges from -0.15 eV for a Si-Si pair in GaN to -0.65 eV for a Ge-Ge pair in AlN (which is 50 % of the binding energy).

The concentration of NN pairs may be estimated based on the results from Tables 1 and 2 and the energy levels of impurities. The pairing of C is negligible in GaN, but can be important in AlN. For Si in both GaN and AlN, the concentration of NN pairs is much smaller than $[Si_{cation}]$ independently of the conditions of growth. For Ge in GaN, the pair concentration may be close to $[Ge_{Ga}]$ in the cation-rich limit, but is negligible in the N-rich limit. In AlN, the concentration of Ge-Ge pairs is close to that of isolated Ge independently of the growth conditions.

This work was supported in part by Grants KBN 2-P03B-178-10, NSF DMR 9408437, and ONR N00014-92-J-1477.

4. References

1. R. F. Davis, *Physica B* **185**, 1 (1993).
2. H. Morkoc *et al.*, *J. Appl. Phys.* **76**, 1363 (1994).
3. P. Bogusławski, E. L. Briggs, and J. Bernholc, *Appl. Phys. Lett.* July (1996).
4. P. Bogusławski and J. Bernholc, *Acta Phys. Polonica*, in print (1996).
5. R. Car and M. Parrinello, *Phys. Rev. Lett.* **55**, 2471 (1985).
6. C. Wang, Q.-M. Zhang, and J. Bernholc, *Phys. Rev. Lett.* **69**, 3789 (1992).
7. G. Li and S. Rabii, unpublished (1992).
8. X. Gonze, R. Stumpf, and M. Scheffler, *Phys. Rev. B* **44**, 8503 (1991).
9. S. B. Zhang and J. Northrup, *Phys. Rev. Lett.* **67**, 2339 (1991). C. G. Van De Walle, D.B. Laks, G. F. Neumark, and S. T. Pantelides, *Phys. Rev. B* **47**, 9425 (1993).
10. Our results for C_{Ga} and Si_{Ga} are reasonably close to those of J. Neugebauer and C. Van de Walle, in *Proc. 22 Int. Conf. Phys. Semicond. Vancouver 1994*, p. 2327, ed. D.J. Lockwood (World Scientific 1995).
11. J. E. Northrup and S. B. Zhang, *Phys. Rev. B* **47**, 6791 (1993).
12. B. Chen, Q.-M. Zhang, and J. Bernholc, *Phys. Rev. B* **49**, 2985 (1994).

Table 2. Binding energies E_{pair} and short-range interaction energies E_{sr} for nearest-neighbor pairs.

| | E_{pair} (eV) | E_{sr} (eV) |
|-------|-----------------|---------------|
| GaN | | |
| C-C | -1.1 | -0.2 |
| Si-Si | -0.8 | -0.15 |
| Ge-Ge | -1.1 | -0.4 |
| AlN | | |
| C-C | -1.3 | -0.4 |
| Si-Si | -0.9 | -0.2 |
| Ge-Ge | -1.3 | -0.65 |

XIII. Ion Implantation of N- and P-type Dopants Into GaN

A. Introduction

The control of the electrical properties of the III-V nitride semiconductors is a major obstacle in the development of these materials for use in optoelectronic and microelectronic devices. To date, the majority of the research has been concentrated on the growth of the material with the desired properties, while very little research has been performed on post growth processing to achieve the desired electrical properties. One post growth processing method that is widely used in the semiconductor industry but that has gotten little attention concerning the III-V nitrides is ion implantation. Ion implantation is a convenient method to incorporate electrically active dopants into the host crystal, post growth, using a highly energetic beam of ions that strike and penetrate into the crystal. This method allows for a precisely controlled amount of impurity to be introduced into the crystal independent of the solubility of the impurity. The major drawback of this method is the enormous amount of damage that is induced on the host crystal due to the kinetic energy of the impinging ions.

The most comprehensive study of ion implantation in the nitrides is the historic work of Pankove and Hutchby [1,2]. In this article, 35 ion species were implanted into gallium nitride and the photoluminescence was reported. It was found that Mg, P, Zn, Cd, Ca, As, Hg, and Ag were the only ion species that gave a characteristic photoluminescence signature with Zn being the most efficient radiative center. The other ions all showed a broad peak around 2.15 eV which is thought to be implantation induced and a peak around 1.75 eV which is believed to be due to the annealing treatment as it was seen in the control sample after annealing. Wilson *et al.* performed a more recent study of Er-implanted GaN and AlN [3]. The Er^{3+} was coimplanted with oxygen and showed optically excited 1.54-micron luminescence. In both these studies, data on the electrical behavior of the material was not given.

Wilson *et al.* in another study, implanted several key elements for the purpose of studying the distribution of the implanted species in the nitride films [4]. The ions implanted were Be, C, Mg, Zn, Si, S, Ge, and Se. Wilson *et al.* found that in most cases the distribution followed a Gaussian behavior. Also Wilson *et al.* studied the redistribution of the implanted species in the films with a post implantation anneal. It was found that even with anneals up to 900°C, the distribution of the implanted species did not change except for S which started to redistribute above 600°C and for Zn and Se which redistributed above 800°C. Again, data on the electrical behavior of the material was not given.

Very little work has been presented on the electrical characterization of the implanted layers. Rubin *et al.* were the first to show, by hot-probe tests, P-type material upon implantation of Mg into intrinsic GaN. This was the first paper to deal with the electrical behavior of the implanted films. The film had a resistivity of 4 Ω/cm [5]. Binari *et al.* reported on the

implantation of H, He, and N to produce semi-insulating GaN. The He implant produced films with as-implanted resistivities as high as $10^{10} \Omega\text{-cm}$. This implanted material remained highly resistive after annealing up to 800°C . N also produced resistive GaN, after an anneal at 400°C . H samples were highly resistive upon implantation but after an anneal at 300°C , the resistivity dropped to less than $10 \Omega\text{-cm}$ [6]. Pearton *et al.* performed a detail study of the electrical behavior of implanted GaN. In this study, activation of both an n- and p-type dopant were achieved. Si^+ was implanted for n-type while Mg^+/P^+ was implanted for p-type. The dopants became activated, 93% for Si and 62% for Mg, after an anneal at $\sim 1100^\circ\text{C}$ [7]. This shows that post growth processing of the GaN can be used to achieve the desired electrical properties for the material.

B. Experimental Procedure

Gallium nitride was grown by MOCVD on $\alpha\text{-SiC}$ substrates. Several ions were investigated for ion implantation and electrical activation in the GaN films and included Si, Mg and Ca/P. The ions were Si, for N-type; Mg, for P-type; and Ca/P for P-Type. The energies, doses, and temperature of the implants are shown in Tables I and II.

Table I. Implantation at Oak Ridge

| Ion (Species, Mass) | Energy (keV) | Dose (cm^{-2}) | Implant Temp. ($^\circ\text{C}$) |
|------------------------|-----------------|------------------------------|---------------------------------------|
| Si,29 | 160 | $1\text{e}14$ | RT |
| Si,29 | 160 | $5\text{e}14$ | RT |
| Si,29 | 160 | $1\text{e}15$ | RT |
| Si,29 | 160 | $1\text{e}14$ | 500 |
| Si,29 | 160 | $5\text{e}14$ | 500 |
| Si,29 | 160 | $1\text{e}15$ | 500 |
| Mg,24 | 120 | $5\text{e}14$ | RT |
| Mg,24 | 120 | $1\text{e}14$ | 500 |
| Mg,24 | 120 | $5\text{e}14$ | 500 |
| Mg,24 | 120 | $1\text{e}15$ | 500 |
| Ca,20/P,15 | 180/130 | $5\text{e}14$ | RT |
| Ca,20/P,15 | 180/130 | $5\text{e}14$ | 550 |
| Ca,20/P,15 | 180/130 | $1\text{e}15$ | 550 |
| Ca,20/P,15 | 180/130 | $4\text{e}15$ | 550 |

Table II. Implantation at Kroko

| Ion (Species, Mass) | Energy (keV) | Dose (cm ⁻²) | Implant Temp (°C) |
|------------------------|-----------------|-----------------------------|----------------------|
| Si,29 | 200 | 1e14 | RT |
| Si,29 | 200 | 1e15 | RT |
| Si,29 | 200 | 1e14 | 650 |
| Si,29 | 200 | 1e15 | 650 |

Capacitance-voltage measurements, Hall measurements, Rutherford backscattering spectrometry/channeling (RBS/C), secondary ion mass spectrometry (SIMS), and photoluminescence (PL) were performed on the samples after the implantation. The samples were then annealed at 900°C, 1100°C, and 1200°C and characterized again using C-V measurements, Hall measurements, PL and RBS/C. The Oak Ridge implanted samples were annealed in an RTA furnace under flowing N₂ at atmospheric pressure while the Kroko implanted samples were annealed in a SiC-resistance heated boat in a vacuum system that was pumped down to 10⁻⁵ Torr then backfilled with N₂ to atmospheric pressure. The cross-sectional TEM samples were made after implantation by cutting two pieces of the specimen and gluing them together face to face. Two Si support pieces were also glued to the outside of the specimen sandwich. The sample was then ground down, polished, dimpled, and ion milled as described in [8] to get a proper TEM sample. The specimens were then imaged using a TOPCON EM0002B electron microscope and a Philips CM200 FEG.

C. Results and Discussion

The electrical characterization, performed by C-V measurements and Hall measurements, showed that activation of the species was not achieved as implanted. The samples were too resistive to measure in the as-implanted state. This result was expected as Pearton, *et al.* had to anneal the implanted species greater than 1050°C in order to achieve activation [7].

As seen in Fig. 1, the depth of the peak Si concentration, determined by SIMS, in the implanted samples was around 1600Å. This is approximately the same as was predicted by TRIM simulations which predicted a peak at 1639Å. The Si profile was approximately Gaussian near the peak in the concentration. However, the implanted samples exhibited a "tail" in the profile as compared to the TRIM profiles which were strictly Gaussian. The peak Si concentration was lower than was predicted by the TRIM Gaussian profile.

Figure 2 shows that the Si and Mg implantation exhibited no damage, seen by RBS/C, as compared to a virgin GaN sample. This was unexpected as the high doses ($1e15 \text{ cm}^{-2}$) would have caused considerable damage in other semiconductor materials (i.e. Si and GaAs).

For the Ca/P ions, small damage was seen after implantation with the largest damage being present in the samples with the largest dose of $4e15 \text{ cm}^{-2}$, as is seen in Fig. 3. Damage was expected at this dose level. However, the relative amount of damage in this material is much lower than in other semiconductor materials. No amorphization was seen by RBS/C, even at the high dose levels.

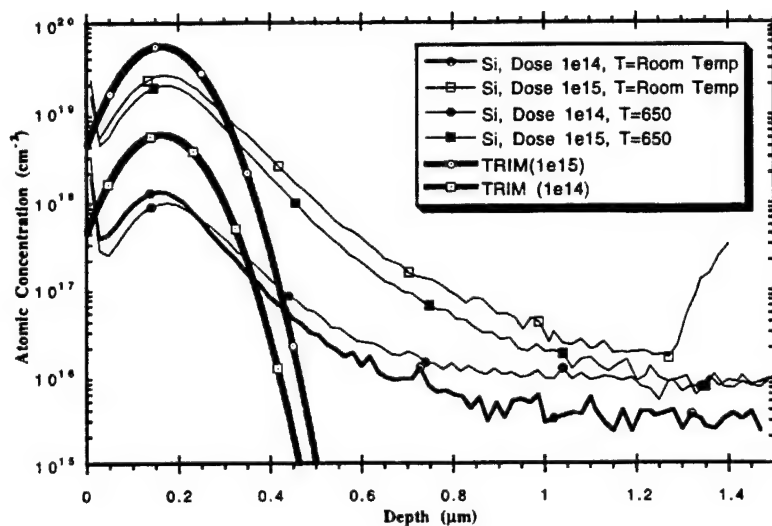


Figure 1. SIMS of Si samples implanted at 200 keV at various temperatures and doses.

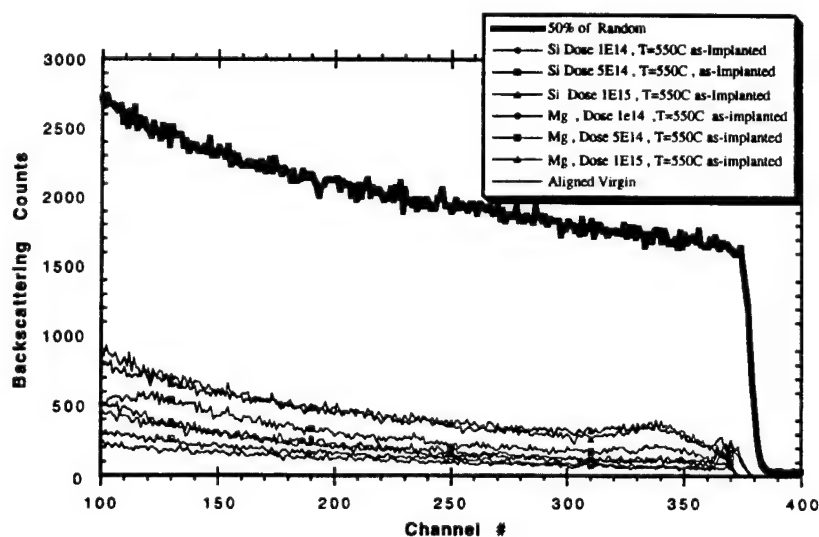


Figure 2. RBS/C of Si and Mg samples implanted at 550°C at various doses.

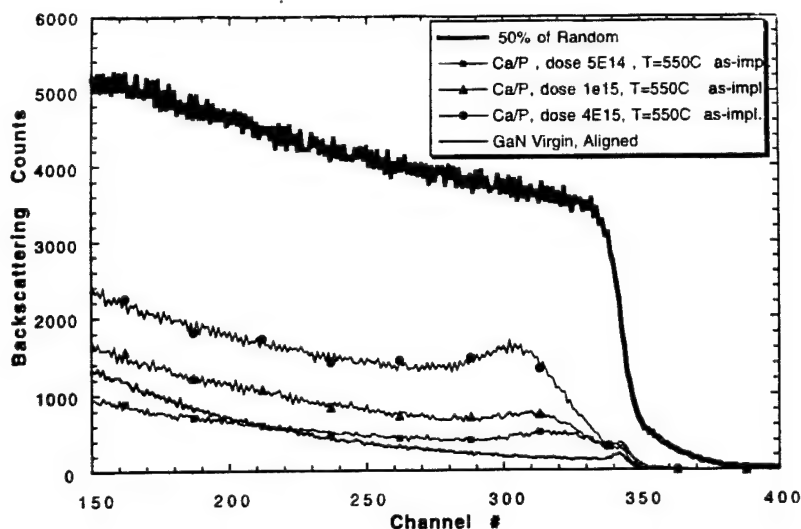


Figure 3. RBS/C of Ca/P samples implanted at 550°C at various doses.

The PL spectra showed that no emission was detected from the implanted regions of the samples even at the lowest dose. This was in contrast to the band edge emission that was observed on the same samples in the regions that were not implanted due to the clip used to mount the samples in the implanter. This implies that enough damage occurred to put a large density of optical states in the band gap that when excited, did not give off photons. The PL results imply damage which is contrary to the RBS/C results.

All cross-sectional TEM images were taken in a $[11\bar{2}0]$ orientation. Figure 4 shows a cross-sectional TEM image of GaN implanted with Mg at 550°C at a dose of $1e15 \text{ cm}^{-2}$. As can be seen, there is a distinctly damaged area near the top surface of the film which is $\sim 275 \text{ nm}$ thick.

Figure 5 shows an enlarged image of this damage layer where the damage can be seen clearly. Figure 6 shows a cross-sectional TEM image of GaN implanted with Si at 550°C. There is a damaged area near the top surface of the film which is $\sim 295 \text{ nm}$ thick. Again the damaged area can be seen clearly and can be distinguished from the undamaged area.

Figures 7 and 8 show high resolution TEM (HRTEM) images of GaN implanted with Mg at 550°C. Figure 7 is from an undamaged region of the GaN film while Fig. 8 is from a region of the GaN damaged by the implantation process. The arrows in Fig. 8 indicate areas of potential damage.

The arrows point to areas of possible implantation damage. The exact nature of the damage, however, could not be determined using HRTEM. The damage can clearly be seen in low resolution TEM images but upon raising the magnification, the damage is no longer distinguishable.



Figure 4. Mg implanted GaN film. The implant damage layer is ~275 nm thick.

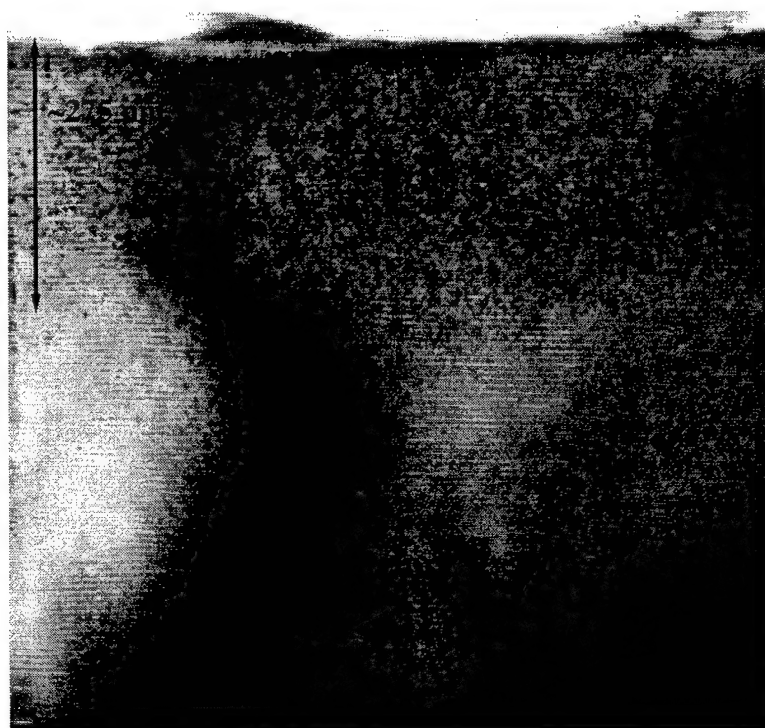


Figure 5. TEM image of damaged layer in a Mg implanted GaN film.

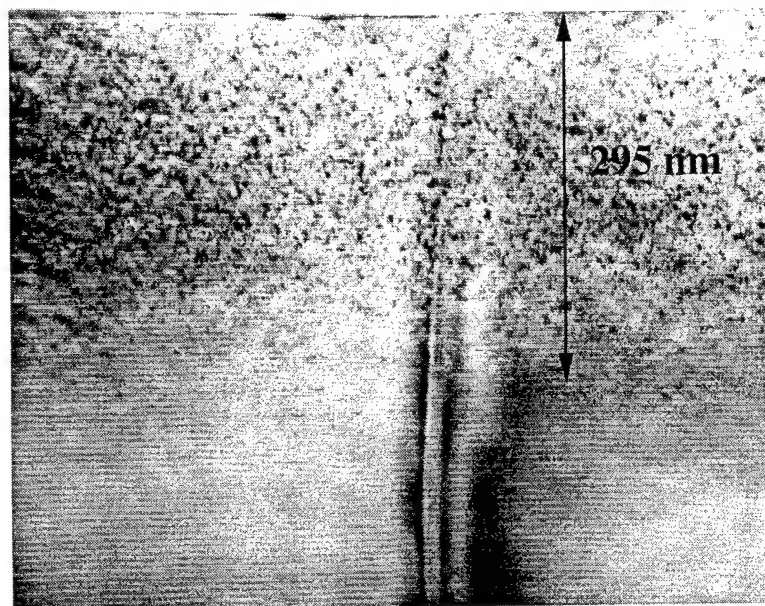


Figure 6. GaN film implanted with Si at 550°C.

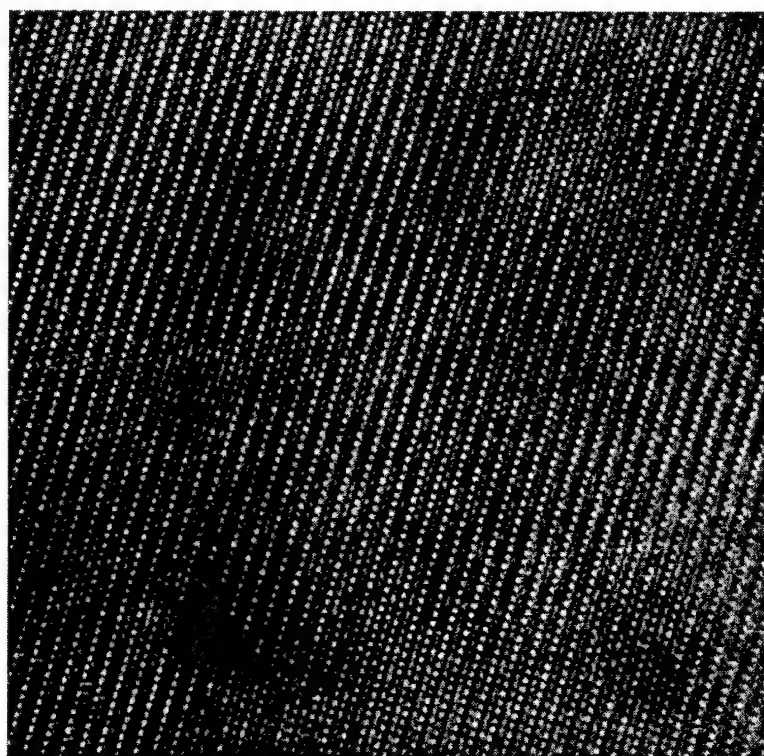


Figure 7. HRTEM of undamaged GaN layer.

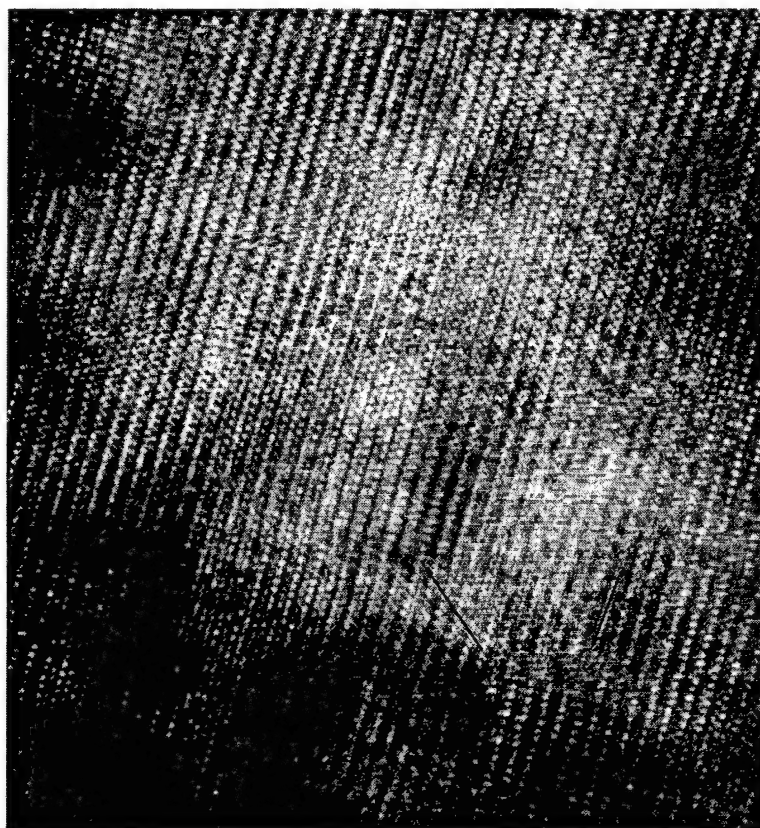


Figure 8. HRTEM of damaged region in Mg implanted GaN.

The implantation damage area observed in Figs. 4, 5, and 6 was similar to damage observed in ion-implanted silicon [9,10,11]. The implantation process damaged the top surface of the GaN film at both RT and 550°C, but a completely amorphous region was not formed. This result indicates that the implantation dose was not high enough to cause complete amorphization of the implanted region [9], but was high enough to either cause small “packets” of amorphous regions in the damaged layer or form point defects (vacancies and interstitials) in the damaged region. The TEM images showed a damaged area at the surface of the implanted sample. This result does not correlate well with RBS/C.

Upon annealing the samples to 900°C for 60 sec., no electrical activation of the species was seen for Si or Mg. The PL spectrum did not show emission from the implanted regions of the samples. A 30 second 1100°C RTA anneal was performed on the Oak Ridge implanted samples. These samples were annealed in a face-to-face orientation with a virgin GaN sample in flowing N₂ at atmospheric pressure. The surface of the samples degraded at this temperature, possibly due to the escape of N from the surface region of the samples or due to oxidation of the surface of the GaN. No electrical characterization was possible due to the surface degradation. The degradation was also apparent in RBS/C as the surface of the samples became more “damaged” after annealing at 1100°C. In order to remedy this situation, an

annealing furnace was used that was equipped with a SiC resistive heating boat. This furnace had the ability to be pumped down to the 10^{-5} Torr range and backfilled with various gases. The samples implanted at Kroko were annealed in this furnace at 1100°C and 1200°C for 15 seconds. These samples did not show the same degradation as was observed in the samples annealed in the RTA. The samples annealed in the annealing furnace were then tested using Hall measurements. The results can be seen in Tables III and IV.

Table III. 1100°C Anneal

| | Sheet Carriers | Mobility | Percent Activation |
|--|----------------|----------|--------------------|
| Si ²⁹ , 200 keV 1e14, RT | 6.88e11 | 367.47 | .688 |
| Si ²⁹ , 200 keV 1e15, RT | 1.436e11 | 260.87 | .1436 |
| Si ²⁹ , 200 keV 1e14, 650°C | 1.5e12 | 232.51 | .15 |
| Si ²⁹ , 200 keV 1e15, 650°C | N/A | N/A | N/A |

Table IV. 1200°C Anneal

| | Sheet Carriers | Mobility | Percent Activation |
|--|----------------|----------|--------------------|
| Si ²⁹ , 200 keV 1e14, RT | 5.4e10 | 321 | .054 |
| Si ²⁹ , 200 keV 1e15, RT | N/A | N/A | N/A |
| Si ²⁹ , 200 keV 1e14, 650°C | 6.5e10 | 398.56 | .0065 |
| Si ²⁹ , 200 keV 1e15, 650°C | 3.99e10 | 269.8 | .004 |

The highest activation percent was seen in the 1100°C anneal sample with .688 % for the 1e14 dose and .15% for the 1e15 dose.

Also, an initial annealing experiment for the Mg implanted samples was done in an attempt to determine the exact nature of the implantation damage. One sample was annealed at 700°C for one minute in a RTA furnace. Another sample was annealed at 900°C for one minute. It was hoped that this annealing would reveal the nature of the implantation damage. If the damage was point defects, one should see a coarsening effect upon annealing. If the damage was amorphous regions, annealing should cause a gradual decrease in the damaged area as the annealing temperature is increased. Figures 9 and 10 show TEM images taken from these annealed samples. As seen in the images, annealing appears to not have affected the damaged regions at all. A more extensive annealing experiment needs to be conducted.

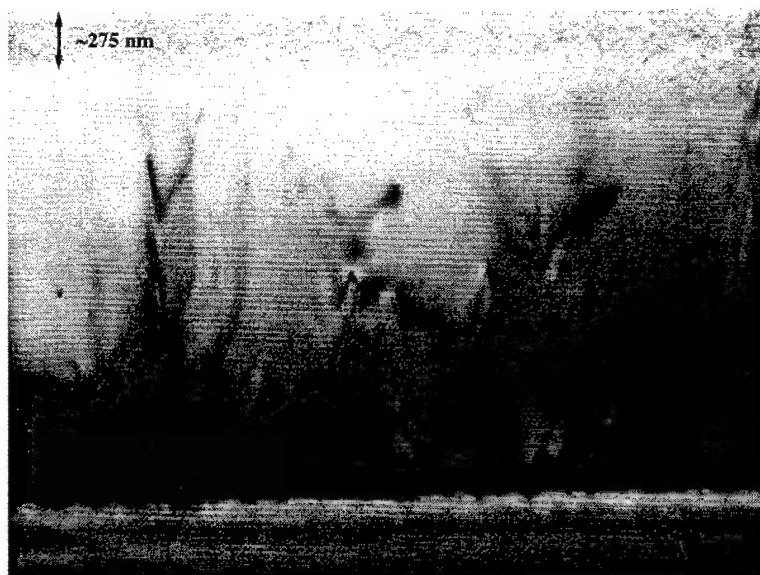


Figure 9. Mg implanted GaN sample annealed at 700°C for one minute.

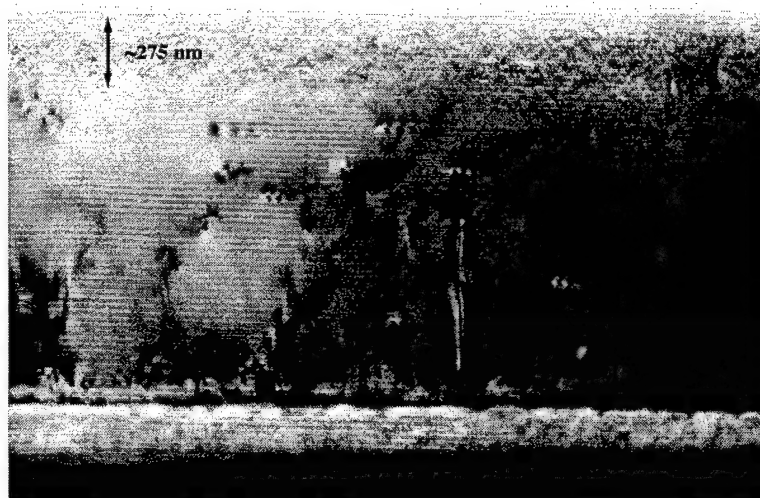


Figure 10. Mg implanted GaN sample annealed at 900°C for one minute.

D. Future Research Plans and Goals

The goal of the implantation is to achieve activation, thus the samples need to be annealed to activate the implanted species as was seen by Pearton, *et al.* An annealing schedule needs to be found that does not damage the surface of the samples and leads to a high enough activation percent. The samples may need to be annealed at higher temperatures in order to raise the percent activation. If the samples are annealed at higher temperatures, then they may need to be

capped in order to keep the surface from degrading during the anneal. This will be investigated using AlN or Si₃N₄ as a capping layer.

In order to determine the exact nature of the implantation damage, a series of annealing experiments is planned. By annealing a series of the implanted samples of GaN at progressively increasing temperatures and observing the microstructure using cross-sectional TEM, the exact nature of the damage should be revealed. If the damage is in small packets of amorphous regions, the TEM images from the annealed samples should show a gradual decrease in the damaged area as the annealing temperature rises. If the damage is in point defects, the TEM images from the annealed samples should show the formation of vacancy clusters and loops which should anneal out as the annealing temperature increases.

E. References

1. J. I. Pankove, and J. A. Hutchby, *J. Appl. Phys.* **47**, 5387 (1976).
2. J. I. Pankove, and J. A. Hutchby, *Appl. Phys. Lett.* **24**, 281 (1974).
3. R. G. Wilson, R. N. Schwartz, C. R. Abernathy, S. J. Pearton, N. Newman, M. Rubin, T. Fu, and J. M. Zavada, *Appl. Phys. Lett.* **65**, 992 (1994).
4. R. G. Wilson, S. J. Pearton, C. R. Abernathy, and J. M. Zavada, *Appl. Phys. Lett.* **66**, 2238 (1995).
5. M. Rubin, N. Newman, J. S. Chan, T. C. Fu, and J. T. Ross, *Appl. Phys. Lett.* **64**, 64 (1994).
6. S. C. Binari, H. B. Dietrich, G. Kelner, L. B. Rowland, K. Doverspike, and D. K. Wickenden, *J. Appl. Phys.* **78**, 3008 (1995).
7. S. J. Pearton, C. B. Vartuli, J. C. Zolper, C. Yuan, and R. A. Stall, *Appl. Phys. Lett.* **67**, 1435 (1995).
8. G. M. Ma, and S. Chevacharoenkul, MCNC Technical Report TR90-33 (1990).
9. J. Narayan, and O. W. Holland, *J. Electrochem. Soc.* **131**, 11 (1984).
10. J. Narayan, D. Fathy, O. S. Oen, and O. W. Holland, *J. Vac. Sci. Technol. A* **2**, 3 (1984).
11. J. Narayan, O. S. Oen, D. Fathy, and O. W. Holland, *Mat. Letts.* **3**, 3 (1985).

XIV. Multicolor Emission from Stacked AlGaIn/InGaIn Double Heterostructures

Abstract

InGaIn ternary alloys can be the basis for light emission from the near UV to the red region of the electromagnetic spectrum. When InGaIn/AlGaIn double heterostructures emitting different colors are stacked in a single structure, simultaneous emission of different wavelengths can be achieved. If the color and the intensity of emission for each well are adjusted properly, tailored emission spectra, including white light, will be feasible. This concept is demonstrated here with two wells emitting at different wavelengths that are stacked between AlGaIn barrier layers. The emitted PL spectra from the stacked structures is found to be the superposition of the emission from individual double heterostructures that were grown separately. The proposed structure can allow the demonstration of a solid state white light bulb.

The AlGaInN material system has the unique property of having a direct band gap that can theoretically be engineered from the far edge of the mid-ultraviolet ($\lambda_{\text{AlN}} = \sim 203 \text{ nm}$) through nearly the entire visible spectrum ($\lambda_{\text{InN}} = \sim 652 \text{ nm}$) [1]. The wide spectral range offered by III-nitride based compounds provides the rare opportunity to fabricate optical devices emitting from the violet through red from a single semiconductor alloy system. In the past several years, dramatic advances in the epitaxial growth, doping and processing of the III-nitride alloys have led to the development of commercially available high brightness blue and green light emitting diodes (LEDs) [2] and the realization of violet/blue emitting laser diodes (LDs) [3]. In particular, $\text{In}_x\text{Ga}_{1-x}\text{N}$ alloys have received considerable attention as active layers in LEDs and LDs, with the emission wavelength being determined primarily by the value of x . While the emission mechanism from $\text{In}_x\text{Ga}_{1-x}\text{N}$ films with relatively high values of x is still being debated [4], there have been reports of InGaIn based optical devices with InGaIn active layers having high InN% emitting in the yellow region of the visible spectrum [2].

To date, optical devices based on the III-nitride materials system are designed to emit one color. There are many applications, however, where several colors, or even white light may be desired from a single device. By combining photons of three primary colors or two complementary colors, various shades of white light will be sensed by the human eye. The relative intensities of the various photon fluxes will determine the perceived color, as illustrated by the CIE (Commission Internationale de l'Éclairage) chromaticity diagram [5]. Examples of prototype white light emitting structures utilizing stacked layers of other materials systems, such as $\text{SrS}:\text{Ce}/\text{CaS}:\text{Eu}$ [6] and organic polymers [7,8] have been reported. A myriad of applications exist for multicolor emitters, including full color indoor/outdoor displays and

spectrally tailored white light sources that are bright, compact, light weight, long lived, and efficient. The potential demand for a solid state white light source as a viable replacement for conventional incandescent or fluorescent light bulbs is by itself enormous. This section discusses the concept and present preliminary results of a device structure designed for multicolor emission that is based on stacked $\text{Al}_y\text{Ga}_{1-y}\text{N}/\text{In}_x\text{Ga}_{1-x}\text{N}$ double heterostructures (DHs). By changing the growth conditions of the $\text{In}_x\text{Ga}_{1-x}\text{N}$ active layers in this stacked structure, two distinct colors are emitted, one color from each active layer, as observed in room temperature (RT) photoluminescence (PL) spectra. The colors emitted from each active layer in the stacked structure correspond to the colors emitted from conventional DHs having $\text{In}_x\text{Ga}_{1-x}\text{N}$ active layers grown under the same conditions as those of the stacked structure.

Epitaxial growth of these $\text{In}_x\text{Ga}_{1-x}\text{N}$ and $\text{Al}_y\text{Ga}_{1-y}\text{N}$ layers was carried out by metalorganic chemical vapor deposition (MOCVD) in a hybrid atomic layer epitaxy (ALE) / MOCVD growth system that has been previously described [9]. Source gases used were, trimethylgallium (TMG, -10°C), trimethylaluminum (TMA, $+18^\circ\text{C}$), ethyldimethylindium (EdMIn, $+10^\circ\text{C}$) and NH_3 ; N_2 was used as the carrier gas. Basal plane sapphire substrates were solvent cleaned and annealed at 1050°C prior to epitaxial growth, followed by deposition of a low temperature buffer layer prior to growth of the stacked structure. A schematic of the complete stacked DH is shown in Fig. 1. Growth of the AlN/GaN buffer layer was performed at 500°C , followed by a 5 minute 1000°C anneal and the growth of a thin ($\sim 800 \text{ \AA}$) GaN base layer. The AlGaN ($\sim 7\text{-}10\%$ AlN) cladding layers were grown at 950°C and have approximate thicknesses, beginning with the lower most layer, of 8000 \AA , 2000 \AA and 1500 \AA respectively. All layer thicknesses have been estimated based on prior growth rate calibrations. Individual DHs, consisting of one $\text{In}_x\text{Ga}_{1-x}\text{N}$ active layer sandwiched between two AlGaN cladding layers, were also grown for comparison to the stacked DH characteristics.

The InGaN active layers, deposited at temperatures between 730 and 800°C , had growth times between 2 and 5 minutes. Both conventional MOCVD and flow modulation MOCVD, in which the organometallic precursors are pulsed into the growth chamber for various duty cycles, were used to grow the active layers. The details of the growth processes of the InGaN films will be published at a later date. The active layers were deposited on InGaN prelayers whose growth temperatures were ramped during growth from $820\text{--}790^\circ\text{C}$ down to the active layer growth temperature between $800\text{--}730^\circ\text{C}$. The InGaN prelayers are believed to provide a graded InGaN buffer that seems to improve the optical properties of the active layer. We find that the graded layer is not critical for low $\text{InN}\%$ in the well, but highly desirable for high values of $\text{InN}\%$ in DHs emitting at wavelengths $> \sim 400 \text{ nm}$.

For purposes of comparison to the stacked DHs, a sequence of four individual DHs were grown with InGaN active layers deposited at temperatures of 730 , 750 , 780 and 800°C ,

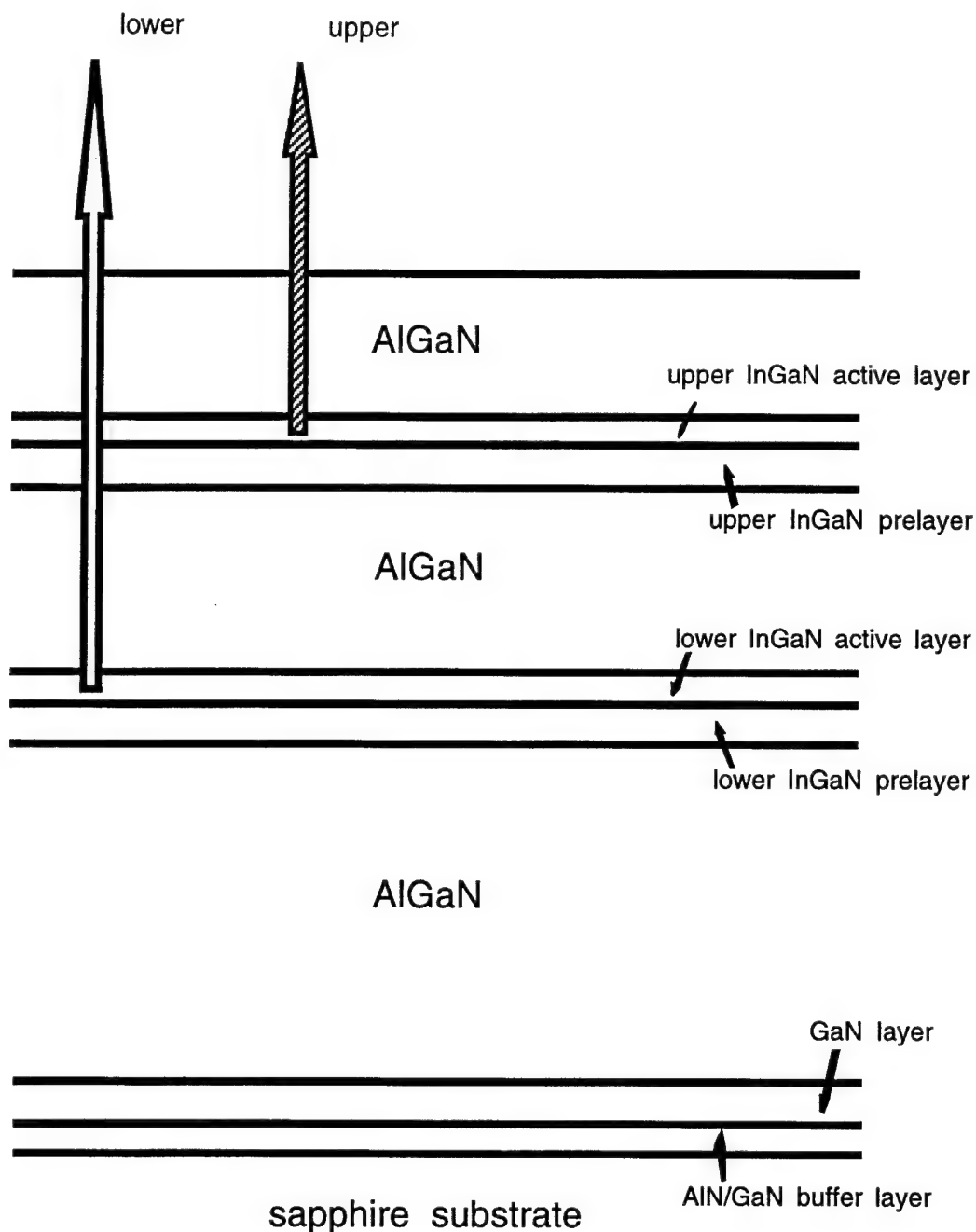


Figure 1. Schematic diagram of the stacked double heterostructure.

respectively. The PL emission peak for each DH was measured over the entire sample, and the range of PL emission is given in Fig. 2, plotted against the growth temperature of the InGaN active layer. The emission wavelength shifted from the violet to the yellow/green as the growth temperature of the active layer was decreased from 800 to 730°C. The PL emission peak, while falling within a reasonable range to study subsequent stacked structures, was not completely

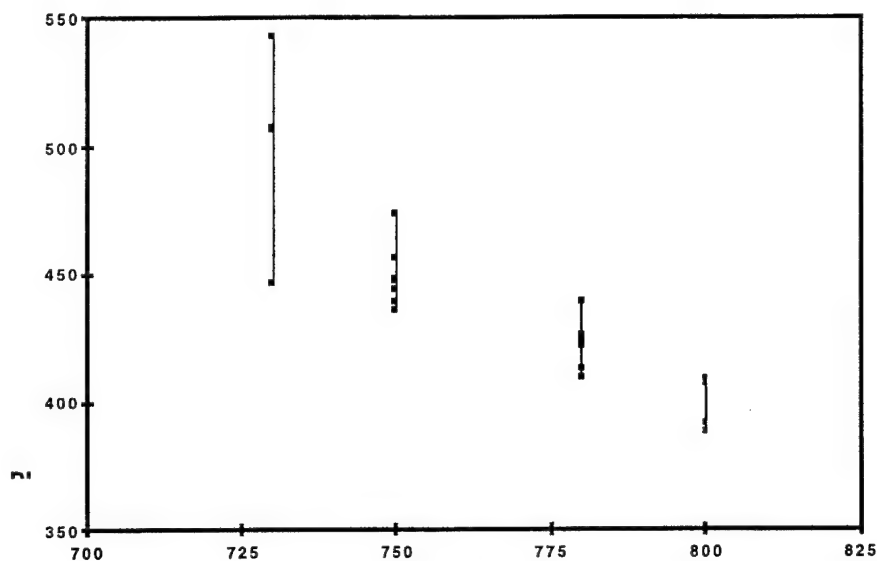


Figure 2. Range of peak position of PL emission from individual DHs vs. growth temperature of the InGaN active layer.

uniform over each sample. The growth reactor used in this study was optimized for the ALE growth of InGaN and, therefore, suffered some deficiencies in achieving optimal MOCVD growth conditions, such as nonoptimized gas dynamics at the substrate during growth. Rainbow-like interference fringes on our nitride films indicate some degree of thickness and perhaps compositional nonuniformity, especially for the In-based nitride layers with high InN%. Atomic layer epitaxy grown InGaN films have better emission and thickness uniformity than those grown by MOCVD, however the ALE growth technique was not applied in this study because of difficulty in achieving emission with longer wavelengths required for this proposed structure.

Several stacked DHs were grown with growth conditions of the upper (i.e., closer to the surface) and lower (i.e., closer to the substrate) InGaN active layers corresponding to the individual DHs whose peak emissions are given in Figure 2. Figure 3a exhibits the PL spectra for a stacked DH having the lower InGaN active layer grown at 750°C and the upper InGaN active layer grown at 800°C. The two prominent emission peaks at 391 and 436 nm, shown in Figure 3a, match the emissions of the individual DHs with InGaN active layers grown at 750 and 800°C respectively and shown in Fig. 2. Figure 3b illustrates the PL emission from another stacked DH that has the lower InGaN active layer grown at 780°C and the upper InGaN active layer grown at 730°C. The two prominent emission peaks at 434 and 500 nm shown in this figure are also within the range of the emission corresponding to individual DHs grown with InGaN active layers at 780 and 730°C, respectively. In each of these spectra a

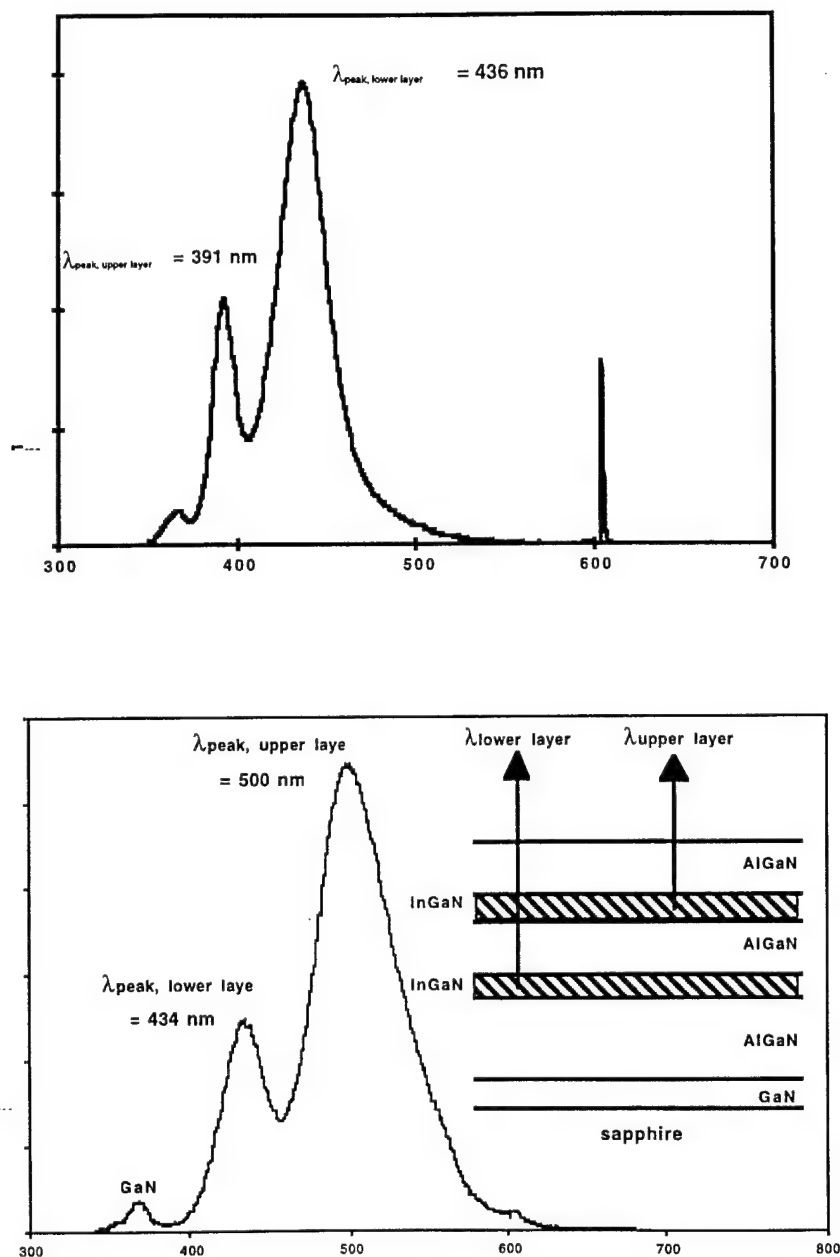


Figure 3. RT PL spectra of stacked DHs with upper and lower InGaN active layers grown at (a) 800 and 750°C, respectively and (b) 730 and 780°C, respectively.

weak, near band edge GaN emission exists that apparently originates from the relatively thin GaN layer near the interface. The sharp, intense emission positioned just beyond 600 nm is attributed to an artifact of our PL system.

The RT PL spectra exhibited by these stacked DHs demonstrated that InGaN active layers grown under different conditions and with apparently different InN% mole fractions could contribute to multicolor emission. It should be possible to integrate three stacked InGaN active layers, each with a controlled InN% mole fraction, to realize a spectrally tailored emission

spectra, including white light. From these preliminary results, it appeared that the emission from the lower active layer was not too severely attenuated by the overlying layers, as shown in Fig. 3b, even if its emission wavelength is of higher energy than the band gap of the overlying layers. PL measurements taken from backside illumination of the structure corresponding to Fig. 3a show similar spectral peak placements but with different intensities. For PL measurements taken with backside illumination, the intensity of the near band edge GaN emission becomes more dominant, with the multicolor emission intensity reduced. Eventually two InGaN based DHs, emitting for example at 450 and 580 nm with appropriate intensities, could offer the realization of a semiconductor white light bulb.

In conclusion, several novel stacked AlGaIn/InGaIn DHs were epitaxially grown on a sapphire substrate. The room temperature PL spectra from these structures exhibited two-color emission at 391/436 nm and 434/500 nm. These emission wavelengths matched the emission wavelengths of conventional DHs with active layers grown under the same conditions as those that comprised the stacked DH. This demonstrated the potential for the realization of multicolor optical devices based on III-nitride stacked DHs. Further work is needed to expand the range of multiple color emission, especially toward the red range of the visible spectrum, so that colors may be mixed to obtain white light emitters. Further refinements in the growth process also need to be made to obtain stacked structures that have a higher degree of uniformity.

This work has been supported by the Office of Naval Research (ONR), University Research Initiative (URI), grant number: N00014-92-J-1477, and the Army Research Office (ARO) / Advanced Research Projects Agency (ARPA), grant number: DAAH04-96-1-0173.

References

1. F. A. Ponce and D. P. Bour, *Nature* **386**, 351 (1997).
2. S. Nakamura, M. Senoh, N. Iwasa, and S. Nagahama, *Jpn. J. Appl. Phys.* **34**, L797 (1995).
3. S. Nakamura, M. Senoh, S. Nagahama, N. Iwasa, T. Yamada, T. Matsushita, Y. Sugimoto, and H. Kiyoku, *Appl. Phys. Lett.* **69**, 4056 (1996).
4. Y. Narukawa, Y. Kawakami, M. Funato, S. Fujita, S. Fujita, and S. Nakamura, *Appl. Phys. Lett.* **70**, 981 (1997).
5. D. L. MacAdam *Color Measurement - Theme and Variations* Springer Series in Optical Sciences **27**, (Springer-Verlag 1981), chap. 1.
6. Y. A. Ono, M. F. Ken-ichi, K. Tamura, and M. Ando, *J. Appl. Phys.* **66**, 5564 (1989).
7. C. C. Wu, J. C. Sturm, R. A. Register, and M. E. Thompson, *Appl. Phys. Lett.* **69**, 3117 (1996).
8. R. H. Jordan, A. Dodabalapur, M. Strukeij, and T. M. Miller, *Appl. Phys. Lett.* **68**, 1192 (1996).
9. J. C. Roberts, F. G. McIntosh, K. S. Boutros, S. M. Bedair, M. Moussa, E. L. Piner, Y. He, and N. A. El-Masry, *Mat. Res. Soc. Proc.* **395**, 273 (1996).

XV. III-V Nitrides for Use in Semiconductor Microelectronic Device Applications

A. Introduction

With their distinct combination of physical and electronic properties, the III-V nitrides are promising materials for optoelectronic and microelectronic applications. AlN, GaN, and InN have direct band gaps of 6.2, 3.2, and 1.9 eV, respectively. In conjunction with their continuous solid solubility, one has the ability to engineer band gaps within the range of 1.9 to 6.2 eV, which can be used to construct blue LEDs and deep UV lasers.

Along with their wide band gaps, the III-V nitrides have advantageous physical properties such as high thermal stability, high physical hardness, and high chemical stability. In combining these properties, the III-V nitrides lend themselves as excellent candidates for high-power and high-temperature devices.[1]

At present, there is one significant drawback to the use of the III-V nitrides, the lack of a homoepitaxial substrate. In order to achieve monocrystalline thin films, heteroepitaxy has been employed using a number of different substrates. This method has allowed the production of single crystal films, but the films have had poor crystal quality and high unintentional doping levels [2].

Recent developments have shown that good single crystal thin films of AlN and GaN can be grown using techniques such as metal organic chemical vapor deposition (MOCVD) and molecular beam epitaxy (MBE) [3-7]. The most successful of these films, which exhibit high resistivity and low unintentional doping, have been grown on Al₂O₃ (sapphire) and α -SiC. Conductive n and p-type GaN films have also been produced using the appropriate doping impurities.

With the production of device quality material successful attempts have been made to produce microelectronic devices using the III-V nitrides [8-15]. Khan *et al.* have made many strides in this area, including being the first to fabricate a MESFET device from the nitrides. Binari *et al.* have also fabricated MESFET devices along with MISFET structures. As shown in Fig. 1, Binari fabricated an depletion mode device using Si₃N₄ as the gate insulator. For a gate length of 0.9 μ m the transconductance was 16 mS/mm at 30°C and 11 mS/mm at 200°C. The frequency response of these devices were measured resulting in an f_T and f_{max} of 5 and 9 GHz respectively.[15]

Much of the research currently concerning MISFET devices is directed towards depletion mode devices. This can be attributed to the inability to successfully process the material. Currently many strides have been made in the areas of implantation and etching [16-18]. Other areas of research which are beginning to be addressed include the investigation of insulator

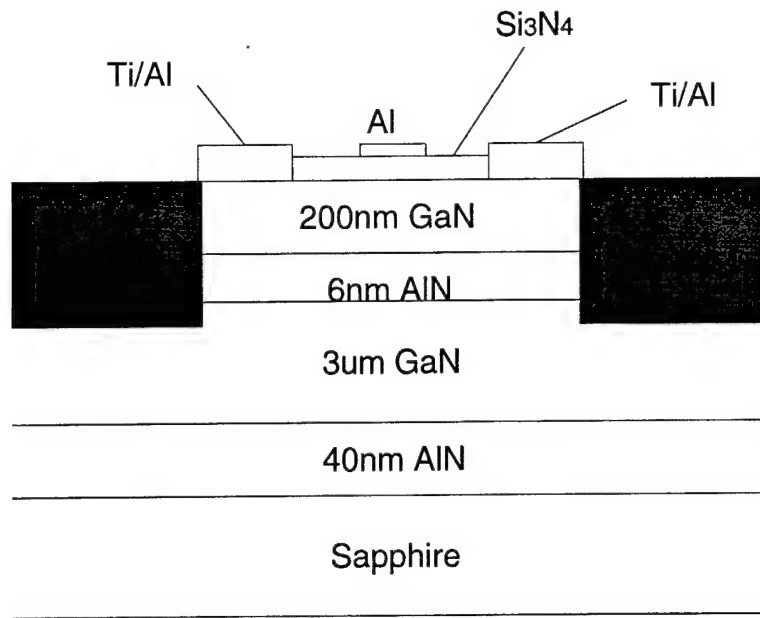


Figure 1. MISFET cross section.

materials. Some initial work has been done by Casey *et al.* on SiO₂-GaN MOS capacitors [19]. His results indicate that SiO₂ grown on GaN by a remote plasma method yielded a structure with low interface trap density.

It is the plan of this project to complete the steps needed to construct a MISFET structure. The steps will be discussed further in the following section.

B. Results

In order to produce a viable IGFET device a suitable insulating material must be found to use as the gate insulator. Three materials have been chosen to be investigated for this research. They include SiO₂, GaO, and AlN. To properly study the characteristics of the insulators on the semiconductor metal insulator semiconductor capacitors used.

To theoretically model these devices, modified versions of the equations derived for two terminal devices Si, from Tsividis [20] and Nicollian and Brews [21], are used. Due to GaN's long generation rate and short minority carrier lifetime, on the order of 10¹¹ years and 10⁻⁸s respectively, the inversion layer contribution to the capacitance can be ignored. This leaves only the accumulation and depletion modes to characterize. From this analysis an equation for the semiconductor capacitance is derived:

$$C_c(y) = \left[F \frac{\sqrt{N_d}}{2} \left(\phi_t e^{\left(\frac{\psi}{\phi_t} \right)} - \psi - \phi_t \right)^{-\frac{1}{2}} \cdot \left(e^{\left(\frac{\psi}{\phi_t} \right)} - 1 \right) \right] \cdot A \quad (1)$$

where $F = (2q\epsilon_{\text{GaN}})^{1/2}$, N_d is the semiconductor doping concentration, ϕ_t is the thermal voltage, and ψ is the surface potential. Substituting the results of the Eq. 1 into the following equation,

$$C_t(\psi) = \left(\frac{1}{C_{ox}} + \frac{1}{C_c(\psi)} \right)^{-1} \quad (2)$$

where C_{ox} is the capacitance of the insulator, the capacitance for the device can be calculated at various surface potentials. The equation for the gate voltage is derived from the potential drops across the capacitor:

$$V_{gb}(\psi) = V_{fb} - \frac{Q_{cs}(\psi)}{C_{ox}} - \psi \quad (3)$$

where V_{fb} is the flatband voltage and $Q_{cs}(\psi)$ is the charge at the semiconductor/insulator interface. From the above equations a theoretical C-V curve can be generated for n-type MIS capacitors.

This research group has demonstrated the ability to grow high-quality single crystal thin films of GaN and AlN with high resistivity and low levels of unintentional doping. These films have been grown by MBE and MOCVD on α -SiC, utilizing a high-temperature monocrystalline AlN buffer layer. Through these methods both n and p type doping of the GaN films has been achieved.

Using the n-type MOCVD GaN as the substrate three insulating materials, SiO_2 , GaO, and AlN, have been grown or deposited upon it. Remote plasma-enhanced chemical vapor deposition (RPECVD) was utilized to deposit the SiO_2 layer [22]. The material was deposited at NCSU in the NSF Engineering Research Center for Advanced Electronic Materials Processing.

MIS capacitors were fabricated using the RPECVD oxide. The capacitors fabricated on the GaN were lateral in orientation. This was done to avoid the insulating AlN buffer layer. Thus the oxide was deposited, patterned with photolithography, and etched. A large Al Ohmic contact was deposited on the GaN via resistive heating evaporation and Al gate contacts were deposited with a shadow mask in the same evaporator.

Capacitance-voltage measurements were performed on the capacitors using a HP 4282A Precision LCR Meter in combination with HP VEE software. The resulting measured curves compared well with the theoretical curve (Fig. 2). At flatband the capacitance in the GaN is

$$C_{FB} = (\epsilon_{GaN}/L_D)A \quad (4)$$

where L_D is the Debye length and A is the area of the MIS capacitor. The flatband capacitance was calculated and used to find the flatband voltage. Using the equation

$$V_{FB} = V_{FB}^0 - qN_f/C_{ox} \quad (5)$$

where C'_{ox} is the oxide capacitance per unit area, N_f is the fixed oxide charge cm^{-2} and V_{FB}^0 is the ideal oxide flatband voltage. This value is obtained from the difference in the work functions of the Al gate and the GaN. The work function of Al is known to be 4.1eV. The work function of GaN is still in question. The electron affinity of GaN has been reported [23] to be 4.1eV. This number was used in place of the work function to calculate the ideal flatband voltage. The measured flatband voltage, found from the calculated flatband capacitance, is 1.1V. The calculated fixed oxide charge for this capacitor is $4.09 \times 10^{11} \text{ cm}^{-2}$. Values for remote plasma oxides on Si are in the range of $4\text{-}6 \times 10^{11} \text{ cm}^{-2}$ [19].

The next insulator investigated was AlN. This insulator was deposited by both MOCVD and MBE within this research group. The capacitors produced from the films grown via MOCVD had poor electrical characteristics. This has been attributed to the quality of the AlN film. Cracks in the film are apparent when viewing with an optical microscope. This could be caused by the thermal mismatch between the AlN and GaN.

In an attempt to circumvent the problem an AlN layer was grown at low temperatures via MBE. SEM images show that no cracking is observed in this film.

The material was processed similarly to the SiO_2 . The resulting capacitors were measured using the same LCR meter as previously described. The resulting curves can be seen in Fig. 3. The large shift and hysteresis in the curves indicate a large amount of interface traps. This is confirmed by the fact that at slower sweep rates the hysteresis begins to close because the traps have more time to fill and empty during the sweep. Studies into reducing the interface trap density are ongoing on this material.

The final insulating material being investigated in this study is gallium oxide. This group has successfully grown a thermal oxide on GaN using a dry oxygen gas as the O_2 source. SEM images (Figs. 4-5) show a polycrystalline surface and EDX (Fig. 6) scans confirm the presence of gallium and oxygen with low amounts of nitrogen. Optimization and electrical studies of these films are currently being accomplished.

C. Discussion

Both the AlN and SiO_2 MIS capacitors have produced promising results as possible candidates for use in an IGFET device. Further work must be done to optimize each of these two systems.

Many aspects of the electrical and physical properties of the native oxide grown on the GaN need to be investigated.

To reach the goal of an IGFET device advances in material processing need to be made. Specifically in the areas of contacts, ion implantation, and etching. All of which are currently being addressed within this research group.

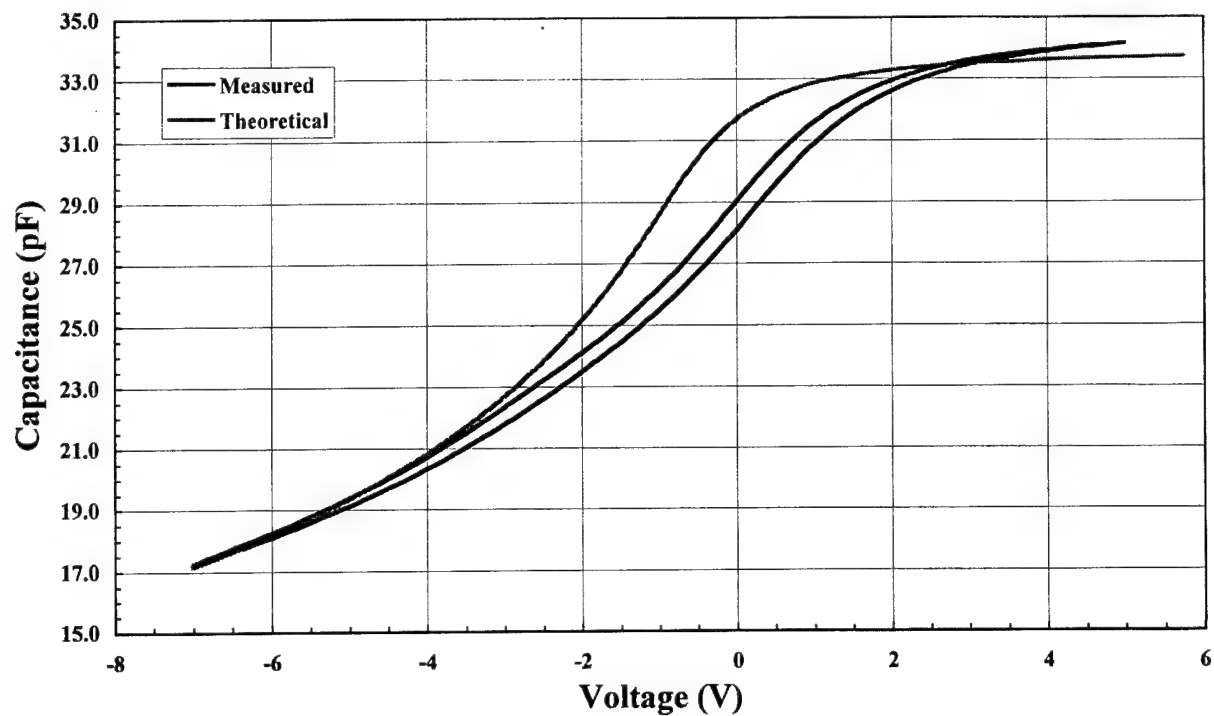


Figure 2. C-V measurements of SiO₂/GaN heterostructure at room temperature.

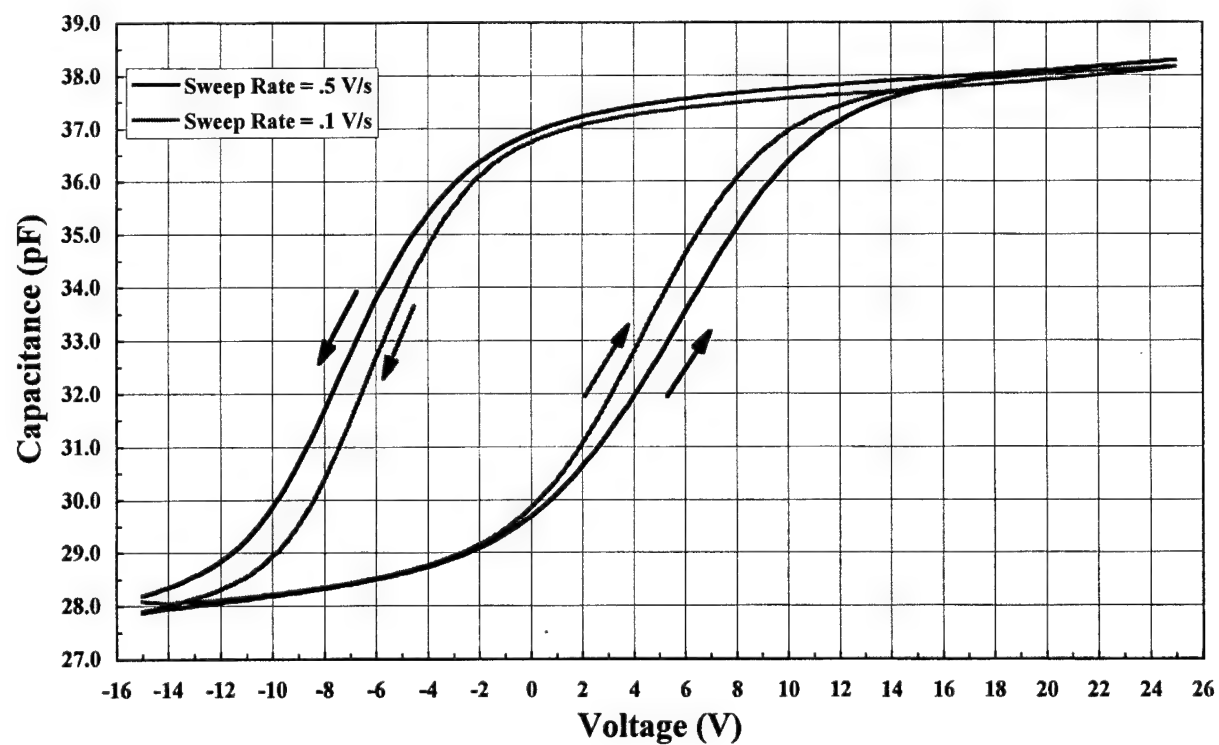


Figure 3. C-V measurements of AlN/GaN heterostructure at room temperature.

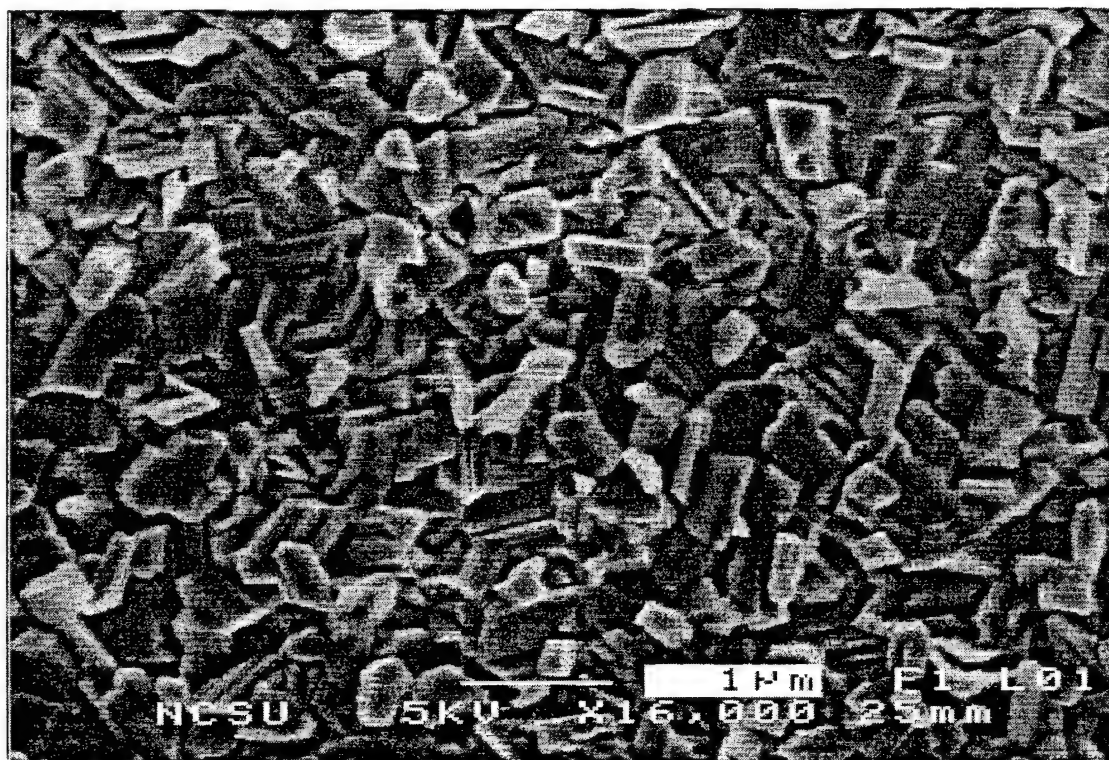


Figure 4. SEM of thermal oxide grown on GaN.

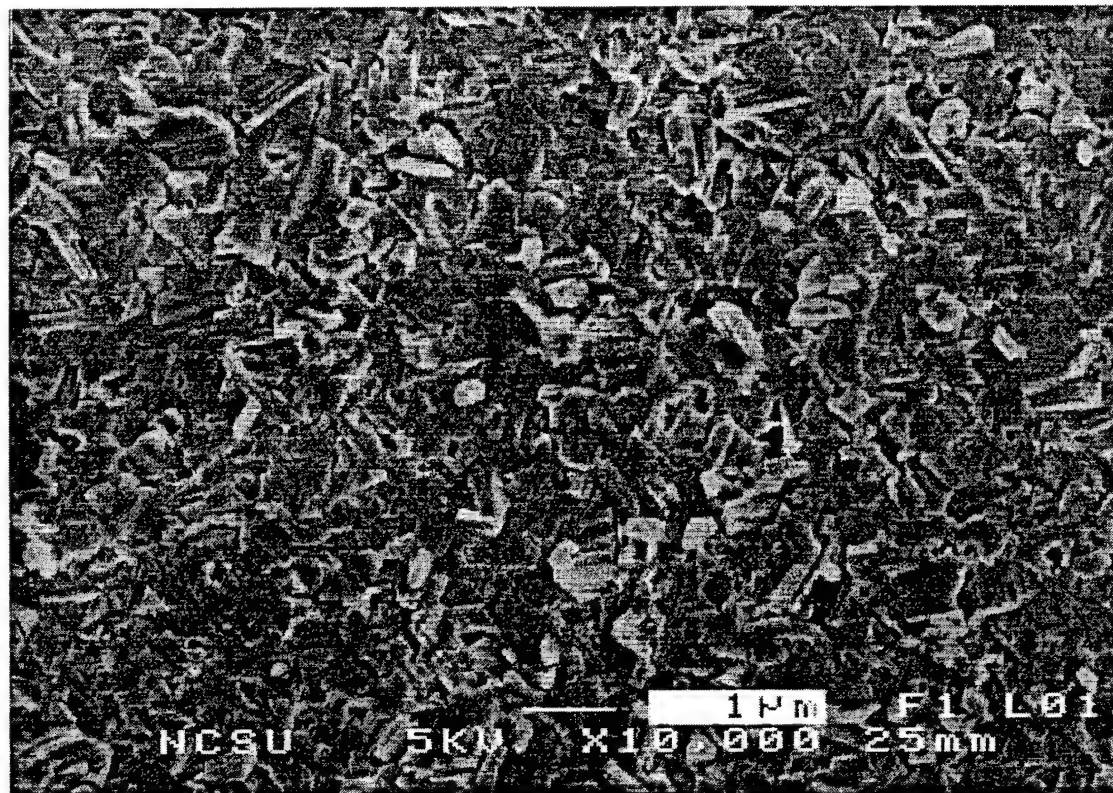


Figure 5. SEM of thermal oxide grown on GaN.

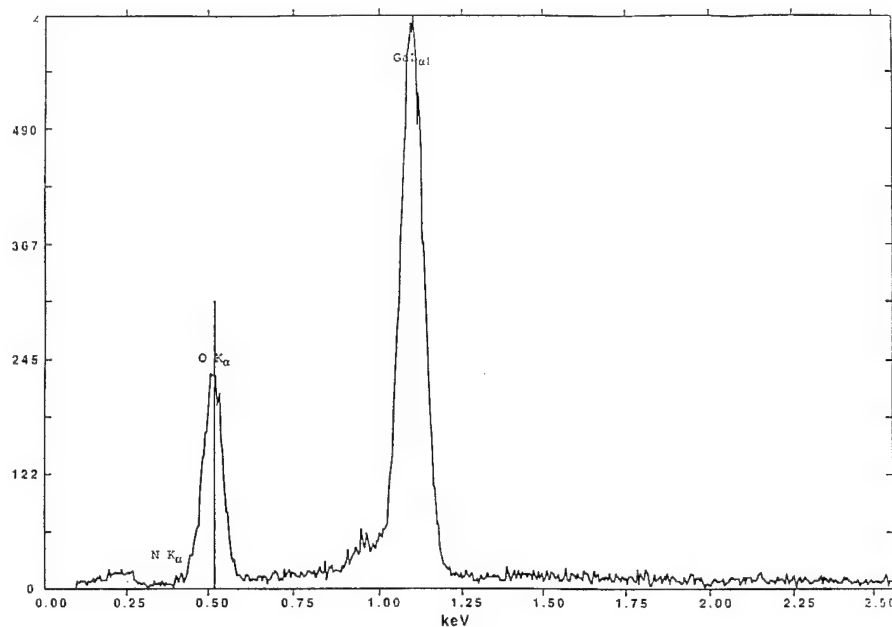


Figure 6. EDX of thermal oxide on GaN.

D. Conclusion

With their combination of thermal and electrical properties, the III-V nitrides have the potential to be excellent materials for use in high-power and high-temperature applications. With the production of device quality material the time has arrived to develop these devices. There are a number of factors that will determine when fabrication will be realized. It is the goal of this project to complete the work needed to achieve a working device.

E. References

1. R.F. Davis, Proc. IEEE **79**, 702 (1991).
2. S. Strite and H. Morkoç, J. Vacuum Sci. Technol. B **10**, 1237 (1992).
3. M. Asif Khan, J.N. Kuznia, J.M. Van Hove, D.T. Olson, S. Krishnankutty, and R.M. Kolbas, Appl. Phys. Lett. **58**, 526 (1991).
4. H Amano, T. Asahi, and I. Akasaki, Jpn J. Appl. Phys. **29**, L205 (1990).
5. S. Yoshida, S. Gonda, and S. Misawa, J. Appl. Phys. **53**, 6844 (1982).
6. M. Hegems and H. C. Montgomery, J Phys. Chem Solids **34**, 885 (1973).
7. C. Wang and R.F. Davis, Appl. Phys. Lett. **63**, 990 (1993).
8. M. Asif Khan, J.N. Kuznia, A.R. Bhattarai, and D.T. Olson, Appl. Phys. Lett. **62**, 1786 (1993).
9. M. Asif Khan, J.M. Van Hove, J.N. Kuznia, and D.T. Olson, Appl. Phys. Lett. **58**, 2408 (1991).
10. M. Asif Khan, J.N. Kuznia, J.M. Van Hove, N. Pan, and J. Carter, Appl. Phys. Lett. **60**, 3027 (1992).
11. M. Asif Khan, A.R. Bhattarai, J.N. Kuznia, and D.T. Olson, Appl. Phys. Lett. **63**, 1214 (1993).

12. M. Asif Khan, J.N. Kuznia, D.T. Olson, W.J. Schaff, J.W. Burm, and M.S. Shur, Appl. Phys. Lett. **65**, 1121 (1994).
13. M. Asif Khan, M.S. Shur, J.N. Kuznia, Q. Chen, J.W. Burm, and W.J. Schaff, Appl. Phys. Lett. **66**, 1083 (1995).
14. S.C. Binari, L.B. Rowland, W. Kruppa, G. Kelner, K. Doverspike, and D.K. Gaskill, Electronics Lett. **30**, 1248 (1994).
15. S.C. Binari, L.B. Rowland, G. Kelner, W. Kruppa, H.B. Dietrich, K. Doverspike, and D.K. Gaskill, Proc. 21st Int. Symp. on Compound Semiconductors, September 1994, San Diego.
16. R.J. Shul, A.J. Howard, S.J. Pearton, C.R. Abernathy, C.B. Vartuli, P.A. Barnes, and M.J. Bozack, J. Vac. Sci. Technol. B **13**, 2016 (1995).
17. G.F. McLane, L. Casas, S.J. Pearton, and C.R. Abernathy, Appl. Phys. Lett., **66**, 3328 (1995).
18. S.J. Pearton., C.B. Vartuli, J.C. Zolper, C. Yuan, and R.A. Stall, Appl. Phys. Lett. **67**, 1435 (1995).
19. H.C. Casey, G.G. Fountain, R.G. Ailey, B.P. Keller, Appl. Phys. Lett., **68**(13), 1850 (1996).
20. Y.P. Tsividis, *Operation and Modeling of the MOS Transistor*, McGraw Hill Book Co., New York, 1987.
21. E.H. Nicollian, J.R. Brews, *MOS(Metal Oxide Semiconductor) Physics and Technology*, John Wiley & Sons, New York, 1982.
22. C.G. Parker, C. Silvestre, M. Watkins, R.T. Kuehn, J.R. Hauser, Proceed. 10th Biannual Univ., Gov., and Industry Microelectronics Symp., 208, 1993.
23. J.I. Pankove, H. Schade, Appl. Phys. Lett., **25**, 53 (1974).

XVI. Raman Analysis of the Configurational Disorder in $\text{Al}_x\text{Ga}_{1-x}\text{N}$ Films

Leah Bergman, Michael D. Bremser*, William G. Perry*, Robert F. Davis*, Mitra Dutta†, and Robert J. Nemanich

Physics Department, and *Department of Materials Science and Engineering, North Carolina State University, Raleigh, NC 27695-8202. †US Army Research Office, Research Triangle Park, NC 27709-12211

Abstract

Raman analysis of the E2 mode of $\text{Al}_x\text{Ga}_{1-x}\text{N}$ in the composition range $0 < x < 1$ is presented. The lineshape was observed to exhibit a significant asymmetry and broadening toward the high energy range. The spatial correlation model is discussed and is shown to account for the lineshape. The model calculations also indicate the lack of a long-range order in the CVD alloys. These results were confirmed by X-ray scattering: the relative intensity of the superlattice line was found to be negligible. The line broadening of the E2 mode was found to exhibit a maximum at a composition $x \approx 0.5$ indicative of a random disordered alloy system.

The realization of achieving high quality $\text{Al}_x\text{Ga}_{1-x}\text{N}$ films has prompted intensive investigation concerning device fabrication and material and device properties. Raman spectroscopy has been proven in the past to be a powerful method in studying alloy systems among which are $\text{Al}_x\text{Ga}_{1-x}\text{As}$, $\text{In}_x\text{Ga}_{1-x}\text{As}$, $\text{Ca}_x\text{Sr}_{1-x}\text{F}_2$, $\text{ZnS}_{1-x}\text{Se}_x$, and many more [1-5]. Raman scattering from a perfect crystal, which consists of a lattice with translational symmetry, involves phonons with wavevector $q \approx 0$ near the Brillouin zone (BZ) center [6]. The alloying may destroy the configurational translational symmetry, and the phonons of $q \geq 0$ may be allowed to participate in the Raman scattering. As a result the Raman lineshape changes, and an investigation of the line characteristics may yield valuable information on the microstructure state of the alloy.

In this Letter, we present for the first time observations and analytical study of an asymmetric E2 Raman lineshape of $\text{Al}_x\text{Ga}_{1-x}\text{N}$ films. The asymmetry of the line is shown to agree with the spatial correlation model which is based on the relaxation of the $q \approx 0$ selection rules due to the alloying. The calculations indicated that the $\text{Al}_x\text{Ga}_{1-x}\text{N}$ lattice lacks a long range order, a result which was confirmed by X-ray diffraction: the superlattice diffraction line was found to exhibit a very weak relative intensity. Moreover, the functional behavior of the E2 linewidth with respect to the composition x in the range 0 - 1 indicated a random distribution of the alloy constituents with maximum disorder at composition $x \approx 0.5$.

Raman spectra were acquired in a backscattering geometry in which the E2 and the A1(LO) are the allowed Raman modes from the c-face of the Wurtzite structure [7]. The 488 nm line of an Ar⁺ ion laser was utilized and the data were acquired at sample temperatures of 300K and at 10K. The experimental error in the linewidth and peak position measurements is $\pm 1.5 \text{ cm}^{-1}$ and 0.5 cm^{-1} respectively. The Al_xGa_{1-x}N films were grown via the organometallic chemical vapor deposition (OMCVD) method at $\sim 1100^\circ\text{C}$ on 6H-SiC(0001) substrates with a 1000 Å AlN buffer layer [8]. The thickness of the films is $\sim 2 \mu\text{m}$ and the composition, x, which was determined via Rutherford backscattering (RBS), energy dispersive X-ray (EDX), and Auger spectroscopy, is: 0.06, 0.12, 0.22, 0.32, and 0.70. The data points for x=0 and x=1 were obtained from GaN film and AlN crystallite [9] respectively.

Figure 1 shows the room-temperature Raman spectra of the E2 line from Al_xGa_{1-x}N films of compositions 0.06, 0.12, 0.22, and 0.70, which exhibit linewidths of 8, 13, 16, and 19 cm^{-1} respectively. As depicted in the figure, the spectral lineshape for films of $x > 0.06$

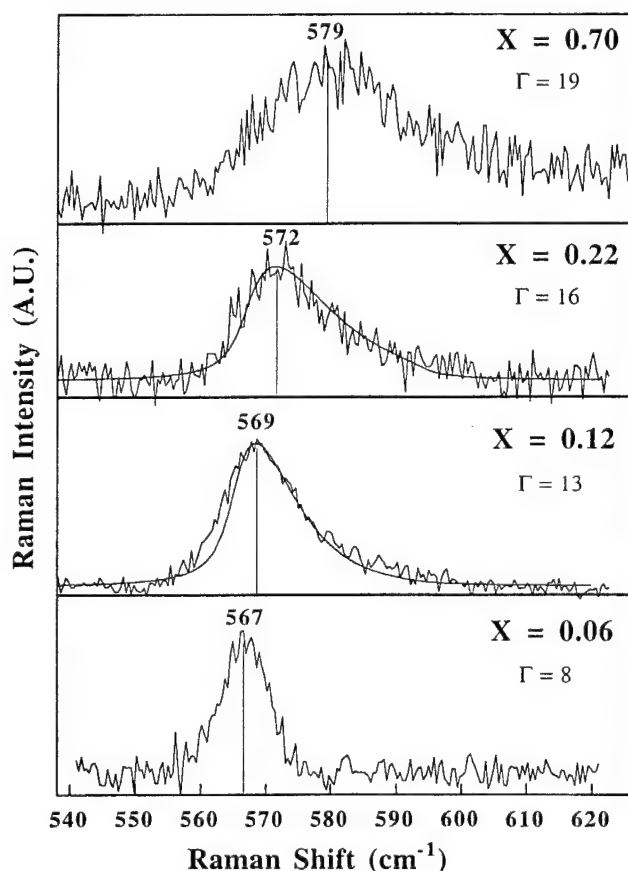


Figure 1. The RT Raman spectra of the E2 mode of Al_xGa_{1-x}N films of composition x=0.06, 0.12, 0.22 and 0.70. The respective linewidths are: 8, 13, 16, and 19 cm^{-1} , and peak positions at: 567, 569, 572, 579 cm^{-1} . The solid lines superimposed on the spectra of films: x=0.12 and 0.22 were calculated from the spatial correlation model presented in Eq. 1.

exhibit asymmetric broadening and a peak shift toward higher frequency. Possible line broadening mechanisms applicable to alloys include thermal broadening, activation of a symmetry forbidden zone-center ($q \approx 0$) mode which lies in the same frequency range as the investigated line, and broadening due to activation of a collective of modes of wavevectors $q \geq 0$. The last two broadening mechanisms result from the elimination of the translational symmetry of the lattice due to alloying.

To investigate the thermal contribution to the line broadening, Raman spectra were acquired at $T=10\text{K}$, and no significant change was observed between the shapes and linewidths of the room and cold temperature spectra. Thus the linewidth in our sample is not strongly affected by temperature. The only effect of the low temperature is the shifting of the peak position by $\sim 2\text{ cm}^{-1}$ toward the high frequency, which was also previously observed in GaN films [10] and crystals [11] and was attributed there to the thermal contraction of the bonding.

The second possible mechanism is the activation of a $q \approx 0$ symmetry forbidden mode which might be convoluted with the E2 line and cause the asymmetric broadening. However, the only mode in the frequency range of the E2 line that is forbidden in the back-scattering geometry is the $A_1(\text{TO})$ mode of GaN at $\sim 560\text{ cm}^{-1}$ [7] which lies at a lower frequency.

A more plausible mechanism to account for the high frequency asymmetric linewidth in our Raman spectra is the spatial correlation model, also known as the confinement model. The model was developed to explain the asymmetry line in BN [12] and Si [13] and has been successfully applied to quantify the lineshape behavior of $\text{Ga}_{1-x}\text{Al}_x\text{As}$ and $\text{Ga}_{1-x}\text{In}_x\text{As}$ alloy systems [1]. The foundation of the model lies in the uncertainty principal: $\Delta q = 2\pi/L$ where Δq is the phonon wavevectors range, L is a spatial dimension into which the phonon is confined, and q is related to the Raman frequency ω via the phonon dispersion relation $\omega(q)$. The size of L in an alloy system may be viewed as the average size of the ordered domains which are embedded in the configurational-disordered matrix. According to the model, as L gets smaller Δq becomes larger: a wider range of frequencies are allowed to participate in the Raman scattering, and as a result the Raman lineshape exhibits a change. The lineshape-change depends on the phonon dispersion curve $\omega(q)$; for a curve of negative slope the line asymmetry is toward lower frequencies and for a positive slope the asymmetry is toward higher frequencies. The peak position also shifts accordingly. However, the position is a function of the alloy-mode as well: an alloy can be categorized as being a one- or two- mode type [14-15] and the behavior of the peak position depends on the type. The deconvolution of the peak position is left to a future investigation; at present we address merely the origin of the asymmetric lineshape and line broadening.

The Raman intensity $I(\omega)$ for the spatial correlation model may be expressed as [1, 12-13]

$$I(\omega) \propto \int \exp\left(\frac{-q^2 L^2}{4}\right) \times \frac{d^3 q}{[\omega - \omega(q)]^2 + \left(\frac{\Gamma_0}{2}\right)^2} \quad (1)$$

where q is in units of $2\pi/a$, a is the lattice constant, and Γ_0 is the linewidth of the material of composition $x=0$ which is GaN in this study. Our GaN films exhibit linewidth in the range 3 - 5 cm^{-1} depending on the film quality [10]. For the calculations we used the upper range value to account for the stress in the alloy which was inferred from the appearance of cracks in the films. In the calculation we assumed a spherical correlation domain and BZ.

To evaluate Eq. 1 we fitted the phonon dispersion curves, which have been calculated by Azuhata et al [16], in the vicinity of BZ center. In their calculations the E2 mode along the Δ direction exhibits a doubly degenerate behavior and is a weak function of q , thus having no effect on the line broadening mechanism. In contrast, the E2 curves along the Σ and T directions both split into a lower and an upper branch, where the former is a decreasing function of q and the later is an increasing function; these curves are expected to influence the Raman lineshape. Our calculations of Eq. 1 best concur with the phonon dispersion curve of the form: $\omega(q) = A + Bq^2$ (in units of cm^{-1} and with $A=568$ and $B=100$) which is the approximated behavior of the upper branch of the Σ and T curves in the vicinity of the zone center. However, when we included the contribution to the lineshape arising from the lower branches of the dispersion curves the fit was not ideal. Similar behavior has been previously observed in the calculation of BN lineshape [12]. The reason for the dominance affect of the upper branches in our calculations is under investigation.

The calculated lines and the Raman data for samples of composition 0.12 and 0.22 are presented in Fig. 1. As depicted in the figure the asymmetric Raman data concur with the spatial correlation model, where the small deviation $\sim 560 \text{ cm}^{-1}$ may be attributed to the activated $A_1(\text{LO})$ mode. The ordered domain size, L , was determined from our calculations to be $\sim 25 - 35 \text{ \AA}$; a relatively small value suggesting the lack of a long range order in the alloy system. In order to further investigate this hypothesis a film of composition $x=0.22$ was characterized by XRD: the scan is presented in Fig. 2. The figure shows the diffraction peak of the (0002) planes of the AlGa_{0.22}N (superimposed is also the SiC substrate peak) and the inset presents the weak (0001) diffraction peak. The (0001) is a forbidden reflection in the WZ structure and appears as a superlattice line only when lattice ordering exists [17]; the intensity ratio (0001)/(0002) is a measure of the extent of the order [18]. Al_xGa_{1-x}N films which were grown by molecular beam epitaxy have been reported by Korakakis et al [17] to exhibit a long range order; the intensity ratio of their XRD lines is ~ 0.05 in contrast to our much smaller intensity ratio of ~ 0.002 . Thus the XRD confirms the Raman analysis, indicating that the alloys in this study do not exhibit significant long range ordering.

More insight into the alloy micro-structure may be obtained from the Raman linewidth behavior. Figure 3 presents the Raman linewidth of the E2 mode as a function of the composition. The linewidth behavior follows a pattern which exhibits a maximum at composition $x \approx 0.5$, a value at which a maximum disorder should be expected in a random system. The solid line in the figure was calculated (in arbitrary units) using the relation for the

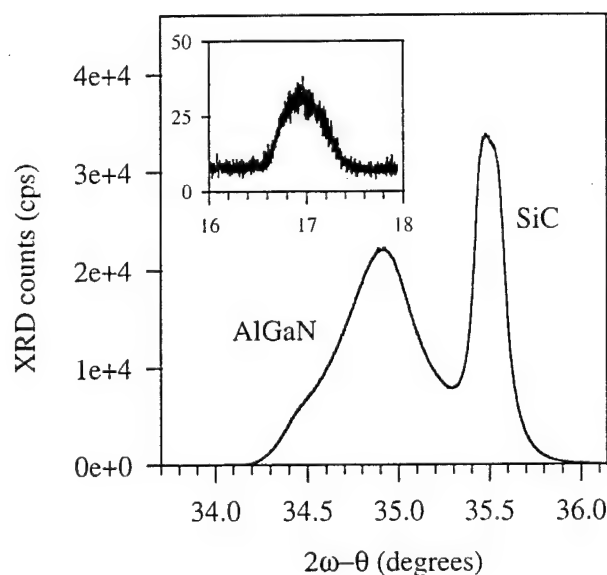


Figure 2. The (0002) X-ray diffraction of $\text{Al}_{0.22}\text{Ga}_{0.78}\text{N}$; the scan displays the SiC substrate peak. The inset to the figure shows the very weak (0001) superlattice line.

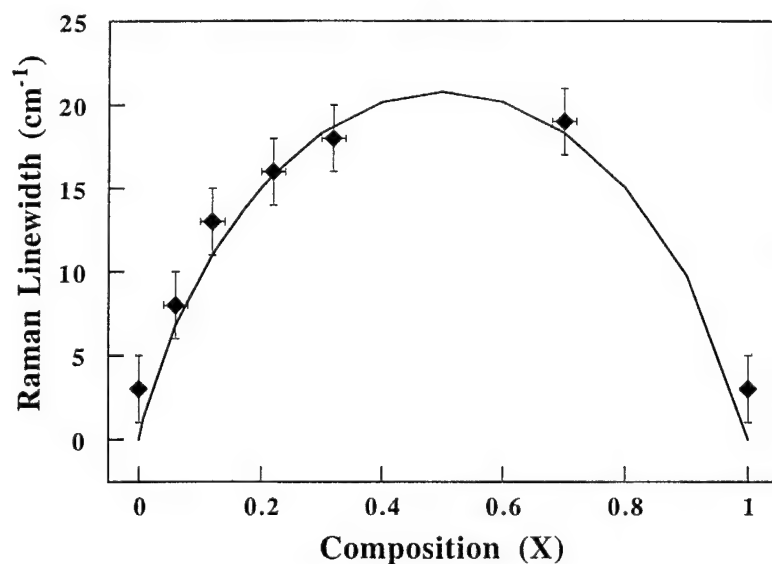


Figure 3. The E2 Raman linewidth as a function of composition (dots). The solid line is obtained from calculations of the entropy of mixing of an alloy system (in arbitrary units).

entropy of mixing which is a measure of the configurational disorder in a random alloy [19]. Thus our data suggest that the distribution of the alloy constituents for the most part is random. The issue of randomness in $A_xB_{1-x}C$ alloys has been previously addressed and it was suggested that the anions, C, are periodically distributed in their sub-lattice sites while the cations, A and B, are randomly distributed in the other sub-lattice [2, 20]. However, achieving an ordered alloy in some families of ternary tetrahedral semiconductors has been demonstrated to be a function of the growth temperature [20]; the conditions for the ordered state in the $Al_xGa_{1-x}N$ system have yet to be explored.

To conclude, the asymmetric behavior of the E2 Raman linewidth of $Al_xGa_{1-x}N$ alloys was attributed to the activation of phonons of $q \geq 0$ arising from the disordered state of the alloys. X-ray diffraction supports the finding; the superlattice relative line-intensity is weak. The line broadening of the E2 Raman mode exhibits a maximum at composition $x \approx 0.5$ which is consistent with a random distributed system.

Acknowledgments

We acknowledge the National Research Council, the Army Research Office, and the Office of Naval Research for supporting this research.

References

1. P. Parayanthal, and F.H. Pollak, Phys. Rev. Lett. **52**, 1822 (1984).
2. I. Sela, V.V. Gridin, R. Beserman, R. Sarfaty, D. Fekete, and H. Morkoc, J. Appl. Phys. **63**, 966 (1988).
3. R.K. Chang, B. Lacin, and P.S. Pershan, Phys. Rev. Lett. **17**, 755 (1966).
4. B. Jusserand, and J. Sapriei, Phys. Rev. **B24**, 7194 (1981).
5. O. Brafman, I.F. Chang, G. Lengyel, and S.S. Mitra, Phys. Rev. Lett. **19**, 1120 (1967).
6. *Topics in Applied Physics-Light Scattering in Solids I*, Edited by M. Cardona, (Springer-Verlag, New York, 1983).
7. C. A. Arguello, D.L. Rousseau, and S.P.S. Porto, Phys. Rev. **181**, 1351 (1969).
8. M.D. Bremser, W.G. Perry, N.V. Edwards, T. Zheleva, N. Parkin, D.E. Aspnes, and R.F. Davis, Mat. Res. Soc. Symp. Proc. **395**, 195 (1995).
9. C.M. Balkas, Z. Sitar, T. Zheleva, L. Bergman, I.K. Shmagin, J.F. Muth, R. Kolbas, R.J. Nemanich, and R.F. Davis, Mat. Res. Soc. Symp. Proc. **449**, 41 (1997).
10. L. Bergman, M.D. Bremser, J.A. Christman, S.W. King, R.F. Davis, and R.J. Nemanich, Mat. Res. Soc. Symp. Proc. **449**, 725 (1997).
11. D.D. Manchon, A.S. Baker, P.J. Dean, and R.B. Zetterstorm, Sol. Stat. Commu. **8**, 1227 (1970).
12. R.J. Nemanich, S.A. Solin, and R.M. Martin, Phys. Rev. **B23**, 6348 (1981).
13. P.M. Fauchet, and I.H. Campbell, Critical Reviews in Solid State and Materials Science **14**, S79 (1988).
14. K. Hayashi, K. Itoh, N. Sawaki, and I. Akasaki, Sol. Stat. Commu. **77**, 115 (1991).
15. L. Bergman, and R.J. Nemanich, Annu. Rev. Mater. Sci. **26**, 551 (1996), (and references within).
16. T. Azuhata, T. Matsunaga, K. Shimada, K. Yoshida, T. Sota, K. Suzuki, and S. Nakamura, Physica **B219/220**, 493 (1996).

17. D. Korakakis, H.M. Ng, K.F. Ludwig Jr., and T.D. Moustakas, Mat. Res. Soc. Symp. Proc. **449**, 233 (1997).
18. B.D. Cullity, *Elements of X-Ray Diffraction*, (Addison-Wesley, Menlo Park, 1978).
19. D. Gaskell, *Introduction to Metallurgical Thermodynamics*, (Hemisphere Publishing Corporation, New York, 1981).
20. A. Zunger, Appl. Phys. Lett. **50**, 164 (1987).

XVII. Theory of C, Si, and Ge Impurities in GaN and AlN

P. Bogusławski^{1,2}, and J. Bernholc²

1. Institute of Physics PAN, 02-668 Warsaw, Poland.

2. Department of Physics, North Carolina State University, Raleigh, NC 27695

Abstract

Electronic structure of substitutional group-IV impurities C, Si, and Ge in hexagonal GaN and AlN were studied by quantum molecular dynamics. C_N is a very shallow acceptor, and thus a promising p -type dopant. Both Si and Ge are excellent donors in GaN. However, in AlGaN alloys the DX configurations are stable for a sufficiently high Al content, which quenches the doping efficiency. Electronic structure of nearest-neighbor $X_{cation}-X_N$ pairs is also discussed.

Current interest in wide band-gap nitrides is due to possible applications in blue/UV light-emitting diodes and lasers, and in high-temperature electronics [1,2]. To exploit fully the potential of these materials, understanding and control of doping needs to be achieved. In the present work we study substitutional group-IV $X=C$, Si , and Ge impurities in the hexagonal (wurtzite) GaN and AlN . These species are potentially important dopants (*e.g.*, Si is frequently used as a n -type dopant of epitaxial GaN). On the other hand, both C and Si may be unintentionally incorporated as contaminants during growth.

In general, a group-IV atom is likely to become a donor when incorporated on the cation site, and an acceptor on the anion site. This possibility of the amphoteric behavior critically depends on the conditions of growth. We have recently shown [3] that C is preferentially incorporated on the N site under Ga-rich conditions of growth, while both Si and Ge occupy cation sites under N-rich conditions. However, under other conditions self-compensation, *i.e.*, a simultaneous incorporation of the dopant on both cation and anion sublattice, is expected. For this reason we discuss here the electronic structure of X_{cation} , X_N , and $X_{cation}-X_N$ nearest-neighbor pairs. We also consider a possible transition of X_{cation} from the substitutional to the DX-like configuration. Such a transition is commonly accompanied by a capture of electron on a stable (or metastable) state, which quenches the doping efficiency. Some of the results for C were published in [4]. The calculations were performed using quantum molecular dynamics [5]. Technical details were given in [6]. Soft pseudopotentials for N and C were used [7], while the pseudopotential of Ge was generated according to Ref. [8].

We first briefly discuss configurations of substitutional impurities and strain effects. A substitutional impurity in a wurtzite crystal has four nearest neighbors. One of them, located along the c -axis relative to the impurity (called here type-1 neighbor), is non-equivalent to the remaining three neighbors (called here type-2 neighbors). For the group-IV atoms considered here, this non-equivalence is small, since the bond lengths with type-1 and type-2 neighbors are equal to within 1 per cent. In all cases, we find breathing mode distortions preserving the local hexagonal symmetry. The calculated changes in bond lengths are given in Table I, together with the energy gain E_{rel} due to the relaxation from the ideal substitutional

configuration to the final one. As follows from Table I, the inclusion of relaxation effects is necessary for a proper description of C_{cation} , Si_N , and Ge_N , due to the large differences between the atomic radii of the impurity and host atoms. The most drastic case is that of Ge_N in AlN: the lattice relaxation releases the elastic energy ΔE_{rel} of 7 eV, rises the acceptor level by 1.05 eV, and increases the Ge-N bonds by 17 per cent. Very similar results are obtained for AlN:Si. The calculated ΔE_{rel} are systematically greater for AlN than for GaN, reflecting the higher stiffness of AlN.

Table I. Effects of atomic relaxations around impurities. Δb is the change of the bond length, ΔE_{rel} is the relaxation energy, E_{imp} is the position of the impurity level, with e.m. denoting the effective-mass state, and ΔE_{imp} is the relaxation-induced shift of the impurity level.

| | Δb (%) | ΔE_{rel} (eV) | E_{imp} (eV) | ΔE_{imp} (eV) |
|-------|----------------|-----------------------|----------------|-----------------------|
| GaN | | | | |
| C:Ga | -18.1 | 1.65 | e.m. | — |
| Si:Ga | - 5.6 | 0.65 | e.m. | — |
| Ge:Ga | - 1.4 | 0.25 | e.m. | — |
| C:N | -2.0 | 0.1 | $E_v+0.2$ | — |
| Si:N | 13.6 | 3.9 | $E_v+1.2$ | 0.8 |
| Ge:N | 13.5 | 4.1 | $E_v+1.35$ | 0.8 |
| AlN | | | | |
| C:Al | -17.2 | 2.6 | $E_c-0.4$ | 1.2 |
| Si:Al | - 7.0 | 0.7 | e.m. | — |
| Ge:Al | - 2.9 | 0.3 | e.m. | — |
| C:N | 2.0 | 0.4 | $E_v+0.4$ | 0.1 |
| Si:N | 16.5 | 6.75 | $E_v+1.7$ | 1.0 |
| Ge:N | 16.7 | 6.95 | $E_v+1.75$ | 1.05 |

As follows from Table I, C, Si, and Ge occupying the cation site in both GaN and AlN are effective-mass donors. The only exception is C_{Al} in AlN, where the C-induced level is at about 0.4 eV below the bottom of the conduction band. In GaN, because of its lower band gap, the C-derived level is a resonance situated at 0.9 eV above the bottom of the conduction band.

In addition to the substitutional configuration of X_{cation} donors, we have investigated the stability of the DX-like configuration [9]. In this configuration one bond between the impurity and its first neighbor is broken, and one of these atoms (or both) are shifted to an interstitial site. We have analyzed only one possible DX state, namely that with the broken bond between the impurity and the type-1 neighbor; the configuration with the broken bond to the type-2 N atom should have very similar properties.

We first consider GaN. We find that C_{Ga}^* is metastable not only in the negative but also in the neutral charge state. The energy of C_{Ga}^* is higher than that of the substitutional C_{Ga} by 0.54 and 0.35 eV for the neutral and the negative charge state, respectively. In the DX state both the host N atom and the impurity are significantly displaced along the c -axis (see Ref. [4] for details). In contrast, Si is unstable in the DX state, since there is no energy barrier for the transition from the initial DX configuration to the substitutional one. This holds for both the neutral and the negatively charged Si. Finally, a DX state is metastable for the negatively charged Ge, and its energy is higher by 0.3 eV than that of Ge_{Ga}^- . Unlike for C_{Ga}^* , Ge atom is located at the lattice site, and the nearest-neighbor N atom is displaced along the c -axis. The Ge-N distance is 2.61 Å, to be compared with 1.93 Å for the substitutional configuration. $Ge_{Ga}^*(-)$ introduces a singlet at about 0.4 eV below the bottom of the conduction band. For the neutral charge state, the DX configuration is unstable.

Turning to AlN, we find that in the negative charge state C_{Al}^* is more stable than C_{Al}^- by 0.2 eV. In the neutral charge state C_{Al}^* is metastable, as its energy is higher by 0.48 eV than that of the ground state. Unlike in GaN, the DX configurations are *stable* for both Si and Ge in the negative charge state. Their energies are lower by 0.15 and 1.2 eV than those of

the respective substitutional cases. In both cases the impurity remains on the substitutional site, and the N atom is strongly displaced. For Si_{Al}^* the distance to the N atom is 2.95 Å compared to 1.78 Å for Si_{Al} , and for Ge the respective values are 2.83 and 1.86 Å. $\text{Si}_{\text{Al}}^*(-)$ introduces a level at -1.5 eV below the bottom of the conduction band. For Ge, the gap state is even deeper, at -2.0 eV below the bottom of the conduction band. Finally, the DX configurations are unstable for both Si and Ge in the neutral charge state.

The different DX configurations found for C, as opposed to Si and Ge, are in part due to atomic size effects. For example, when C substitutes the much bigger Ga atom, the C-N bonds are highly stretched, because they are shorter than the equilibrium Ga-N bonds by about 15 %. In the DX state one C-N bond is broken, and C is free to relax and to shorten the three remaining C-N bonds. Consequently, the C_{Ga}^* -N bonds are shorter by about 7 % than C_{Ga} -N bonds in the substitutional case. At equilibrium, C^* forms a nearly planar configuration with the type-2 neighbors. Such a geometry is additionally stabilized by the tendency of C to form planar sp^2 bonds. Both factors may contribute to the stabilization of C_{Ga}^* in the neutral charge state. In contrast, these factors are not operative for Si and Ge impurities, which remain on the substitutional site.

The predicted stability of DX^- states for C, Si, and Ge in AlN implies that the reaction $2d^0 \rightarrow d^+ + \text{DX}^-$ is exothermic, and the electrons are captured by the deep DX-derived levels. Consequently, the doping efficiency is quenched. In $\text{Al}_{1-x}\text{Ga}_x\text{N}$ alloys the doping efficiency with C, Si, and Ge should thus strongly depend on the alloy composition. These dopants should be efficient donors up to a crossover composition given by the stability of the DX state. A theoretical estimate for the crossover may be obtained by a linear interpolation between the results obtained for the pure end compounds. This composition is 0.65 for C, and 0.2 for Ge.

We shall now consider the acceptors X_N . In zinc-blende crystals, acceptor levels of group-IV atoms are three-fold degenerate. Due to the wurtzite symmetry of GaN and AlN, the triplets are split into doublets and singlets by the energy E_{split} . In all cases considered here, the energies of doublets (given in Table I), E_D , are higher than those of singlets, E_S .

Both the acceptor energies and the splittings strongly depend on the impurity. We find that C is a shallow acceptor with $E_D=0.2$ eV in GaN, which is in an excellent agreement with the recent experimental data [10]. Thus, C is a promising p -type dopant, since it is a shallower acceptor than the commonly used Mg [2]. In AlN, C is deeper ($E_D=0.4$ eV) and more localized. The doublet-singlet splitting E_{split} is about 0.2 eV in both materials. In contrast, both Si and Ge are deep acceptors. For GaN:Si $E_D=1.2$ eV and $E_{split}=0.6$ eV, and for GaN:Ge $E_D=1.35$ eV and $E_{split}=0.6$ eV. In AlN the binding energies and the splittings are even higher, and we find $E_D=1.7$ (1.75) eV and $E_{split}=0.7$ (0.7) eV for Si_N and Ge_N , respectively).

Finally, we turn to the electronic structure of the nearest-neighbor $X_{cation}^+-X_N^-$ pairs. Compared to the case of distant X_{cation} and X_N impurities, the main modification is a substantial increase of the doublet-singlet splittings. In the case of GaN, E_{split} rises from 0.6 to 1.0 eV for Si-Si pairs, and from 0.6 to 1.05 eV for Ge-Ge pairs. For AlN, the increase is from 0.7 to 1.4 eV for Si-Si pairs, and from 0.7 to 1.35 eV for Ge-Ge pairs. This effect is due to the close proximity of the X_{cation} donor, located along the c -axis relative to the acceptor X_N . The presence of the donor enhances the non-equivalence between the z -symmetry singlet and the (x, y) -symmetry doublet states.

As it follows from our results, properties of Si and Ge are similar, but they are qualitatively different from those of C. These differences are due to both different atomic energies of s and p orbitals (lower for C than for Si and Ge by about 1 eV), and differences in atomic radii, which affect both atomic relaxations and hybridization of the orbitals.

This work was supported in part by Grants KBN 2-P03B-178-10, ONR N00014-92-J-1477, and NSF DMR 9408437.

REFERENCES

- [1] R. F. Davis, *Physica B* **185**, 1 (1993).
- [2] H. Morkoc, S. Strite, G. B. Gao, M. E. Lin, B. Sverdlov, and M. Burns, *J. Appl. Phys.* **76**, 1363 (1994).
- [3] P. Bogusławski and J. Bernholc, to be published.
- [4] P. Bogusławski, E. M. Briggs, and J. Bernholc, *Appl. Phys. Lett.*, in print.
- [5] R. Car and M. Parrinello, *Phys. Rev. Lett.* **55**, 2471 (1985).
- [6] P. Bogusławski, E. M. Briggs, and J. Bernholc, *Phys. Rev. B* **51**, 17255 (1995).
- [7] G. Li and S. Rabi, unpublished (1992).
- [8] X. Gonze, R. Stumpf, and M. Scheffler, *Phys. Rev. B* **44**, 8503 (1991).
- [9] D. J. Chadi and K. J. Chang, *Phys. Rev. Lett.* **61**, 873 (1988).
- [10] S. Fisher, C. Wetzel, E. E. Haller, and B. K. Meyer, *Appl. Phys. Lett.* **67**, 1298 (1995).

XVIII. Strain Effects on the Interface Properties of Nitride Semiconductors

Marco Buongiorno Nardelli, Krzysztof Rapcewicz and J. Bernholc

Department of Physics, North Carolina State University, Raleigh, NC 27695-8202

Abstract

An *ab initio* study of nitride-based heteroepitaxial interfaces that explicitly treats the strain due to lattice-mismatch is presented. AlN is the preferred substrate and strain effects on the band offsets range from 20% to 40%. The AlN/GaN/InN interfaces are all of type I, while the Al_{0.5}Ga_{0.5}N/AlN zinc-blende (001) interface may be of type II. Further, the calculated bulk polarizations in wurtzite AlN and GaN are -1.2 and -0.45 $\mu\text{C}/\text{cm}^2$, respectively, and the interface contribution to the polarization in the GaN/AlN wurtzite multi-quantum-well is small.

71.15.Hx, 71.15.Nc, 81.05.Ea, 73.40.Kp

With the recent demonstration of stimulated emission in the blue region of the spectrum from a nitride-based multi-quantum-well structure [1], interest in the nitride-based semiconductors has burgeoned. This discovery has served to underscore the very attractive properties of the nitride-based materials, which include a wide band-gap and the ability to form a continuous range of solutions of GaN, AlN and InN, materials which have very different band gaps. This latter property makes possible the engineering of band gaps which span the range from the deep ultra-violet to the visible [2].

Not surprisingly the potential technological importance of these materials has elicited the interest of a number of theoretical groups [3–7]. In spite of this, the strained interfaces of these lattice-mismatched materials have not been studied. We find that strain effects are significant and AlN lattice-matched substrates are clearly preferred for pseudomorphic heteroepitaxial growth. Further, the strain induces changes of 20% to 40% in the value of the band offset and these changes increase with decreasing in-plane lattice parameter. The AlN/GaN/InN interfaces are all of type I, while the $\text{Al}_{0.5}\text{Ga}_{0.5}\text{N}/\text{AlN}$ zinc-blende (001) interface is found to be of type II. Finally, we studied the GaN/AlN wurtzite interface, where qualitatively new features, namely pyro- and piezoelectric effects, appear due to the low symmetry of the wurtzite lattice.

The standard *ab initio* plane-wave pseudopotential method [8–10] was employed in the calculations. The energy cut-off for the plane-wave expansion was 50 Ry to ensure convergence of the nitrogen pseudopotential. We used the equivalent of 10 k-points for bulk and superlattice calculations in the zinc-blende structure [11] and 6 k-points for calculations of the wurtzite structure [12]. Convergence both in the size of the plane-wave basis and in the number of special points has been carefully checked. The Perdew-Zunger parametrization [13] of the Ceperley-Alder form [14] of the exchange-correlation energy was used. For interface calculations, we employed 4+4 superlattices (16 atoms) along the (001) and (0001) directions. The non-local, norm-conserving pseudopotentials [15–17] were included using the Kleinman-Bylander approach [18]. For nitrogen, we used a neutral configuration as the atomic reference for all states.

In pseudopotentials where d -electrons are treated as core electrons, experience with II-VI semiconductors [19] has shown that the inclusion of the nonlinear core correction [20] results in a substantial improvement of the bulk properties. As an early work demonstrated [5], the reference atomic state plays a critical role in the generation of the pseudopotential. In order that the pseudopotential be consistently descreened, it is necessary, when using the nonlinear core correction, that the reference atomic state be the same for all angular-momentum channels. This is in contrast with standard Bachelet, Hamann and Schlüter prescription [15] in which the atomic ground state is used as a reference for each angular-momentum channel present in the ground state, while, to improve transferability, an appropriately ionized, excited-atom configuration is used as the reference state for the angular-momentum channels present only in the excited states. Dal Corso et al. [21] have dealt with the inconsistency between the restriction imposed by the use of the nonlinear core correction and the importance of different atomic reference configurations for different angular-momentum channels by simultaneously fitting the pseudopotential and the core charge to more than one configuration.

The approach used here resolves this inconsistency while maintaining the improved transferability obtained through the choice of different, atomic reference configurations. This is achieved by choosing as the initial reference configuration the neutral ground state and generating the angular momenta channels for it together with the core charge. For angular momenta present only in the excited states, we use the appropriately ionized, excited-atom configuration of the frozen-core atom (with the core from the neutral ground state). We generated pseudopotentials for aluminium, gallium and indium with this procedure using the standard reference configurations for the empty d -channel [16,22], namely $3s^{0.75} 3p^0 3d^{0.25}$ for aluminium, $4s^{0.75} 4p^0 4d^{0.25}$ for gallium and $5s^1 5p^{0.75} 5d^{0.25}$ for indium.

The calculated bulk properties are presented in Table I. In general, agreement with experiment is excellent [23,24]. The theoretical lattice parameters of both the zinc-blende and wurtzite forms agree very well with experiment; a similar level of accuracy is expected for the interface calculations described below. We have also calculated the bulk properties of

GaN treating the 3*d*-electrons of gallium as valence electrons following Ref. [7]. With a cut-off of 240 Ry, we find $a_0 = 4.46$ Å and $B_0 = 2.14$ Mbar, which reproduces the experimental values to the same degree as our calculations employing the present pseudopotentials with the *d*-electrons in core.

The properties of nitride-based semiconductor devices are critically dependent upon their interface properties. Due to the lattice-mismatch between AlN and GaN (3.5%) and between InN and AlN (12.8%), superlattices of these materials are expected to be strained [25]. We investigate first the (001) zinc-blende interface. The supercell for the strained superlattice was determined using macroscopic elasticity theory [26]. In this theory, each half of the heterojunction is treated as a strained bulk with a fixed in-plane lattice constant $a_{||}$. The perpendicular lattice constant of the epilayer c is obtained by minimizing the strain energy of the system subject to the fixed in-plane constant. For AlN, GaN and InN, the calculated elastic constants used to determine the strains are given in Table II. Using total energy calculations, we find that macroscopic elasticity theory predicts well the perpendicular lattice constant for the epilayer. The residual relaxation of the atoms at the interface is negligible (< 0.05 Å) and does not affect the band offset of the interface.

The interface energy for the (001) direction can be calculated in a straightforward manner because the supercell contains two identical interfaces. The interface energy of the interface AC/BC is

$$E_{interface} = \frac{1}{2}(E_{supercell} - N_{AC}E_{AC} - N_{BC}E_{BC}), \quad (1)$$

where E_{AC} (E_{BC}) is the energy of the AC (BC) pair in the appropriately strained bulk and N_{AC} (N_{BC}) is the number of AC (BC) pairs in the supercell. We considered three different interfaces, namely the strained GaN/AlN (with AlN in-plane lattice constant), the strained AlN/GaN (with GaN in-plane lattice constant) and the “unstrained” GaN/AlN (with average lattice parameter) interfaces. In each case, the interface energy was found to be extremely small, ~ 1 meV/interface atom, which is of the order of the precision of the calculations. Therefore, all of the interfaces show similar bonding characteristics. This is not

the case, however, with the elastic energies of the interfaces. The elastic energy, which is the difference of the strained energy and the unstrained energy per pair, manifests itself as an extrinsic volume effect governing the thickness of the pseudomorphic layer. We find that the elastic energy is 46 meV/pair for GaN/AlN and is 63 meV/pair for AlN/GaN. The elastic energy in the “unstrained” case is comparable to that in AlN/GaN. Thus the critical thickness for pseudomorphic AlN/GaN is significantly smaller than GaN/AlN, an observation which is consonant with the fact that epitaxially grown GaN/AlN results in higher quality samples [2]. In the light of these conclusions, we restrict further considerations to interfaces grown on an AlN substrate, i.e. the in-plane lattice constant for all the superlattices is the AlN value.

We have investigated the band offsets of the (001) GaN/AlN, InN/AlN and InN/GaN strained heterojunctions following the procedure of Ref. [27]. In each case AlN is taken to be the substrate. The results are shown in Fig. 1 [28]. We find that each interface is of type I, with the InN band edges sandwiched by the band-edges of the other materials, since the band gap in InN is the smallest. The transitivity rule is satisfied. We do not observe any interface states in the gap of the superlattice. As might be expected, states at the top of the valence band are mostly localized to the epilayer with the smaller gap. Similar behavior is observed for the conduction-band minimum; the degree of localization of the states at the conduction-band minimum increases with increasing band offset. Strain effects on the valence-band offsets have been investigated for the interfaces formed by AlN and GaN. They vary between 20% and 40%. In particular, the valence-band offsets are -0.75 eV for GaN/AlN, -0.44 eV for AlN/GaN and -0.58 eV for “unstrained” GaN/AlN.

The case of the wurtzite (0001) GaN/AlN interface was also investigated. Strain effects were explicitly included using macroscopic elasticity theory [29] and a total energy optimization. The calculated valence-band offset is estimated to be -0.57 eV, a value smaller than the result for the strained non-polar (001) GaN/AlN interface. The ratio of the conduction-band to valence-band offset is 65:20. Our results agree very well with the experimental measurements of the (0001) wurtzite interface [30].

The possible sources of systematic error of the calculation include the neglect of the anion p - and cation d -state repulsion [31] and the well-known neglect of many-body effects in the LDA. In GaN/AlN interfaces, the inclusion of the $3d$ -electrons as valence electrons results in a constant shift of 0.2 eV, which is less than the experimental error [30], and does not change the character of the interface. Incorporating this shift gives results in agreement with previous estimates using a d -valence pseudopotential [6] and an all-electron calculation [4]. The importance of many-body effects on the band offsets is not known and awaits a future GW calculation.

Because of its low symmetry, the wurtzite system may display pyroelectric and piezoelectric behavior [32]. These effects, if present, will manifest themselves macroscopically in multi-quantum-wells along those directions that do not have a perpendicular mirror-plane [33,34]. Thus, for instance, macroscopic fields are not observed in the strained (001) interfaces in zinc-blende structure, while they are observed in strained (111) interfaces [33]. Indeed, a polarization will be induced only if off-diagonal components of the strain are present. In (0001) strained GaN/AlN, we observe a substantial electric field as has been previously noted by Satta and coworkers [35]. In order to distinguish the bulk pyroelectric and piezoelectric contributions to this field from that induced by the interface, we have calculated the spontaneous bulk polarization of unstrained AlN and the strain induced polarization for the GaN epilayer [36]. The spontaneous polarization (P_3) of AlN and GaN in equilibrium are $-1.227 \mu\text{C}/\text{cm}^2$ and $-0.448 \mu\text{C}/\text{cm}^2$ respectively; the polarization of the strained GaN is $-0.454 \mu\text{C}/\text{cm}^2$. These values are comparable to the computed bulk polarization in BeO [36]. The effect of the interface dipole is small; the polarization in the GaN/AlN multi-quantum-well is well described by the superposition of the polarizations of the constituent epilayers of the multi-quantum-well. The estimated contribution of the interface dipole (which includes the response of one epilayer to the field of the other) is $0.057 \mu\text{C}/\text{cm}^2$, which is of opposite sign and an order of magnitude smaller than the bulk polarizations. The computed value of the polarization in the superlattice agrees with that estimated from experiment by Martin *et al.* [30].

Alloying provides another way to tune band offsets through changes to the strain in the system and changes to the electronic structure. The virtual crystal approximation in which the pseudopotentials of the constituent species are averaged by their fractional composition has been shown to adequately describe band offsets in certain alloy interfaces [37]. We have studied the zinc-blende (001) $\text{Al}_{0.5}\text{Ga}_{0.5}\text{N}/\text{AlN}$ interface in the virtual crystal approximation. First, we used the virtual crystal approximation to calculate the elastic properties of the zinc-blende alloy (with theoretical lattice constant of 4.44 \AA), finding $c_{11} = 23.55 \times 10^{11} \text{ dyne/cm}^2$ and $c_{12} = 11.84 \times 10^{11} \text{ dyne/cm}^2$, and used macroscopic elasticity theory to predict the strains. In contrast to the pure nitride interfaces, we found that this particular alloy interface is a staggered type II interface. The valence-band offset is -0.39 eV and the conduction-band offset -0.17 eV . In order to verify the accuracy of the approach, we compared the lineup of the virtual crystal approximation with a fully relaxed $(\text{GaN})_1(\text{AlN})_1/\text{AlN}$ interface; the alloy was replaced by the 1×1 superlattice, an extreme example of an ordered alloy. The results are -0.37 eV and -0.09 eV for the valence- and conduction-band offsets, respectively. Further, the character of the interface remains unchanged. Therefore, the virtual crystal approximation well describes the band offsets of this alloy superlattice and, within the present theoretical scheme, the interface will change its character as the gallium composition of the alloy is increased.

In summary, we have investigated the influence of strain on the interface properties of nitride-based heterostructures. In these lattice-mismatched heterojunctions, the in-plane lattice constant can be varied by changing the characteristics of the substrate and so tune the band offset. The elastic energy of the AlN/GaN interface is appreciably larger than that of the GaN/AlN interface, making AlN the preferred substrate for pseudomorphic growth. Strain effects on the band offsets in GaN/AlN range from 20% to 40%. The bulk spontaneous polarization of the constituent materials, which range from -1.227 to $-0.448 \times 10^{-2} \text{ C/m}^2$ for AlN and GaN , respectively, constitutes the preponderant contribution to the polarization present in the low symmetry wurtzite GaN/AlN interface, i.e. the interface contribution to the polarization is small. Finally, the pure interfaces are all of type I, while

the $\text{Al}_{0.5}\text{Ga}_{0.5}\text{N}/\text{AlN}$ interface may be of type II, suggesting that a change of character will occur as the gallium composition of the alloy is increased.

We acknowledge helpful conversations with Drs. D. J. Sullivan and E. L. Briggs.

REFERENCES

- [1] S. Nakumura et al., Jpn. J. Appl. Phys. **35**, L74 (1996).
- [2] See, for instance, H. Morkoç et al., J. Appl. Phys. **76**, 1363 (1994), M. Paisley and R. Davis, J. Cryst. Growth **127**, 136 (1992).
- [3] These include: A. Rubio, J. Corkill and M.L. Cohen, Phys. Rev. B **49**, 1952 (1994), C. Yeh, S. Wei and Z. Zunger, Phys. Rev. B **50**, 2715 (1994) and M. Palummo, L. Rein- ing, R.W. Godby, C.M. Bertoni and N. Bornsen, Europhys. Lett. **26**, 607 (1995). For a general reference, W. Lambrecht and B. Segall, in *Properties of Group III Nitrides*, edited by J. Edgar, EMIS Data Series (IEE, London, 1994), chapt. 5.
- [4] E. Albanesi, W. Lambrecht and B. Segall, J. Vac. Sci. Technol. B **12**, 2470 (1994).
- [5] B. Min, C. Chan and K. Ho, Phys. Rev. B **45**, 1159 (1992).
- [6] V. Fiorentini, M. Methfessel and M. Scheffler, Phys. Rev. B **47**, 13353 (1993).
- [7] A. Wright and J. Nelson, Phys. Rev. B **50**, 2159 (1994); Phys. Rev. B **51**, 7866 (1995).
- [8] M. Payne, M. Teter, D. Allan, T. Arias and J. Joannopoulos, Rev. Mod. Phys. **64**, 1045 (1992).
- [9] W. Pickett, Comp. Phys. Rep. **9**, 115 (1989).
- [10] D. Remler and P. Madden, Mol. Phys. **70**, 921 (1990).
- [11] S. Froyen, Phys. Rev. B, **39**, 3168 (1989).
- [12] D.J. Chadi and M.L. Cohen, Phys. Rev. B **8**, 5747 (1973).
- [13] J. Perdew and A. Zunger, Phys. Rev. B **23**, 5048 (1981).
- [14] D. Ceperley and B. Alder, Phys. Rev. Lett. **45** 566 (1980).
- [15] G. Bachelet, D. Hamann and M. Schlüter, Phys. Rev. B **26**, 4199 (1982).

- [16] D. Hamann, M. Schlüter and C. Chiang, Phys. Rev. Lett. **43**, 1494 (1979).
- [17] D. Hamann, Phys. Rev. B **40**, 2980 (1989).
- [18] L. Kleinman and D. Bylander, Phys. Rev. Lett. **48**, 1425 (1982).
- [19] G. Engel and R. Needs, Phys. Rev. B **41**, 7876 (1990) and A. Qteish and R. Needs, Phys. Rev. B **43**, 4229 (1991).
- [20] S. Louie, S. Froyen and M.L. Cohen, Phys. Rev. B **26**, 1738 (1982).
- [21] A. Dal Corso, R. Resta, S. Baroni and S. de Gironcoli, Phys. Rev. B **47**, 3588 (1994) and A. Dal Corso, Ph.D. Thesis, Trieste, (1993).
- [22] X. Gonze, P. Käckell and M. Scheffler, Phys. Rev. B **17**, 12264 (1990).
- [23] Transferability was also verified by calculating the bulk properties of AlAs, GaAs and InAs; we find the same degree of accuracy as commonly used pseudopotentials.
- [24] Calculations for aluminium metal show excellent agreement with experiment and prior calculations, E. Briggs, (private communication, 1996).
- [25] The percentages given refer to the computed mismatch in the zinc-blende structure and the computed mismatch of the in-plane lattice constant in wurtzite, which are the same for both structures. Further, the experimental lattice-mismatch between AlN and GaN is 2.5% while between AlN and InN it is 12.1%.
- [26] C. Van de Walle and R.M. Martin, Phys. Rev. B **34**, 5621 (1986).
- [27] A. Baldereschi, S. Baroni and R. Resta, Phys. Rev. Lett. **61**, 734 (1988).
- [28] In order to correct for the well-known underestimation of the band gaps by the LDA, the conduction-band offsets were corrected by shifting the conduction-band minima to recover the experimental band-gaps.
- [29] The experimental ratio [38], $c_{13}/c_{33} = 0.59$, was used to determine the starting point

of the total energy minimization.

- [30] G. Martin et al., Appl. Phys. Lett. **65**, 610 (1994), *ibid.* **68**, 2541 (1996).
- [31] S. Wei and A. Zunger, Phys. Rev. Lett. **59**, 144 (1987).
- [32] N. W. Ashcroft and N. D. Mermin, *Solid State Physics* (Saunders College, Philadelphia 1976). Ch. 27.
- [33] D. Smith, Solid State Commun. **57**, 919 (1986).
- [34] A. Bykhovski, B. Gelmont and M. Shur, Appl. Phys. Lett. **63**, 2243 (1993); J. Appl. Phys. **74**, 6734 (1993).
- [35] A. Satta, V. Fiorentini, A. Bosin, F. Meloni and D. Vanderbilt, preprint (1996)
- [36] M. Posternak, A. Baldereschi, A. Catellani and R. Resta, Phys. Rev. Lett. **64**, 1777 (1990).
- [37] M. Peressi, S. Baroni, A. Baldereschi and R. Resta, Phys. Rev. B **41**, 12106 (1990).
- [38] *Landolt-Börnstein: Numerical Data and Functional Relationships in Science and Technology*, ed. O. Madelung (Springer, New York, 1982), vol. 17.

TABLES

TABLE I. Calculated bulk properties of zinc-blende and wurtzite nitride semiconductors. The values of the gap at the Γ -pt (E_{Γ}) and of the valence-band width (ΔE_{vbw}) are the LDA results. Experimental values are in brackets and follow Ref. [7].

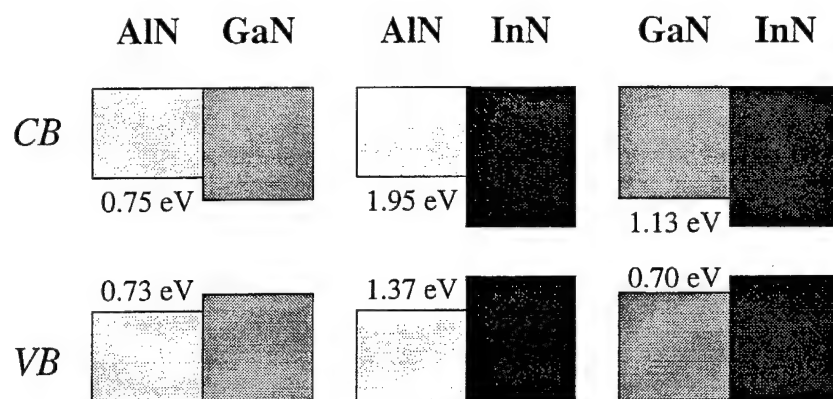
| zinc-blende | | | |
|-----------------------|---------------|-------------------|-------------------|
| | AlN | GaN | InN |
| a_0 (Å) | 4.37 (4.38) | 4.52 (4.5) | 5.01 (4.98) |
| B_0 (MBar) | 2.02 (2.02) | 1.70 (1.90) | 1.58 (1.37) |
| E_{Γ} (eV) | 4.09 | 2.24 (3.45) | 0.16 |
| ΔE_{vbw} (eV) | 14.86 | 15.48 | 14.01 |
| wurtzite | | | |
| a (Å) | 3.09 (3.11) | 3.20 (3.19) | 3.55 (3.54) |
| c/a | 1.62 (1.60) | 1.63 (1.63) | 1.63 (1.61) |
| u (units of c) | 0.378 (0.382) | 0.376 (0.377) | 0.375 |
| B_0 (MBar) | 1.99 (2.02) | 1.69 (1.95, 2.37) | 1.62 (1.26, 1.39) |
| E_{Γ} (eV) | 4.44 (6.28) | 2.29 (3.50) | 0.16 (1.89) |
| ΔE_{vbw} (eV) | 14.89 | 15.60 | 14.00 |

TABLE II. Elastic constants calculated for zinc-blende AlN, GaN and InN (in units of 10^{11} dyne/cm²). The experimental values in brackets are from wurtzite [38].

| | AlN | GaN | InN |
|----------|-------|------------------------|-------|
| c_{11} | 24.85 | 23.74 (29.6 \pm 1.8) | 20.24 |
| c_{12} | 13.37 | 11.23 (13.0 \pm 1.1) | 12.96 |

FIGURES

FIG. 1. Calculated band offsets for the three interfaces described in the text assuming an AlN substrate.



Marco Buongiorno Nardelli et al.

Figure 1.

XIX. UV Photoemission Study of Heteroepitaxial AlGaN Films Grown on 6H-SiC Surfaces

A. Introduction

There is increasing interest in electronic devices composed of III-nitride materials for optoelectronic applications in the blue and UV region [1]. An alternative application of these semiconductors is in electron emission devices. Recent studies have demonstrated that diamond surfaces can exhibit a negative electron affinity (NEA). NEA surfaces may prove to be critical elements for cold cathode devices, vacuum microelectronics, and photodetectors [2,3]. In addition to diamond, thin films of AlN grown on 6H SiC have been shown to exhibit a negative electron affinity (NEA) [4,5]. Some AlN NEA surfaces were obtained from air exposed surfaces, and do not appear to be readily poisoned. In contrast to diamond, AlN and GaN materials exhibit the wurtzite crystal structure. One of the most significant limitations in the application of diamond is that reliable n-type doping has not been achieved. In contrast, n-type doping has been obtained for GaN and some AlGaN alloys.

The wurtzite AlN and GaN form a continuous solid solution of $\text{Al}_x\text{Ga}_{1-x}\text{N}$ for $0 \leq x \leq 1$ with band gaps that range from 3.4 eV (GaN) to 6.2 eV (AlN). Figure 1 displays the band gap of several materials as a function of the equivalent hexagonal lattice constant. The alloys are also miscible with In, hence the inclusion of InN could extend the range to 1.9 eV. The electron affinity of a semiconductor is related to the surface dipole and to the fundamental energy levels

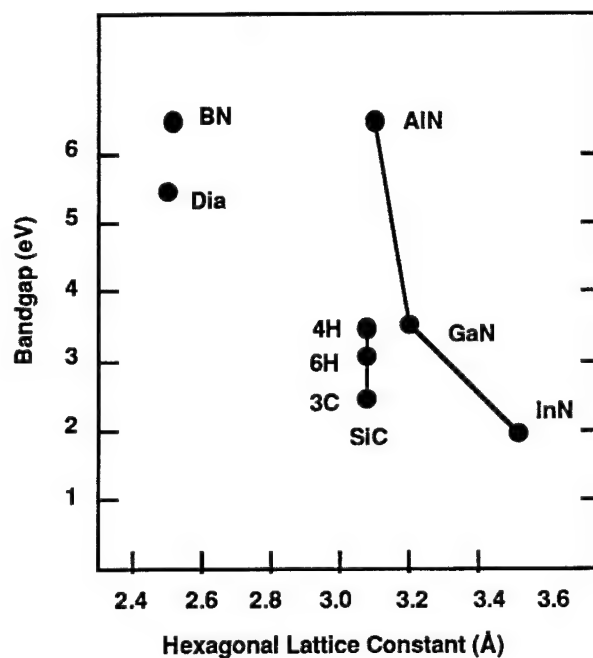


Figure 1. The band gap vs. hexagonal lattice constant (a) for a variety of wide band gap semiconductors. The lattice constant for the cubic materials has been determined from the (111) plane.

of the materials. Because the valence and conduction bands of the semiconductors have origin in the sp^3 bonding and antibonding levels, it may be suggested that the larger band gap materials will exhibit a smaller or negative electron affinity. In comparison with diamond, it might be assumed that AlGaN alloys with a band gap greater than 5.4 eV could exhibit an NEA. In this section, studies of AlN grown on alternative substrate orientations are reported.

The AlGaN films used in this study were grown on 6H-SiC substrates. The n-type SiC substrates used had a small lattice mismatch with AlN (3.08 Å vs. 3.11 Å) and GaN ($a = 3.19$ Å). The small lattice mismatch enabled heteroepitaxial growth of the wurtzite (2H) structure. Furthermore, the fact that the substrates were conducting avoided charging problems associated with photoemission from large band gap and insulating materials.

The electron affinity of a semiconductor or the presence of an NEA can be determined by ultraviolet photoemission spectroscopy (UPS) [6-8]. The experiments described here involve directing 21.2 eV light (the He I resonance line) to the surface of the sample and detecting the spectrum of the emitted photo excited electrons as a function of electron kinetic energy. Typically, UPS is used to obtain a profile of the valence band (VB) electronic states. As such, most studies of UPS of semiconductors present data of the most energetic electrons emitted from the surface. Electrons scattered to lower energy and secondary electrons will be displayed in the spectrum at lower kinetic energies. In addition, for a semiconductor which exhibits an NEA surface, a distinctive peak may be observed at the low kinetic energy (highest binding energy) end of the photoemission spectra. Figure 2 depicts a schematic representation of the photoemission spectra from a semiconductor with a negative or positive electron affinity. The low kinetic energy feature is due to secondary electrons which (quasi) thermalize to the

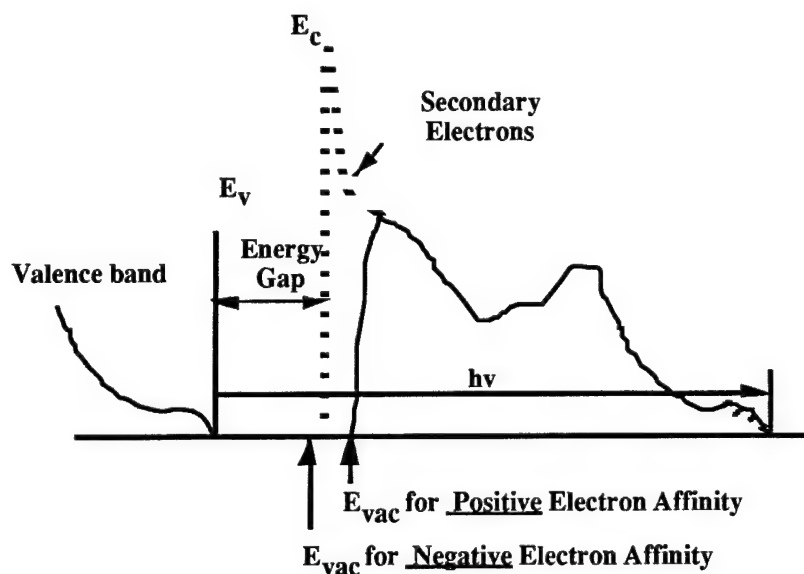


Figure 2. A schematic of the difference in the photoemission spectra of a semiconductor with a positive or negative electron affinity.

conduction band minimum. Note that the solid line indicates a material with a positive electron affinity while the dashed line is a feature indicative of an NEA. Samples with both positive and negative affinity surfaces will be discussed.

The sharp features typical of an NEA have been observed from spectra of (111) and (100) diamond surfaces [6-10]. In the studies of diamond, a correlation was made between the presence of hydrogen and the NEA peak [9,10]. In addition, it was also shown that thin metal layers such as Ti or other moderate work function metals could induce an NEA on the diamond surface [10,11]. These measurements verify that the surface dipole can be influenced by surface processing and that the effects contribute to the observation of an NEA.

B. Experimental Procedure

The 6H-SiC substrates used in this study were supplied by Cree Research, Inc. The samples were n-type with doping concentrations of 10^{16} to $10^{18}/\text{cm}^3$. To avoid surface contamination the AlGaN samples were grown in the integrated UHV transfer system by gas source molecular beam epitaxy (GSMBE). This allowed the alloys examined in this report to be completely studied in vacuum. This transfer system included the UPS system, LEED, Auger, hydrogen and argon plasma processing chamber, and XPS as well as the GSMBE. The system is described elsewhere [9,11].

Nitride thin films were previously grown on n-type, Si-face α (6H)-SiC(0001) substrates at 1000-1050°C. The as-received SiC pieces were degreased, dipped into a 10% HF solution for 10 minutes to remove the thermally grown oxide layer and blown dry with N_2 before being loaded onto the transfer system. Several compositions were examined including pure AlN and GaN.

The growth took place in a GSMBE. The cleaning procedure is described above, once in vacuum the substrate was annealed in a silane flux [12]. The samples were not intentionally doped, but since very thin films were employed, charging problems were avoided. Al and Ga are solid sources in K cells while Ammonia (NH_3) provides the N source.

The UPS measurements were excited with 21.21 eV radiation (He I resonance line), and emitted electrons are collected with a hemispherical energy analyzer. The base pressure of the UPS system is 2×10^{-10} Torr, and operating conditions involve pressures up to 1×10^{-9} Torr, but the higher pressure was due to the helium inflow and does not contaminate the sample. The 50 mm mean radius hemispherical electron analyzer was operated at a 0.15 eV energy resolution and a 2° angular resolution. The analyzer (VSW HA50) was mounted on a double goniometer and can be tilted with respect to the sample in two independent directions. The samples were fastened with tantalum wire to a molybdenum sample holder. The sample holder is biased by up to 3 V to allow low energy electrons to overcome the work function of the analyzer. The Fermi level of the system (sample and analyzer) was determined by UPS

measurement of the sample holder with no sample bias (i.e., grounded). The sample holder can be heated to 1150 °C, and the temperature was measured by a thermocouple.

C. Results and Discussion

The UV photoemission spectra of four representative samples studied here are shown in Fig. 3. The AlN films were prepared in by GSMBE and transferred under UHV to the photoemission system. Samples were biased with 2-3 V to overcome the work function of the analyzer, and all spectra were shifted to be aligned at the valence band maximum. The spectra were scaled such that the strongest emission was the same for all curves.

A more precise description of the relation of the NEA is obtained from the spectral width. The spectral width is obtained from a linear extrapolation of the emission onset edge to zero intensity at both the low kinetic energy cutoff and at the high kinetic energy end (reflecting the valence band maximum). For a material with a positive electron affinity, Fig. 2 shows that $\chi = h\nu - E_g - W$, and for a material with a negative electron affinity Fig. 2 indicates that $0 = h\nu - E_g - W$, or rewriting, $h\nu = E_g + W$. Note that the photoemission measurements cannot be used to determine the energy position of the electron affinity for the NEA case.

To determine the energy position of the valence band maximum, the spectral gain was increased, and the intensity was extrapolated to 0 emission. The spectra are aligned in Fig. 3 at the deduced valence band maximum. In applying the relations noted above, the band gap of the bulk AlN and GaN must also be known. The literature values of the AlN and GaN band gaps are 6.2 eV and 3.4 eV, respectively.

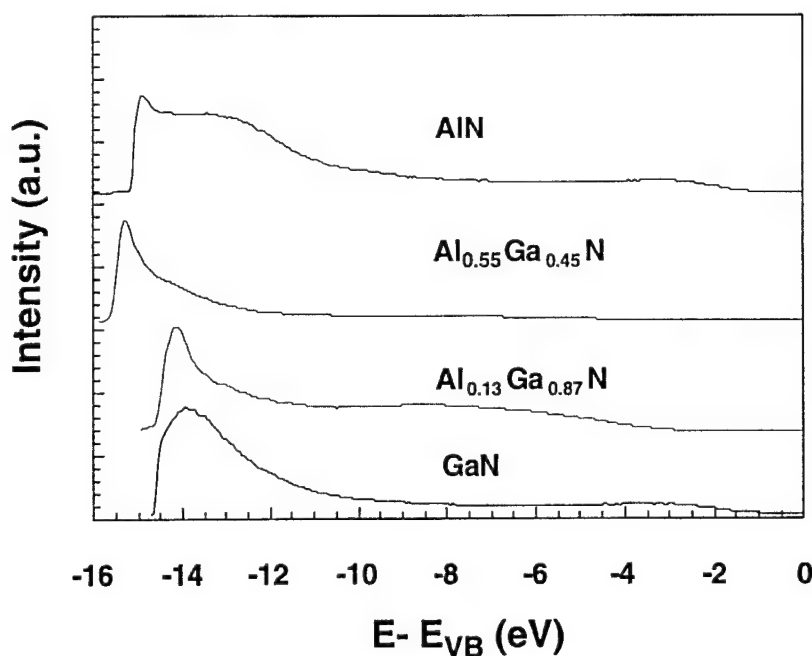


Figure 3. The UV photoemission spectra of $\text{Al}_x\text{Ga}_{1-x}\text{N}$ for $x=0, 0.13, 0.55, 1$. Spectra were aligned at the valence band maximum.

Another aspect that is evident from the photoemission spectra is the position of the surface Fermi level relative to the valence band maximum. It was found that E_F ranges from 2 to 3.5 eV above the valence band maximum for each sample. For the Ga rich surfaces, these values position E_F in the upper part of the gap while the Al rich surfaces' Fermi level is pinned roughly midgap. The pinning at midgap may be an indication of increased impurity incorporation. In particular, the strong affinity of Al with oxygen often results in increased oxygen incorporation for these films.

While previous results have shown that hydrogen can induce a negative electron affinity surface on diamond [7,10], AlN NEA surfaces exposed to H termination and H plasma treatment become positive affinity surfaces. It is evident that further studies are necessary to characterize the surfaces more completely.

AlN grown on silicon surfaces were studied also. Samples grown in our integrated system showed no LEED pattern and exhibited positive affinity. It was observed that AlN grown on (0001) SiC will exhibit positive affinity if no LEED pattern is evident. These two observations lead us to conclude that surface disorder tends to produce positive affinity surfaces.

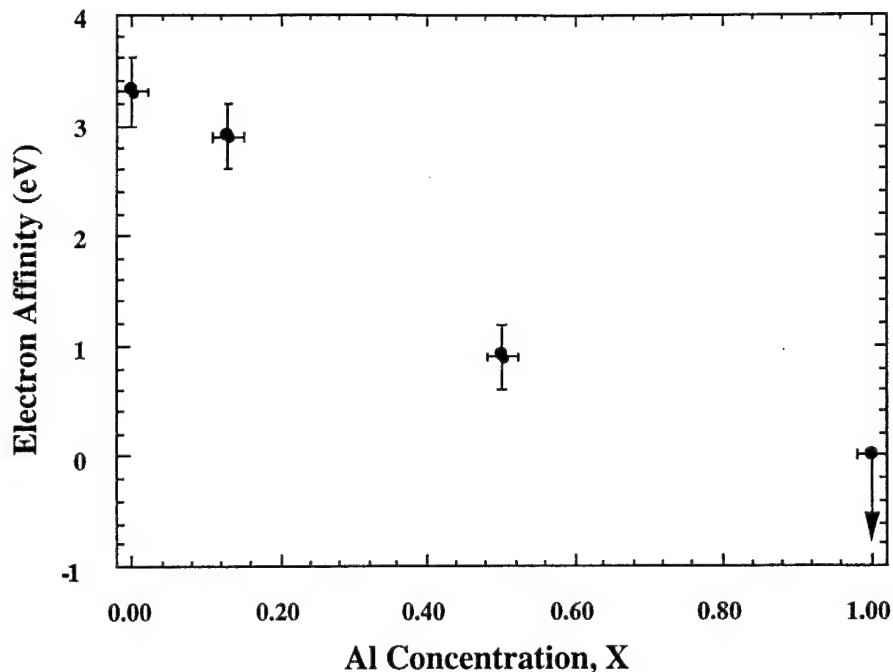


Figure 4. Electron affinities of $\text{Al}_x\text{Ga}_{1-x}\text{N}$ alloys vs. Al concentration. The arrow indicates that the electron affinity is less than (or equal) 0, but the value cannot be determined from the UV photoemission measurements.

In previous studies, no effort was made to control the surface termination for these samples. For diamond, it was found that the observation of an NEA is critically dependent on the surface termination. In this report we have, for the first time, a complete range of alloys free of ambient exposure.

By trial and error, the transition point was determined to be $65 \% \pm 2 \%$. This value is above the point that growers can currently dope ($\sim 40 \%$).

D. Conclusions

In summary, features have been observed in the UPS spectra indicative of an NEA surface for AlGa_N alloys for aluminum concentrations greater than 65%.

The AlGa_N NEA surfaces spectra exhibited both the sharp features at low kinetic energy that have been found to be characteristic of an NEA, and the width of the spectra was also consistent with the observed effect.

The surface Fermi level was found to be towards the middle of the band gap for the samples, and this may indicate oxygen impurities below the surface as AES shows no or little oxygen.

E. Acknowledgments

This work was supported in part by the Office of Naval Research through grants N0014-92-J-1477 and N0014-92-J-1604. The SiC substrates used were supplied by Cree Research.

F. References

1. S. Strite and H. Morkoç, J. Vac. Sci. Technol. B 10 1237 (1992).
2. J.H. Edgar, J. Mater. Res., 7, 235 (1992).
3. M.D. Williams, M.D. Feuer, S.C. Shunk, N.J. Sauer, and T.Y. Chang, J. Appl. Phys. 71, 3042 (1992).
4. M.C. Benjamin, C. Wang, R.F. Davis, R.J. Nemanich, Appl. Phys. Lett. 64, (1994).
5. M.C. Benjamin, C. Wang, R.S. Kern, R.F. Davis, R.J. Nemanich, Mat. Res. Soc. Symp. 339, 81 (1994).
6. F.J. Himpsel, J.A. Knapp, J.A. van Vechten and D.E. Eastman, Phys. Rev. B 20, 624 (1979).
7. B.B. Pate, Surf. Sci. 165, 83 (1986).
8. B.B. Pate, M.H. Hecht, C. Binns, I. Lindau and W.E. Spicer, J. Vac. Sci. Technol. 21, 364 (1982).
9. J. van der Weide and R.J. Nemanich, J. Vac. Sci. Technol. B 10, 1940 (1992).
10. J. van der Weide and R.J. Nemanich, Appl. Phys. Lett. 62, 1878 (1993).
11. J. van der Weide and R.J. Nemanich, Phys. Rev. B 15 49 13629 (1994).
12. R. Kaplan, Surface Science 215, 111 (1989).

XX. Thin Films of Aluminum Nitride and Aluminum Gallium Nitride for Cold Cathode Applications

Cold cathode structures have been fabricated using AlN and graded AlGa_xN structures (deposited on n-type 6H-SiC) as the thin film emitting layer. The cathodes consist of an aluminum grid layer separated from the nitride layer by a SiO₂ layer and etched to form arrays of either 1, 3, or 5 μm holes through which the emitting nitride surface is exposed. After fabrication, a hydrogen plasma exposure was employed to activate the cathodes. Cathode devices with 5 μm holes displayed emission for up to 30 min. before failing. Maximum emission currents ranged from 10-100 nA and required grid voltages ranging from 20-110V. The grid currents were typically 1 to 10^4 times the collector currents.

The electrical properties of wide band gap semiconductors in combination with the high temperature chemical stability make these materials candidates for use in high-power and high-frequency devices. Moreover, wide band gap semiconductors such as diamond [1], AlN [2], and Al_xGa_{1-x}N for $x \geq .75$ [3] show promise for use as cold cathode materials since these materials have been observed to exhibit a negative electron affinity (NEA).

The presence of a negative electron affinity for wide band gap semiconductors means that electrons excited into the conduction band can be freely emitted into the vacuum. Prior studies that detected the presence of a NEA for these materials employed UV photo excitation. Thus, carriers excited into the conduction band near the surface could escape and be detected. In contrast, for field emission from a NEA material, if electrons can be supplied to the conduction band then they would be freely emitted into the vacuum. An ideal wide band gap semiconductor would then exhibit a NEA and also sufficient n-type doping to supply electrons into the conduction band and to form low resistance contacts. To date, it has proved difficult to produce an n-type wide band gap NEA semiconductor. While n-type GaN is routinely obtained by Si doping, n-type characteristics of AlN have not been confirmed.

Much wide band gap field emission research has been dedicated to depositing diamond on various field emitting tips [4, 5] or depositing selectively grown GaN pyramids on n-type 6H-SiC [6, 7]. Indeed, some research has been dedicated to using diamond films for field emission device applications [8, 9]. Previous experiments showed that field emission from nitride materials exhibited Fowler-Nordheim behavior similar to that from diamond [10]. The approach then is to use a planar nitride surface as the emitter rather than a structure that deliberately exploits field enhancement at a sharp projection. The advantage of this approach is that sputtering and other tip degradation processes are avoided. This approach is similar to recently fabricated diamond cathodes [11].

The basic approach employed in this study is presented in the nitride cold cathode design shown in Fig. 1. An aluminum grid was separated from the nitride emitting layer by a SiO₂ layer. An array of square emission holes was etched through the aluminum and SiO₂ to the

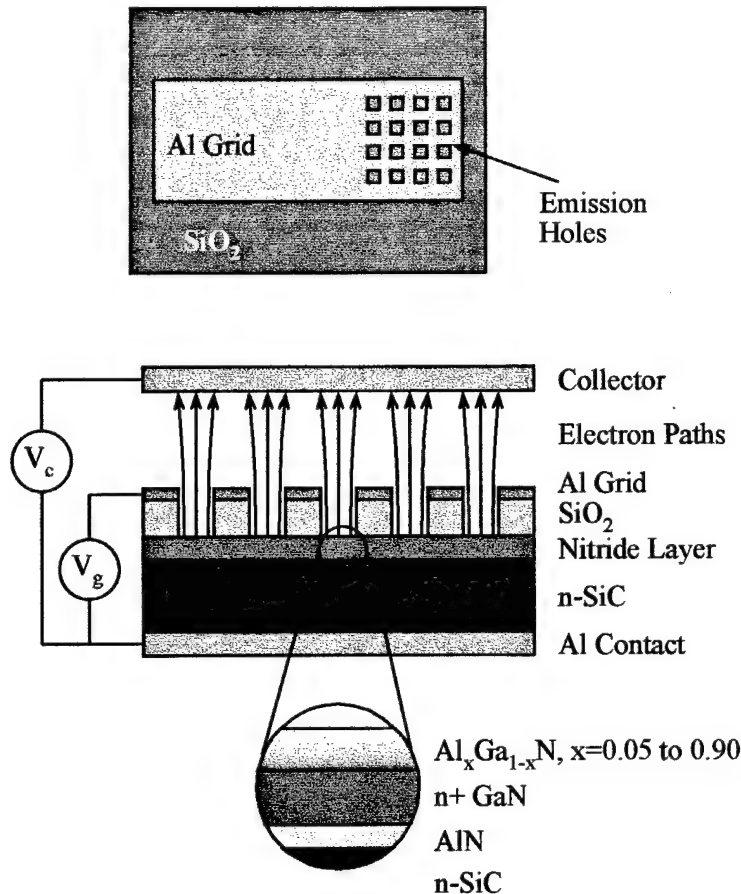


Figure 1. Schematic of the cold cathode structures. The top view (left) shows a 5×5 array of emission holes. The Al grid is 1×2 mm, the emission holes are either 1, 3, or 5 μm , and the hole spacing varies from 5 to 75 μm . The nitride layer is exposed through the holes. The schematic cross section (bottom) is across the emission holes. The inset shows the nitride layers used in the graded AlGaN devices.

nitride layer. At the bottom of the emission hole, the electron emission occurred at the vacuum-nitride interface induced by the grid voltage (V_g) between the aluminum pad and the backside contact.

Two different nitride emitting layer structures were employed. In one structure, a thin AlN layer was deposited on a n-type 6H-SiC substrate. In this case, electrons from the SiC were extracted through the AlN layer. AlN had a direct band gap of 6.2 eV while 6H-SiC had an indirect band gap of 3.0 eV. The heterojunction conduction band offset between the AlN and SiC was between 1.8 to 2.4 eV with the conduction band of the AlN above that of the SiC [2]. The second approach involved an n-type GaN base layer with an $\text{Al}_x\text{Ga}_{1-x}\text{N}$ graded layer. This graded layer varied in composition from $x=0.05$ at the interface with the GaN base layer to $x=0.90$ at the emitting surface. Electrons were supplied to the n-type GaN and then emitted

through the NEA Al rich AlGaN layer. If the grading was completely smooth then there would be no sharp barriers for the conduction electrons.

Prior to patterning, the nitride emitting layer was deposited on a 6H-SiC substrate using the metalorganic chemical vapor deposition system described elsewhere [12, 13]. The first structure employed a 1000Å AlN layer deposited directly on the SiC substrate. The second structure used a 1000Å AlN buffer layer deposited on the SiC substrate. The n+ GaN base layer was grown on this buffer layer and was 1µm thick doped to $n=1 \times 10^{19} \text{ cm}^{-3}$ with silicon. The graded $\text{Al}_x\text{Ga}_{1-x}\text{N}$ layer was 0.5µm thick and was graded from $x=0.05$ to $x=0.90$. The surfaces of both nitride emitting layers were expected to exhibit a NEA [2]. As shown by atomic force microscopy, the nitride films are smooth with root mean square roughness of ~20Å on a $1 \times 1 \text{ µm}$ scan. However, cracking of the top surface was observed by scanning electron microscopy (SEM) for the graded AlGaN emitting layer. The cracks were ~0.1µm wide with an average domain size of 5 µm^2 between cracks.

Fabrication of the cold cathodes is accomplished with a two mask process. A SiO_2 layer (~1µm thick) is deposited on the nitride layer at 400°C by low pressure chemical vapor deposition using diethylsilane and oxygen precursors. The grid layer is formed with 200-300 nm of thermally evaporated aluminum. The first mask step creates the emission holes which are either 1, 3, or 5 µm squares. Square holes were used for convenience of the lithography system. The aluminum is patterned with a standard aluminum etch. Reactive ion etching (with SF_6 and O_2) is used to etch the oxide in order to obtain high aspect ratio features. Since the RIE environment may damage the emitting surface, a wet oxide etch is used to etch the last ~0.1µm of oxide to expose the nitride layer. The second mask step defines the $1 \times 2 \text{ mm}$ metal pads that form the grids. The last processing step is thermal evaporation of 200-300 nm of aluminum onto the backside of the SiC to form an electrical contact.

The electrical testing system has two electrical probes. One probe is used to make contact to the grid and the other probe is used to collect the emission current ~1 mm above the holes. In this configuration only the total emission current for a single device is obtained. The grid voltage can be varied from 0-110 V and the collector voltage from 0-1100V using two Keithley source measure units (SMU). The SMU can simultaneously source a voltage and measure the current through the circuit. The maximum current is limited by the compliance value which was 1 µA for the collector probe and 10mA or 100mA for the grid probe. The pumping system is oil free and testing is performed at pressures $< 5 \times 10^{-7} \text{ Torr}$.

The nitride cathodes were electrically tested directly after processing and no collector or grid currents above the noise level were measured for the several devices tested. It was determined that a post processing clean was necessary to activate emission from the nitride cathodes. Since the aluminum grids are exposed, we are limited to cleans which will not etch away the grids or damage the nitride layer. The samples were cleaned ultrasonically in

methanol for 10 min. and then subjected to a remote hydrogen plasma clean at 25 mTorr and 450°C for 10 min. A hydrogen plasma exposure with these parameters has been shown to remove hydrocarbons from AlN and GaN surfaces [14]. Also, a hydrogen plasma will remove residual photoresist. After plasma exposure, the sample is immediately transported in air to the electrical testing system.

Both AlN and AlGaIn cathode structures exhibited collector currents well above the current background level. Only cathodes with 5 μm emission holes displayed emission, and the cathode lifetimes varied from several up to 30 minutes. For all measurements shown in this paper, the grid and collector currents were measured at a constant grid voltage while the collector voltage was varied. These measurements were repeated at different grid voltages for each device. This procedure was employed to verify that it was indeed the grid voltage that induced the emission. No significant direct dependence on collector voltage was observed, but the emission signal varied significantly at different times. At a constant grid voltage, the varying collector current is attributed to cathode instability rather than to the changing collector voltage.

Identical structures but without emission holes were also fabricated to test the SiO_2 properties. These test structures are on the same wafer as the cathodes, and therefore undergo the exact same processing and plasma treatments. The oxide breakdown voltage for these structures was found to be >800 V which is much higher than the grid voltages of 0-110 V used during normal cathode testing. No collector currents above the noise level have been measured for the structures without emission holes.

Figure 2a shows the average current-voltage data for four cathodes that operated for ~ 30 min. As expected, the collector current (I_c) increases with increasing grid voltage. The collector current and grid current (I_g) were essentially independent of the collector voltage and depended mainly upon the grid voltage as shown in Figure 2b. This AlGaIn cathode had the largest collector current of the graded film devices measured ($I_c \cong 10\text{nA}$). Grid currents for the AlGaIn devices were 10^3 to 10^4 times the collector current. The electrical measurement was improved and the noise baseline was reduced for the AlN devices. Similar data was obtained from the AlN cathodes with the ratio of the grid current to the collector current ranging from 1-100.

The cathodes that functioned followed similar patterns during testing. Initially, the grid current would be high, either 10 or 100 mA, depending on the SMU compliance value, and no emission was detected at the collector. Then the grid current would drop and a collector current could be measured. SEM of the cathodes after testing revealed evidence of melting of the aluminum grid layer around the emitting holes and at the point of contact between the aluminum pad and the grid probe. The emission holes would be enlarged and rounded, and sometimes

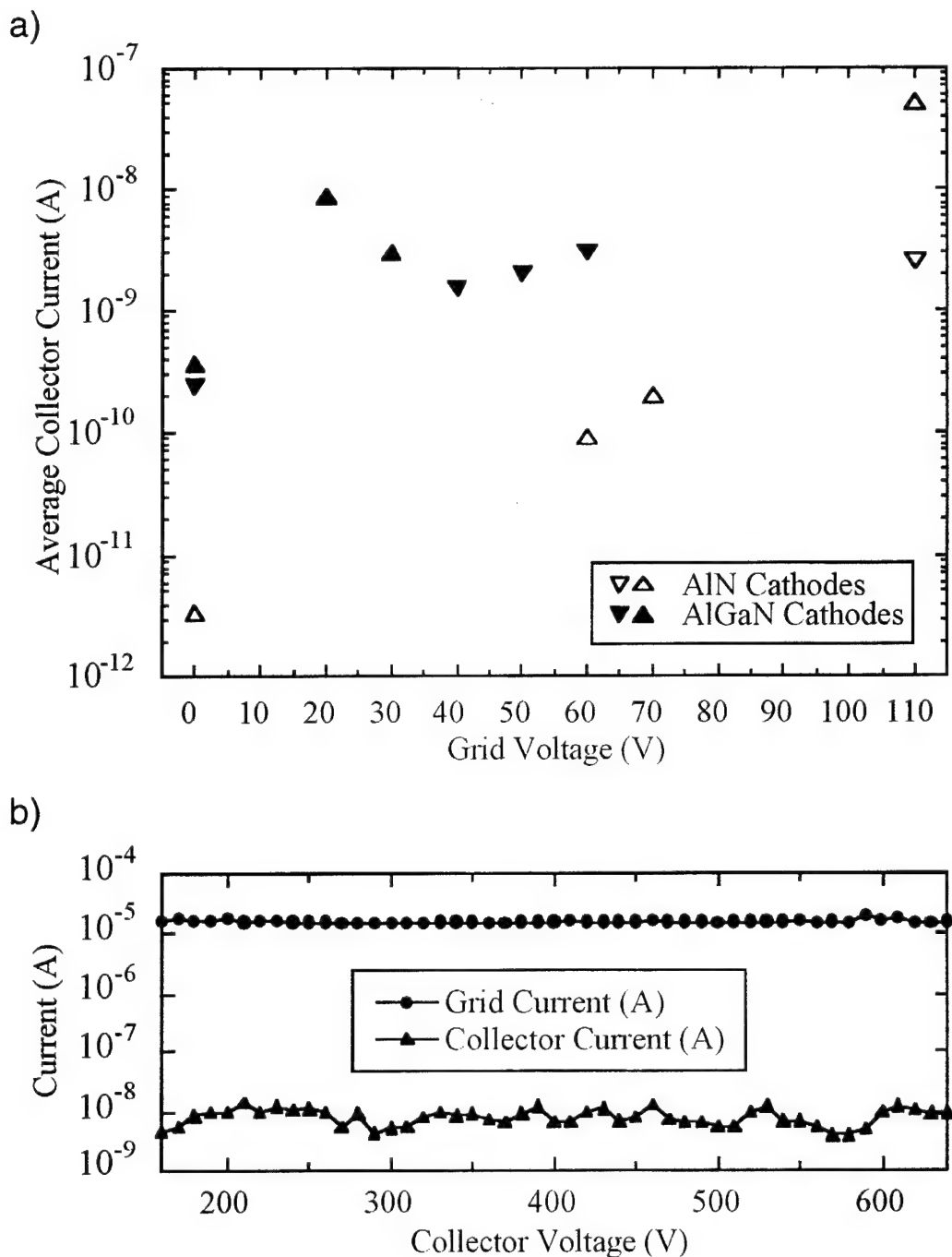


Figure 2. a) Current-voltage characteristics for four cathode devices. The open and closed triangular markers represent data obtained from devices with the thin AlN emitting layer and the graded AlGaN emitting layer, respectively. The up and down triangles are associated with different devices. The electrical measurements were improved for the AlN devices which lowered the noise baseline. b) Grid and collector currents obtained from an AlGaN cathode with $V_g = 20V$.

more severely damaged. This effect is attributed to either current flowing along the sidewalls of the emission holes or electrons emitted from the nitride surface and then collected on the aluminum grid. We suspect that after the H-plasma clean, a conducting residue coats the sides

of the emission holes. This creates a short between the grid and the nitride layer. During initial device testing, a high current flows through the residue which eventually decomposes the residue, and the current may also melt areas of the grid around the holes. After this decomposition occurs, an electric field can build up at the nitride surface and electron emission is detected. We also suspect that the devices with 1 and 3 μ m holes do not function because of residue that remains after processing.

It is difficult to make a quantitative comparison between the two nitride emitting layers. This is primarily due to the limited lifetime of the devices. As a result, data was not obtained from all devices under identical voltage conditions. In general, the AlGa_N devices required lower grid voltages than the AlN devices to begin operating. However, once emission was achieved, similar collector currents were obtained for both emitting layers. In addition, the high grid currents obtained preclude a Fowler-Nordheim analysis of the collected current.

We suggest several changes for improved operation of the nitride cathode devices. The AlN buffer layer required for high quality growth may be a significant barrier for the emission particularly from the graded films. A top contact type structure in which the electron supply contact is made to the n-type GaN layer would circumvent this problem. It is also apparent that improved fabrication processes are necessary. In addition further studies are required on the effect of various surface treatments on the electron emission from AlN or AlGa_N layers.

The authors express their appreciation to the NCSU Microelectronic Fabrication Laboratory staff for help with the lithography and processing necessary to fabricate the cathodes. We acknowledge Bill Partlow of Northrup-Grumman for additional field emission measurements and for helpful discussions. We also thank Chris Hatfield and Griff Bilbro for helpful discussions and device simulations. This research is supported by the Office of Naval Research and the Northrup-Grumman Science and Technology Center.

References

1. J. van der Weide, R. J. Nemanich, Phys. Rev. B **49**, 13629 (1994).
2. M. C. Benjamin, C. Wang, R. F. Davis, R. J. Nemanich, Appl. Phys. Lett **64**, 3288 (1994).
3. M. C. Benjamin, M. D. Bremser, J. T. W. Weeks, S. W. King, R. F. Davis, R. J. Nemanich, Appl. Surf. Sci. **104/105**, 455-460 (1996).
4. E. I. Givargizov, J. Vac. Sci. Technol. B **13**, 414-417 (1995).
5. J. Liu, V. V. Zhirnov, G. J. Wojak, A. F. Myers, W. B. Choi, J. J. Hren, S. D. Wolter, M. T. McClure, B. R. Stoner, J. T. Glass, Appl. Phys. Lett. **65**, 2842-2844 (1994).
6. O. H. Nam, M. D. Bremser, B. L. Ward, R. J. Nemanich, R. F. Davis, *III-V Nitrides* edited by F. A. Ponce, T. D. Moustakas, I. Akasaki, and B. A. Monemar (Mater. Res. Soc. Proc. **449**, Pittsburgh, PA, 1997) pp. 107-112.
7. R. D. Underwood, D. Kapolnek, B. P. Keller, S. Keller, S. P. DenBaar, U. K. Mishra, Topical Workshop on Nitrides, Nagoya, Japan, September (1995).
8. N. S. Xu, Y. Tzeng, R. V. Latham, J. Phys. D: Appl. Phys. **27**, 1988-1990 (1994).
9. M. W. Geis, J. C. Twichell, Appl. Phys. Lett. **67**, 1-4 (1995).

10. R. J. Nemanich, M. C. Benjamin, S. W. King, M. D. Bremser, R. F. Davis, B. Chen, Z. Zhang, and J. Bernholc, *GaN and Related Materials* edited by F. A. Ponce, R. D. Dupuis, S. Nakamura, and J. A. Edmond (Mater. Res. Soc. Proc. **395**, Pittsburgh, PA, 1996) pp. 375-380.
11. M. W. Geis, J. C. Twichell, N. N. Efremow, K. E. Krohn, C. Marchi, T. M. Lyszczarz, Proceedings of the 8th International Vacuum Microelectronics Conference, **p. 277** (1995).
12. M. D. Bremser, W. G. Perry, N. V. Edwards, T. Zheleva, N. Parikh, D. E. Aspnes, R. F. Davis, Mater. Res. Cos. Symp. Proc. **395**, 195 (1996).
13. M. D. Bremser, W. G. Perry, T. Zheleva, N. V. Edwards, O. H. Nam, N. Parikh, D. E. Aspnes, R. F. Davis, MRS Internet J. Nitride Semicond. Res. **1**, 8 (1996).
14. S. W. King, L. L. Smith, J. P. Barnak, J. Ku, J. A. Christman, M. C. Benjamin, M. D. Bremser, R. J. Nemanich, and R. F. Davis, in *GaN and Related Materials* edited by F. A. Ponce, R. D. Dupuis, S. Nakamura, and J. A. Edmond (Mater. Res. Soc. Proc. **395**, Pittsburgh, PA, 1996) pp. 739-744.

XXI. Theory of Interfaces in Wide Gap Nitrides

M. BUONGIORNO NARDELLI, K. RAPCEWICZ, E.L. BRIGGS, C. BUNGARO, J. BERNHOLC

Department of Physics, North Carolina State University
Raleigh, NC 27695, nardelli@quinn.physics.ncsu.edu

ABSTRACT

The results of theoretical studies of the bulk and interface properties of nitrides are presented. As a test the bulk properties, including phonons of GaN at the Γ -point, are calculated and found to be in excellent agreement with the experimental data. At interfaces, the strain effects on the band offsets range from 20% to 40%, depending on the substrate. The AlN/GaN/InN interfaces are all of type I, while the $\text{Al}_{0.5}\text{Ga}_{0.5}\text{N}$ on AlN zinc-blende (001) interface is of type II. Further, an interface similar to those used in the recent blue laser diodes is of type I and does not have any electronically active interface states. The valence band-offset in the (0001) GaN on AlN interface is -0.57 eV and the conduction band-offset is 1.87 eV.

INTRODUCTION

Interest in wide band-gap nitrides stems from possible applications in blue/UV light-emitting diodes and lasers, and in high-temperature electronics [1, 2]. The recent demonstration of stimulated emission in the blue region has served to highlight the potential of nitride-based devices.[3]

In this paper we describe several of our recent results [4] concerning the bulk properties of the III-V nitrides and their interfaces.

Using novel pseudopotentials that permit the treatment of the Ga 3-d and In 4-d electrons as core electrons, we have investigated the bulk properties of the nitrides and also phonons in GaN. With these pseudopotentials, we have also studied interfaces of AlN/GaN/InN [4]. The calculated values of the valence-band offset for AlN on GaN is -0.44 eV, while for GaN on AlN it is -0.73 eV, indicating that the effects of strain on the valence-band offset are significant. The band offsets between AlN, GaN and InN were computed using the AlN in-plane lattice constant and including strain effects. They are all of type I and the transitivity rule is satisfied. We have also studied the zinc-blende (001) $\text{Al}_{0.5}\text{Ga}_{0.5}\text{N}$ on AlN and $\text{Al}_{0.2}\text{Ga}_{0.8}\text{N}$ on $\text{In}_{0.1}\text{Ga}_{0.9}\text{N}$ interfaces in the virtual crystal approximation. The latter is based upon the laser diode of Nakamura et al. [3].

The standard *ab initio* plane-wave pseudopotential method was employed in the calculations. For the phonons, density functional linear response theory [5] was used. Further details can be found in Ref. [4]. An efficient multigrid-based method that uses a real-space grid as a basis was also used in connection with a large cell in order to simulate an interface based on the recently demonstrated blue laser diode [6].

BULK PROPERTIES

The calculated bulk properties are presented in Table 1. In general, agreement with experiment is excellent [4].

| | AlN | GaN | InN |
|-----------------------|---------------|-------------------|-------------------|
| zinc-blende | | | |
| a_0 (Å) | 4.37 (4.38) | 4.51 (4.50) | 5.01 (4.98) |
| B_0 (MBar) | 2.02 (2.02) | 1.92 (1.90) | 1.58 (1.37) |
| E_Γ (eV) | 4.09 | 2.15 (3.45) | 0.16 |
| ΔE_{vbw} (eV) | 14.86 | 15.73 | 14.01 |
| wurtzite | | | |
| a (Å) | 3.09 (3.11) | 3.20 (3.19) | 3.55 (3.54) |
| c/a | 1.62 (1.60) | 1.63 (1.63) | 1.63 (1.61) |
| u (units of c) | 0.378 (0.382) | 0.376 (0.377) | 0.375 |
| B_0 (MBar) | 1.99 (2.02) | 1.91 (1.95, 2.37) | 1.62 (1.26, 1.39) |
| E_Γ (eV) | 4.44 (6.28) | 2.29 (3.50) | 0.16 (1.89) |
| ΔE_{vbw} (eV) | 14.89 | 15.60 | 14.00 |

Table 1: Calculated bulk properties of zinc-blende and wurtzite nitride semiconductors. The values of the gap at the Γ -pt (E_Γ) and of the valence-band width (ΔE_{vbw}) are the LDA results. Note that the LDA indirect gap in zinc-blende AlN is 3.2 eV. Experimental values are in brackets and follow Ref. [7].

For comparison, the bulk properties of GaN were calculated with the 3d-electrons of gallium as valence electrons after Ref. [7]. With a cut-off of 240 Ry, we find $a_0 = 4.46$ Å and $B_0 = 2.14$ Mbar. The quality of agreement of this result with experiment is of the same order as our calculations employing pseudopotentials with the d -electrons in core.

| | c_{11} (10^{11} dyne/cm ²) | c_{12} (10^{11} dyne/cm ²) |
|-----|---|---|
| GaN | 26.62 (26.4) | 15.49 (15.3) |
| AlN | 24.85 | 13.37 |
| InN | 20.24 | 12.96 |

Table 2: Elastic constants calculated for zinc-blende AlN, GaN and InN (in units of MBar). The experimental values, in brackets, are from Ref. [8].

The calculated elastic constants are shown in Table 2. These elastic constants were used to determine the strain present in interfaces. In addition, we have calculated the band-gap deformation potential for zinc-blende GaN and find it to be -8.9 eV. Experimental measurements are available only for wurtzite and they range from -7.8 to -9.8 eV. Since in a previous theoretical calculation of this quantity, the values for wurtzite and zinc-blende were found to be very close, our results are in good agreement with the existing experimental data and we expect that our treatment of strain effects on the band structure is accurate. The frequencies of the phonon modes at the Γ -point are shown in Table 3. The agreement with experiment is satisfactory.

| | Present Theory | Experiments |
|---------|----------------|-------------|
| E_2^1 | 138 | 144 |
| B_1^1 | 334 | — |
| A_1 | 556 | 533 |
| E_1 | 568 | 560 |
| E_2^2 | 574 | 568 |
| B_1^2 | 694 | — |

Table 3: Phonon dispersion at Γ in wurtzite GaN. Experimental data are from Ref. [8].

INTERFACES OF WIDE-GAP NITRIDES

Superlattices based upon the nitrides will be strained as a result of the lattice-mismatch between AlN and GaN (2.5%) and between InN and AlN (12.1%). The interface energy, defined as the excess or deficit energy due to the presence of the interface, is extremely small, namely ~ 1 meV/atom, which is of the order of the precision of the calculations. The interfaces therefore show similar bonding characteristics.

The band offsets of the strained heterojunctions have also been studied. As the elastic energy of GaN on AlN is lower than the elastic energy of AlN on GaN, AlN is taken to be the substrate in all of the cases presented below. The valence-band offsets shown in Table 3 indicate that the effect of strain on the value of the valence-band offset in GaN on AlN is significant. In each case, VBO_{ave} was computed from the average of the split valence-band manifold.

| | ΔV | VBO | VBO_{ave} |
|--------------------------|------------|-------|-------------|
| AlN lattice constant | 1.05 | -0.73 | -0.55 |
| Average lattice constant | 0.33 | -0.58 | -0.53 |
| GaN lattice constant | 0.74 | -0.44 | -0.53 |

Table 4: Electrostatic potential line-up ΔV and valence-band offsets, VBO and VBO_{ave} . All quantities are in eV and are quoted with respect to AlN.

We also investigated the band offsets of the (001) GaN on AlN, InN on AlN and InN on GaN strained heterojunctions. The band offsets are shown in Figure 1. In determining the conduction-band offsets, the conduction band minima were shifted to their experimental values using the so-called scissors operator. In each case, the interface is of type I and, overall, the transitivity rule is satisfied. Further, there are no interface states in the gap of the superlattice and the states at the top of the valence band are largely confined to the epilayer with the smaller gap.

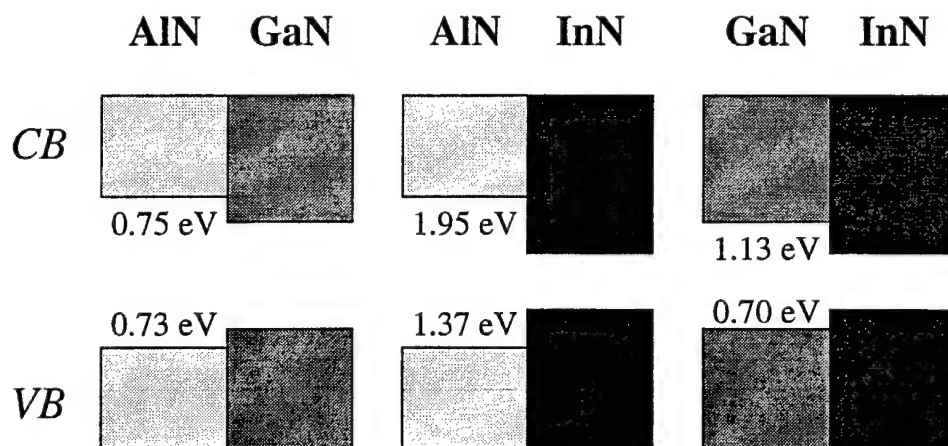


Figure 1: Calculated band offsets for the three interfaces described in the text (an AlN substrate is assumed).

The case of the wurtzite (0001) GaN on AlN interface was examined. As for the (001) interfaces, strain effects were included using macroscopic elasticity theory [10] and a total energy optimization. The calculated valence-band offset is estimated to be -0.57 eV. This value is smaller than the result for the strained non-polar (001) GaN on AlN interface.

The ratio of the conduction-band to valence-band offset is 65:20. These values agree well with the experimental measurements of the (0001) wurtzite interface [11].

The low symmetry of the wurtzite system means that pyroelectric and piezoelectric behavior may be present [12]. In accordance with the observations of Satta and coworkers [15], we find that there is a substantial electric field in (0001) strained GaN on AlN. We have calculated the spontaneous bulk polarization of unstrained AlN and the strain induced polarization for the GaN epilayer [16] in order to distinguish the bulk pyroelectric and piezoelectric contributions to this field from that induced by the interface. The spontaneous polarization (P_3) of AlN and GaN in equilibrium are $-1.227 \mu\text{C}/\text{cm}^2$ and $-0.448 \mu\text{C}/\text{cm}^2$ respectively; the polarization of the strained GaN is $-0.454 \mu\text{C}/\text{cm}^2$. These values are comparable to the computed bulk polarization in BeO [16]. The estimated contribution of the interface dipole, which includes the response of one epilayer to the field of the other, is only $0.057 \mu\text{C}/\text{cm}^2$. It is an order of magnitude smaller and has the opposite sign to the bulk polarizations. The computed value of the polarization in the multi-quantum-well agrees with that estimated from experiment by Martin *et al.* [11].

The band offsets can be tuned both through changes to the strain in the system and changes to the electronic structure accomplished by alloying. The virtual crystal approximation, in which the pseudopotentials of the constituent species are averaged according to their fractional composition [17], is the theoretical tool by which this was achieved. Strain effects were explicitly included using macroscopic elasticity theory (using the theoretically determined elastic constants) and a total energy minimization. The values for scissors corrections of the band gap of the alloys were estimated using a Vegard-type rule, namely the gap of the alloy was taken to be the average of the band gap of the pure phase weighted by its fractional composition.

We first analyzed the behavior of the zinc-blende (001) $\text{Al}_{0.5}\text{Ga}_{0.5}\text{N}$ on AlN interface. As opposed to the situation in the pure nitride interfaces, this particular alloy interface is a staggered type II interface and a change in the character of the interface is to be expected upon variation in the Ga concentration. In pure zinc-blende AlN, the gap is indirect ($\Gamma_1^v \rightarrow X_1^c$), while the gap in pure zinc-blende GaN is direct. In superlattices grown along the (001) direction X is folded into Γ and the gap is determined by the smaller of the two. In the alloy, the gap at Γ is much more strongly dependent upon the gallium composition than is the gap at X . Consequently, the dependence of the conduction band offset on gallium concentration has two distinct regimes: for small gallium concentrations, ($\leq 50\%$), where the gap is at X , ΔE_{gap} is small, the VBO dominates and the interface is of type II; for large gallium concentrations, where the gap is at Γ , the larger difference in the gaps make the interface of type I. This behavior is common to other systems, like $\text{Al}_{1-x}\text{Ga}_x\text{As}$ on AlAs, where the same effect has been experimentally observed [18].

In the same theoretical framework, we also studied an alloy interface based upon the nitride-based multi-quantum-well structure that Nakamura *et al.* [3] used to demonstrate stimulated emission in the blue region of the spectrum. The band offsets are for the valence and conduction band -0.26 eV and 0.70 eV respectively. The interface is of type I and there are no interface states in the gap. To verify this latter conclusion, we have simulated the multi-quantum-well using a 192 atom cell in which we have not made the virtual crystal approximation but, rather, have used a number of atoms exactly corresponding to the concentration of each epilayer, namely $\text{Al}_{0.2}\text{Ga}_{0.8}\text{N}$ and $\text{In}_{0.1}\text{Ga}_{0.9}\text{N}$. This calculation confirmed the absence of electrically active interface states.

The omission of the anion p - and cation d -state repulsion [9], spin-orbit effects and the well-known neglect of many-body effects in the LDA constitute the major sources of

systematic error. Spin-orbit effects in both AlN and GaN have been shown to be of the order of 20 meV, so that their difference is indeed negligible [19]. In GaN on AlN interfaces, the inclusion of the 3d-electrons as valence electrons results in a constant shift of 0.2 eV, which is less than the experimental error [11], and does not change the character of the interface. Incorporating this shift gives results in agreement with previous estimates using a *d*-valence pseudopotential [20] and an all-electron calculation [21]. The importance of many-body effects on the band offsets is not known.

REFERENCES

- [1] R. F. Davis, *Physica B* **185**, 1 (1993).
- [2] H. Morkoc, S. Strite, G. B. Gao, M. E. Lin, B. Sverdlov, and M. Burns, *J. Appl. Phys.* **76**, 1363 (1994).
- [3] S. Nakamura et al., *Jpn. J. Appl. Phys.* **35**, L74 (1996).
- [4] M. Buongiorno Nardelli, K. Rapcewicz and J. Bernholc, submitted to *Phys. Rev. B* (1996).
- [5] S. Baroni, P. Giannozzi, and A. Testa, *Phys. Rev. Lett.* **58**, 1861 (1987); P. Giannozzi, S. de Gironcoli, P. Pavone, and S. Baroni, *Phys. Rev. B*, **43**, 7231 (1991).
- [6] E. L. Briggs, D. J. Sullivan and J. Bernholc, *Phys. Rev. B* **52**, R5471 (1995).
- [7] A. F. Wright and J. S. Nelson, *Phys. Rev. B* **50**, 2159 (1994).
- [8] K. Kim, W.R.L. Lambrecht and B. Segall, *Phys. Rev. B*, **53**, 16310 (1996).
- [9] S. Wei and A. Zunger, *Phys. Rev. Lett.* **59**, 144 (1987).
- [10] The starting point of the total energy minimization was determined using the experimental ratio [22], $c_{13}/c_{33} = 0.59$.
- [11] G. Martin et al., *Appl. Phys. Lett.* **65**, 610 (1994).
- [12] N. W. Ashcroft and N. D. Mermin, *Solid State Physics* (Saunders College, Philadelphia 1976). Ch. 27.
- [13] D. Smith, *Solid State Commun.* **57**, 919 (1986).
- [14] A. Bykhovski, B. Gelmont and M. Shur, *Appl. Phys. Lett.* **63**, 2243 (1993); *J. Appl. Phys.* **74**, 6734 (1993).
- [15] A. Satta, V. Fiorentini, A. Bosin, F. Meloni and D. Vanderbilt, *MRS Proceedings* **395**, 515 (1996).
- [16] M. Posternak, A. Baldereschi, A. Catellani and R. Resta, *Phys. Rev. Lett.* **64**, 1777 (1990).
- [17] M. Peressi, S. Baroni, A. Baldereschi and R. Resta, *Phys. Rev. B* **41**, 12106 (1990).
- [18] B.A. Wilson, P. Dawson, C.W. Tu and R.C. Miller, *J. Vac. Sci. Technol. B* **4**, 1037 (1986).

- [19] M. Suzuki, T. Uenoyama and A. Yanase, Phys. Rev. B **52** 8132 (1995).
- [20] V. Fiorentini, M. Methfessel and M. Scheffler, Phys. Rev. B **47**, 13353 (1993).
- [21] E. Albanesi, W. Lambrecht and B. Segall, J. Vac. Sci. Technol. B **12**, 2470 (1994).
- [22] *Landolt-Börnstein: Numerical Data and Functional Relationships in Science and Technology*, ed. O. Madelung (Springer, New York, 1982), vol. 17.

XXII. Distribution List

| | |
|---|---|
| Dr. Colin Wood Office of Naval Research Electronics Division, Code: 312 Ballston Tower One 800 N. Quincy Street Arlington, VA 22217-5660 | 3 |
| Administrative Contracting Officer Office of Naval Research Regional Office Atlanta 100 Alabama Street, Suite 4R15 Atlanta, GA 30303 | 1 |
| Director, Naval Research Laboratory ATTN: Code 2627 Washington, DC 20375 | 1 |
| Defense Technical Information Center 8725 John J. Kingman Road, Suite 0944 Ft. Belvoir, VA 22060-6218 | 2 |